Numerical and Experimental Investigation of Hygrothermal Aging in Laminated Composites

Rocha, I.B.C.M.

DOI
10.4233/uuid:0eab23c7-9ba4-4d27-91ee-58f9f140dd34

Publication date
2019

Document Version
Final published version

Citation (APA)
Rocha, I. B. C. M. (2019). *Numerical and Experimental Investigation of Hygrothermal Aging in Laminated Composites*. [Dissertation (TU Delft), Delft University of Technology]. https://doi.org/10.4233/uuid:0eab23c7-9ba4-4d27-91ee-58f9f140dd34

Numerical and Experimental Investigation of Hygrothermal Aging in Laminated Composites

Numerical and Experimental Investigation of Hygrothermal Aging in Laminated Composites

Proefschrift

ter verkrijging van de graad van doctor
aan de Technische Universiteit Delft,
op gezag van de Rector Magnificus prof. dr. ir. T.H.J.J. van der Hagen,
voorzitter van het College voor Promoties,
in het openbaar te verdedigen op maandag 21 januari 2019 om 10:00 uur

door

Iuri Barcelos Carneiro Montenegro da Rocha

Mestre em Engenharia Civil: Estruturas e Construção Civil
Universidade Federal do Ceará, Brazilië
geboren te Fortaleza, Brazilië

Dit proefschrift is goedgekeurd door de

Promotor: Prof. dr. ir. L. J. Sluys
Copromotor: Dr. ir. F. P. van der Meer

Samenstelling promotiecommissie:

Rector Magnificus,	Voorzitter
Prof. dr. ir. L. J. Sluys,	Technische Universiteit Delft
Dr. ir. F. P. van der Meer,	Technische Universiteit Delft
Onafhankelijke leden:	
Prof. dr. ir. S. van der Zwaag,	Technische Universiteit Delft
Prof. dr. ir. I. Doghri,	Université Catholique de Louvain
Prof. dr. ir. M. Wisnom,	University of Bristol
Dr. ir. P. Kerfriden,	Cardiff University
Prof. dr. ir. M. Veljkovic,	Technische Universiteit Delft, reservelid
Overig lid:	
Dr. ir. R. P. L. Nijssen,	Knowledge Centre WMC / Inholland University of Applied Sciences

Keywords: Fiber-reinforced composites, hygrothermal aging, multiscale analysis, multiphysics, reduced-order modeling

Printed by: Gildeprint, Enschede, The Netherlands

ISBN 978-94-6323-483-2

An electronic version of this dissertation is available at
http://repository.tudelft.nl/.

None but those who have experienced them can conceive of the enticements of science. In other studies you go as far as others have gone before you, and there is nothing more to know. But in a scientific pursuit there is continual food for discovery and wonder.

Mary Shelley, *Frankenstein*

CONTENTS

SUMMARY

Although being a crucial step in structural design of laminated composites, prediction of their long-term mechanical performance remains a challenging task for which no comprehensive and reliable solution is currently available. Nevertheless, structures such as wind turbine blades, of which laminated composites constitute the main load bearing parts, must be designed to withstand 20 years of service while being subjected to a combination of fatigue loads and interaction with often extreme environmental conditions. In the end, a compromise is reached by compensating the lack of knowledge on the complex material degradation and failure mechanisms spanning multiple spatial and time scales that determine mechanical performance by adopting higher safety factors. This in turn leads to heavier, less efficient and more expensive designs. A better understanding of these mechanisms through discerning experiments and the development of fast and accurate numerical prediction tools are therefore necessary.

This work focuses on the phenomenon of hygrothermal aging (a combination of high temperatures and moisture ingression) on unidirectional laminated composites. The complexities of the aging problem, a combination of physical and chemical degradation mechanisms that affect fibers, resin and interface differently, are investigated through a combination of experiments, microscopic observation techniques and state-of-the-art numerical modeling. The result is an efficient multiscale and multiphysics framework for the prediction of failure and hygrothermal degradation in composites.

First, an experimental campaign is conducted on unidirectional glass/epoxy composite samples and on pure epoxy specimens immersed in water at 50 °C and tested quasi-statically and in fatigue. By comparing results of unaged, partially saturated, saturated and redried samples, the contributions of reversible and irreversible hygrothermal aging mechanisms are measured. The results indicate a strong correlation of degradation with the water concentration field inside the specimens. Furthermore, significant differences in strength reduction between composites and pure resin specimens point to damage in the fiber-matrix interfaces.

In order to realistically model the diffusion process that drives degradation, an experimental/numerical study is conducted on the anisotropic diffusion behavior of laminated composites. Thin material slices extracted from a thick composite panel are immersed until saturation and the obtained anisotropic diffusivity parameters are numerically reproduced through a microscopic diffusion model with periodic concentration field. The existence of an interphase transition region around the fibers is confirmed through microscopic experiments and included in the model through a level set field.

Since both the diffusion process and the resultant material degradation are highly influenced by the microstructure of the material, a multiphysics and multiscale analysis approach becomes necessary. A numerical framework for modeling of the aging process is proposed combining a macroscopic Fickian diffusion analysis with a multiscale stress equilibrium analysis based on the FE^2 method. Since the multiscale approach does not

rely on any constitutive hypotheses at the macroscale, complex failure behavior combined with plasticization and differential swelling can be accurately captured.

In order to expand the framework to allow for modeling of cyclic loading and cyclic environmental exposure, a number of additional model ingredients are developed. Firstly, a new constitutive model for epoxy combining viscoelasticity, viscoplasticity and a damage formulation with rate-dependent fracture onset is presented. The model is calibrated through a series of quasi-static and fatigue experiments on pure resin specimens at multiple strain rates and both before and after hygrothermal aging. The calibrated model is able to accurately capture the observed strain rate dependency and stiffness and strength degradations after aging, as well as correctly capturing damage activation in low-cycle fatigue. Secondly, the significant computational cost associated with the use of a cyclic multiphysics/multiscale analysis with nested micromodels is alleviated through a number of acceleration techniques. Time homogenization is used to explicitly divide the loading into a nonlinear macrochronological part and a linear computationally inexpensive microchronological one. Furthermore, the size of the microscopic boundary value problem is reduced through a combination of Proper Orthogonal Decomposition (POD) and the Empirical Cubature Method (ECM), resulting in a hyper-reduced model. The resultant reduced and time homogenized micromodel allows for speed-ups higher than 1000, dramatically accelerating the solution of the problem.

The modified version of the framework is used to numerically reproduce the experimentally obtained interlaminar shear behavior of composite samples aged for different durations. Use of the multiphysics/multiscale approach allows for accurately describing the stress state in specimens with non-uniform water concentration fields. The viscoelsatic/viscoplastic resin model is capable of capturing differences in stress response between the very slow conditioning phase and the much faster mechanical test. The model is completed by a cohesive-zone model for fiber-matrix interface debonding including friction calibrated with a set of Single Fiber Fragmentation tests performed on dry and saturated samples.

Iuri Barcelos Carneiro Montenegro da Rocha
Delft, June 2018

SAMENVATTING

Hoewel het een cruciale stap is in het ontwerp van composietlaminaten, blijft het voorspellen van hun lange-termijn mechanische eigenschappen een uitdagende taak met tot op heden geen allesomvattende en betrouwbare oplossing. Desondanks moeten constructies zoals windturbinebladen, die gemaakt worden van composietlaminaten, worden ontworpen tegen vermoeiingsbelastingen en extreme weeromstandigheden voor een levensduur van 20 jaar. In de praktijk, wordt dit gebrek aan kennis over de complexe degradatie- en faalmechanismen die op verschillende schaalniveaus opereren gecompenseerd door hogere veiligheidsfactoren. Dit leidt tot zwaardere, minder efficiënte en duurdere constructies. Het is derhalve noodzakelijk om beter inzicht te krijgen in deze mechanismen door relevante experimenten en nauwkeurige numerieke methoden.

Dit proefschrift concentreert zich op het fenomeen van hygrothermische veroudering (een combinatie van hoge temperaturen en vochtopname) van unidirectionele composietlaminaten. De complexiteit van het verouderingsproces, een combinatie van fysieke en chemische degradatiemechanismen die vezels, hars en vezel-matrix interfaces beïnvloeden, is onderzocht met een combinatie van experimenten, microscopische observatietechnieken en numerieke modellering. Het resultaat is een efficiënt multischaal en multifysisch raamwerk geschikt om zowel het bezwijken als de hygrothermische degradatie van unidirectionele composieten te voorspellen.

Ten eerste is een experimenteel onderzoek uitgevoerd aan epoxy en unidirectionele glasvezel/epoxy proefstukken geconditioneerd in 50 °C water en getest onder quasi-statische en vermoeiingsbelastingen. Door de eigenschappen van niet verouderde, gedeeltelijk verzadigde, verzadigde en wederom gedroogde proefstukken te vergelijken, zijn de bijdragen van tijdelijke en permanente hygrothermische degradatiemechanismen gemeten. De resultaten wijzen op een correlatie tussen degradatie en concentratie van water in de proefstukken. Grote verschillen in sterkteafname tussen composieten en hars wijzen op schade op de vezel-matrix interfaces.

Om het diffusieproces dat de degradatie bepaalt realistisch te modelleren, is een experimenteel/numeriek onderzoek uitgevoerd aan de anisotropische diffusiegegrag van composietlaminaten. Dunne proefstukken van het materiaal zijn uit een dikke composiet plaat genomen en de verkregen anisotropische diffusiecoëfficiënten zijn gereprouceerd met een microscopisch diffusiemodel met een periodiek concentratieveld. De aanwezigheid van een overgangszone tussen vezels en pure hars, de zogenaamde *interphase*, is bevestigd door middel van microscopische experimenten en wordt gemodelleerd met een *level set* veld.

Omdat diffusie en degradatiegedrag in grote mate afhangen van de microscopische structuur van het materiaal, is een multifysisch en multischaal modelbenadering nodig. Een numeriek raamwerk voor het verouderingsproces is ontwikkeld bestaande uit een diffusiemodel gebaseerd op de Wet van Fick en een multischaal mechanische evenwichtanalyse gebaseerd op de FE^2 methode. Omdat het macroscopische model geen constitu-

tieve aannames bevat, kunnen complexe degradatie- en faalmechanismen nauwkeurig worden gemodeleerd.

Om het raamwerk uit te breiden naar cyclische belastingen, is een aantal aanvullende modellen ontwikkeld. Ten eerste is een nieuw constitutief model voor epoxy voorgesteld met een combinatie van visco-elasticiteit, visco-plasticiteit en schade met reksnelheidsafhankelijke scheurinitiatie. Het model is gecalibreerd met *quasi*-statische en vermoeiingsproeven op epoxy proefstukken op verschillende reksnelheden zowel voor als na veroudering. Het model kan het experimenteel waargenomen reksnelheidsafhankelijke statische en vermoeiingsgedrag goed reproduceren en de afnames in stijfheid en sterkte veroorzakt door het verouderingsproces goed voorspellen. Ten tweede is de hoge numerieke inspanning die hoort bij een cyclisch multischaal/multifysisch model met ingebedde micromodellen, verlicht door middel van een aantal versnellingstechnieken. *Time Homogenization* wordt toegepast om de cyclische belasting op te splitsen in macro-chronologische (niet-lineaire) en micro-chronologische (lineaire) delen. Verder is de complexiteit van het microscopische randwaardeprobleem gereduceerd door een combinatie van de *Proper Orthogonal Decomposition (POD)* en *Empirical Cubature Method (ECM)* methoden. Het hyper-gereduceerde tijd-gehomogeniseerde model leidt tot versnellingen in rekentijd tot een factor 1000.

Het aangepaste raamwerk wordt gebruikt om het experimenteel gemeten *interlaminar* afschuifgedrag van verouderde composieten proefstukken te reproduceren. De multischaal/multifysische benadering zorgt voor een nauwkeurige beschrijving van de tijdsafhankelijke spanningsverdeling veroorzakt door niet-uniforme vochtconcentratie velden. Het viscoelastisch/viscoplastische harsmodel vertoont het verwachte materiaalgedrag zowel tijdens het langzame verouderingsproces als tijdens de relatief snelle mechanische test. Het model wordt gecompleteerd door een cohesieve wet met frictie voor de vezel-matrix interface gecalibreerd door *Single Fiber Fragmentation* proeven uitgevoerd op droge en verzadigde proefstukken.

Iuri Barcelos Carneiro Montenegro da Rocha
Delft, Juni 2018

ACKNOWLEDGEMENTS

First of all, I would like to thank my supervisor and friend Rogier Nijssen, who gave me the opportunity to come to this beautiful country which I now call home. Thank you for spotting me in the crowd and for giving me this once-in-a-lifetime opportunity. I would like to express my deepest gratitude to my promotor, Bert Sluys, for giving me the chance to be part of the Computational Mechanics group and for the valuable supervision and encouragement throughout these last four years. Thank you very much for making me, despite being an external student, feel at home when I am at the university.

Second in order — but absolutely not in importance — I would like to thank my supervisor Frans van der Meer. Without your advice and encouragement, this thesis would have been quite different, and the work much less relevant, challenging and fun. Our meetings, although usually involving a strong headache on the way home from the extended mental strain, were the high points of my PhD journey. Thank you for giving me the freedom to try the many new things I got excited about and also for bringing me down to earth when I tried to go off-track or was too ambitious. Thank you for the valuable advice on pursuing a scientific career after my PhD and for representing the very academic equilibrium point I want to converge to one day.

Many thanks to my friend and colleague Sibrand Raijmaekers, for his invaluable help with the experimental part of this work. Now, many hundreds of tested specimens later, I look back at our work collaboration and friendship throughout these four years with fondness. I am very grateful to my WMC friends Nick Lennings, Tjeerd van der Zee and Catharina Visser, for helping me form a brand new circle of friends after moving across the globe. Thanks also go to Remco Brood, Luc Smissaert, Koen Schellevis and Koert Lindenburg for the fun conversations. I am glad my office was close to the coffee machine and attracted so many nice people. A big thanks to Ben Hendriks for affording me the freedom to carry out my work.

I would like to thank the project partners involved in the MIMIC project, for their advice during many fruitful meetings. A special thanks goes to Hartmut Fischer for the help with the interphase experiments. I should also thank Lars Mikkelsen for kindly hosting me for a month at the DTU facilities in Roskilde and Erik Vogeley for helping me use their very nice X-ray CT machine. Funding from the TKI-WoZ and IRPWind projects are gratefully acknowledged.

Finally, I would like to thank my family for the love and support, especially my parents and sister. This work is as much yours as it is mine. Much love and gratitude to my in-laws. A special thanks to my dearest friend Felipe Lima for being there for me *"desde que eu me entendo por gente"*. Last, but most important, I would like to express my infinite gratitude to my wife Cristyna for her love, companionship and daily encouragement, without which I would never have endured the hardships of a PhD journey.

Iuri

1

INTRODUCTION

Here and elsewhere we shall not obtain
the best insight into things until we
actually see them growing from the beginning.

Aristotle, *Politics*

1.1. BACKGROUND

With an increase in human population, approximately 7.6 billion people at the time of writing, the need for energy is also increasing dramatically. According to the International Energy Agency (IEA), there are still more than 1 billion people without access to electricity, particularly in developing countries [1]. As those countries reach higher levels of development, their energy demands are expected to increase sharply [2].

In this scenario, the search for new energy sources and the improvement of current technologies are vital in order to allow for a sustainable growth of human population. In particular, with political and ideological shifts towards greener technologies, renewable energy sources such as wind energy play an increasingly significant role as they allow for energy generation with low environmental impact. As a result, the cumulative worldwide installed wind energy capacity saw a 350 % increase in the last 10 years (Fig. 1.1).

In recent years, the wind energy industry has been giving special attention to offshore wind farms. According to the Global Wind Energy Council (GWEC), the cumulative offshore wind energy capacity has seen significant growth between 2011 and 2017 (Fig. 1.2), with most of the new wind farms being installed in Europe. Siting wind turbines offshore is advantageous since wind speeds are higher and farms pose a reduced environmental impact. On the other hand, construction of offshore farms involves significantly higher installation and electricity transmission costs [4].

In order to reduce offshore wind farm costs relative to onshore ones, the power generated by each installed turbine must be maximized. Apart from exposing the turbine

1

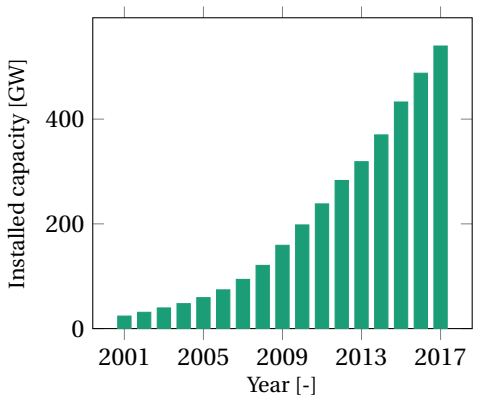

Figure 1.1: Global cumulative installed wind capacity (adapted from [3]).

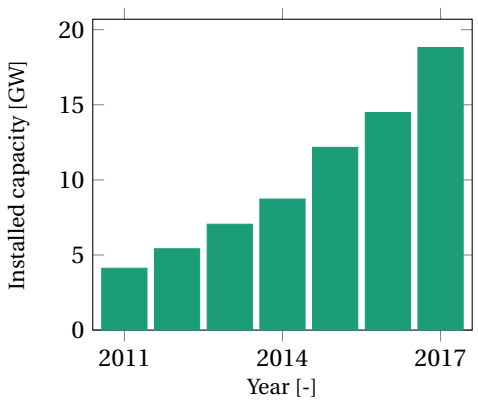

Figure 1.2: Cumulative offshore wind capacity (adapted from [3]).

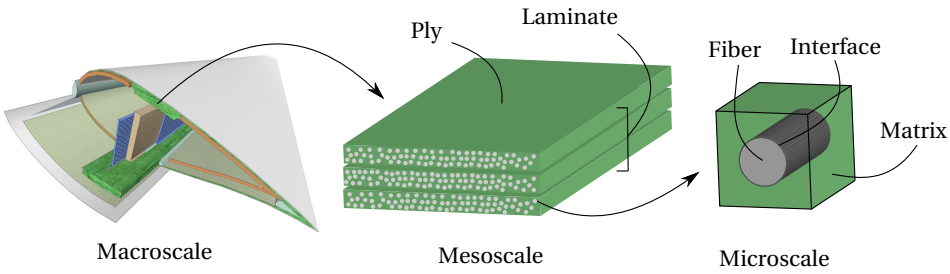

Figure 1.3: Schematic representation of a laminated composite and its scales of observation.

to faster offshore winds, higher power generation can be achieved by increasing the rotor diameter and consequently its swept area [4]. However, this leads to an increase in the gravity fatigue bending moment proportional to the fourth power of the diameter increase. Thus, adding more material actually has a detrimental effect on the fatigue life of turbine blades. To circumvent this scenario, it is necessary to optimize the use of the composite materials that compose the main load bearing structure of these blades.

Composite materials are defined as the combination of two or more base materials to obtain a new material which performs better than its constituents in isolation [5]. These materials are widely used in industrial applications, from aerospace structures to sports apparel. In the specific case of wind turbine blades, laminated composite materials, a combination of stacked plies composed of a polymeric matrix and fiber reinforcements, are employed (Fig. 1.3).

Being a highly heterogeneous combination of two materials with large stiffness gradients, laminated composites feature a complex mechanical behavior which is still not fully understood. Furthermore, as the fibers used typically feature diameters in the order of a few micrometers, the physical processes that drive material performance and durability take place at a scale much smaller than the one considered in design. Ultimately, this lack of detailed knowledge on material behavior is compensated by higher design safety factors and large experimental programmes in coupon-sized specimens which give little to no insight in the underlying microscopic processes driving material behavior.

Significant gains in design efficiency — and consequently lower design weights — are expected through deepening the knowledge on these microscopic processes and developing better prediction tools for mechanical behavior and durability of laminated composites. In particular, the interaction between the material and its service environment, commonly referred to as *aging*, is poorly understood. Material aging can significantly impact the mechanical performance of composites through the combined action of physical and chemical processes that occur at multiple time scales and can either be reversible or irreversible [6–8]. Among many types of aging, the combination of high temperatures and moisture ingression — often referred to as *hygrothermal aging* or *hot-wet aging* — is regarded as the most critical one [9–11]. Taking these aging processes into account significantly increases the complexity of predicting composite material behavior and long-term durability.

With the advent of easily accessible computational power, the use of numerical ma-

terial models as prediction tools has seen tremendous growth in the past few years. Albeit computationally expensive, high-fidelity numerical modeling presents clear advantages over closed-form analytical methods, being able to deal with complex geometries, loads and boundary conditions. It also allows the use of complex material models that include descriptions of plasticity, fracture and time-dependent behavior.

Micromechanical numerical analysis is especially advantageous for laminate composites, allowing for explicitly modeling its complex material microstructure and employing relatively simple constitutive models for each material constituent (fibers, matrix and interfaces) [12, 13]. The microscopic mechanical behavior can in turn be used to predict the macroscopic one in a multiscale approach through homogenization techniques [14, 15], while the coupling with other physical processes such as heat conduction and moisture diffusion can be handled by employing a multiphysics approach [16–18].

However, the computational cost of complex multiscale models can be exceedingly high and render the modeling effort infeasible. This is especially aggravated when the analysis is carried out at both spatial scales simultaneously (concurrent multiscale) or when a large number of analysis steps is performed — for instance when modeling cyclic loads or predicting long-term durability. A rapidly growing field of research arose in order to tackle this issue, focusing on the development of so-called reduced-order modeling (ROM) techniques [19–22]. These techniques attempt to reduce the computational complexity of a model through data compression and machine learning while minimizing loss of accuracy.

1.2. SCOPE AND OUTLINE

In this thesis, a combination of macro- and microscopic experiments and state-of-the-art numerical modeling techniques is used to investigate the phenomenon of hygrothermal aging in laminated composites. The goal is to provide a fast and accurate computational framework suitable for high-fidelity numerical analysis of unidirectional composites subjected to a combination of mechanical loads and moisture ingression. The experimental campaign is used to identify model ingredients suitable for modeling of relevant physical processes, to calibrate the employed material models and to validate the resultant framework. The methods and results presented here are limited to an epoxy resin system reinforced with glass fibers. Other composite systems may require additional model ingredients. Nevertheless, the framework can be used as a starting point for the analysis of different systems.

The rest of this chapter provides a brief introduction on a number of topics treated in the remaining chapters. The rest of the thesis is organized as follows:

- In Chapter 2, the results of an experimental campaign on hygrothermal aging are presented. The investigation includes tests on unidirectional composites and pure resin specimens, both before and after aging. The most relevant hygrothermal aging mechanisms and their relative contributions to the measured degradation are identified.

- In Chapter 3, the complexities of the moisture diffusion process in unidirectional composites are investigated through experiments and micromechanical modeling. The rates of moisture diffusion in each of the three main material direc-

tions are obtained and the role of the material microstructure on the observed anisotropy is studied.

- In Chapter 4, a multiscale and multiphysics numerical framework for hygrothermal aging is presented. At the macroscale, the model includes diffusion and stress analysis components with a one-way coupling. Micromodels are embedded at each macroscopic material point and include an elastoplastic matrix and mixed-mode cohesive interfaces.

- In Chapter 5, the elastoplastic epoxy model employed at the microscale is modified to include viscoelasticty, viscoplasticity and rate-dependent fracture initiation. An experimental campaign on pure resin specimens is presented and its results are used both to calibrate the model and to assess its capabilities.

- Chapter 6 presents a set of techniques that reduce the exceedingly high computational cost associated with concurrent multiscale models. Time homogenization is used to accelerate long-term mechanical analyses involving cyclic loads. The Proper Orthogonal Decomposition (POD) and Empirical Cubature Method (ECM) techniques are used to reduce the number of degrees of freedom and integration points of the microscopic boundary-value problem.

- In Chapter 7, the framework of Chapter 4, modified with the new developments of Chapters 5 and 6, is used to numerically reproduce hygrothermal degradation on unidirectional specimens tested in three-point bending. A new set of experiments is performed with additional aging conditions. An estimation of the fiber-matrix interface properties is obtained through micromechanical experiments. The modified framework is assessed and its drawbacks and missing ingredients are identified.

- Chapter 8 contains detailed information on the computational implementation of the numerical tools used in this thesis, with the aim of providing a suitable knowledge basis for future replication and expansion efforts.

- Finally, the scientific contributions of the work, its main conclusions and suggestions for future research directions are summarized in Chapter 9.

1.3. AGING IN LAMINATED COMPOSITES

1.3.1. TEMPERATURE

In this section, a number of degradation effects caused by thermal conditioning (isothermal and cyclic) will be briefly presented. For the specific case of the glass/epoxy composite considered in this work, the glass fibers are usually regarded as impervious to temperature changes. Therefore, focus will be given to degradation effects related to the epoxy resin, namely molecular relaxation and oxidation. Furthermore, the influence of temperature on the mechanical response of the fiber-matrix interface due to differential thermal expansion will be discussed.

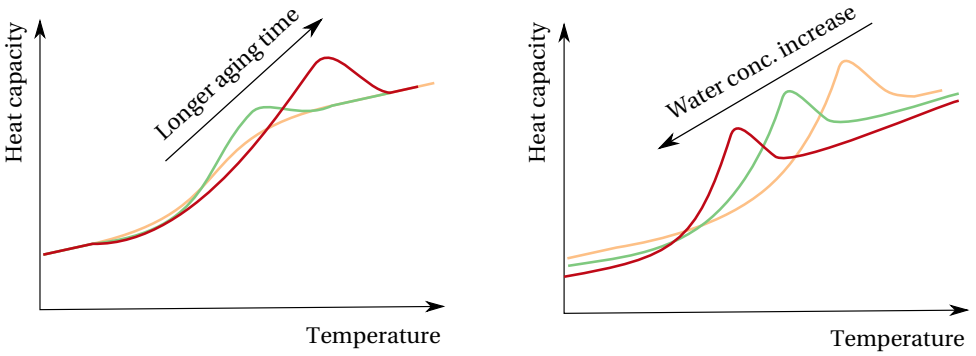

(a) Physical aging (b) Plasticization

Figure 1.4: Typical glass transition behavior of an aged polymer as measured by a DSC test.

Molecular relaxation This phenomenon, also known as *physical aging*, concerns molecular level changes on polymer chain arrangement upon exposure to temperatures below the glass transition temperature (T_g) for extended periods of time — a process commonly referred to as *annealing*. This type of aging distinguishes itself from oxidation in that the chemical structure of the polymer chains remains unchanged [23].

The reason for such relaxation behavior stems from the fact that polymers are amorphous or semi-crystalline materials that tend to seek more stable equilibrium configurations at lower energy levels. During curing, crosslinking reactions take place and tend to create an entangled configuration of polymer chains with a number of fixed crosslinked nodes that deter the formation of an energetically stable crystalline structure. Nevertheless, annealing promotes progressive changes in free volume and internal energy of the polymer chains towards lower energy states [23–25].

This enthalpy relaxation increases the necessary energy required to promote glass transition, an effect which manifests as an apparent increase in the measured glass transition temperature [23]. This effect can be detected, for instance, in a Differential Scanning Calorimetry (DSC) test, during which a constant heating ramp is applied to the polymer while tracking the energy necessary to induce this temperature change (*i.e.* its heat capacity). Near the T_g, a greater amount of energy is measured on aged polymers, as shown schematically in Fig. 1.4a.

A more compact polymer chain structure tends to affect other relevant material properties. Increases in compression strength and fracture toughness have been noted after aging [26], as well as in the thermal expansion coefficient and water diffusivity [27]. As hygrothermal conditioning often involves drying phases in which the composite material is annealed in order to promote water desorption, isolating the degradation part due exclusively to water ingression requires knowledge on the potential effects of physical aging.

Oxidation This chemical degradation effect involves a chain reaction between the resin and oxygen molecules present in air. First, free radicals acquired during processing react with oxygen molecules forming peroxide radicals. These in turn break polymer

chains and form additional free radicals from which the reaction chain continues [6]. This breaking of chains (*chain scission*) lowers the glass transition temperature [8] and promotes mechanical degradation [28].

The oxidation process is accelerated at higher temperatures and in oxygen-rich environments. In general, oxidation is associated to aging at relatively high temperatures (above 100 °C), well above the T_g of a number of polymers. In a hygrothermal aging study focused on the effects of water ingression, the impact of oxidation can therefore be limited by using relatively low (sub-T_g) conditioning temperatures and drying specimens in an evacuated environment.

Thermal expansion Differential thermal strains in composite materials manifest from the moment when fibers and resin are cured together due to a mismatch in the thermal expansion coefficient of the two materials. These residual strains at the fiber-matrix interface can be written as:

$$\boldsymbol{\varepsilon}_{\text{res}} = (\alpha_{\text{f}} - \alpha_{\text{m}})\,(T - T_0)\,\mathbf{I} \tag{1.1}$$

where $\mathbf{I}$ is the identity matrix, the subscripts m and f refer to the matrix and fiber, respectively, α is thermal expansion coefficient (isotropy is assumed) and T and T_0 are the current and curing temperature, respectively.

Changes in temperature modify this internal differential stress state and may promote fiber-matrix interface debonding [29]. When applied cyclically, interface cracks may arise due to thermal stress fatigue, for instance after a large number of day/night cycles on a climate with high temperature gradients [30, 31].

1.3.2. MOISTURE

Upon exposure to moisture, either through immersion in liquid water or through exposure to a humid environment, water diffuses into the resin. Glass fibers, on the other hand, do not absorb water and tend to act as barriers to diffusion in the resin around them, leading to anisotropic diffusion in composites. Water diffusion is a thermally activated process and diffusivity is therefore strongly influenced by conditioning temperature. On the other hand, the equilibrium moisture level is usually considered to be independent of temperature and to depend only on the humidity level of the conditioning environment.

For research purposes, it is advantageous to condition specimens at high temperatures and immersed in a water bath in order to minimize conditioning time. It is, however, unclear how representative such an accelerated aging process is of a real life service scenario. This discussion, albeit of significant relevance and still subject of scientific discussion [6], is left out of the scope of this work. In any case, it is worth mentioning that hygrothermal aging does indeed occur during service, even in structures protected from the outside environment by a coating layer. Sayer *et al.* [32] investigated water uptake on a rotor blade after 18 years of service and measured the water content at different depths inside the unidirectional composite structure that forms the blade spar caps. The authors found a constant uptake level of approximately 50 % of the water uptake attained through immersion, indicating the material had indeed reached a saturation level corresponding to the average relative humidity it experienced throughout its service life.

Since moisture diffusion is driven by concentration gradients, a one-phase Fickian behavior [33] is able to describe diffusion with acceptable accuracy for many resin systems [9, 10, 34]. This is also the case for the epoxy resin used in this work. It is worthy, however, to mention in passing that diffusion in a number of resin systems deviates from the classic Fickian behavior and more complex diffusion-reaction models are needed to accurately describe the diffusion process [35–37]. Once absorbed, water molecules tend to drive a number of degradation mechanisms, some of which are briefly presented in the following.

Plasticization Weak interactions between water molecules and polymer chains, ranging from Van der Waals bonds to single hydrogen bonds, promote a plasticizing effect, causing an increase in chain mobility and ductility [37, 38]. This in turn leads to decreases in glass transition temperature (Fig. 1.4), stiffness and strength [34, 35, 39]. In contrast to chemical reactions, these weaker physical and chemical bonds tend to be reversible upon drying.

Hydrolysis Water molecules may act as a corrosion agent and promote polymer chain scission. Similar to thermo-oxidation, breakage of chain segments leads to T_g decreases and degradation of mechanical performance in terms of stiffness and strength. Due to the irreversible nature of hydrolytic chemical reactions, this degradation is not recoverable upon drying.

Although epoxies are in general less susceptible to this type of degradation than other polymer types (*e.g.* polyesters), water can attack the coupling agent applied to the fibers meant to promote fiber-matrix interface bonding [9, 40] and therefore lead to degradation of interface performance.

Both of the aforementioned degradation mechanisms create new chemical compounds that tend to accumulate in the interior of the degraded material. If these compounds are not allowed to leach to the surrounding environment, an osmotic mechanism may be triggered which significantly accelerates water diffusion and promotes fracture due to increased hydrostatic pressure [9].

Swelling The increased polymer chain mobility and the disruption of interchain Van der Waals forces lead to a molecular rearrangement that increases the volume of the bulk resin material [38]. The resultant swelling strain is proportional to the amount of absorbed water and is usually assumed to increase linearly with water concentration:

$$\boldsymbol{\varepsilon}_{\text{sw}} = c\alpha_{\text{sw}}\mathbf{I} \tag{1.2}$$

where c is the water concentration and α_{sw} is a swelling coefficient. Since the fibers do not absorb water, swelling in the composite material leads to differential swelling stresses that may drive fracture at the fiber-matrix interfaces [9, 10, 41]. The newly created empty spaces may in turn act as secondary absorption locations and lead to deviations from the classic Fickian diffusion behavior [9, 11].

1.4. NUMERICAL MODELING

1.4.1. THE FINITE ELEMENT METHOD

The Finite Element Method (FEM) is a numerical solution technique for solving field problems. In static or quasi-static problems, the fields sought in the solution only vary in space, while transient or dynamic problems also show field variations in time. As many natural phenomena can be modeled as field problems, FEM stands out as a powerful and versatile numerical method.

The basic idea of FEM comes from modifying the classic Ritz method of obtaining approximate solutions to boundary-value problems [42]. In this method, the exact solution u of a spatial field problem is approximated by the linear combination of a number of trial functions:

$$u_{\text{trial}} = \sum_{i=1}^{n} f_i a_i \tag{1.3}$$

where f_i are trial functions that satisfy the essential boundary conditions of the problem and a_i are generalized degrees of freedom with no physical meaning [43]. Convergence towards the exact solution is achieved by adding more trial functions, which increases the fitting capability of the model.

FEM expands upon this method by substituting the generalized degrees of freedom for the field values at a number of nodal points throughout the solution domain Ω. Finite elements of size Ω_e are defined by interconnecting these nodal points. An approximation similar to Eq. (1.3) is done inside of each element:

$$u\big|_{\Omega_e} = \sum_{i=1}^{n} N_i \bar{u}_i \tag{1.4}$$

where $\bar{u}_i$ are the nodal displacements, n is the number of nodes that form the element and N_i are polynomial shape functions. A global solution in terms of the nodal degrees of freedom u_i is obtained by combining the contribution of every element and enforcing a differential field equation in a weak sense [43]. Refinement can either happen by using higher-order shape functions or by discretizing the domain Ω with a finer mesh of elements. In the following, FEM solutions for stress equilibrium and transient mass diffusion will be derived.

STRESS EQUILIBRIUM IN A CONTINUUM

Consider the two-dimensional body shown in Fig. 1.5 of volume Ω subjected to body loads $\mathbf{b}$, prescribed displacements at Γ_u and prescribed stresses at Γ_σ. Deformation is represented by a change in infinitesimal vector $d\mathbf{x}$ at the undeformed configuration to a vector $d\mathbf{X}$ at the same point of the deformed configuration. These vectors can be related by the deformation gradient tensor $\mathbf{F}$ [44]:

$$d\mathbf{X} = \mathbf{F} d\mathbf{x} \tag{1.5}$$

which, in terms of the displacements $\mathbf{u}$ by substituting $d\mathbf{X} = d\mathbf{x} + \mathbf{u}$ into 1.5:

$$\mathbf{F} = \frac{\partial \mathbf{u}}{\partial \mathbf{x}} + \mathbf{I} \tag{1.6}$$

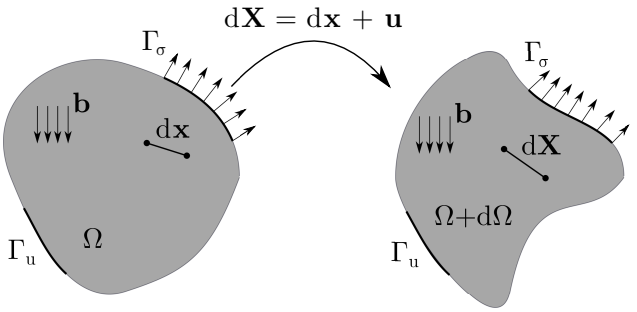

Figure 1.5: Quasi-static deformation of a two-dimensional body

where **I** is the identity matrix. The deformation gradient can in turn be used to define a measure of strain. Here, the Green strain tensor **E** is considered:

$$\mathbf{E} = \frac{1}{2}\left(\left(\frac{\partial \mathbf{u}}{\partial \mathbf{x}}\right)^{\mathrm{T}} + \frac{\partial \mathbf{u}}{\partial \mathbf{x}} + \left(\frac{\partial \mathbf{u}}{\partial \mathbf{x}}\right)^{\mathrm{T}} \frac{\partial \mathbf{u}}{\partial \mathbf{x}}\right) \tag{1.7}$$

Adopting the hypothesis of small strains, the quadratic term in Eq. (1.7) can be dropped. This results in the classic form of the small strain tensor $\boldsymbol{\varepsilon}$:

$$\boldsymbol{\varepsilon} = \frac{1}{2}\left(\left(\frac{\partial \mathbf{u}}{\partial \mathbf{x}}\right)^{\mathrm{T}} + \frac{\partial \mathbf{u}}{\partial \mathbf{x}}\right) \tag{1.8}$$

By definition, the body strains under the action of loads of prescribed displacements until stress equilibrium is reached. Equilibrium can be mathematically enforced by solving:

$$\frac{\partial}{\partial \mathbf{x}} \cdot \boldsymbol{\sigma} + \mathbf{b} = \mathbf{0} \tag{1.9}$$

where $\boldsymbol{\sigma}$ is the stress tensor. Both Eqs. (1.8) and (1.9) must be satisfied at every point of Ω while satisfying the constitutive behavior of the material being modeled:

$$\boldsymbol{\sigma} = \mathscr{D}(\boldsymbol{\varepsilon}, \mathbf{v}) \tag{1.10}$$

where $\mathscr{D}$ represents a general constitutive operator and **v** are internal variables that store the state of the material. Crafting new constitutive models with the necessary physics for each specific application entails the definition of $\mathscr{D}$ and its associated internal variables [45–47]. The equilibrium problem is completed with the definition of the boundary conditions acting on surfaces Γ_{u} and Γ_{σ}:

$$\mathbf{u}\big|_{\Gamma_{\mathrm{u}}} = \mathbf{u}_{\mathrm{p}} \quad \boldsymbol{\sigma}\mathbf{n}\big|_{\Gamma_{\sigma}} = \mathbf{f}_{\mathrm{p}} \tag{1.11}$$

with $\mathbf{u}_{\mathrm{p}}$ and $\mathbf{f}_{\mathrm{p}}$ being prescribed displacements and forces, respectively, and **n** is the normal to the surface Γ_{σ}.

In order to solve the problem using FEM, it is useful to transform Eqs. (1.8) and (1.9) in integrals, which allows for the contribution of all finite elements to be combined. Us-

ing the Virtual Work Principle and representing strains and stresses as vectors (Voigt notation), the following weak integral form is obtained [43]:

$$\int_{\Omega} (\delta\boldsymbol{\varepsilon})^{\mathrm{T}}\,\boldsymbol{\sigma}\,\mathrm{d}\Omega = \int_{\Omega} (\delta\mathbf{u})^{\mathrm{T}}\,\mathbf{b}\,\mathrm{d}\Omega + \int_{\Gamma_{\sigma}} (\delta\mathbf{u})^{\mathrm{T}}\,\mathbf{f}_{\mathrm{p}}\,d\Gamma \tag{1.12}$$

where $\delta\mathbf{u}$ is a small displacement perturbation that satisfies essential boundary conditions and $\delta\boldsymbol{\varepsilon}$ are its associated strains.

Recalling the nodal interpolation in Eq. (1.4), displacements inside element e can be written as:

$$\mathbf{u}_e = \begin{bmatrix} N_1 & 0 & \cdots & N_n & 0 \\ 0 & N_1 & \cdots & 0 & N_n \end{bmatrix} \bar{\mathbf{u}}_e \quad \Rightarrow \quad \mathbf{u}_e = \mathbf{N}_{\mathrm{u},e}\bar{\mathbf{u}}_e \tag{1.13}$$

where $\mathbf{u}_e$ are nodal displacements and a two-dimensional element is considered for the sake of simplicity. Substitution of Eq. (1.13) into Eq. (1.8) yields:

$$\boldsymbol{\varepsilon}_e = \begin{bmatrix} \frac{\partial N_1}{\partial x} & 0 & \cdots & \frac{\partial N_n}{\partial x} & 0 \\ 0 & \frac{\partial N_1}{\partial y} & \cdots & 0 & \frac{\partial N_n}{\partial y} \\ \frac{\partial N_1}{\partial y} & \frac{\partial N_1}{\partial x} & \cdots & \frac{\partial N_n}{\partial x} & \frac{\partial N_n}{\partial y} \end{bmatrix} \bar{\mathbf{u}}_e \quad \Rightarrow \quad \boldsymbol{\varepsilon}_e = \mathbf{B}_{\mathrm{u},e}\bar{\mathbf{u}}_e \tag{1.14}$$

Substituting Eqs. (1.13) and (1.14) into both sides of Eq. (1.12) yields expressions for the variations of the internal and external virtual works for element e:

$$\delta W_e^{\mathrm{int}} = \delta\bar{\mathbf{u}}_e^{\mathrm{T}} \left(\int_{\Omega_e} \mathbf{B}_{\mathrm{u},e}^{\mathrm{T}}\boldsymbol{\sigma}\,\mathrm{d}\Omega \right) \quad \delta W_e^{\mathrm{ext}} = \delta\bar{\mathbf{u}}_e^{\mathrm{T}} \left(\int_{\Omega_e} \mathbf{N}_{\mathrm{u},e}^{\mathrm{T}}\mathbf{b}\,\mathrm{d}\Omega + \int_{\Gamma_{\sigma e}} \mathbf{N}_{\mathrm{u},e}^{\mathrm{T}}\mathbf{f}^{\Gamma}\,\mathrm{d}\Gamma \right) \tag{1.15}$$

Combining the contribution of every element through an assembly procedure that takes into account element connectivity (represented here by an upper-case A operator) and recalling that Eq. (1.12) must be valid for every small but admissible displacement perturbation $\delta\bar{\mathbf{u}}$, the global equilibrium problem is obtained:

$$\mathbf{f}^{\Omega}(\bar{\mathbf{u}}) = \mathbf{f}^{\Gamma} \tag{1.16}$$

where $\mathbf{f}^{\Omega}$ and $\mathbf{f}^{\Gamma}$ are the global internal and external force vectors, respectively, given by:

$$\mathbf{f}^{\Omega} = \mathop{\mathrm{A}}_{e=1}^{n_{\mathrm{e}}} \left(\int_{\Omega_e} \mathbf{B}_{\mathrm{u},e}^{\mathrm{T}}\boldsymbol{\sigma}\,\mathrm{d}\Omega \right) \quad \mathbf{f}^{\Gamma} = \mathop{\mathrm{A}}_{e=1}^{n_{\mathrm{e}}} \left(\int_{\Omega_e} \mathbf{N}_{\mathrm{u},e}^{\mathrm{T}}\mathbf{b}\,\mathrm{d}\Omega + \int_{\Gamma_{\sigma e}} \mathbf{N}_{\mathrm{u},e}^{\mathrm{T}}\mathbf{f}_{\mathrm{p}}\,\mathrm{d}\Gamma \right) \tag{1.17}$$

where n_{e} is the number of elements in the mesh. This global system of equations can be solved directly or iteratively, depending on the behavior of the constitutive operator $\mathscr{D}$. The equilibrium paths of nonlinear problems are usually found using a Newton-Raphson algorithm at each load or displacement increment [48]. More complex equilibrium paths with snap-through or snap-back behaviors can be followed by so-called arc-length algorithms [48–52].

Although not explicitly arising from the virtual work formulation, computing a tangent stiffness matrix is necessary in order to solve Eq. (1.16):

$$\mathbf{K}^{\Omega} = \frac{\partial\mathbf{f}^{\Omega}}{\partial\bar{\mathbf{u}}} = \mathop{\mathrm{A}}_{e=1}^{n_{\mathrm{e}}} \left(\int_{\Omega_e} \mathbf{B}_{\mathrm{u},e}^{\mathrm{T}}\mathbf{D}\mathbf{B}_{\mathrm{u},e}\,\mathrm{d}\Omega \right) \tag{1.18}$$

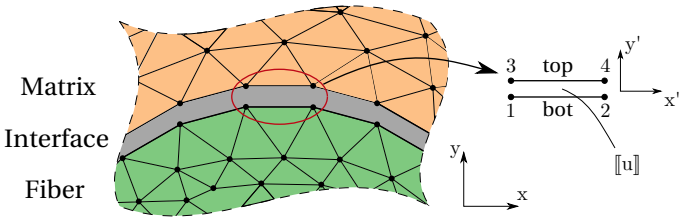

Figure 1.6: A two-dimensional interface element embedded between a fiber and surrounding matrix.

where $\mathbf{D}$ is the tangent constitutive matrix:

$$\mathbf{D} = \frac{\partial \boldsymbol{\sigma}}{\partial \boldsymbol{\varepsilon}} \tag{1.19}$$

Consistent linearization of the constitutive response is crucial in order to assure optimal convergence of the Newton-Raphson iterative procedure [48]. Convergence issues are particularly problematic when nonlinear constitutive models with sharp transitions (for instance at the onset of fracture or when unloading is triggered) are employed. In these situations, correct definition of $\mathbf{D}$ significantly improves the numerical robustness of the model.

STRESS EQUILIBRIUM ACROSS A DISCONTINUITY

The preceding FEM solution for stress equilibrium assumes the displacement field $\mathbf{u}$ is continuous in Ω. However, since fracture is a discontinuous phenomenon by nature, cracks are better represented by displacement discontinuities. In the specific context of this thesis, allowing for discontinuities to form between fibers and resin provides a realistic way to model fiber-matrix interface debonding.

The most straightforward way to introduce a displacement discontinuity in a continuum model, and the one adopted in this work, is by inserting a so-called interface element between two continuum elements [53, 54], as illustrated in Fig. 1.6. For the sake of simplicity, the formulation presented here considers two-dimensional interfaces, but extension to three dimensions is trivial.

In a non-deformed state, the two faces of the element lie on top of each other. During loading they are drawn apart and the relative displacement between them is used to define a displacement jump. Referring to the element faces as *top* and *bottom* (Fig. 1.6), standard finite element interpolation can be applied to each one separately:

$$\mathbf{u}^{\text{top}} = \mathbf{N}\bar{\mathbf{u}}^{\text{top}} \quad \mathbf{u}^{\text{bot}} = \mathbf{N}\bar{\mathbf{u}}^{\text{bot}} \quad \mathbf{N} = \begin{bmatrix} N_1 & 0 & N_2 & 0 \\ 0 & N_1 & 0 & N_2 \end{bmatrix} \tag{1.20}$$

where the functions N_i are the same used for continuum elements. The displacement jump $[\![\mathbf{u}]\!]$ is defined as:

$$[\![\mathbf{u}]\!] = \mathbf{u}^{\text{top}} - \mathbf{u}^{\text{bot}} = \begin{bmatrix} \mathbf{N}^{\text{u}} & -\mathbf{N}^{\text{u}} \end{bmatrix} \begin{Bmatrix} \bar{\mathbf{u}}^{\text{top}} \\ \bar{\mathbf{u}}^{\text{bot}} \end{Bmatrix} \quad \Rightarrow \quad [\![\mathbf{u}]\!] = \mathbf{N}^{\text{u}}_{\text{int}} \bar{\mathbf{u}} \tag{1.21}$$

In order to control the displacement jump growth — and therefore the fracture energy dissipation — cohesive tractions are applied to both element faces (Fig. 1.6) and take the place of the stresses of Eq. (1.10):

$$\mathbf{t} = \mathscr{D}_{\text{int}}\left(\llbracket \mathbf{u} \rrbracket, \mathbf{v}\right) \tag{1.22}$$

where $\mathscr{D}_{\text{int}}$ is a general traction-separation law and $\mathbf{v}$ is a set of internal variables. The contribution of the interface tractions to the internal force and tangent stiffness matrix can be written as:

$$\mathbf{f}_{\text{int}}^{\Gamma} = \mathop{\mathsf{A}}_{e=1}^{n_{\text{e}}} \int_{\Gamma_{\text{int},e}} \mathbf{N}_{\text{int},e}^{\text{T}} \mathbf{t}\, \mathrm{d}\Gamma \quad \mathbf{K}_{\text{int}}^{\Gamma} = \mathop{\mathsf{A}}_{e=1}^{n_{\text{e}}} \int_{\Gamma_{\text{int},e}} \mathbf{N}_{\text{int},e}^{\text{T}} \mathbf{T} \mathbf{N}_{\text{int},e}\, \mathrm{d}\Gamma \tag{1.23}$$

where $\mathbf{T}$ is the tangent constitutive matrix for interface elements:

$$\mathbf{T} = \frac{\partial \mathbf{t}}{\partial \llbracket \mathbf{u} \rrbracket} \tag{1.24}$$

Interface elements perform optimally when employed to model actual boundaries between materials, which is the case for the micromechanical models developed in this thesis. In situations for which the crack path is not known *a priori*, positioning interface elements can be a complex task. The straightforward approach to circumvent this drawback is to include interfaces along every continuum element boundary [55]. However, apart from the added computational effort caused by duplicated nodes and additional integration points, a mesh bias may be introduced as the element edge orientations influence the direction of crack propagation.

It is therefore worth mentioning a number of alternative techniques that have been rising in popularity in the past few years, such as Partition of Unity (PUM), also called XFEM (Extended Finite Element Method) or GFEM (Generalized Finite Element Method) [56–58] and the Phantom Node Method [59]. These methods allow for cracks to run inside continuum elements with an arbitrary orientation.

TRANSIENT DIFFUSION

Consider the two-dimensional body shown in Fig. 1.7 with a concentration field c varying in space, prescribed concentration at Γ_{c} and prescribed mass flux at Γ_{j}. Diffusion manifests as a movement of matter from regions of higher concentrations to regions of lower concentrations. This mass flux can be written as:

$$\mathbf{j} = -\mathbf{D}\frac{\partial c}{\partial \mathbf{x}} \tag{1.25}$$

where $\mathbf{j}$ is the flux vector and $\mathbf{D}$ is a diffusivity matrix that determines diffusion speed. Similar to a constitutive model for stress analysis, $\mathbf{D}$ may be a constant (linear diffusivity) or depend on c or other fields (nonlinear diffusivity). It is interesting to note that Eq. (1.25) is similar to Fourier's law for heat conduction. Numerical treatment of heat conduction and mass flow is therefore similar.

With the definition of flux, the variation of concentration in time at a certain point in space can be seen as the net flux on a differential plane (or volume) element around it.

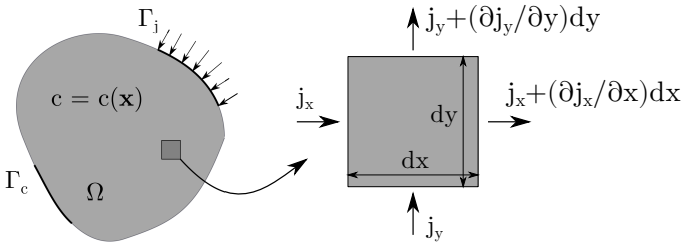

Figure 1.7: Diffusion through a two-dimensional body, with a differential material plane in detail.

Fig. 1.7 shows such an element, from which the concentration variation can be written as:

$$\frac{\partial c}{\partial t} + \frac{\partial}{\partial \mathbf{x}} \cdot \mathbf{j} = 0 \tag{1.26}$$

which is known as Fick's second law of diffusion [33], which must be solved for c at each time step. The problem is completed by formalizing the concentration and flux boundary conditions:

$$c\big|_{\Gamma_c} = c_p \quad \mathbf{jn}\big|_{\Gamma_j} = \mathbf{j}_p \tag{1.27}$$

where $\mathbf{n}$ is the vector normal to the surface Γ_j and c_p and $\mathbf{j}_p$ are prescribed concentration and flux values, respectively.

Discretization of the domain Ω in finite elements allows the constructions of nodal interpolations for both the concentration c and its variation in time, denoted by $\dot{c}$:

$$c_e = \begin{bmatrix} N_1 & N_2 & \cdots & N_n \end{bmatrix} \bar{\mathbf{c}}_e \quad \Rightarrow \quad c_e = \mathbf{N}_{c,e}\bar{\mathbf{c}}_e \tag{1.28}$$

$$\dot{c}_e = \begin{bmatrix} N_1 & N_2 & \cdots & N_n \end{bmatrix} \dot{\bar{\mathbf{c}}}_e \quad \Rightarrow \quad \dot{c}_e = \mathbf{N}_{c,e}\dot{\bar{\mathbf{c}}}_e \tag{1.29}$$

where $\bar{\mathbf{c}}_e$ and $\dot{\bar{\mathbf{c}}}_e$ are vectors of nodal values at element e. Similar to Eq. (1.14) for stress analysis, the concentration gradients of Eq. (1.25) are also interpolated:

$$\frac{\partial c_e}{\partial \mathbf{x}} = \begin{bmatrix} \frac{\partial N_1}{\partial x} & \frac{\partial N_2}{\partial x} & \cdots & \frac{\partial N_n}{\partial x} \\ \frac{\partial N_1}{\partial y} & \frac{\partial N_2}{\partial y} & \cdots & \frac{\partial N_n}{\partial y} \end{bmatrix} \bar{\mathbf{c}}_e \quad \Rightarrow \quad \frac{\partial c_e}{\partial \mathbf{x}} = \mathbf{B}_{c,e}\bar{\mathbf{c}}_e \tag{1.30}$$

A weak integral form of the problem inside a single element is obtained through a Galerkin approach [43]:

$$\int_{\Omega_e} \mathbf{N}_{c,e}^{\mathrm{T}} \left(\frac{\partial}{\partial \mathbf{x}} \left(\mathbf{D} \frac{\partial c}{\partial \mathbf{x}} \right) - \dot{c} \right) \mathrm{d}\Omega = \mathbf{0} \tag{1.31}$$

Applying integration by parts to the first term of Eq. (1.31) and summing the contribution of every finite element, the following compact form is obtained:

$$\mathbf{K}^{\Omega}\bar{\mathbf{c}} + \mathbf{C}^{\Omega}\dot{\bar{\mathbf{c}}} = \mathbf{j}^{\Gamma} \tag{1.32}$$

where $\mathbf{K}^{\Omega}$ is the global diffusion matrix, $\mathbf{C}^{\Omega}$ is the global capacity matrix and $\mathbf{j}^{\Gamma}$ is the global flux vector:

$$\mathbf{K}^{\Omega} = \mathop{\mathsf{A}}_{e=1}^{n_e} \left(\int_{\Omega_e} \mathbf{B}_{c,e}^{\mathrm{T}} \mathbf{D} \mathbf{B}_{c,e} \, \mathrm{d}\Omega \right) \quad \mathbf{C}^{\Omega} = \mathop{\mathsf{A}}_{e=1}^{n_e} \left(\int_{\Omega_e} \mathbf{N}_{c,e}^{\mathrm{T}} \mathbf{N}_{c,e} \, \mathrm{d}\Omega \right) \quad \mathbf{j}^{\Gamma} = \mathop{\mathsf{A}}_{e=1}^{n_e} \left(\int_{\Gamma_{j,e}} \mathbf{N}_{c,e}^{\mathrm{T}} \mathbf{j}_p \, \mathrm{d}\Gamma \right) \tag{1.33}$$

Eq. (1.32) is solved with a suitable time integration algorithm which can be either implicit or explicit [48, 60].

1.4.2. MATERIAL MODELS

This section briefly presents a number of types of constitutive law that can be employed to model nonlinear material behavior. In essence, the models presented in the following can be used to fill in the role of the constitutive operators $\mathscr{D}$ and $\mathscr{D}_{\text{int}}$ of Eqs. (1.10) and (1.22), respectively. Here, only the general idea of each type of model is presented. Further details on the specific formulations used in this work will be presented in the remaining chapters as the need for their use arises.

ELASTICITY

At the microscopic scale and for pristine material conditions (*i.e.* in the linear regime), both fibers and resin are modeled with a simple isotropic linear-elastic constitutive model based on Hooke's law:

$$\boldsymbol{\sigma} = \mathbf{D}\boldsymbol{\varepsilon} \tag{1.34}$$

where $\mathbf{D}$ is a stiffness tensor defined in terms of the Young's (E) and shear (G) moduli of the material being modeled. In this work, only the resin and interfaces are assumed to display nonlinear behavior. Fiber behavior is assumed to remain linear-elastic inside the strain ranges considered here.

Viscoelasticity Polymers, among which the epoxy resin considered here, are known to exhibit viscoelastic behavior that manifests as strain rate dependency [46, 61], ratcheting [62], stress relaxation [63] and hysteresis [64]. Since all of these phenomena happen within the elastic domain (*i.e.* strains and stresses are fully recoverable upon unloading), it is necessary to include a time-dependent element in Eq. (1.34).

One straightforward way to achieve this is by using a rheological element composed of a spring and a dashpot arranged in series, known as a Maxwell element. For a unidimensional element, this results in an exponentially decaying stress in time upon instantaneous application of an initial strain ε_0 given by [48]:

$$\sigma(t) = E\varepsilon_0 \left(\frac{-tE}{\eta} \right) \tag{1.35}$$

where η is the viscosity of the dashpot.

In practice, a single spring-dashpot element is not sufficient to fully describe the viscoelastic behavior of polymers across time scales. One can therefore opt for a chain of Maxwell elements arranged in parallel, each with its own stiffness (E_i) and viscosity (η_i), coupled with a long-term stiffness element that is time-independent, resulting in a total instantaneous stiffness $E_0 = E_\infty + \sum E_i$. A rheological representation of the model and its relaxation response are shown in Fig. 1.8.

PLASTICITY

Plasticity is a popular constitutive framework used to describe nonlinear material behavior, particularly for metals and quasi-brittle materials like rock, concrete and ceramics [48, 65, 66]. The basic idea of plasticity is that nonlinearity arises through the development of permanent (plastic) strains. In the specific case of glassy polymers such

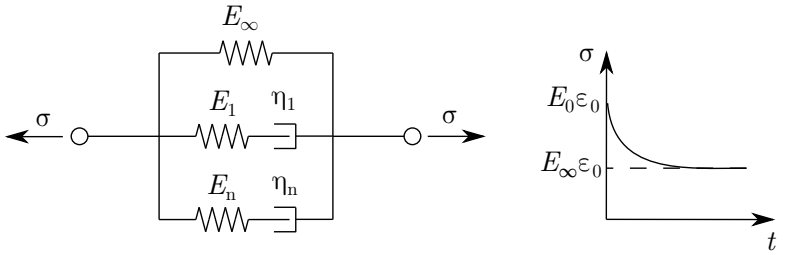

(a) Rheological model (b) Time-dependent response

Figure 1.8: Maxwell chain viscoelastic model.

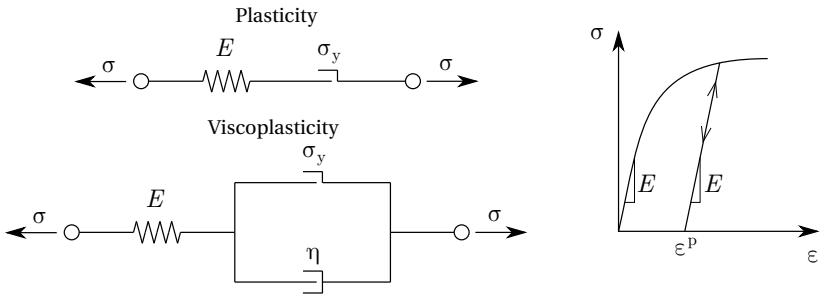

(a) Rheological models (b) Stress-strain response

Figure 1.9: Rheological representation and typical stress-strain behavior of plasticity models

as epoxy, these permanent strains are attributed to irreversible movement of polymer chains relative to one another and changes in segmental orientation [67–69]. Although arising from intrinsically different mechanisms as the ones responsible for plasticity in metals, classic metal plasticity formulations are often used for polymers. This behavior can be rheologically represented by a frictional slider element (Fig. 1.9a).

The model supposes a decomposition of strain in elastic and plastic parts, and stress is computed as:

$$\boldsymbol{\sigma} = \mathbf{D}\left(\boldsymbol{\varepsilon} - \boldsymbol{\varepsilon}^{\mathrm{p}}\right) \tag{1.36}$$

where $\mathbf{D}$ is the elastic stiffness tensor of Eq. (1.34). This results in the elastic unloading behavior shown in Fig. 1.9b. Plastic strain evolution is dictated by a flow rule with general form given by:

$$\dot{\boldsymbol{\varepsilon}}^{\mathrm{p}} = \dot{\lambda}\mathbf{m} \tag{1.37}$$

where λ is a scalar plastic multiplier and $\mathbf{m}$ is the plastic flow direction, and a yield surface $f = f(\boldsymbol{\sigma})$ determines $\dot{\lambda}$ through the classic Kuhn-Tucker conditions:

$$\dot{\lambda} \geq 0 \quad f \leq 0 \quad \dot{\lambda} f = 0 \tag{1.38}$$

which usually results in a nonlinear system of equations solved by a return mapping algorithm [48, 70].

Viscoplasticity A special class of plasticity models allows for strain rate dependent plastic strain development, which consequently leads to stress equilibrium states that lie beyond the yield surface — that is, f is allowed to attain positive values. This requires substituting the Kuhn-Tucker conditions of Eq. (1.38) for alternative formulations of λ. A popular approach, known as the Perzyna model [46, 48, 71], is to compute the plastic multiplier as:

$$\dot{\lambda} = \frac{1}{\eta_{\mathrm{p}}} \langle f \rangle \tag{1.39}$$

where η_{p} is a viscoplastic parameter and $\langle \cdot \rangle$ are the Macaulay's brackets, which return the positive part of their operand. Eq. (1.39) is the simplest form of a Perzyna model, but formulations with additional parameters can also be found in literature [46, 71].

DAMAGE

Continuum damage models offer a straightforward way to take into account fracture phenomena in a smeared sense. The main idea of damage models is that the effective material area bearing the stresses decreases as it fractures. This can be written as [48, 72]:

$$A = (1 - d)\, A_0 \tag{1.40}$$

where d is a damage variable which is zero for the pristine material (corresponding to the initial area A_0) and 1 for the completely damaged material. The damage variable is usually defined as a function $d = d(\mathbf{r})$ of one or more internal variables. The secant (damaged) stiffness $\mathbf{D}^{\mathrm{s}}$ is used to compute stresses:

$$\boldsymbol{\sigma} = \mathbf{D}^{\mathrm{s}} \boldsymbol{\epsilon} \tag{1.41}$$

In the simplest of damage formulations, the secant matrix is given by:

$$\mathbf{D}^{\mathrm{s}} = (1 - d)\mathbf{D} \tag{1.42}$$

which implies that both bulk and shear stiffnesses are equally degraded and the Poisson's ratio remains constant. In contrast with plasticity models, the stiffness is modified instead of dividing the strains in elastic and plastic parts. This leads to a secant unloading behavior (Fig. 1.10).

Evolution of the internal variables — and consequently of the damage parameter d — is governed by a fracture surface f analogous to a yield surface. For a damage model with one internal variable r, the Kuhn-Tucker conditions are used to explicitly compute $\dot{r}$:

$$\dot{r} \geq 0 \quad f \leq 0 \quad \dot{r} f = 0 \tag{1.43}$$

where the fracture function f is usually based on an equivalent strain measure [45, 48, 73]. The updated internal variable is then used to compute d, whose evolution with r is usually a function of fracture toughness and strength.

Mesh dependency Continuum damage models suffer from mesh sensitivity problems. In contrast to discretization errors that vanish upon mesh refinement, this mesh dependency issue is aggravated as the mesh is refined [74]. It manifests upon softening as

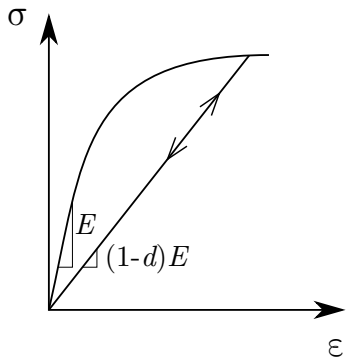

Figure 1.10: Loading-unloading behavior of a damage model

strain localization in a single element or band of elements. The resultant energy dissipation is proportional to the volume of a single element and therefore vanishes at the limit of discretization. Apart from the resultant unrealistic energy dissipation, the structural response suffers from sharp snapbacks and consequent Newton-Raphson convergence issues.

A number of techniques can be used to mitigate this mesh dependency issue. The most straightforward one is the Crack Band method [75], which introduces the element length as a scaling parameter for energy dissipation. Another approach involves introducing a viscous damage behavior analogous to viscoplasticity that retards strain localization and forces damage initiation in neighboring elements [72]. Lastly, non-local formulations explicitly introduce an internal length scale for strain localization derived from phenomena occurring at lower scales [76].

Cohesive-zone models Variations of continuum damage models can be employed as cohesive laws for interface elements (Eq. (1.22)). In this case, Eq. (1.41) is substituted for a traction-separation law:

$$\mathbf{t} = (1-d)\mathbf{K}_{\mathrm{d}}[\![\mathbf{u}]\!] \tag{1.44}$$

where $\mathbf{K}_{\mathrm{d}}$ is a stiffness operator that promotes interconnectivity between element faces and prevents their interpenetration. The rest of the formulation is similar to the one for the continuum case, with the fracture surface f now being a function of $[\![\mathbf{u}]\!]$. In contrast with continuum damage models, cohesive-zone models do not suffer from mesh dependency and energy dissipation is a direct function of fracture toughness.

1.4.3. MULTISCALE ANALYSIS

The three material scale levels of interest for modeling of laminated composites can be seen in Fig. 1.3. Moving down in scale has two main advantages: Firstly, the fidelity of the analysis is improved as the intrinsic boundaries between materials are discerned and microscopic failure processes and degradation mechanisms can be taken into account. Secondly, increasingly simpler constitutive models can be employed, as much of the physics that can only be included in higher-scale models in a phenomenological

way emerges naturally on lower-scale models. Conversely, increasingly complex constitutive models are needed as one moves up in scale, which also implies a larger number of parameters that need to be experimentally calibrated.

Obviously, the ideal model would explicitly model the microscopic material components (*e.g.* fibers, resin and interfaces) for the whole macroscopic structure (*e.g.* a wind turbine blade) — an approach referred to as *Direct Numerical Simulation* (DNS). This is, however, computationally infeasible even for relatively small macroscopic domains. The main appeal of multiscale analysis is therefore to harness the advantages of lower scale models while still obtaining relevant predictions at higher scales with reasonable computational cost.

The multiscale techniques present in literature can be divided in two categories:

- *Domain decomposition*: In this type of analysis, the microstructure of domain regions with high strain gradients (*e.g.* the region around a crack path) are explicitly included in a coarser macroscopic mesh while computationally efficient homogenized constitutive models are used for the rest of the domain [77–79]. Obviously, the progressive remeshing and consistent coupling of macro- and microscopic mesh regions are not trivial and demand considerable implementation effort.
- *Homogenization*: In this set of methods, the analysis scales are explicitly separated. Material properties of the smaller scale are averaged into an equivalent homogeneous medium and used as constitutive model at the macroscale.

Homogenization methods are by far the most popular of the two types. In the following, the main types of homogenization will be briefly mentioned and relevant references will be provided.

Analytical Homogenization These are closed-form mathematical expressions which give equivalent properties based on assumed periodic microstructures. These range from the widely used *Rule of Mixtures* solutions [80, 81], to asymptotic homogenization solutions such as Eshelby's [82], Mori-Tanaka [83], Self-consistent homogenization [84, 85], among others. These solutions are computationally efficient and provide good accuracy as long as the assumptions made during their formulations remain valid, namely material periodicity and small macroscopic strain gradients. However, material failure usually leads to loss of periodicity and strain localization, invalidating both assumptions.

Numerical Homogenization In these models, also known as *Unit Cell* methods, material parameters required for macroscopic constitutive models are derived from virtual experiments at smaller scales [12, 13, 15]. Scale transitions are done before the analysis and are only performed once. The macroscopic response is dictated by a calibrated macroscopic constitutive model. This approach is computationally efficient and avoids the need for experimental calibration of the macroscopic constitutive behavior.

However, the performance of numerical homogenization drops when highly nonlinear microscopic phenomena are modeled. In many cases, the microscopic behavior becomes too complex to be reasonably predicted by phenomenological macroscopic constitutive models built upon a series of simplifying assumptions. Moreover, by disregarding the microscopic behavior during the analysis, relevant information about the

evolution of failure, such as propagation of microscopic cracks, is lost. Such information could in turn be useful in realistically modeling macroscopic failure (*e.g.* determining the orientation of macroscopic cracks based on the orientation of the microscopic strain localization band).

Computational Homogenization In this type of analysis, also referred to as *concurrent* analysis or the *FE*^{2} *method*, the constitutive behavior of each macroscopic integration point is determined during the analysis using nested numerical models [14, 86]. This means that no simplifying constitutive assumptions are made at the macroscale, allowing for modeling of complex non-linear phenomena that would be difficult or impossible to capture in homogenized constitutive models. In contrast to domain decomposition methods, the microscopic mesh is not explicitly inserted in the macroscopic one. Instead, macroscopic strains are applied to the nested microscopic models as prescribed displacements and the resultant microscopic stress field is homogenized in order to compute the macroscopic stress and stiffness.

Computational homogenization (CH) is a relatively novel method and subject of intense research. Early investigations on the subject can be found in [87, 88], while a comprehensive review on the current trends of the field can be found in [89]. One major drawback of the method is its significant computational demands, which follows from the fact that for each analysis step a nested micromodel has to be solved for each macroscopic integration point. This is especially aggravated if the models at both scales feature dense meshes. Furthermore, homogenization of micromodels with localized strain bands to continuum macroscopic elements leads to an ill-posed problem that is not objective with respect to micromodel size [90, 91]. Lastly, coupling a concurrent multiscale analysis with a multiphysics formulation presents a number of difficulties with respect to the coupling between physical processes and scale transitions of non-mechanical fields [16, 17, 92].

Extension to time scales Even though the preceding discussion dealt with a numerical analysis that takes place in two or more spatial scales of interest, it is worth mentioning that many of the same techniques can be employed to deal with multiple time scales. This is especially advantageous for the prediction of the long-term behavior of structures subjected to cyclic loads.

In a time-homogenized model, the equilibrium problem is decomposed into microchronological and macrochronological parts analogous to micro and macroscopic models in space [61, 71, 93, 94]. This allows for larger time steps to be used without compromising solution accuracy. Furthermore, the constitutive response of the microchronological problem (*e.g.* a single load cycle) is simplified as a consequence of the employed homogenization operators, often leading to linear problems that do not require the use of an iterative solver.

1.4.4. REDUCED-ORDER MODELING

The computational cost involved in solving multiscale/multiphysics models with nonlinear microscopic material behavior can be exceedingly high. Research on model-order reduction techniques arose from the need to accelerate the computation of high-fidelity

numerical models, particularly in many-query applications — when the same numerical mesh is solved multiple times with different boundary conditions and input properties. Concurrent multiscale can be immediately identified as one such application, but one could also point to parametric sensitivity studies or design optimization as other examples [22].

The basic idea of reduced-order modeling (ROM) is to substitute the original high-fidelity model by a significantly less complex reduced model with minimum loss of accuracy. In a finite element context, complexity reduction entails reductions in the number of degrees of freedom and in the number of integration points where material response is computed. It is important at this point to discern the reduction operations treated here from conventional finite element refinement. While it is, by definition, possible to construct a reduced model by simply employing a coarser mesh, the resultant loss of accuracy for the same reduction (or compression) levels reached by ROM techniques, defined as the ratio between the number of degrees of freedom of the full and reduced models, would be unacceptably high. It is also worth mentioning that resolving fine microscopic features such as groups of fibers closely packed together severely limits the possibility of using coarser meshes.

Model order reduction relies on the premise that the full-order solution can be accurately represented in a lower-dimensional solution subspace that carries highly compressed information of the full solution space. Assuming that such a reduced subspace can be defined by a set of basis vectors, the task of constructing the reduced model lies in determining these vectors. This is the role of the so-called *offline* training phase: The full-order model is solved for a representative set of inputs and a dimensionality reduction technique is used to find a set of solution modes that compose the basis of the reduced subspace. The trained model is then used in the many-query *online* application by projecting the global equilibrium equation onto the reduced subspace.

Displacement projection Solving a full-order finite element problem with N displacement degrees of freedom in the *offline* phase and applying a reduction technique such as the Proper Orthogonal Decomposition (POD) [20] to the obtained solution vectors, a basis matrix $\boldsymbol{\Phi} \in \mathbb{R}^{N\times n}$ with n basis vectors is obtained. The original equilibrium problem (Eq. (1.16)) is then projected onto the reduced basis (Galerkin projection):

$$\boldsymbol{\Phi}^{\mathrm{T}}\left(\mathbf{f}^{\Omega}-\mathbf{f}^{\Gamma}\right)=\mathbf{0} \quad \Rightarrow \quad \mathbf{f}_{\mathrm{r}}^{\Omega}-\mathbf{f}_{\mathrm{r}}^{\Gamma}=\mathbf{0} \tag{1.45}$$

where the subscript r represents reduces entities. This reduced solution is a linear combination of the basis modes contained in $\boldsymbol{\Phi}$:

$$\bar{\mathbf{u}}=\boldsymbol{\Phi}\boldsymbol{\alpha} \tag{1.46}$$

where $\boldsymbol{\alpha}$ is a vector of reduced degrees of freedom that represents the contribution of each displacement mode (Fig. 1.11). The reduction process can therefore be seen as compressing as much information as possible in a single degree of freedom. In the original problem, a degree of freedom contains only information on the displacement of a single node, while a reduced degree of freedom contains information on the deformation of the whole mesh. It is interesting to note the similarity between the reduced model and the Ritz solution of Eq. (1.3).

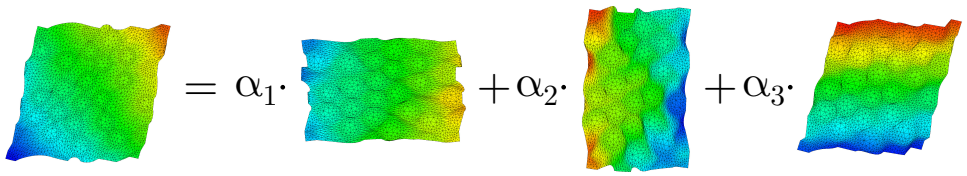

Figure 1.11: Reduced model response by a combination of displacement modes.

Further procedures can be applied to the displacement basis, in what can be seen as additional reduction stages. For instance, machine learning techniques such as k-means clustering can be used to construct subsets of basis vectors from a larger initial set and change between bases during the *online* analysis [22, 95, 96].

Hyper-reduction Computing the internal force vector $\mathbf{f}^{\Omega}$ of Eq. (1.45) still requires integrating the internal force of each finite element, which in turn requires computing expensive nonlinear constitutive models for every integration point. A second reduction stage can be employed to alleviate this computational cost, leading to a so-called *hyper-reduced* model [97]. In such a model, the constitutive response is computed only in a subset of integration points that is heuristically determined during the *offline* training phase. These sampling points are then used to compute an approximation of $\mathbf{f}^{\Omega}$ or $\mathbf{f}_{\mathrm{r}}^{\Omega}$. Two main approaches can be used to obtain such an approximation:

- *Gappy Data*: This is essentially the same operation shown in Eq. (1.46) but one where a subsampled version of the global force takes the place of $\boldsymbol{\alpha}$ and a nonlinear least-squares interpolation matrix fills the role of $\boldsymbol{\Phi}$ [98], resulting in an approximation for the full-order vector $\mathbf{f}^{\Omega}$. This is the basis for methods such as the Discrete Empirical Interpolation Method (DEIM) [22, 99].
- *Modified Cubature*: Sampling integration points are selected and modified integration weights are computed which lead to a sparse version of $\mathbf{f}^{\Omega}$ after standard FE assembly which accurately approximates the reduced global vector $\mathbf{f}_{\mathrm{r}}^{\Omega}$ after being compressed by $\boldsymbol{\Phi}$ (Eq. (1.46)). The Empirical Cubature Method [21] and other cubature formulations [100, 101] fall in this category.

1.5. VISION AND CHALLENGES

Despite the large body of literature on the subject, hygrothermal aging in composites is still not fully understood, which consequently hinders the progress on modeling the phenomenon and developing accurate durability prediction tools. Studies often focus on macroscopic experiments which, although providing valuable information on material degradation at scales closer to the ones considered in design, offer only limited insight in the underlying microscopic aging mechanisms [31, 102–104]. Furthermore, inclusion of these mechanisms into existing modeling approaches is a complex task involving multiple physical processes, spatial and time scales [37, 61, 105]. In order to develop a suitable modeling framework for the problem at hand, a number of challenges must be overcome:

- *Moisture diffusion*: Since hygrothermal aging is driven by moisture ingression, it is important to understand the diffusion process across spatial scales. In this regard, although it is well known that the fibers create a barrier effect that leads to faster diffusion along the fibers [35], this is often not enough to explain the experimentally measured level of anisotropy [10]. In particular, the existence of an interphase region around the fibers and its role on accelerating the diffusion process is not clear.

- *Hygrothermal degradation*: The relative contribution of each of the mechanisms mentioned in Section 1.3.2 on the resultant hygrothermal degradation in composites must be experimentally determined. This not only entails mechanical tests on composite specimens but also an explicit comparison between composite and pure resin specimens, an approach which very few authors follow. Furthermore, the amount of available experimental data on specimens tested after a complete immersion-redrying cycle is limited, making it difficult to discern to which extent the degradation is reversible. Finally, direct measurements of hygrothermal degradation of fiber-matrix interface performance through micromechanical tests are not extensively available.

- *Multiscale/multiphysics modeling*: The presence of transient swelling stresses in specimens with non-uniform water concentration fields [106] and the potential influence that these stresses can have in driving microscopic failure motivate the use of a concurrent (FE^2) analysis (Section 1.4.3). Although stress analysis in FE^2 is well documented, treatment of other field problems such as heat transfer [17], diffusion [16] and coupled diffusion-reaction [105] are still not extensively documented. Furthermore, no consensus exists on how to perform macro to micro transitions of non-mechanical fields [16, 92].

- *Computational efficiency*: Employing a concurrent multiscale modeling approach comes at the cost of computational efficiency, in particular when computationally expensive material models are used at the microscale or when a large number of load cycles is considered. Therefore, a suitable combination of homogenization and reduced-order modeling techniques must be found in order to accelerate the solution of the microscopic boundary value problem from which the macroscopic material behavior is derived.

REFERENCES

[1] International Energy Agency (IEA), *World energy outlook 2017,* (2017).

[2] A. D. Pasternak, *Global energy futures and human development: A framework for analysis,* (2000).

[3] Global Wind Energy Council (GWEC), *Global wind statistics 2017,* (2018).

[4] J. F. Walker and N. Jenkins, *Wind energy technology* (John Wiley and Sons, 1997).

[5] J. N. Reddy, *Mechanics of laminated composite plates and shells: Theory and analysis* (CRC Press, 2004).

[6] J. R. White and T. A. Turnbull, *Review: Weathering of polymers: mechanisms of degradation and stabilization, test strategies and modelling,* Journal of Materials Science **29**, 584 (1994).

[7] S. A. Grammatikos, B. Zafari, M. C. Evernden, J. T. Mottram, and J. M. Mitchels, *Moisture uptake characteristics of a pultruded fibre reinforced polymer flat sheet subjected to hot/wet aging,* Polymer Degradation and Stability **121**, 407 (2015).

[8] R. Polanský, V. Mantlík, P. Prosr, and J. Sušír, *Influence of thermal treatment on the glass transition temperature of thermosetting epoxy laminate,* Polymer Testing **28**, 428 (2009).

[9] L. Gautier, B. Mortaigne, and B. V., *Interface damage study of hydrothermally aged glass-fibre-reinforced polyester composites,* Composites Science and Technology **59**, 2329 (1999).

[10] Y. Joliff, W. Rekik, L. Belec, and J. F. Chailan, *Study of the moisture/stress effects on glass fibre/epoxy composite and the impact of the interphase area,* Composite Structures **108**, 876 (2014).

[11] A. Gagani and A. T. Echtermeyer, *Fluid diffusion in cracked composite laminates - Analytical, numerical and experimental study,* Composites Science and Technology **160**, 86 (2018).

[12] F. Naya, C. González, C. S. Lopes, S. van der Veen, and F. Pons, *Computational micromechanics of the transverse and shear behaviour of unidirectional fiber reinforced polymers including environmental effects,* Composites: Part A (2016).

[13] F. P. van der Meer, *Micromechanical validation of a mesomodel for plasticity in composites,* European Journal of Mechanics - A/Solids **60**, 58 (2016).

[14] C. Miehe, J. Schotte, and J. Schröder, *Computational micro-macro transitions and overall moduli in the analysis of polycrystals at large strains,* Computational Materials Science **16**, 372 (1999).

[15] C. Qian, T. Westphal, and R. P. L. Nijssen, *Micro-mechanical fatigue modelling of unidirectional glass fibre reinforced polymer composites,* Computational Materials Science **69**, 62 (2013).

[16] K. Terada and M. Kurumatani, *Two-scale diffusion-deformation coupling model for material deterioration involving micro-crack propagation,* International Journal for Numerical Methods in Engineering **83**, 426 (2010).

[17] I. Özdemir, W. A. M. Brekelmans, and M. G. D. Geers, *Computational homogenization for heat conduction in heterogeneous solids,* International Journal for Numerical Methods in Engineering **73**, 185 (2008).

[18] A. Sengupta, P. Papadopoulos, and R. L. Taylor, *A multiscale finite element method for modeling fully coupled thermomechanical problems in solids,* International Journal for Numerical Methods in Engineering **91**, 1386 (2012).

[19] P. Kerfriden, P. Gosselet, S. Adhikari, and S. P. A. Bordas, *Bridging proper orthogonal decomposition methods and augmented newton-krylov algorithms: An adaptive model order reduction for highly nonlinear mechanical problems,* Computer Methods in Applied Mechanics and Engineering **200**, 850 (2011).

[20] P. Kerfriden, O. Goury, T. Rabczuk, and S. P. A. Bordas, *A partitioned model order reduction approach to rationalise computational expenses in nonlinear fracture mechanics,* Computer Methods in Applied Mechanics and Engineering **256**, 169 (2013).

[21] J. A. Hernández, M. A. Caicedo, and A. Ferrer, *Dimensional hyper-reduction of nonlinear finite element models via empirical cubature,* Computer Methods in Applied Mechanics and Engineering **313**, 687 (2017).

[22] F. Ghavamian, P. Tiso, and A. Simone, *POD-DEIM model order reduction for strain-softening viscoplasticity,* Computer Methods in Applied Mechanics and Engineering **317**, 458 (2017).

[23] G. M. Odegard and A. Bandyopadhyay, *Physical aging of epoxy polymers and their composites,* Journal of Polymer Science: Part B **49**, 1695 (2011).

[24] Y. G. Lin, H. Sautereau, and J. P. Pascault, *Epoxy network structure effect on physical aging behavior,* Journal of Applied Polymer Science **32**, 4595 (1986).

[25] S. Montserrat, *Physical aging studies in epoxy resins. I. Kinetics of the enthalpy relaxation process in a fully cured epoxy resin,* Journal of Polymer Science: Part B **32**, 509 (1994).

[26] T. D. Chang and J. O. Brittain, *Studies of epoxy resin systems: Part C: Effect of sub-T_g aging on the physical properties of a fully cured epoxy resin,* Polymer Engineering and Science **22**, 1221 (1982).

[27] E. S. W. Kong, *Physical aging in epoxy matrices and composites,* Advances in Polymer Science **80**, 125 (1986).

[28] S. Ciutacu, P. Budrugeac, and I. Niculae, *Accelerated thermal aging of glass-reinforced epoxy resin under oxygen pressure,* Polymer Degradation and Stability **31**, 365 (1991).

[29] N. Sato and T. Kurauchi, *Effect of fibre sizing on composite interfacial deformation studied by thermo-acoustic emission measurement,* Journal of Materials Science Letters **11**, 362 (1992).

[30] L. Cormier and S. Joncas, *Effects of cold temperature, moisture and freeze-thaw cycles on the mechanical properties of unidirectional glass fiber-epoxy composites,* in *51st AIAA/ASME/ASCE/AHS/ASC Structures, Structural Dynamics and Materials Conference* (2010).

[31] M. C. Lafarie-Frenot, *Damage mechanisms induced by cyclic ply-stresses in carbon-epoxy laminates: Environmental effects,* International Journal of Fatigue **28**, 1202 (2006).

[32] F. Sayer, F. Bürkner, B. Buchholz, M. Strobel, A. M. van Wingerde, H. Bussmann, and H. Seifert, *Influence of a wind turbine service life on the mechanical properties of the material and the blade,* Wind Energy **16**, 163 (2013).

[33] A. Fick, *On liquid diffusion,* Poggendorfs Annalen **94**, 59 (1855).

[34] S. A. Grammatikos, M. Evernden, J. Mitchels, B. Zafari, J. T. Mottram, and G. C. Papanicolaou, *On the response to hygrothermal ageing of pultruded FRPs used in the civil engineering sector,* Materials and Design **96**, 283 (2016).

[35] H. S. Choi, K. J. Ahn, J.-D. Nam, and H. J. Chun, *Hygroscopic aspects of epoxy/carbon fiber composite laminates in aircraft environments,* Composites: Part A **32**, 709 (2001).

[36] J. El Yagoubi, G. Lubineau, F. Roger, and J. Verdu, *A fully coupled diffusion-reaction scheme for moisture sorption-desorption in an anhydride-cured epoxy resin,* Polymer **53**, 5582 (2012).

[37] C. Yu, G. Kang, and K. Chen, *A hygro-thermal-mechanical coupled cyclic constitutive model for polymers with considering glass transition,* International Journal of Plasticity **89**, 29 (2017).

[38] J. Zhou and J. P. Lucas, *Hygrothermal effects of epoxy resin. part I: the nature of water in epoxy,* Polymer **40**, 5505 (1999).

[39] P. Davies, F. Mazéas, and P. Casari, *Sea water aging of glass reinforced composites: Shear behaviour and damage modelling,* Journal of Composite Materials **35**, 1343 (2000).

[40] J. L. Thomason, *The interface region in glass fibre-reinforced epoxy resin composites: 1. sample preparation, void content and interfacial strength,* Composites **26**, 467 (1995).

[41] T. Morii, N. Ikuta, K. Kiyosumi, and H. Hamada, *Weight-change analysis of the interphase in hygrothermally aged FRP: Consideration of debonding,* Composites Science and Technology **57**, 985 (1997).

[42] W. Ritz, *Über eine neue Methode zur Lösung gewisser Variationsprobleme der mathematischen Physik,* Journal für die Reine und Angewandte Mathematik **135**, 1 (1909).

[43] R. D. Cook, D. S. Malkus, M. E. Plesha, and R. J. Witt, *Concepts and applications of finite element analysis* (John Wiley and Sons, 2001).

[44] L. E. Malvern, *Introduction to the mechanics of a continuous medium* (Prentice Hall, 1977).

[45] A. R. Melro, P. P. Camanho, F. M. Andrade Pires, and S. T. Pinho, *Micromechanical analysis of polymer composites reinforced by unidirectional fibres: Part I - Constitutive modelling,* International Journal of Solids and Structures **50**, 1897 (2013).

[46] A. Krairi and I. Doghri, *A thermodynamically-based constitutive model for thermoplastic polymers coupling viscoelasticity, viscoplasticity and ductile damage,* International Journal of Plasticity **60**, 163 (2014).

[47] X. Poulain, A. A. Benzerga, and R. K. Goldberg, *Finite-strain elasto-viscoplastic behavior of an epoxy resin: Experiments and modeling in the glassy regime,* International Journal of Plasticity **62**, 138 (2014).

[48] R. de Borst, M. A. Crisfield, J. J. C. Remmers, and C. V. Verhoosel, *Nonlinear finite element analysis of solids and structures* (Wiley, 2012).

[49] E. Ramm, *Strategies for tracing the non-linear response near limit-points,* in *Nonlinear Finite Element Analysis in Structural Mechanics*, edited by W. Wunderlich, E. Stein, and K. J. Bathe (Springer, 1981) pp. 63–89.

[50] M. A. Crisfield, *A fast incremental/iterative solution that handles snap-through,* Computers and Structures **13**, 55 (1981).

[51] F. P. van der Meer, C. Oliver, and L. J. Sluys, *Computational analysis of progressive failure in a notched laminate including shear nonlinearity and fiber failure,* Composites Science and Technology **70**, 692 (2010).

[52] E. Parente Jr, A. S. Holanda, and S. M. B. A. Silva, *Tracing nonlinear equilibrium paths of structures subjected to thermal loading,* Computational Mechanics **38**, 505 (2006).

[53] G. I. Barenblatt, *The mathematical theory of equilibrium cracks in brittle fracture,* Advances in Applied Mechanics **7**, 55 (1962).

[54] A. Hillerborg, M. Modeér, and P. E. Petersson, *Analysis of crack formation and crack growth in concrete by means of fracture mechanics and finite elements,* Cement and Concrete Research **6**, 773 (1976).

[55] M. G. A. Tijssens, B. L. J. Sluys, and E. van der Giessen, *Numerical simulation of quasi-brittle fracture using damaging cohesive surfaces,* European Journal of Mechanics - A/Solids **19**, 761 (2000).

[56] J. M. Melenk and I. Babuška, *The partition of unity finite element method: Basic theory and applications,* Computer Methods in Applied Mechanics and Engineering **139**, 289 (1996).

[57] N. Moës and T. Belytschko, *Extended finite element method for cohesive crack growth,* Engineering Fracture Mechanics **69**, 813 (2002).

[58] T. Strouboulis, I. Babuška, and K. Copps, *The design and analysis of the generalized finite elemnt method,* Computer Methods in Applied Mechanics and Engineering **181**, 43 (2000).

[59] A. Hansbo and P. Hansbo, *A finite element method for the simulation of strong and weak discontinuities in solid mechanics,* Computer Methods in Applied Mechanics and Engineering **193**, 3523 (2004).

[60] J. Remmers, *Mode-jumping simulations using the new implicit time integrator in b2000,* in *2nd B2000/MEMCOM workshop* (1998).

[61] Q. Yu and J. Fish, *Temporal homogenization of viscoelastic and viscoplastic solids subjected to locally periodic loading,* Computational Mechanics **29**, 199 (2002).

[62] G. Tao and Z. Xia, *Ratcheting behavior of an epoxy polymer and its effect on fatigue life,* Polymer Testing **26**, 451 (2007).

[63] G. Tao and Z. Xia, *Mean stress/strain effect on fatigue behavior of an epoxy resin,* International Journal of Fatigue **29**, 2180 (2007).

[64] G. Tao and Z. Xia, *An experimental study of uniaxial fatigue behavior of an epoxy resin by a new noncontact real-time strain measurement and control system,* Polymer Engineering and Science **47**, 780 (2007).

[65] R. Hill, *The mathematical theory of plasticity* (Oxford University Press, 1950).

[66] E. A. Souza Neto, D. Peric, and D. R. J. Owen, *Computational methods for plasticity: Theory and applications* (John Wiley and Sons, 2008).

[67] E. van der Giessen, *Localized plastic deformations in glassy polymers,* European Journal of Mechanics - A/Solids **16**, 87,106 (1997).

[68] A. S. Argon, *A theory for the low-temperature plastic deformation of glassy polymers,* Philosophical Magazine **28**, 839 (1973).

[69] T. A. Tervoort, R. J. M. Smit, W. A. M. Brekelmans, and L. E. Govaert, *A constitutive equation for the elasto-viscoplastic deformation of glassy polymers,* Mechanics of Time-Dependent Materials **1**, 269 (1998).

[70] J. C. Simo and R. L. Taylor, *Consistent tangent operators for rate-independent plasticity,* Computer Methods in Applied Mechanics and Engineering **48**, 101 (1985).

[71] S. Haouala and I. Doghri, *Modeling and algorithms for two-scale time homogenization of viscoelastic-viscoplastic solids under large numbers of cycles,* International Journal of Plasticity **70**, 98 (2015).

[72] J. C. Simo and J. W. Ju, *Strain- and stress-based continuum damage models - I. Formulation,* International Journal of Solids and Structures **23**, 821 (1987).

[73] J. Mazars and G. Pijaudier-Cabot, *Continuum damage theory – Application to concrete,* ASCE Journal of Engineering Mechanics **115**, 345 (1989).

[74] R. de Borst, L. J. Sluys, H.-B. Muhlhaus, and J. Pamin, *Fundamental issues in finite element analyses of localisation of deformation,* Engineering Computations **10**, 99 (1993).

[75] Z. P. Bažant and B. Oh, *Crack band theory for fracture of concrete,* Matériaux et Construction **16**, 155 (1983).

[76] R. H. J. Peerlings, R. de Borst, W. A. M. Brekelmans, and H. P. de Vree, *Gradient enhanced damage for quasi-brittle materials,* International Journal for Numerical Methods in Engineering **39**, 3391 (1996).

[77] P. A. Guidault, O. Allix, L. Champaney, and J. P. Navarro, *A two-scale approach with homogenization for the computation of cracked structures,* Computers and Structures **85**, 1360 (2007).

[78] F. Greco, L. Leonetti, and P. N. Blasi, *Adaptive multiscale modeling of fiber-reinforced composite materials subjected to transverse microcracking,* Composite Structures **113**, 249 (2014).

[79] O. Lloberas-Valls, D. J. Rixen, A. Simone, and L. J. Sluys, *Multiscale domain decomposition analysis of quasi-brittle heterogeneous materials,* International Journal for Numerical Methods in Engineering **89**, 1337 (2012).

[80] W. Voigt, *Theoretische Studien über die Elasticitätsverhältnisse der Krystalle,* Abhandlungen der Königlichen Gesellschaft der Wissenschaften in Göttingen **34**, 3 (1887).

[81] A. Reuss, *Berechnung der Fliessgrense von Mischkristallen auf Grund der Plastizitätsbedingung für Einkristalle,* Zeitschrift Angewandte Mathematik und Mechanik **9**, 49 (1929).

[82] J. D. Eshelby, *The determination of the elastic field of an ellipsoidal inclusion, and related problems,* Proceedings of the Royal Society of London: Series A **241**, 376 (1957).

[83] T. Mori and K. Tanaka, *Average stress in matrix and average elastic energy of materials with misfitting inclusions,* Acta Metallurgica **21**, 571 (1973).

[84] R. Hill, *Theory of mechanical properties of fibre-strengthened materials – III. self-consistent model,* Journal of Mechanics and Physics of Solids **13**, 189 (1965).

[85] B. Budiansky, *On the elastic moduli of some heterogeneous materials,* Journal of Mechanics and Physics of Solilds **13**, 223 (1965).

[86] V. Kouznetsova, W. A. M. Brekelmans, and F. P. T. Baaijens, *An approach to micro-macro modeling of heterogeneous materials,* Computational Mechanics **27**, 37 (2001).

[87] P. M. Suquet, *Local and global aspects in the mathematical theory of plasticity,* in *Plasticity today: Modelling, methods and applications* (1985) pp. 279–310.

[88] R. J. M. Smit, W. A. M. Brekelmans, and H. E. H. Meijer, *Prediction of the mechanical behaviour of non-linear heterogeneous systems by multi-level finite element modelling,* Computer Methods in Applied Mechanics and Engineering **155**, 181 (1998).

[89] M. G. D. Geers, V. G. Kouznetsova, and W. A. M. Brekelmans, *Multi-scale computational homogenization: Trends and challenges,* Journal of Computational and Applied Mathematics **234**, 2175 (2010).

[90] V. P. Nguyen, O. Lloberas Valls, M. Stroeven, and L. J. Sluys, *On the existence of representative volumes for softening quasi-brittle materials - a failure zone averaging scheme,* Computer Methods in Applied Mechanics and Engineering **199**, 45 (2010).

[91] T. J. Massart, R. H. J. Peerlings, and M. G. D. Geers, *An enhanced multiscale approach for masonry wall computations with localization of damage,* International Journal for Numerical Methods in Engineering **69**, 1022 (2007).

[92] I. Özdemir, W. A. M. Brekelmans, and M. G. D. Geers, *FE^2 computational homogenization for the thermo-mechanical analysis of heterogeneous solids,* Computer Methods in Applied Mechanics and Engineering **198**, 602 (2008).

[93] R. Crouch, C. Oskay, and J. Fish, *Multiple spatio-temporal scale modeling of composites subjected to cyclic loading,* Computational Mechanics **51**, 93 (2013).

[94] C. Oskay and J. Fish, *Fatigue life prediction using 2-scale temporal asymptotic homogenization,* International Journal for Numerical Methods in Engineering **61**, 329 (2004).

[95] B. Peherstorfer, D. Butnaru, K. Wilcox, and H. J. Bungartz, *Localized discrete empirical interpolation method,* SIAM Journal on Scientific Computing **36**, 168 (2014).

[96] B. Haasdonk, M. Dihlmann, and M. Ohlberger, *A training set and multiple basis generation approach for parametrized model reduction based on adaptive grids in parameter space,* Mathematical and Computer Modelling of Dynamical Systems **17**, 423 (2011).

[97] D. Ryckelynck, *Hyper-reduction of mechanical models involving internal variables,* International Journal for Numerical Methods in Engineering **77**, 75 (2009).

[98] R. Everson and L. Sirovich, *Karhunen-Loeve procedure for gappy data,* Journal of the Optical Society of America A **12**, 1567 (1996).

[99] S. Chaturantabut and D. C. Sorensen, *Nonlinear model reduction via discrete empirical interpolation,* SIAM Journal on Scientific Computing **32**, 2737 (2010).

[100] S. An, T. Kim, and D. James, *Optimizing cubature for efficient integration of subspace deformations,* ACM Transactions on Graphics **27**, 165 (2009).

[101] C. Farhat, P. Avery, T. Chapman, and J. Cortial, *Dimensional reduction of nonlinear finite element dynamic models with finite rotations and energy-based mesh sampling and weighting for computational efficiency,* International Journal for Numerical Methods in Engineering **98**, 625 (2014).

[102] F. Ellyin and C. Rorhbacher, *Effect of aqueous environment and temperature on glass-fibre epoxy resin composites,* Journal of Reinforced Plastics and Composites **19**, 1405 (2000).

[103] B. Dewimille and A. R. Bunsell, *Accelerated ageing of a glass fibre-reinforced epoxy resin in water,* Composites , 35 (1983).

[104] M. Malmstein, A. R. Chambers, and J. I. R. Blake, *Hygrothermal ageing of plant oil based marine composites,* Composite Structures **101**, 138 (2013).

[105] Z. Yuan, T. Jiang, J. Fish, and G. Morscher, *Reduced-order multiscale-multiphysics model for heterogeneous materials,* **12**, 45 (2014).

[106] G. Pitarresi, M. Scafidi, S. Alessi, M. Di Filippo, C. Billaud, and G. Spadaro, *Absorption kinetics and swelling stresses in hydrothermally aged epoxies investigated by photoelastic image analysis,* Polymer Degradation and Stability **111**, 55 (2015).

2

HYGROTHERMAL AGING BEHAVIOR OF GLASS/EPOXY COMPOSITES

In time and with water,
everything changes.

Leonardo da Vinci

2.1. INTRODUCTION

In this chapter, an investigation is performed on damage processes induced by hygrothermal aging on an epoxy system reinforced with E-Glass fibers representative of the material used in wind turbine blade design. The water ingression process is tracked and a finite element modeling approach combined with an optimisation-based parameter identification technique is used to identify Fickian and non-Fickian absorption phases and determine the diffusivity parameters. In order to evaluate the combined effect of interface and matrix degradation, ILSS (Interlaminar Shear Strength) short-beam specimens are tested quasi-statically and in fatigue.

Furthermore, in an attempt to isolate the contribution of matrix degradation, neat epoxy specimens are also conditioned and tested. In order to isolate the irreversible part of the degradation due to water immersion, a combination of mechanical and thermal tests is also conducted on specimens dried after saturation and on moisture-free isothermically conditioned specimens.

Lastly, the material damage processes incurred during the immersion process and the consequent changes in failure modes observed in the mechanical tests are investigated through the use of optical microscopy. The combination of wet and dry tests

Apart from minor changes to its introductory section, this chapter was integrally extracted from [1].

on composite and resin specimens allows for a reconstruction of the chronology of the complex process of aging in composites.

2.2. EXPERIMENTS

2.2.1. MATERIALS

The resin system used is the Momentive EPIKOTE RIMR 135 / EPIKURE RIMH 1366, consisting of a monomer (70-100% 4,4'-Isopropylidenediphenol-Epichlorohydrin Copolymer and 0-30% 1,6-Hexanediol Diglycidyl Ether) and a hardener (25-50% Alkyletheramine, 20-25% Isophoronediamine and up to 20% Aminoethylpiperazine) [2] mixed in a 100:30 ratio in weight. For the composite panels, a unidirectional fabric composed of PPG Hybon 2002 glass fiber rovings (95% of the fibers oriented at 0° with 5% composing stability rovings oriented at 90°) was used. This glass/epoxy material is one of the most commonly used systems to compose the main load bearing structures of wind turbine blades.

Composite panels with 4 and 6 plies (3mm and 4.5mm thick, respectively) and neat resin panels of 4mm thickness were manufactured through vacuum infusion molding. The curing cycle consisted of 2h at 30°C and 5h at 50°C, followed by postcuring for 10h at 70°C. Specimens were cut from the panels using a CNC milling machine. Composite specimens were 0° unidirectional short-beams with geometry according to the ISO 14130 standard. As for neat epoxy specimens, dog-bone specimens according to specimen geometry 1B of the ISO 527-2 standard and flexural beams according to the ISO 178 standard were used.

2.2.2. SAMPLE CONDITIONING

An overview of the applied conditioning procedures can be seen in Figure 2.1, where each point marked in the curve represents a point in time when specimens were removed from conditioning and tested. In accelerated aging studies, the choice of the reference (unaged) state can be a complex one. For the particular case of hygrothermal aging, the ideal reference state would be a moisture-free one, allowing for the correct determination of the maximum water uptake and degree of irreversible material degradation through the redrying of saturated specimens. However, unless such state is achieved by drying (and redrying) the material at room temperature, which can be prohibitively time-consuming, interactions with other aging processes such as physical aging and oxidation are difficult to avoid when the material is dried at higher temperatures. These additional aging processes can in turn modify not only the material mechanical properties [3, 4] but also properties related to the diffusion process itself such as maximum uptake, diffusivity and swelling coefficient [5, 6].

Here, the *Unaged* state was defined by seeking a balance between a moisture-free state and an unmodified polymer chain structure. This was achieved by drying all specimens for 72h in a desiccator with silica gel at 50°C. Therefore, most of the moisture could be removed while minimising the effects of physical aging. Oxidative reactions were also minimised by appyling vacuum to the desiccator. In order to keep track of the correct initial water uptake and provide a consistent comparison basis for specimens dried after being immersed, part of the specimens (*Dry* set) was kept in the desiccator for an addi-

tional 2500h, after which a moisture-free state was reached and physical aging processes were considered to be stabilised [6].

From the unaged state, sets of specimens were immersed in demineralised water at 50°C for 500h, 1000h, 1500h and 4800h (*Saturated* set) according to Procedure A of the ASTM D5229/D5229M standard. This particular temperature was chosen based on DSC test results conducted on saturated resin material. Since DSC specimens are small blocks of material, their short saturation time allows for a quick determination of the wet glass transition temperature (T_g). For the resin system considered here, the wet T_g was approximately 70°C (see Section 2.3.4 and Table 2.6 for details) and since the material behavior changes drastically after this threshold, a safety temperature margin of 20°C was adopted. The effect of changing the immersion temperature on the diffusion process and material degradation is well documented in the literature [7–9] and is out of the scope of this work.

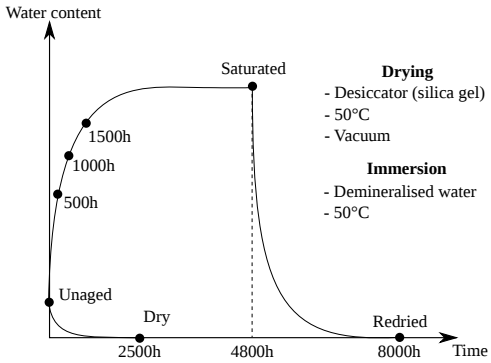

Figure 2.1: Overview of conditioning procedures.

From the saturated state, a final set of specimens was redried in the desiccator at 50°C until weight stabilisation was reached (*Redried* set). These specimens are used to investigate the possibility of mass loss or residual water after drying and to provide a measure of the irreversible material damage brought by immersion. As the drying process is long and may involve additional physical aging, the results of this set were compared with the ones from the *Dry* set for consistency.

2.2.3. MATERIAL INVESTIGATIONS

An overview of the mechanical and thermal tests performed for each condition and specimen type can be seen in Table 2.1, where the number of specimens used for each set is indicated in parentheses. Composite short-beam specimens with 4 and 6 plies were tested in three-point bending according to the ISO 14130 standard in an MTS test frame with a 10kN load cell. Quasi-static tests were conducted in displacement control at a speed of 1mm/min until a significant load drop was observed. Fatigue tests were conducted only on 6-ply specimens in a compression-compression setup in load control at 3Hz, with an R-value of 10.

Resin dog-bone specimens were tested quasi-statically in tension at a speed of 1mm/min and in tension-tension fatigue at 2Hz with an R-value of 0.1. In order to accurately

	Unaged	500h	1000h	1500h	Saturated	Dry	Redried
ILSS	$C_4S(12)/C_6S(12)/C_6F(7)$	$C_4S(3)$	$C_4S(3)$	$C_4S(3)$	$C_4S(6)/C_6S(6)/C_6F(6)$	$C_4S(6)/C_6S(6)$	$C_4S(6)/C_6S(6)$
Tension	ES(6)/EF (5)	-	-	-	ES(6)/EF(9)	ES(6)	ES(6)
Bending	ES(6)	-	-	-	ES(6)	ES(6)	ES(6)
DMA	E(6)	-	-	-	E(6)	E(6)	E(6)
DSC	E(3)	-	-	-	E(3)	E(3)	E(3)
Optical	-	-	-	-	$C_4(3)/C_6(3)$	$C_4(3)/C_6(3)$	-

C_4 - Composite (4-ply), C_6 - Composite (6-ply), E - Neat Epoxy, S - Quasi-static, F - Fatigue

Table 2.1: Overview of the performed investigations for each condition. The number of specimens for each set is indicated in parentheses.

measure strains in quasi-static tests, strain gauges were used both in longitudinal and transverse directions. Neat epoxy bending specimens were also tested using the same fixture mentioned for composite ones. For these tests, a 1kN load cell was used to measure force. In this case, only quasi-static tests were performed, at a speed of 2mm/min.

Dynamic Mechanical Analysis (DMA) tests were conducted in neat epoxy bending specimens by applying a displacement-controlled tension-compression cyclic load with an amplitude of 0.1 mm and a frequency of 1Hz. At the same time, a temperature ramp was applied to the specimen, from 25°C to 130°C at a rate of 2°C/min. After logging the obtained force readings for the complete temperature ramp, the procedure outlined in the standard ISO 6721-5 was used to obtain measurements of the storage and loss moduli, as well as the loss factor. Then, by observing variations in the storage modulus as temperature increases, an estimate of the glass transition temperature was obtained.

Differential Scanning Calorimetry (DSC) tests were performed on resin specimens using a Netzsch DSC 200 F3 Maia apparatus. In the tests, small material blocks are subjected to a temperature ramp of 20°C/min while having their specific heat capacity measured by a calorimeter. During the ramp, the transition to the rubbery state can be identified by an increase in the energy necessary to maintain the constant temperature ramp as the material requires additional energy to make the transition. Besides providing glass transition temperature measurements, specific heat capacity peaks around the T_g are indicative of polymer relaxation linked to physical aging [6].

In order to obtain additional information about the irreversible effects brought by water immersion, the first temperature ramp is followed by an isothermal period of 20 minutes at 130°C to erase the polymer relaxation history (thermal rejuvenation) [6] and completely remove the water molecules inside. The material is then quenched back to room temperature and a second ramp is executed. Results from this second ramp are then used to investigate whether irreversible chain scission or additional crosslinking have occurred during the immersion and drying steps.

Lastly, microscopic observations of dry and saturated composite specimens were made both before and after mechanical tests in order to assess microscopic material failure events occurred during immersion and changes in failure behavior during the performed tests. Microscopy samples were prepared by cutting slices from specimens along one of their orthotropy planes. The slices were then polished using a Labopol 30 polishing machine by progressively grinding the material with sanding surfaces ranging from 320 to 4000 grit and polishing the final surface using a suspension of diamond par-

ticles with an average diameter of $1\,\mu m$. After preparation, the slices were observed in a Motic BA210 optical microscope.

2.3. RESULTS AND DISCUSSION

2.3.1. WATER UPTAKE AND DESORPTION

The average water uptake curves with time can be seen in Figure 2.2, where the uptake percentage at time t was calculated as:

$$w(t) = 100 \cdot \left(\frac{m(t) - m_{72}^{\mathrm{u}}}{m_{72}^{\mathrm{u}}} - \frac{m_{72}^{\mathrm{d}} - m_{\mathrm{dry}}}{m_{\mathrm{dry}}} \right) \tag{2.1}$$

where the reference weight m_{72}^{u} was measured for the *Unaged* set prior to immersion. The points are then adjusted using weight measurements on specimens of the *Dry* set, which were dried until a moisture-free state was achieved. Thus, the plots do not start at zero but rather at the initial water content level of the unaged specimens. For neat epoxy, both specimen geometries have a similar final uptake of approximately 3.94%. In the curves for composite specimens, a difference in uptake speed is observed between the thinner 4-ply and the thicker 6-ply specimens, as expected. Eventually, they both attain the same final uptake of approximately 1.25%.

Water transport in polymers and polymer matrix composites is often modeled as Fickian, represented by a smooth molecular flux **J** driven by a concentration gradient with components given by:

$$J_s = -D_s \frac{\partial c}{\partial s} \tag{2.2}$$

where c is the water concentration field and J_s and D_s are the flux component and diffusivity in the s direction, respectively. By considering all flux components in an infinitesimal material volume, the concentration variation with time ($\partial c/\partial t$) can be obtained via:

$$\frac{\partial c}{\partial t} = \mathbf{D}\nabla^2 c \tag{2.3}$$

with ∇^2 being the Laplace operator with respect to the spatial coordinates and **D** is the diffusivity matrix, which is usually considered orthotropic for unidirectional fiber-reinforced polymer specimens.

Equation 2.3 is usually solved analytically for the simple case of unidimensional diffusion [7, 10, 11], a suitable approach for specimens such as panels, where the thickness is considerably smaller than the other dimensions. Here, such assumption is not valid and the contribution of all three dimensions must be considered. Instead of resorting to analytically solving Eq. 2.3, the Finite Element Method can be used to solve it numerically by dividing the spatial domain in finite elements and solving the weak integral form of the problem:

$$\mathbf{K}\mathbf{c} + \mathbf{C}\dot{\mathbf{c}} = \mathbf{f} \tag{2.4}$$

where **c** and $\dot{\mathbf{c}}$ are now nodal vectors of concentration and its variation with time, **K** is a diffusion matrix which depends on the shape functions and on the diffusivity matrix **D**, **C** is a capacity matrix that depends only on the shape functions and **f** is a vector of externally applied water fluxes.

Each specimen type is meshed with 512 8-node hexahedrical finite elements and the concentration at every boundary node is prescribed to be the final uptake w_∞. Finally, the uptake curve is obtained by averaging the concentration field in the whole volume of the specimen at each time step.

In order to fit the experimental data using the proposed model, suitable values for the diffusivity coefficients in each direction (D_x, D_y and D_z) and the maximum uptake (w_∞) have to be found. In order to evaluate the quality of the fit, the sum of the squared differences between experimental (w_{exp}) and numerical (w_{num}) uptakes is used and cast as a function f of the model parameters:

$$f(\mathbf{D}, w_\infty) = \sum_t \left[w_{\text{exp}}(t) - w_{\text{num}}(\mathbf{D}, w_\infty, t) \right]^2 \tag{2.5}$$

The problem of identifying the parameter set that produces the best fit can be seen as an optimization problem in which we seek to minimise the function f subjected to the variable bounds $D_x, D_y, D_z, w_\infty \geq 0$ and to the transverse isotropy condition $D_y = D_x$. Furthermore, for neat resin specimens, complete isotropy is assumed ($D_z = D_x$) while for composites the following relationship is considered [12]:

$$D_z = D_x \cdot \frac{(1 - V_f)}{(1 - 2\sqrt{V_f/\pi})} \tag{2.6}$$

in order to account for the faster diffusion along the fibers, where V_f is the fiber volume fraction. It is important to note that such expression does not account for eventual capillarity effects but only for the geometric effect of fibers acting as obstacles and hindering the diffusion process in the x and y directions. For the laminate considered in this work, $V_f = 0.46$ (obtained through loss on ignition) and therefore $D_z = 2.3 D_x$. The problem can then be solved for D_x and w_∞ using a quasi-Newton nonlinear optimization algorithm.

The parameter identification results can be seen in Figure 2.2 and Table 2.2 (labelled *Optimised* w_∞), where the value of f was adimensionalised with respect to w_∞ to produce relative differences. For neat resin, a good fit was obtained for both specimen types and the identified value of w_∞ coincided with the experimentally obtained one. This indicates that the resin behavior can be correctly represented by Fick's law. For composite specimens, high relative errors were found at long immersion times, as can be seen in plots (b) and (c) of Figure 2.2, suggesting the occurrence of non-Fickian absorption processes. The same conclusion is reached if the value of w_∞ is fixed at the maximum experimental value and the optimisation problem is used to find only D_x (with label *Maximum* w_∞), with the fit being better at longer times but worse at shorter times, with an overall higher value for f.

Even though an accurate Fickian fit cannot be obtained for the complete curves of the composite samples, closer inspection of the 4-ply curve shows an apparent saturation at 1.19% between 1000h and 2000h, suggesting that the absorption behavior takes place in two distinct phases. Fixing $w_\infty = 1.19\%$ and optimising for D_x (*Adjusted* w_∞), a very close fit is obtained for the first 2000h, shown as the f value inside parantheses in Table 2.2. This first absorption phase can therefore be considered as Fickian and is followed by a secondary time-dependent phase. For 6-ply specimens, the same adjusted

value of w_∞ = 1.19% also gives a good fit for the early phase of fast water uptake and an underestimate for the later phase. It is concluded that water uptake on composite specimens is not a purely Fickian process. This can be indicative for topological changes in the material microstructure.

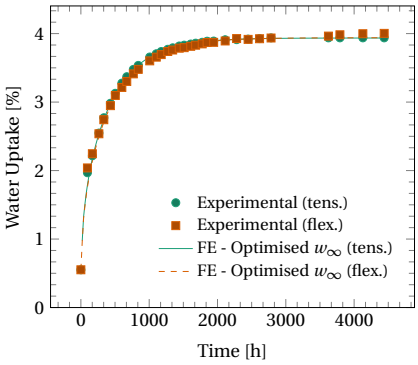

(a) Neat resin specimens

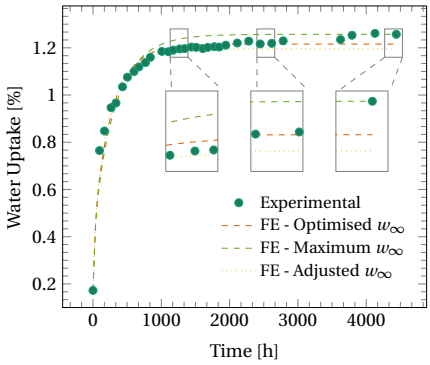

(b) 4-ply composite specimens

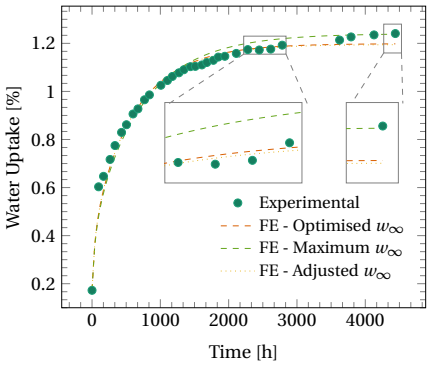

(c) 6-ply composite specimens

Figure 2.2: Water uptake values and Fick's law fit. Each point is an average of measurements in three specimens.

Figure 2.3 shows specimen weights measured during the desorption process for both neat resin and composite, a process that took approximately 3200h. Both types of composite specimens showed weight loss (0.15% loss for 4-ply and 0.06% loss for 6-ply specimens). Such material loss was also observed by other authors [4, 7, 9], particularly when high immersion temperatures are used, and is usually attributed to leaching of hydrolised components from the bulk resin and interphase regions.

For neat resin, on the other hand, a residual water uptake of 0.31% was observed at equilibrium, suggesting that part of the water could not be removed through drying at 50°C. Such behavior was also observed by Zhou and Lucas [13], who describe two types of chemical bonds which occur between water molecules and epoxy polymer chains. Type I bonds have a lower activation energy and are readily removed through drying, but type II bonds have higher energy and require higher drying temperatures in order to be

	Optimised w_∞				Maximum w_∞		Adjusted w_∞	
	Tens.	Flex.	4 plies	6 plies	4 plies	6 plies	4 plies	6 plies
D_x $(\cdot 10^{-13})$ $[m^2/s]$	**7.41**	**7.92**	7.84	7.57	6.46	6.43	**8.57**	**7.68**
D_z $(\cdot 10^{-13})$ $[m^2/s]$	**7.41**	**7.92**	18.03	17.41	14.86	14.79	**19.71**	**17.67**
w_∞ [%]	**3.94**	**3.94**	1.21	1.20	1.26	1.24	**1.19**	**1.19**
f/w_∞^2 $(\cdot 10^{-2})$ [-]	0.33	0.15	1.24	1.18	3.05	1.89	1.84 (0.74)	1.21 (0.01)

Table 2.2: Uptake curve fitting results, with adopted values shown in bold.

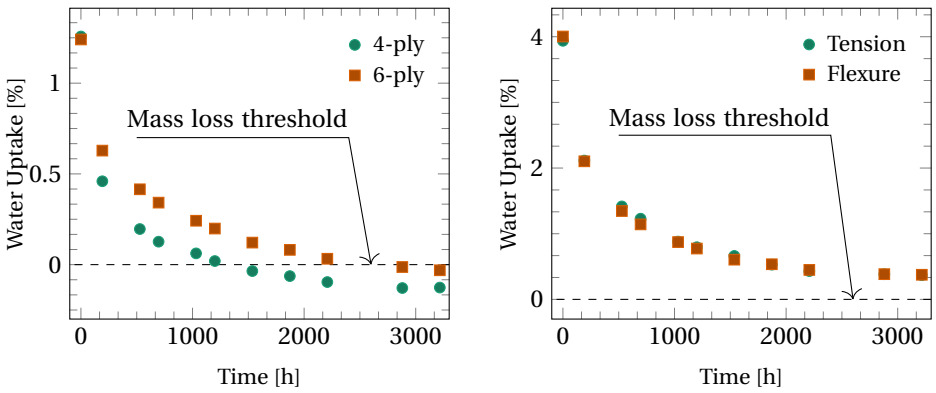

(a) Composite (b) Neat resin

Figure 2.3: Water desorption curves showing weight loss for composites and residual uptake for resin

removed. Two out of the three types of epoxy considered by Zhou and Lucas [13] showed a residual uptake of approximately 0.30% after immersion and drying at 60°C, while the third one retained 0.18% of the absorbed water. The results obtained in this work seem to confirm the existence of such stronger bonds. Furthermore, irreversible water uptake in neat resin implies that the actual amount of material washed away in composite specimens is higher than what follows directly from weight loss measurements.

2.3.2. MECHANICAL TESTS

In order to investigate the evolution of the composite material degradation during water uptake, sets of 4-ply ILSS specimens were tested after 500h, 1000h and 1500h of immersion and at saturation. Figure 2.4 shows stress-displacement curves for specimens tested after each immersion time. To avoid clutter, only one representative curve was chosen from each set. Also shown is the evolution of strength plotted together with the measured water uptake values.

From the results, material degradation both in terms of stiffness and strength can be observed, with up to 36% strength reduction. Such degradation is usually attributed to the combined effect of hydrolytic attack on both the resin and the silanic coupling agent around the fibers [14], differential swelling between fiber and matrix [15] and matrix

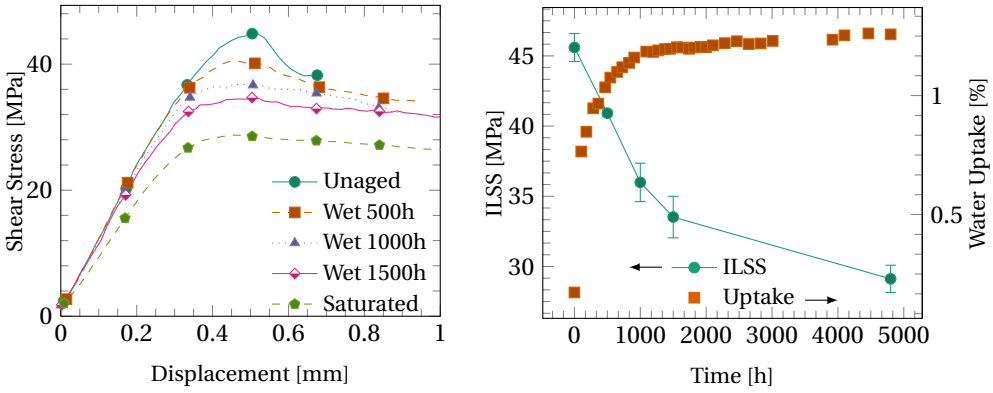

Figure 2.4: Static ILSS results for specimens immersed for multiple durations (4-ply composites).

plasticization [16]. By conducting both mechanical and thermal tests and fractographic observations, the relative contributions of each of these mechanisms will be assessed throughout the rest of this paper.

Closer inspection of the stress-displacement curves of Figure 2.4 suggests that the failure behavior becomes more ductile as immersion time increases, with gradual load drops instead of the more sudden drops observed in reference specimens, suggesting the occurrence of matrix plasticization. Regarding the evolution of strength with immersion time, it can be seen that the degradation keeps increasing well beyond the apparent saturation phase between 1000h and 2000h. This suggests that degradation is not only a function of water uptake but is also time-dependent. Two distinct mechanisms may be suggested as being responsible for such behavior. Firstly, hydrolytic chemical reactions and subsequent leaching of material at the fiber/matrix interfaces lead to a weakening of the interfacial bond and creation of additional spaces for water uptake [17]. Secondly, differential swelling stresses [15, 18] at the weakened interfaces promote crack initiation and propagation, further increasing the available space for water uptake. It is important to note that such mechanisms may act in isolation or in combination, synergistically reinforcing one another.

Results for 6-ply specimens can be seen in Figure 2.5, for which a 34% strength reduction was observed, with similar failure behavior when compared to the 4-ply specimens. In this case, stress-displacement curves for all specimens are shown. Results for both specimen types can also be seen in Table 2.3.

For fatigue, S-N curves were obtained by fitting the experimental data to a straight line in log-log space given by:

$$\log_{10} N = A + B \cdot \log_{10} |\tau_{\max}| \tag{2.7}$$

where N is the number of cycles before failure occurs, $|\tau_{\max}|$ is the absolute value of the maximum attained shear stress and A and B are the intercept and slope parameters, respectively. From the obtained curves, it can be observed that conditioned specimens suffered a fatigue life reduction of three orders of magnitude for a given load level, while

the maximum stress showed decreases of approximately 40% for a given number of cycles, a degradation level similar to the one obtained in the static tests.

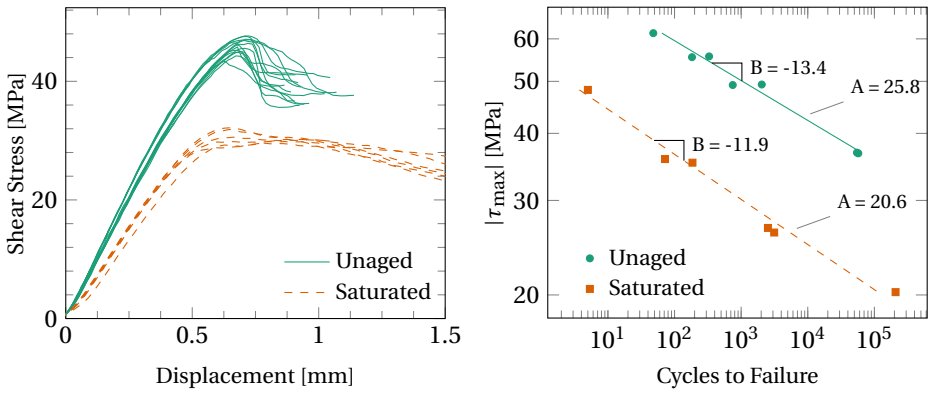

Figure 2.5: Static and fatigue ILSS results for unaged and saturated specimens (6-ply composites).

	Unaged	500h	1000h	1500h	Saturated	Dry	Redried
4 plies							
τ_{max} [MPa]	45.6 ± 1.0	40.9 ± 0.2	35.9 ± 1.4	33.5 ± 1.5	29.1 ± 0.9	53.7 ± 1.6	44.6 ± 1.3
6 plies							
τ_{max} [MPa]	46.1 ± 1.3	-	-	-	30.3 ± 1.1	52.3 ± 1.8	41.7 ± 1.0

Table 2.3: ILSS values of composite specimens for every type of conditioning.

Although interlaminar shear fatigue results after hygrothermal aging for the current material system could not be found in literature, a limited comparison can be made with works dealing with other resin systems or test types. Hu et al. [19] reported 90° tension-tension fatigue results on the same glass/epoxy system used in this work, with strength reductions of up to 44% for low cycle tests, similar to the present results. As 90° tension and interlaminar shear tests are both dominated by a combination of resin and interface properties, similar levels of degradation were expected. However, a drastic slope reduction was obtained by the authors, resulting in near-horizontal S-N curves for wet samples and seemingly no effect of aging in high cycle tests. Such behavior, which was also reported by Vauthier et al. for a different glass/epoxy system [20], was not observed here.

In order to investigate the relative contributions of interface and matrix damage after immersion, neat epoxy specimens were tested in tension and bending. Stress-displacement curves for reference and conditioned specimens are shown in Figures 2.6 and 2.7, while average results can be seen in Tables 2.4 and 2.5. For both specimen types, the Young's modulus and strength decreased by approximately 17% after saturation. A slight change in failure mode was also noticed for tension specimens, as can be seen in Figure 2.10, with saturated specimens showing a markedly ductile behavior with extensive

necking. In fatigue, the number of cycles to failure decreased by two orders of magnitude for a given stress level and a slightly steeper slope was obtained, which is again opposite to the behavior observed by other authors [19, 20].

Here, two possible major degradation mechanisms exist, namely plasticization and breakage of polymer chains through hydrolytic reactions. While the more ductile failure mode suggests that plasticization is the main effect, the thermal tests of Section 2.3.4 will be used to confirm this hypothesis. Comparing results of resin and composite specimens, it can be seen that the observed magnitude of resin degradation (17%) is not enough to explain the one obtained for composites (35%), indicating that interfacial hydrolysis and differential swelling play an equally important role in the total property reduction.

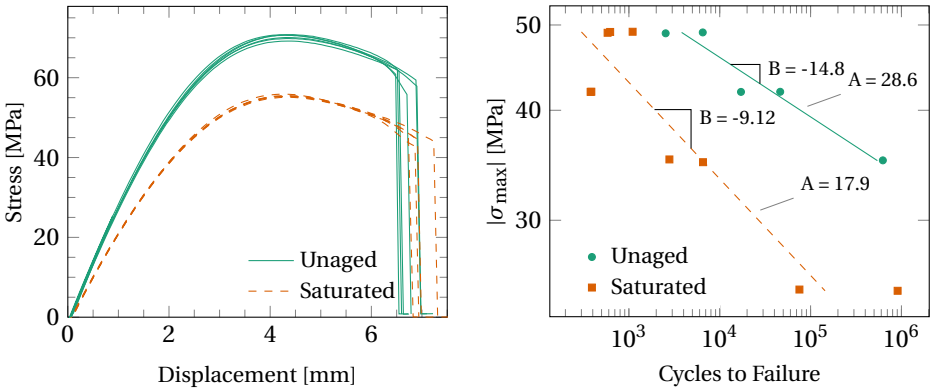

Figure 2.6: Static and fatigue tension results for unaged and saturated specimens (neat resin).

	Unaged	Saturated	Dry	Redried
σ_{max} [MPa]	70.3 ± 0.6	55.5 ± 0.3	72.2 ± 0.3	58.1 ± 11.5
ϵ at σ_{max} [%]	4.53 ± 0.05	4.35 ± 0.08	4.53 ± 0.05	2.71 ± 1.05
ν [-]	0.381 ± 0.010	0.399 ± 0.018	0.382 ± 0.007	0.374 ± 0.011
E [GPa]	3.15 ± 0.06	2.53 ± 0.07	3.06 ± 0.03	3.05 ± 0.03

Table 2.4: Results of tension tests in neat epoxy specimens for every type of conditioning.

	Unaged	Saturated	Dry	Redried
$\sigma_{flex,max}$ [MPa]	113.8 ± 0.4	95.1 ± 0.6	116.2 ± 0.7	113.8 ± 1.4
ϵ at $\sigma_{flex,max}$ [%]	5.98 ± 0.12	5.85 ± 0.09	5.84 ± 0.08	5.89 ± 0.11
E_{flex} [GPa]	2.88 ± 0.23	2.47 ± 0.03	3.03 ± 0.02	3.03 ± 0.10

Table 2.5: Results for bending tests in neat epoxy specimens for every type of conditioning.

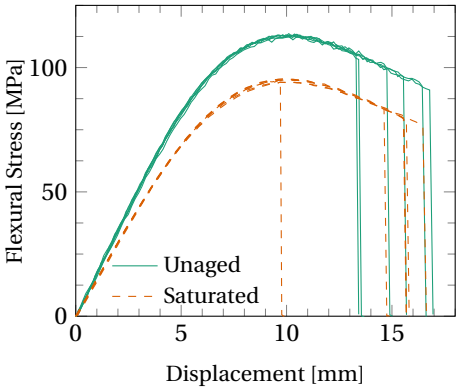

Figure 2.7: Static bending results for unaged and saturated specimens (neat resin).

As both differential swelling and softening effects caused by plasticization are reversible upon moisture removal, tests on redried specimens are useful in order to isolate the contribution of the non-reversible mechanisms. As mentioned in Section 2.2.2, results from the *Redried* set will be compared with those from the *Dry* set, since both are tested after complete drying at 50°C and after stabilisation of polymer relaxation processes. Figures 2.8 and 2.9 show stress-displacement curves for both sets, with average results shown in Tables 2.3, 2.4 and 2.5.

For composites, an irreversible shear strength degradation of 17% for 4-ply and 20% for 6-ply specimens was found, with similar permanent reductions observed for the shear stiffness. This irreversible degradation indicates a significant contribution of the combined effect of hydrolytic interface weakening and cracking driven by differential swelling stresses, a process which is also consistent with the observed non-Fickian absorption uptake phase and the mass loss upon drying.

It is also important to investigate the resin behavior after redrying, since any irreversible effects on the resin will also impact the composite behavior. Here, in contrast to previous observations, the effect on stiffness is markedly different from the one on strength and fracture behavior. For both tensile and bending specimens, a complete recovery of stiffness was obtained after drying. However, a transition from ductile to brittle failure behavior was observed (Figure 2.10). This effect can be observed for bending specimens in the form of a lower strain at failure for redried specimens, but is much more drastic for tensile specimens, with only one specimen out of six reaching the end of the plastic hardening regime and sudden failure with a large amount of scatter for all other specimens.

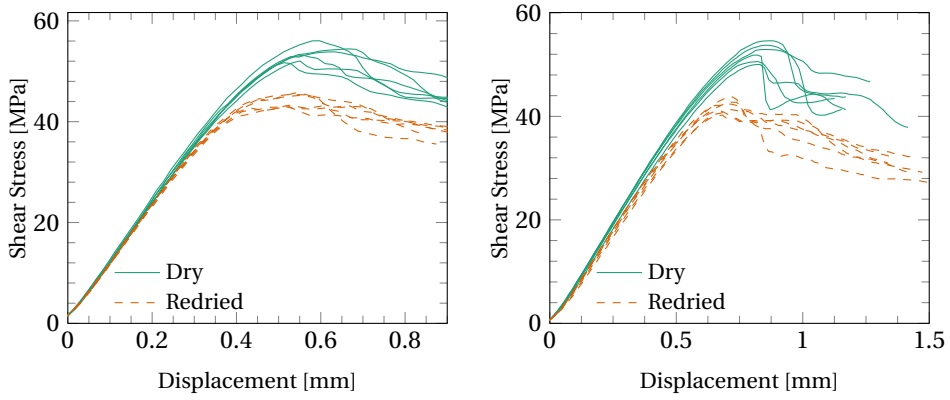

(a) 4-ply specimens (b) 6-ply specimens

Figure 2.8: Static ILSS results for dry and redried specimens (4-ply and 6-ply composites) .

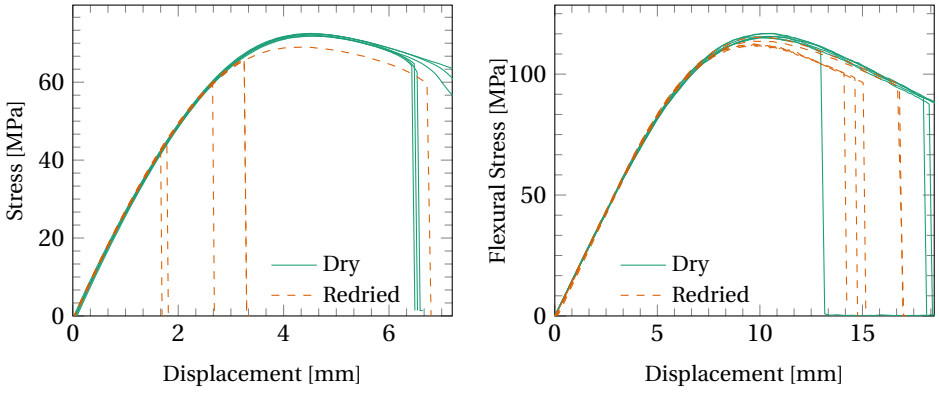

(a) Tension (b) Flexure

Figure 2.9: Static tension and bending results for dry and redried specimens (neat resin).

Assuming that the possibility of post-curing and chain breakage during the immersion and redrying steps can be ruled out (see Section 2.3.4 for details), two explanations can be proposed for the observed decrease in the strain at failure. First, even though both specimen sets were given enough time for polymer relaxation to happen until stabilisation [6], the movement of water molecules during the uptake-desorption cycle experienced by the redried specimens may have modified their free volume structure, as argued by Wong and Broutman [5], which would bring changes to their fracture behavior. Second, the residual water retained in the specimens after redrying may be promoting secondary crosslinks between polymer chains, as proposed by Zhou and Lucas [13]. Such stronger link between the water molecules and polymer chains also helps explaining why they require a higher energy in order to be removed.

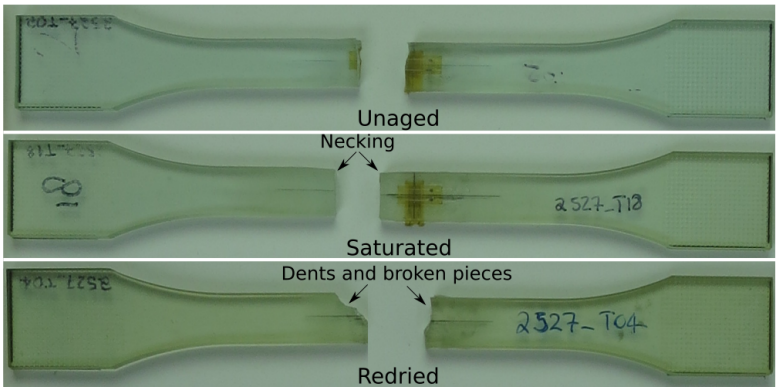

Figure 2.10: Change of failure pattern between unaged, saturated and redried tension specimens.

2.3.3. MICROSCOPIC OBSERVATIONS

Composite specimens from the *Dry* and *Saturated* sets were inspected using an optical microscope both before and after being tested. The inspections conducted before testing were carried out to find evidences of material degradation from immersion, while the ones conducted after testing investigated changes in failure behavior caused by such degradation.

Figure 2.11 shows x-y plane views of a dry and a saturated specimen (plies are stacked along the z axis). After immersion, the fiber bundles, which were barely visible in reference specimens, can be visually identified, suggesting that interface debonding took place. In particular, this is visible in the areas marked (a) and (b), showing debonding in fibers oriented both in 0° and 90° directions. Figure 2.12 shows views of the x-z plane of two different saturated specimens at two different points along their thickness. In the pictures, the fabric stitches can be seen as shadows in the spaces between two consecutive plies and are indicated in white. In both pictures, regions of intact and darkened fibers can be identified, with the latter being marked by arrows. Such darkened fibers are indicative of cracks running along the interfaces and are considered as a sign of weak interface adhesion since they do not propagate to the surrounding resin [21, 22]. These observations reinforce the hypothesis that the combination of high differential swelling stresses and a weakened interface cause cracks to propagate along them and create new loci for water absorption.

Figures 2.13 and 2.14 show y-z views of dry and saturated specimens after being tested in three-point bending, with the fiber direction oriented out of plane. The general failure behavior is the same for both condition types, with longitudinal shear cracks running through the whole width of the specimens. For dry specimens, a single crack or a pair of symmetric cracks is observed around the fiber bundle located at mid-thickness, where the material experiences the maximum value of shear stress. For saturated specimens, on the other hand, cracks occur at multiple locations, including in regions close to the specimen surfaces, as shown in Figure 2.14a. This observation is consistent with the fact that regions closer to the surfaces were the first to get saturated and therefore the ones exposed for the longest time to the time-dependent degradation mechanisms

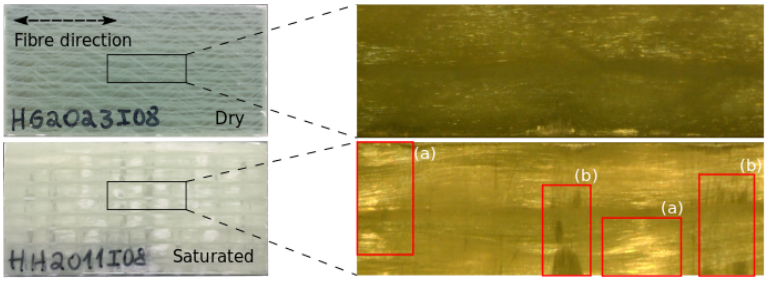

Figure 2.11: In-plane microscopic comparison of dry and saturated specimens, with (a) debonding in the 0° direction and (b) debonding in the 90° stabilization roving.

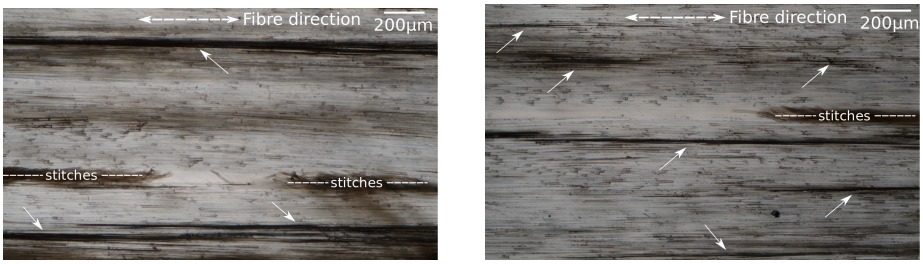

Figure 2.12: Through-thickness micrographs of a saturated specimen with arrows indicating debonded regions.

mentioned in Section 2.2. The crack propagation behavior was also different between dry and saturated specimens. In dry samples, the main crack tends to run along the boundaries of fiber bundles, with secondary cracks moving inside the bundles being arrested. In saturated samples, the cracks tend to run inside the bundles, where differential swelling creates high stress concentrations.

Finally, upon further investigation of the crack surfaces at higher magnifications, more differences between dry and saturated specimens become apparent. Crack surfaces in dry specimens suggest a failure dominated by clean fiber/matrix interface debonding (Figure 2.13b). For saturated specimens, at multiple points along the cracks (marked with arrows in Figure 2.14a), damage was more distributed, with the presence of resin fragments between fibers (marked areas in Figure 2.14b), suggesting that the main crack was formed by the propagation and coalescence of multiple smaller interface cracks. This reinforces both hypotheses of a plasticized resin and a weakened fiber/matrix interface after immersion and the consequent crack arrest mechanisms explain the increasingly ductile material behavior as more water is absorbed (Figure 2.4).

2.3.4. THERMAL TESTS

Figure 2.15 shows storage modulus curves obtained through DMA testing, where the crossing of tangents to the inflection points in the storage modulus curve is considered to be the glass transition temperature (T_g) of the resin. Loss factor curves are also plotted

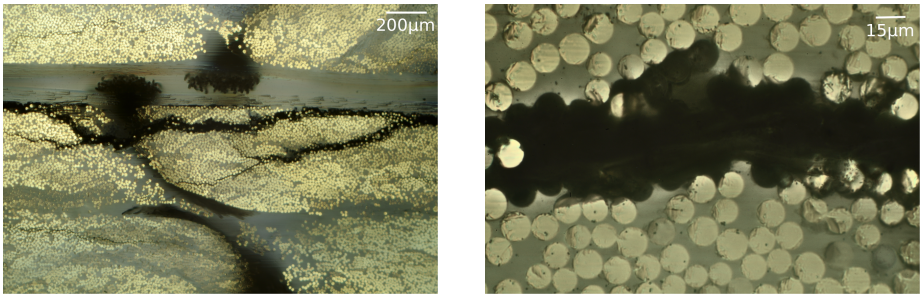

(a) Crack propagation (b) Detail of the crack surface

Figure 2.13: Microscopic observation of the crack surfaces of a dry specimen after testing.

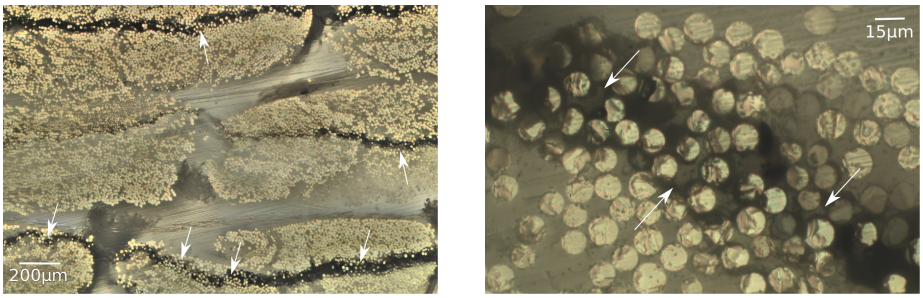

(a) Crack propagation (b) Detail of the crack surface

Figure 2.14: Microscopic observation of the crack surfaces of a saturated specimen after testing, with arrows indicating regions of predominant plastic resin failure.

and peak values are marked (T_{fp}). Average values are reported in Table 2.6. In saturated specimens, the measured glass transition temperature was on average 17°C lower than in *Unaged* specimens. Such decrease is in line with the observed decreases in stiffness and strength of the resin, since it also points to the occurrence of matrix plasticization.

Comparing results from the *Dry* and *Redried* sets, previous exposure to moisture resulted in an increase of 4°C to the measured T_g, which agrees with the observed change to brittle failure modes in mechanical tests. As an increase in T_g is expected both in the case of additional crosslinking and polymer relaxation associated with a reduction of specific free volume [6], the results observed here support the hypothesis that these processes can explain the decrease in strain at failure discussed in Section 2.3.2. Similar changes were observed for the loss peak temperature, although a second peak is observed for the *Saturated* set. This phenomenon was also observed by other authors [23, 24], who attributed it to a phase change of water molecules not attached to the polymer structure. However, since the temperature for the second peak is similar to the one for *Unaged* samples, it may also point to the presence of unplasticized polymer chains in the saturated material.

Figure 2.16 shows Differential Scanning Calorimetry (DSC) curves for one representative specimen of each set. To facilitate the comparison between specimens, the curves

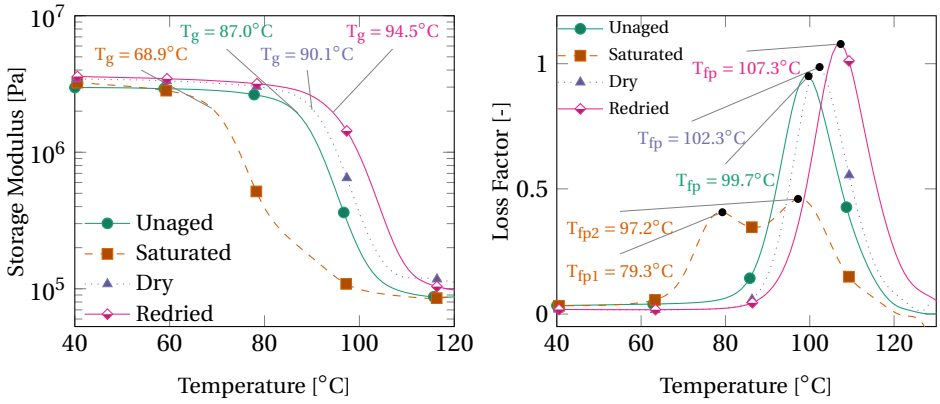

(a) Storage modulus (b) Loss Factor

Figure 2.15: DMA results for every type of conditioning (neat resin).

	Unaged	Saturated	Dry	Redried
Dynamic Mechanical Analysis (DMA)				
T_g [°C]	86.8 ± 0.3	70.0 ± 0.6	90.3 ± 0.4	94.3 ± 0.4
T_{fp} [°C]	99.1 ± 0.5	80.3 ± 0.8 & 98.9 ± 1.1	101.9 ± 0.4	107.4 ± 0.4
Differential Scanning Calorimetry (DSC)				
T_{g1} [°C]	86.6 ± 0.3	69.3 ± 0.5	90.1 ± 1.7	87.9 ± 2.5
T_{g2} [°C]	90.1 ± 0.8	88.2 ± 0.5	89.4 ± 1.2	89.0 ± 0.3
Δh [J/g]	1.44 ± 0.55	6.16 ± 0.48	2.99 ± 0.45	2.64 ± 0.31

Table 2.6: Thermal analysis results on neat resin.

were scaled based on the heat capacity value at 140°C. The main conclusion here comes by considering the results from the second heat cycle, after the specimens were kept at 130°C in order to erase their polymer relaxation history and remove residual water molecules. The T_{g2} of specimens for all conditions, measured at the onset of the phase change, was the same, indicating that no additional monomer-hardener crosslinks occurred during drying or redrying of the samples and that chain breakage through hydrolysis was not significant during immersion.

Finally, T_g measurements are also taken during the first heating cycle. As expected, T_{g1} values of saturated specimens were lower than those of the other sets due to the presence of plasticized polymer chains. However, comparing the *Dry* and *Redried* sets, no significant difference in T_{g1} was found, in contrast to the results obtained with DMA tests. As the first cycle usually includes an enthalpy relaxation peak caused by physical aging occurred during manufacturing and conditioning, it is also interesting to evaluate their magnitudes (Δh) by subtracting the first and second cycle curves and taking the area below the resultant curve in a 30°C temperature range starting at the glass tran-

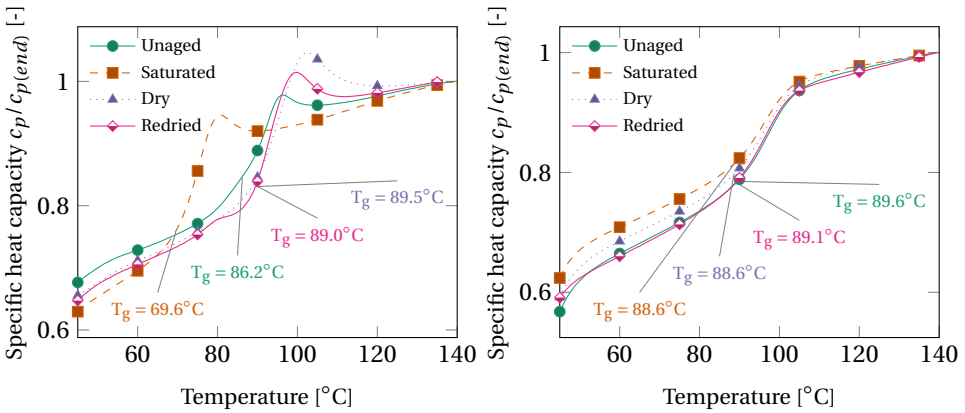

(a) First heating cycle

(b) Second heating cycle

Figure 2.16: DSC results for every type of conditioning (neat resin).

sition onset. As the *Unaged* condition was chosen in order to minimise the effects of polymer relaxation, an expected increase in Δh is observed for *Dry* and *Redried* samples. Differences were also observed between the two dry sets, indicating differences in their polymer structure and agreeing with DMA and mechanical test results. Lastly, the relaxation of *Saturated* specimens was the highest and can be associated with the combined phase change of the resin and unbounded water molecules.

2.4. CONCLUSIONS

This chapter investigated material degradation effects caused by hygrothermal aging in composite and neat epoxy specimens for a fiber and resin system representative of the material used in wind turbine blades. Water uptake and desorption behaviors were investigated. Specimens were conditioned in hot water (50°C) for 4800h, dried after having been immersed and isothermally dried without immersion. Static and fatigue properties of aged and unaged specimens were measured and compared. Additionally, a combination of thermal analytical techniques and optical microscopy was used in order to explain the relative contributions of each degradation effect.

An optimisation-based parameter identification procedure was used to fit a 3D Fick finite element model to the measured uptake data. For neat resin, the behavior was Fickian, while for composites it was composed of an initial Fickian phase followed by a secondary non-Fickian absorption phase at longer immersion times. Upon redrying, composite specimens showed weight loss linked to the combined action of interface decomposition and crack propagation driven by differential swelling stresses with subsequent leaching of material. For neat resin specimens, part of the water could not be removed through redrying, an evidence suggesting that part of the water molecules form stronger bonds with the polymer network [13] and that the material loss observed for composite specimens is higher than what follows from weight measurements.

Material degradation in composite specimens as measured through mechanical tests

was not only dependent on the water uptake but also on immersion time, with shear strength reductions of up to 36% and fatigue life up to three orders of magnitude shorter. For resin specimens, a degradation level of approximately 17% was observed, both in tension and in bending. After redrying, an irreversible mechanical property reduction of 17% was found for composite samples, while for resin the stiffness and maximum attainable stress are fully recovered and a notable decrease in the strain level at failure is observed. Even though different test types were used in the comparison between composite and resin, the observed differences in magnitude and reversibility of degradation strongly indicate that composite degradation cannot be fully explained by only considering mechanisms that act on the resin. Fractographic analysis in unaged composite samples indicated that cracks tend to run along the fiber bundle boundaries and concentrate close to the specimen mid-thickness. For saturated ones, cracks are evenly distributed along the specimen thickness and tend to propagate inside the bundles, suggesting the presence of high differential swelling stresses.

Based on the conducted material investigations, the following chronology is proposed for the hygrothermal aging process in the present glass/epoxy system: Water diffuses through the material and promotes resin plasticization, degradation of interfacial strength and differential swelling. The combination of the time-dependent weakening of the interfaces with the high differential swelling stresses promotes crack formation along the interfaces and cause additional water uptake in the newly created empty volumes. Upon redrying, the plasticization is reversed and differential swelling subsides, leading to property recovery, although the resin free volume is irreversibly changed and part of the water molecules remain strongly bonded to polymer chains. However, as the irreversible effects on resin specimens do not significantly impact their mechanical behavior, it can be concluded that the interface cracks formed in composites during uptake are the main reason for the observed permanent reductions in stiffness and strength. With the obtained information about the relative contributions of each degradation effect and their interactions, numerical models can be developed to simulate the aging process and subsequent material failure during service fatigue loading.

REFERENCES

[1] I. B. C. M. Rocha, S. Raijmaekers, R. P. L. Nijssen, F. P. van der Meer, and L. J. Sluys, *Hygrothermal ageing behaviour of a glass/epoxy composite used in wind turbine blades,* Composite Structures **174**, 110 (2017).

[2] *Technical data sheet - EPIKOTE resin MGS RIMR 135 and EPIKURE curing agent MGS RIMH 134-RIMH 137*, Tech. Rep. (Momentive, 2006).

[3] R. Polanský, V. Mantlík, P. Prosr, and J. Sušír, *Influence of thermal treatment on the glass transition temperature of thermosetting epoxy laminate,* Polymer Testing **28**, 428 (2009).

[4] P. Davies, F. Mazéas, and P. Casari, *Sea water aging of glass reinforced composites: Shear behaviour and damage modelling,* Journal of Composite Materials **35**, 1343 (2000).

[5] T. C. Wong and L. J. Broutman, *Water in epoxy resins part II. diffusion mechanism,* Polymer Engineering and Science **25**, 529 (1985).

[6] G. M. Odegard and A. Bandyopadhyay, *Physical aging of epoxy polymers and their composites,* Journal of Polymer Science: Part B **49**, 1695 (2011).

[7] B. Dewimille and A. R. Bunsell, *Accelerated ageing of a glass fibre-reinforced epoxy resin in water,* Composites , 35 (1983).

[8] H. S. Choi, K. J. Ahn, J.-D. Nam, and H. J. Chun, *Hygroscopic aspects of epoxy/carbon fiber composite laminates in aircraft environments,* Composites: Part A **32**, 709 (2001).

[9] S. A. Grammatikos, B. Zafari, M. C. Evernden, J. T. Mottram, and J. M. Mitchels, *Moisture uptake characteristics of a pultruded fibre reinforced polymer flat sheet subjected to hot/wet aging,* Polymer Degradation and Stability **121**, 407 (2015).

[10] F. Ellyin and C. Rorhbacher, *Effect of aqueous environment and temperature on glass-fibre epoxy resin composites,* Journal of Reinforced Plastics and Composites **19**, 1405 (2000).

[11] G. Pitarresi, M. Scafidi, S. Alessi, M. Di Filippo, C. Billaud, and G. Spadaro, *Absorption kinetics and swelling stresses in hydrothermally aged epoxies investigated by photoelastic image analysis,* Polymer Degradation and Stability **111**, 55 (2015).

[12] C. H. Shen and G. S. Springer, *Environmental effects on composite materials* (Technomic, 1981).

[13] J. Zhou and J. P. Lucas, *Hygrothermal effects of epoxy resin. part I: the nature of water in epoxy,* Polymer **40**, 5505 (1999).

[14] L. Salmon, F. Thominette, J. Verdu, and M. Pays, *Hydrolytic degradation of model networks simulating the interfacial layers in silane-coupled epoxy/glass composites,* Composites Science and Technology **57**, 1119 (1997).

[15] Y. Joliff, W. Rekik, L. Belec, and J. F. Chailan, *Study of the moisture/stress effects on glass fibre/epoxy composite and the impact of the interphase area,* Composite Structures **108**, 876 (2014).

[16] L. Gautier, B. Mortaigne, and B. V., *Interface damage study of hydrothermally aged glass-fibre-reinforced polyester composites,* Composites Science and Technology **59**, 2329 (1999).

[17] S. A. Grammatikos, M. Evernden, J. Mitchels, B. Zafari, J. T. Mottram, and G. C. Papanicolaou, *On the response to hygrothermal ageing of pultruded FRPs used in the civil engineering sector,* Materials and Design **96**, 283 (2016).

[18] T. Morii, N. Ikuta, K. Kiyosumi, and H. Hamada, *Weight-change analysis of the interphase in hygrothermally aged FRP: Consideration of debonding,* Composites Science and Technology **57**, 985 (1997).

[19] Y. Hu, A. W. Lang, X. Li, and S. R. Nutt, *Hygrothermal aging effects on fatigue of glass fibre/polydicyclopentadiene composites,* Polymer Degradation and Stability **110**, 464 (2014).

[20] E. Vauthier, J. C. Abry, T. Bailliez, and A. Chateauminois, *Interactions between hygrothermal ageing and fatigue damage in unidirectional glass/epoxy composites,* Composites Science and Technology **58**, 687 (1998).

[21] C. L. Schutte, W. McDonough, M. Shioya, M. McAuliffe, and M. Greenwood, *The use of a single-fibre fragmentation test to study environmental durability of interfaces/interphases between dgeba/mpda epoxy and glass fibre: the effect of moisture,* Composites **25**, 617 (1994).

[22] A. Sjögren, R. Joffe, L. Berglund, and E. Mader, *Effects of fibre coat (size) on properties of glass fibre/vinyl ester composites,* Composites: Part A **30**, 1009 (1999).

[23] B. De'Nève and M. E. R. Shanahan, *Water absorption by an epoxy resin and its effect on the mechanical properties and infra-red spectra,* Polymer **34**, 5099 (1993).

[24] C. Li, R. A. Dickie, and K. N. Morman, *Dynamic mechanical response of adhesively bonded beams: Effect of environmental exposure and interfacial zone properties,* Polymer Engineering and Science **30**, 249 (1990).

3

ANISOTROPIC MOISTURE DIFFUSION IN GLASS/EPOXY COMPOSITES

The worst form of inequality it to try to make unequal things equal.

Aristotle, *Politics*

3.1. INTRODUCTION

Since the aging process is driven by water ingression, as the results in Chapter 2 indicate, it is important to understand the process of water diffusion across scales. For fiber reinforced polymers, the material microstructure brings complexity to the diffusion phenomenon since water molecules have to go around the fibers for diffusion in transverse direction [2], giving rise to orthotropic diffusion behavior. Furthermore, chemical interaction between the epoxy and fiber sizing creates an interphase region around the fibers where water diffusivity can be different from the one in bulk resin regions [3].

In this chapter, a combined experimental and numerical approach is used to elucidate the water diffusion process in composite laminates. For the experimental part, a thick unidirectional glass/epoxy composite panel was manufactured and thin slices were cut along the three orthotropy planes of the material. The slices were immersed in demineralised water at 50°C and weighed at regular intervals. By fitting a unidimensional analytical solution of Fick's second law of diffusion to the experimentally obtained

Apart from minor changes to its introductory section, this chapter was integrally extracted from [1].

water uptake curves, the orthotropic diffusivity constants were retrieved. Using a combination of scanning thermal microscopy and local thermal analysis, the presence of an interphase was confirmed for the present composite system and its approximate thickness was measured.

The diffusivity coefficients were also numerically obtained through homogenisation of the microscopic diffusion behavior. For this purpose, a three-dimensional Representative Volume Element (RVE) was subjected to water concentration gradients in each direction. By integrating the flux components in the microscopic volume, homogenised diffusivity values were obtained. In order to account for the impact of the fiber/matrix interphase on the diffusion process, the resin diffusivity was made a function of the distance to the nearest fiber. A parametric study on the RVE size and mesh density was performed and the model was used to verify the validity of a number of hypotheses put forward in literature that may explain the observed anisotropy.

3.2. EXPERIMENTS

3.2.1. MATERIALS

The material system considered in the present study consists of the epoxy resin EPIKOTE 135/1366, manufactured by Momentive [4], with embedded unidirectional glass fiber fabrics (Saertex PPG 2002 2400tex [5]). For the resin preparation, the monomer and hardener were mixed in a 100:30 ratio and the resultant mixture was degassed in vacuum in order to minimise void content. Unidirectional glass fiber plies were stacked and infused through vacuum bagging in a heated flat mould.

In order to experimentally investigate the anisotropic diffusion behavior through weight measurements, specimens must be devised in such a way that the water movement in a certain direction is promoted while diffusion in the other directions is minimised. This can be achieved by selectively sealing specimen edges [6] or by cutting thin material slices in each direction [2]. Here, the latter procedure was chosen and a thick laminate of 50 unidirectional (UD) plies (total thickness of 30 mm) was manufactured in order to obtain specimens with high width/thickness and length/thickness ratios for three different orientations.

Each UD fabric ply used in the manufacturing was mainly composed of fibers oriented at 0° (95% in weight) with stability rovings oriented at 90° accounting for 5% of their weight. In order to obtain a purely UD laminate, the stability rovings were manually removed prior to infusion. The panel was cured for 3 hours at 30°C and 5 hours at 50°C, with a subsequent post-curing period of 10 hours at 70°C. After curing, 30 x 30 mm^2 slices were cut from the panel along the three orthotropy planes of the material, as shown in Figure 3.1.

Three slices were cut in each direction using a water-cooled diamond saw and were grinded with a Labopol 30 polishing machine using progressively higher sanding grits ranging from 320 to 1200 until a thickness of 0.9 mm was reached, resulting in width/thickness and length/thickness ratios of approximately 30. The average thickness among the nine slices was 0.94±0.06 mm, while the average ratio was 31.9±2.3. Finally, the surfaces were polished using a suspension of diamond particles with average diameter of 1 μm. The final surfaces were inspected for defects using a Motic BA210 optical micro-

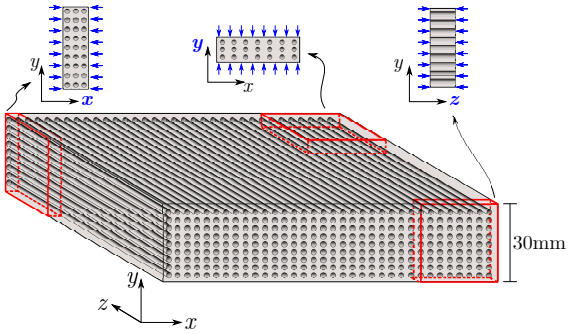

Figure 3.1: Material slices and preferred diffusion directions.

scope, although the occurrence of microscopic failure events such as interface debonding during specimen preparation cannot be completely ruled out. Using three additional specimens, average values of fiber volume fraction of 53.1±0.27% and void content of 0.85±0.21% were obtained through loss on ignition, according to the ISO 1172 standard.

3.2.2. CONDITIONING

In order to obtain accurate measurements of the maximum water uptake, the slices were first dried for approximately 200 h in a desiccator at 50°C, after which a stable weight was achieved. The choice of the reference state in diffusion experiments on polymer matrix composites can be a complex one, since additional aging processes such as physical aging and oxidation can occur during the initial drying phase. Due to changes in the polymer structure caused by these additional aging mechanisms, the diffusivity and the maximum uptake may suffer both reversible and irreversible changes [7, 8]. In this work, oxidative reactions were avoided by applying vacuum to the desiccator during the drying process, while the short duration of the drying phase, enabled by the use of thin slices, helped to minimise the influence of physical aging.

The slices were subsequently immersed in demineralised water kept at a temperature of 50±1.5°C. This immersion temperature was chosen in order to accelerate water uptake while keeping a safety margin of 20°C from the glass transition temperature (T_g) measured in saturated resin specimens (70°C). The T_g of the unaged resin is 87°C (Section 2.3.4). Dependency of the diffusivity on the immersion temperature is well documented in literature [9] and will not be treated in the present work.

Water uptake was individually tracked for each slice through weight measurements, according to the ASTM D5229/D5229M-14 standard, using a Kern ALJ 160-4NM analytical balance with 0.1 mg resolution. Hourly weighings were performed in the first 8 hours of immersion, two weighings were performed on the second day and the frequency was decreased to one weighing per day for the remainder of the experiment. Only one slice was taken out of immersion at a time, with the complete weighing procedure for each individual slice taking approximately one minute.

3.2.3. DIFFUSIVITY COMPUTATION

The experimental water uptake w_{exp} at time t is computed from the measured weight m according to the ASTM D5229/D5229M-14 standard:

$$w_{\text{exp}}(t) = 100 \cdot \left(\frac{m(t) - m_{\text{dry}}}{m_{\text{dry}}} \right) \tag{3.1}$$

where m_{dry} is the weight measured after the initial drying phase. The diffusion process is considered as one-phase Fickian. Due to the high width/thickness and length/thickness ratios of the slices, the diffusion is modeled as a one-dimensional process in the thickness direction:

$$\frac{\partial c}{\partial t} = D_s \frac{\partial^2 c}{\partial s^2} \tag{3.2}$$

where $s \in \{x, y, z\}$ is the preferred diffusion direction which depends on the cutting direction of the slice and $c = c(s)$ is the water concentration field. An analytical solution for the volume averaged water uptake during immersion of an initially dry specimen, w_{fick}, can be obtained [6]:

$$w_{\text{fick}}(D_s, w_\infty, t) = w_\infty \left\{ 1 - \frac{8}{\pi^2} \sum_{n=0}^{\infty} \left[\frac{1}{(2n+1)^2} \exp\left(-\frac{D_s (2n+1)^2 \pi^2 t}{h^2} \right) \right] \right\} \tag{3.3}$$

where w_∞ is the uptake level at saturation and h is the thickness of the slice.

Suitable values for the Fick model parameters D_s and w_∞ have to be chosen in order to fit the experimental uptake points. The fitting procedure can be cast as an unconstrained optimisation problem involving the minimisation of an objective function f which gives the sum of the squared difference between experimental and analytical data:

$$f(D_s, w_\infty) = \sum_t [w_{\text{exp}}(t) - w_{\text{fick}}(D_s, w_\infty, t)]^2 \tag{3.4}$$

which can be solved for D_s and w_∞.

3.2.4. SCANNING THERMAL MICROSCOPY AND LOCAL THERMAL ANALYSIS

To study the composite surfaces in search of an interphase region around the fibers, a micro-thermal analyser μTA$^{\text{TM}}$ 2990 from TA-Instruments was used. A number of authors conducted studies on the measurement of interphases in thermoset composite materials using μTA [3, 10–13], showing that micro-thermal analysis may be used to characterize interphases in such composites. The instrument was calibrated following the procedures described in [14]. Two modes of operation were employed. In a surface mapping mode, the thermal probe was used in AFM-contact mode over a 100μm x 100μm area. The probe was held at a temperature of 60°C (below the glass transition temperature of the epoxy resin). This resulted in images of the topography and of the thermal conductivity. In a second mode, localised thermal analysis (L-TA) was performed. The probe was held in contact at a location selected after the mapping. The temperature of the probe was raised from 25°C to 250°C with a rate of 10 K/s while recording the vertical position of the probe (L-TMA, localised thermomechanical analysis) and the power difference between sample and reference probe needed to realize the

programmed temperature ramp (L-CA, localised calorimetry) simultaneously. A measurement in the air was used as a baseline signal.

Glass transition temperatures were evaluated as the onset of the drop in the sensor deflection signal. This corresponds to the beginning of polymer softening. For L-CA measurements, glass transition temperatures are not easily detected for highly crosslinked thermoset materials [12]. After each L-TA measurement, the probe was heated to 600°C over a period of 1 s to remove any residue of polymeric material. The results have been shown to be reproducible.

3.3. NUMERICAL MODELING

3.3.1. MICROSCOPIC DIFFUSION PROBLEM

At the macroscopic scale, diffusion is assumed to be orthotropic and can therefore be described by three independent diffusivities D_x, D_y and D_z, with z being the direction parallel to the fibers (Figure 3.1). It is hypothesised that such orthotropic behavior is a consequence of the microscopically inhomogeneous nature of the composite material. Therefore, the diffusivity coefficient in each direction can be retrieved through homogenisation of the microscopic diffusion behavior. Furthermore, it is assumed that the diffusivity coefficient does not depend on time or on water concentration.

At the microscopic scale, the composite material is represented by a three-dimensional RVE composed of unidirectional fibers and surrounding matrix. Since water does not diffuse through the fibers, only the resin is modeled. The fiber arrangements were generated using the discrete element package HADES [15]. A fiber volume fraction of 53.1% was used and the fiber diameter was fixed at 15 μm. A minimum distance of 0.5μm between the fibers was adopted during the contact analysis in order to avoid fiber overlap. The diffusion process is idealised as steady-state [16, 17]:

$$\nabla \cdot \mathbf{j} = 0 \tag{3.5}$$

where $\mathbf{j}$ is the flux vector. After applying an average (macroscopic) concentration gradient $(\nabla c)^{\mathrm{M}}$ to the RVE, the microscopic water concentration field can be decomposed without loss of generality in:

$$c(\mathbf{x}) = c^0 + (\nabla c)^{\mathrm{M}}\mathbf{x} + \tilde{c}(\mathbf{x}) \tag{3.6}$$

where c^0 is the concentration of the origin of the microscopic coordinate frame and $\tilde{c}$ is a fluctuation field [17].

Consistent homogenisation requires that the volume average of the microscopic concentration gradients must be equal to the applied gradients $(\nabla c)^{\mathrm{M}}$, with the same holding true for the resultant flux $\mathbf{j}^{\mathrm{M}}$:

$$(\nabla c)^{\mathrm{M}} = \frac{1}{|\omega|}\int_{\omega} (\nabla c)\, d\omega \qquad \mathbf{j}^{\mathrm{M}} = \frac{1}{|\omega|}\int_{\omega} \mathbf{j}\, d\omega \tag{3.7}$$

with ω being the RVE volume. The use of such homogenisation operators requires the average of gradients and fluxes to be zero at the RVE boundaries [16]. This requirement is enforced by imposing periodicity of concentration at the edges of the micromodel. More

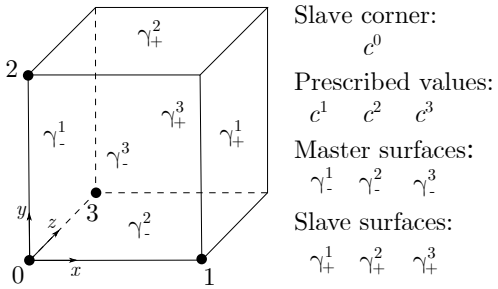

Figure 3.2: Periodic RVE with prescribed nodes, master and slave surfaces.

details on the homogenization and asymptotic analysis concepts used in the present formulation can be found in [16].

Figure 3.2 shows the node groups involved in the definition of such periodic boundary conditions. The macroscopic concentration gradient components in the x, y and z directions are applied to the control nodes 1, 2 and 3, respectively:

$$c^s = (\nabla c)^{\mathrm{M}} \mathbf{x}^s \tag{3.8}$$

where $\mathbf{x}^s$ is a vector with the coordinates of controlling node $s \in \{1,2,3\}$. The concentrations on opposing boundary surfaces are then related by:

$$c\big|_{\gamma_+^s} = c\big|_{\gamma_-^s} + c^s \tag{3.9}$$

In order to ensure that a unique solution exists for the microscopic concentration field, the slave corner node concentration c^0 is adjusted so that the volume average of the concentration is equal to a prescribed value. Recalling that the diffusivity is assumed to be independent of the concentration, an average value of zero was adopted for convenience.

Finally, the directional macroscopic diffusivity is obtained from the homogenised flux for a unit macroscopic concentration gradient in that direction:

$$D_s = \frac{j_s^{\mathrm{M}}}{(\nabla c)_s^{\mathrm{M}}} = \int_\omega j_s \, d\omega \tag{3.10}$$

It is worth mentioning that the concentration gradients and flux components considered in the present formulation are computed only for the resin, since the fibers are not included in the model. The water concentration, gradient and flux for the composite material can be recovered through the relations:

$$c_{\mathrm{comp}} = V_{\mathrm{resin}}\, c_{\mathrm{resin}} \qquad (\nabla c)_{\mathrm{comp}} = V_{\mathrm{resin}}\, (\nabla c)_{\mathrm{resin}} \qquad \mathbf{j}_{\mathrm{comp}} = V_{\mathrm{resin}}\, \mathbf{j}_{\mathrm{resin}} \tag{3.11}$$

where V_{resin} is the resin volume fraction. It follows that the diffusivity value resulting from integrating only over the resin volume is consistent with the one that would be obtained by also taking the fiber volume into account.

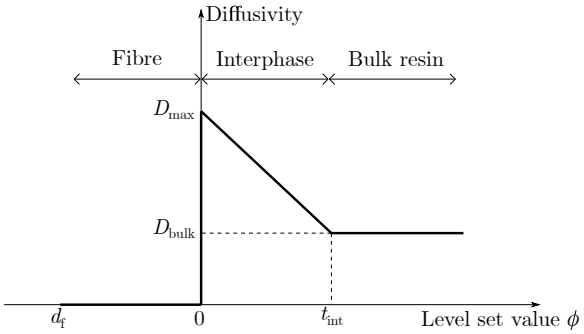

Figure 3.3: Diffusivity values versus distance to nearest fiber.

3.3.2. INTERPHASE MODELING

In the preceding formulation, no assumption was made on the diffusivity behavior of the resin. A simple approach is to consider that the diffusivity of the resin is isotropic, constant at every microscopic point and equal to the one obtained from neat resin immersion experiments. However, literature evidence [3] suggests that diffusion may happen faster in the interphase region close to the fibers [10–13, 18]. An attempt to experimentally detect the interphase region in the present composite system will be described in Section 3.4.2.

Joliff *et al.* [3] modeled the interphase as a region with a higher diffusivity than the one of the surrounding bulk resin. Although the authors in [3] considered a constant interphase diffusivity, their own experimental observations suggest that the degree of material modification changes continuously with the distance to the fiber surface. Here, such effect is modeled by using a level set field ϕ to define the distance of any given point to the nearest fiber surface:

$$\phi(\mathbf{x}^{\mathrm{m}}) = \min_{f=1}^{n_{\mathrm{f}}} \left(\sqrt{x\, x_f^{\mathrm{c}} + y\, y_f^{\mathrm{c}}} - r_f \right) \tag{3.12}$$

where n_{f} is the number of fibers, x^{c} and y^{c} are the coordinates of the fiber centre and r is the radius of the fiber. Since only x and y coordinates are used to compute ϕ, the resultant field is prismatic. The diffusivity at integration point p is then defined as a linear function of ϕ (Figure 3.3):

$$D_p = D_{\mathrm{max}} - \phi_p \frac{D_{\mathrm{max}} - D_{\mathrm{bulk}}}{t_{\mathrm{int}}} \tag{3.13}$$

where D_{max} and D_{bulk} are the diffusivities at the fiber surface and at the bulk resin, respectively, and t_{int} is the thickness of the interphase region. The choice for a linear function allows for a more realistic representation of the interphase than the one shown in [3] while maintaining the same number of parameters. Figure 3.4 shows the resultant diffusivity field for an interphase thickness of 4 μm.

It is important to note that even though diffusivity in pure resin (D_{bulk}) is usually considered isotropic, the same might not hold for the interphase region, for instance due to changes in polymer chain orientation at the immediate vicinity of the fibers [19].

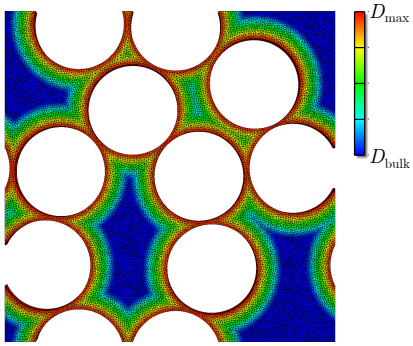

Figure 3.4: Diffusivity field with an interphase thickness of 4 μm.

Therefore, no *a priori* assumption will be made regarding the isotropy of D_{max} in the present study.

3.4. RESULTS

3.4.1. EXPERIMENTAL UPTAKE

In Figure 3.5, experimental water uptake values are plotted for diffusion in each of the x, y and z directions. The represented Fickian diffusion curve for each direction was obtained by fitting the average uptake of 3 specimens using the procedure described in Section 3.2.3. The final uptake level of approximately 0.91% was similar for all directions.

A Fickian behavior was observed for all specimen types, although small deviations are observed for diffusion along the z direction between 20 h and 50 h of immersion. The diffusivities obtained for the x and y directions of approximately 0.52 $\mu m^2/s$ were similar, which was expected due to the similar fiber arrangement inside the samples. For these two directions, saturation was reached after approximately 300 h of conditioning. On the other hand, a diffusivity of 1.638 $\mu m^2/s$ was obtained for diffusion in the z direction, approximately 3 times higher than in the other directions. In this case, saturation was reached after approximately 100 h of immersion.

The observed anisotropy in diffusivity was expected and also observed by other authors [2, 6]. This effect is usually attributed to the fact that the fibers act as barriers to the water movement in the x and y directions, whereas diffusion in the z direction runs along the fibers and is therefore unhindered. For the present epoxy system, the diffusivity in pure resin specimens is 0.741 $\mu m^2/s$ [20]. As expected, diffusivities in the x and y directions are lower than the pure resin one due to the aforementioned barrier effect. For the z direction, however, a value approximately twice as high as for pure resin is obtained. It is clear that the barrier effect caused by the fibers is not enough to fully explain the anisotropic diffusion behavior observed for this material system as it cannot explain such increase in diffusivity in the z direction.

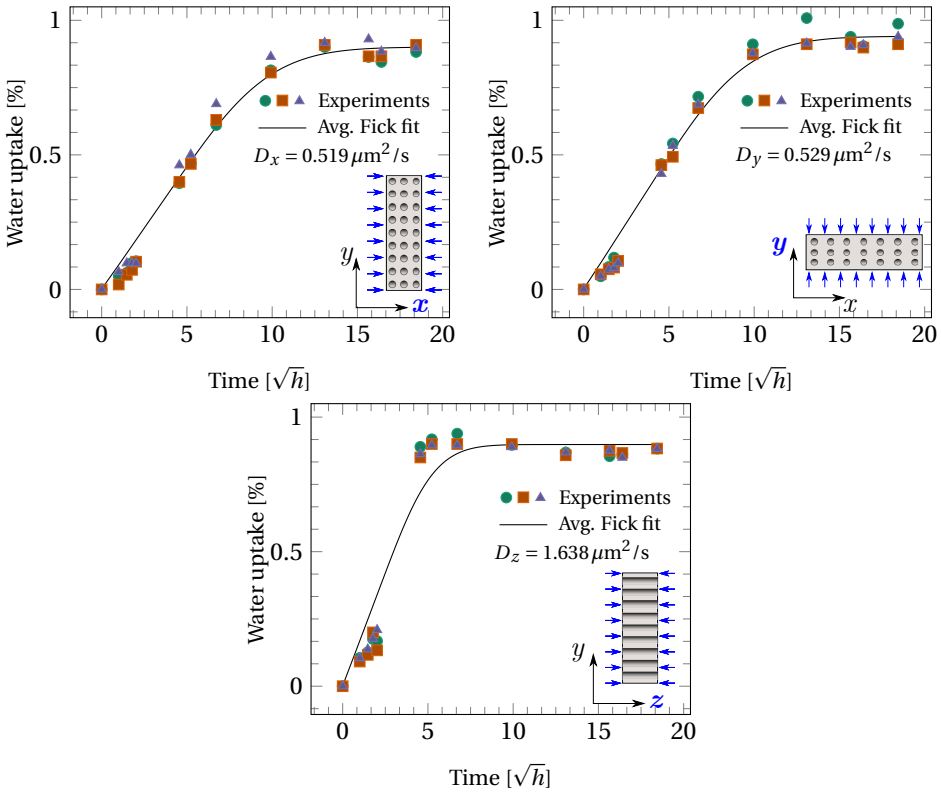

Figure 3.5: Experimental water uptake results with Fick fit.

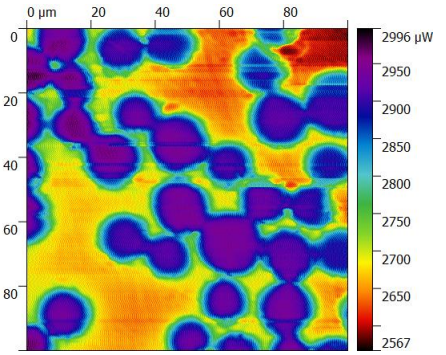

Figure 3.6: Thermal conductivity profile in a 0.01mm^2 area of a z-direction slice.

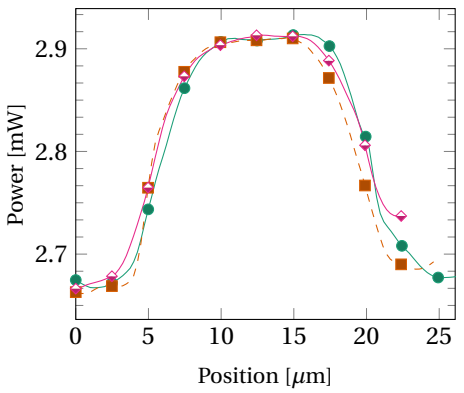

Figure 3.7: Three different line scans of thermal conductivity in the vicinity of a fibre.

3.4.2. INTERPHASE MEASUREMENT

In Figure 3.6, the thermal conductivity map obtained with micro-thermal analysis is shown, clearly displaying the contrasts between fibers and the surrounding epoxy resin. In such conductivity mapping, the fibers are observed as zones with a higher power value, since the bulk thermal conductivity for the glass is about four times higher than the value for epoxy resin. As the probe moves away from a fiber, the thermal conductivity decreases gradually to a lower level corresponding to the resin. To determine the width of the interphase in the thermal map, line scans drawn in several directions across the detected glass fibers show a transition zone which extends over 4-5 μm (Figure 3.7).

To determine the origin of this thermal conductivity gradient, L-TMA measurements were made in positions with different (increasing) distances from the centre of the fiber (Figure 3.8). In the bulk of the material, sufficiently far from the fibers, the glass transition temperature is constant. As the distance to the fiber decreases, the glass transition temperature decreases by 10-15 K in an interphase region of 4-5μm (Figure 3.9) and may be defined as the area where the softening temperature is lower than the softening temperature of the bulk. The distance over which this decreasing T_g stretches is comparable

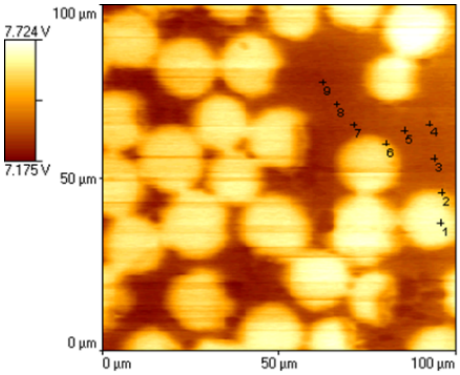

Figure 3.8: Surface map obtained through μTA in a 0.01mm^2 area of a z-direction slice showing L-TMA test locations.

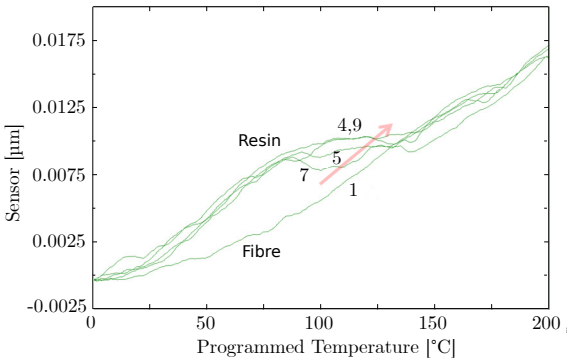

Figure 3.9: L-TMA experiments at increasingly distant locations from a glass fiber.

to the distance over which the gradual evolution in thermal conductivity is observed in the surface mapping (Figure 3.6). The L-TMA curve measured on the fiber shows only thermal expansion. The presence of an interphase may be attributed to incomplete curing or modification of the bulk resin after chemical reactions with the sizing applied to the fibers, also seen for instance by Mallarino *et al.* [13].

In a similar study performed by Joliff *et al.* [3], the authors measured interphase thickness values using both micro-thermal analysis and atomic force microscopy (AFM), with values ranging from 1 μm obtained through AFM force measurements to 4 μm of highly modified resin and 6 μm of slightly modified resin obtained through local T_g measurements. Since significantly different values are obtained for the same material system by using different techniques, the models of the next sections will consider both a thin interphase of 1 μm and a thick interphase of 4 μm.

3.4.3. RVE STUDY

The anisotropic diffusivity behavior of the present material system was obtained through homogenisation of the response of a Representative Volume Element (RVE) according to

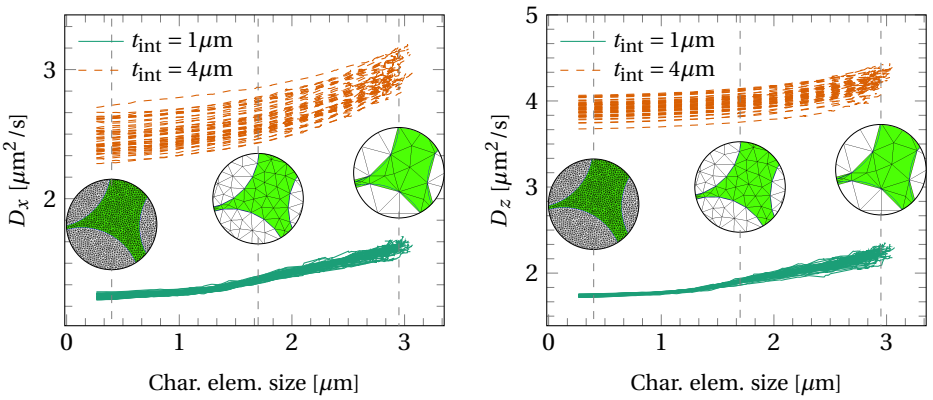

(a) x direction. (b) z direction.

Figure 3.10: Changes in diffusivity of 50 different micromodels with increasing mesh density.

the formulation presented in Section 3.3. This section describes the parametric study performed in order to chose a representative micromodel for comparison with the experimental behavior.

In order to correctly represent the diffusivity behavior of the interphase region, particularly where the distance between fibers is small, an adequate mesh density is required. Figures 3.10a and 3.10b show the obtained diffusivity values in the x and z directions for 50 different 5 x 5 fiber micromodels (90 μm x 90 μm) with varying characteristic element size ranging from 3 μm to 0.3 μm in steps of 0.05 μm. In all cases, the discretisation in the z direction consisted of a single layer of elements, which is sufficient to solve the steady state flow in that direction exactly for the given prismatic geometry. For the parametric study, D_{max} was considered isotropic and a ratio D_{max}/D_{bulk} of 10 was adopted in order to investigate the relative differences between models with thin and thick interphases. Choosing an appropriate ratio is not crucial at this point since only relative differences between the two interphase thicknesses are of interest for the parametric study. Wedge elements with three integration points were used.

As expected, the diffusivities converge to stable values as the mesh density increases. For both directions and interphase thicknesses, such stabilisation happened at an element length of approximately 0.5 μm. For both directions, the final diffusivities for the thick interphase models showed significantly higher scatter than the thin interphase ones. It is possible that this behavior is induced by the larger area of influence of fibers with thick interphases. The interphases of adjacent fibers tend to overlap more often and the resultant interaction between fibers makes the thick interphase model more sensitive to changes in fiber arrangement.

With a fixed element length of 0.5 μm, the next calibration step involved choosing an RVE size large enough to ensure that the resultant homogenised diffusivity does not change considerably if the size is further increased. Figures 3.11a and 3.11b show homogenised diffusivity values in the x and z directions for both thin and thick interphase thicknesses with increasing RVE size, expressed by its number of fibers (from 1 x 1 to 9 x 9

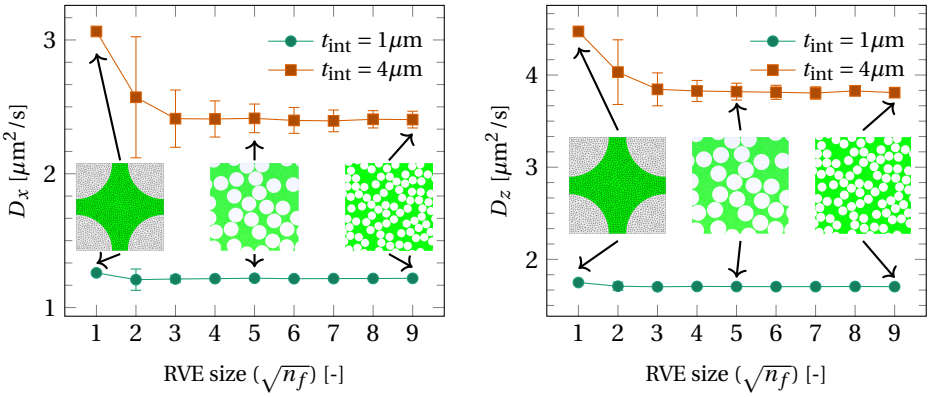

(a) x direction.

(b) z direction.

Figure 3.11: Effect of RVE size on the obtained diffusivities.

fibers). The plotted values represent average values from 50 different micromodels and the bars represent standard deviations.

Consistent with the results obtained for 5 x 5 micromodels, the response of models with a thick interphase had a higher scatter when compared to models with a thin interphase. Nevertheless, the average response of both types of model reached a stable value from a 3 x 3 RVE size. For the final comparison with experimental results, an RVE size of 5 x 5 fibers was chosen as a compromise between precision and computational effort.

3.4.4. VALIDATION OF THE STEADY STATE ASSUMPTION

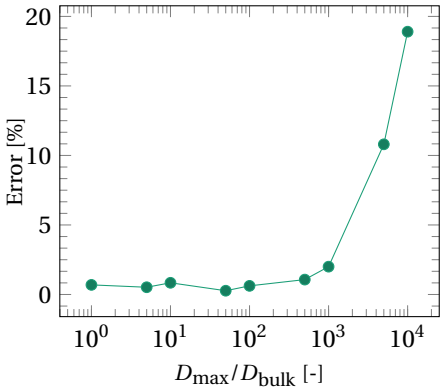

Figure 3.12: Steady-state model error.

For high D_{max}/D_{bulk} ratios, flow in the z direction mostly takes place through the interphases. In the limit case, the interphases are instantly saturated along the whole thickness of the specimen, with subsequent diffusion happening radially from the fibers

into the surrounding resin in the x and y directions. In such case, the assumption of steady-state flow in the z direction is invalid and a full microscale transient analysis becomes necessary to capture the physics of water uptake in slices that are thin in the z direction.

In order to validate the steady state assumption, transient analyses were also performed to simulate the uptake in the z direction. For these simulations, the micromodel was extruded to match the actual thickness of the slice. The same fitting procedure as for the experimental results was used to obtain an effective diffusivity parameter from the transient analysis results.

Figure 3.12 shows the error $(D_{\text{trans}} - D_{\text{steady}})/D_{\text{trans}}$ in the diffusivity obtained with the steady-state micromodel with respect to the one obtained from the transient analysis. For ratios of up to 500 between the interphase and bulk diffusivities, the steady-state assumption led to errors smaller than 1%. Further increasing the ratio causes the error to increase, with up to 20% difference observed for $D_{\max}/D_{\text{bulk}} = 10000$. Since such high ratios are not realistic, the steady-state assumption is valid for obtaining the diffusivity in all three directions.

3.4.5. NUMERICAL RESULTS AND DISCUSSION

The proposed RVE diffusion model was used in an attempt to reproduce the obtained experimental results. A 5 x 5 fiber RVE size was adopted and the results were computed as an average of 50 executions with different RVE geometries since scatter is still present for such size. The characteristic element size was fixed at 0.5 μm in the x-y plane, with a single layer of elements in the z direction. The resultant diffusivities for all models are shown in Table 3.1 and the resultant uptake curves can be seen in Figure 3.13.

	D_{bulk}	$\left(\frac{D_{\max}}{D_{\text{bulk}}}\right)_{x,y}$	$\left(\frac{D_{\max}}{D_{\text{bulk}}}\right)_{z}$	t_{int}	D_x	D_y	D_z
	[μm^2/s]	[-]	[-]	[μm]	[μm^2/s]	[μm^2/s]	[μm^2/s]
Experimental	-	-	-	-	**0.519**	**0.529**	**1.638**
No interphase	0.741	-	-	-	**0.397**	**0.389**	**0.741**
Thick int. [3]	0.741	5.0	5.0	4.0	**1.368**	**1.353**	**2.149**
Thin int. [3]	0.741	5.0	5.0	1.0	**0.832**	**0.826**	**1.187**
Thick int. fit	0.741	1.5	1.5	4.0	**0.538**	**0.529**	**0.928**
Thin int. fit	0.741	2.1	2.1	1.0	**0.537**	**0.529**	**0.863**
Anisotropic fit	0.741	1.5	3.5	4.0	**0.538**	**0.529**	**1.638**

Table 3.1: Comparison between experiments and numerical simulations.

For the first model (*no interphase*), the level set field was not used and the diffusivity of every material point was equal to D_{bulk}. Therefore, only the effect of geometric inhomogeneity was taken into account in this case. As expected, the homogenised diffusivities in the x and y directions were lower than the neat resin one, due to the barrier effect caused by the fibers. In the z direction, since no obstacles are present, the ob-

tained diffusivity is equal to D_{bulk}. Compared with the experimental results, the values provided by the model are approximately 27% lower for D_x and D_y and 55% lower for D_z, suggesting the presence of additional mechanisms that accelerate the diffusion process.

For the next two models (*thick int.*, *thin int.*), the level set field was used to allow for higher diffusivity at the interphase regions and the ratio $D_{\text{max}}/D_{\text{bulk}} = 5$ proposed by Joliff *et al.* [3] was adopted. For these models, isotropic diffusivity was assumed at the interphase. As expected, the inclusion of an interphase yields higher homogenised diffusivity values. For both cases, however, the resultant values for D_x and D_y were higher than the experimental ones. The $D_{\text{max}}/D_{\text{bulk}}$ ratio proposed in [3] is therefore not valid for the present material system.

Since the diffusivity ratio proposed by Joliff *et al.* [3] was not based on a direct measurement, only the values for t_{int} were kept for the next two models (*thick int. fit*, *thin int. fit*) and D_{max} was adjusted in order to fit the experimental value for D_y. For a thick interphase, the obtained ratio between D_{max} and D_{bulk} was 1.5, while a ratio of 2.1 was found for a thin interphase. Even though both models correctly capture the diffusion mechanics in the x-y plane, the diffusivity along the fibers was still approximately 43% lower than the one obtained from the experiments.

The results indicate that the combination of geometric inhomogeneity and linearly increasing diffusivity at the interphase is not enough to explain the experimental value for D_z. We see three different potential explanations for this effect. Firstly, polymer chain orientation close to the fiber/matrix interface is unlikely to be isotropic [19, 21], which could give rise to anisotropic water diffusivity. Secondly, water movement through capillarity in micro cracks would be significantly faster than diffusion in bulk resin [22, 23]. These cracks are caused by fiber/matrix debonding and are therefore oriented parallel to the fibers. It is reasonable to suppose that such cracks would accelerate diffusion the most in the fiber direction. Thirdly, z direction slices are more delicate and therefore more susceptible to manufacturing damage. If the two first explanations are dominant, they can be represented in a homogenised sense by assuming anisotropic diffusion in the interphase, similar to the approach proposed in [23]. To demonstrate this, a fit for all directions can be obtained by relaxing the assumption of isotropic diffusion at the interphase (*anisotropic fit*). Keeping the hypothesis of a thick interphase, a ratio $\left(D_{\text{max}}/D_{\text{bulk}}\right)_z$ of 3.5 was found to give an optimal fit for the uptake in the z direction. It is important to note that since another fit parameter was added, no unique solution exists for this case and a similar fit could be obtained with a thin interphase.

3.5. CONCLUSIONS

In this work, a combined numerical and experimental investigation of the anisotropic water diffusion behavior of unidirectional glass/epoxy composites has been performed. The experimental procedure consisted of manufacturing a thick unidirectional panel from which material slices were cut in each of the orthotropy planes of the material and immersed in water at 50°C. The experimental diffusivities were obtained by fitting an analytical Fick solution to the uptake results. Furthermore, a measure of the interphase thickness in the vicinity of the fibers was performed through micro-thermal analysis. In order to gain further insight in such anisotropic water movement, the diffusion process

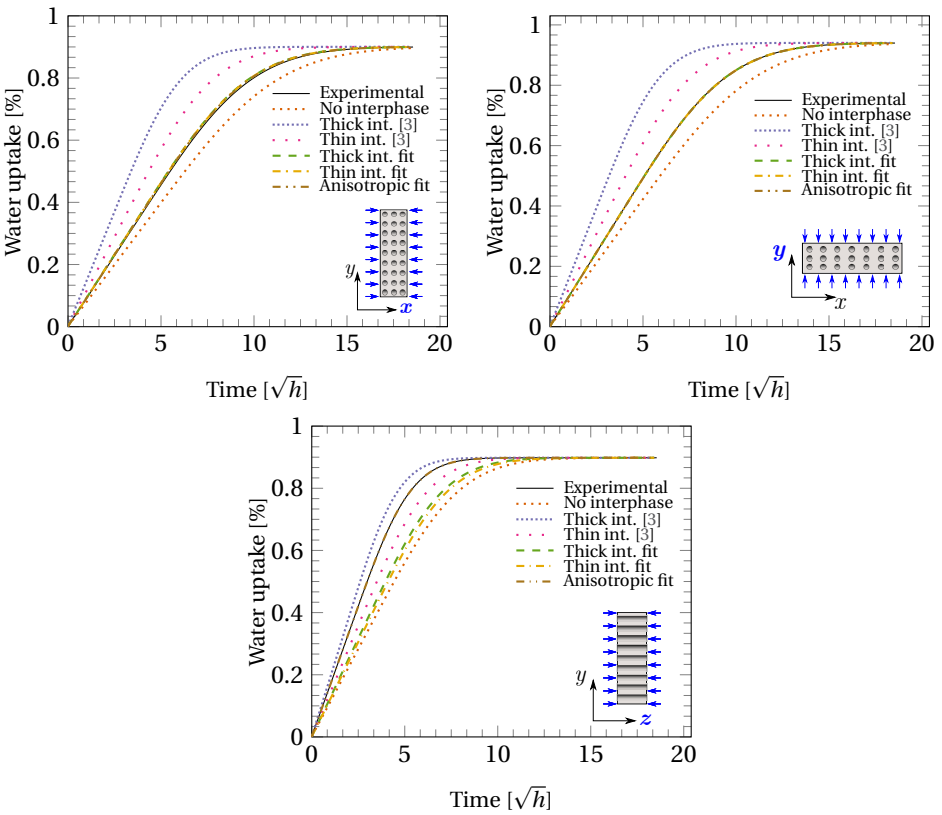

Figure 3.13: Numerical water uptake results.

was modeled in a three-dimensional RVE from which homogenised diffusivity values were obtained. A level set field was used to retrieve the distance of any resin point to the nearest fiber and allow for faster diffusion in the interphase region.

From the experimental results, a similar uptake behavior was observed for diffusion in directions transverse to the fibers due to a comparable fiber arrangement, with saturation being attained after approximately 300 hours of immersion. On the other hand, diffusion in the longitudinal direction was significantly faster and a saturated state was reached after approximately 100 hours. Even though the diffusivities in the transverse directions followed the expected trend of being lower than the neat resin one due to a barrier effect caused by the fibers, the diffusivity along the fibers was found to be twice as high as the neat resin one, a fact that cannot be explained by the barrier effect alone. From thermal analysis, an interphase region of softer resin with a thickness of 4-5 μm was detected, suggesting that diffusion may happen at a faster rate close to the fibers.

For the numerical investigation, a parametric study was performed on the RVE size and finite element mesh density. For comparison with the experimental diffusivities, a characteristic element size of 0.5 μm was chosen and the homogenised diffusivities were obtained as the average result of 50 realisations with different fiber arrangements. Results showed that the geometric effect of fibers acting as barriers for the water movement is indeed responsible for part of the observed anisotropy. However, it was not possible to fit the experimental values by using only the bulk epoxy diffusivity. With the addition of an interphase around the fibers, a fit could be obtained for diffusion in both transverse directions, although the diffusivity ratios proposed in [3] were not valid for the present material system. Nevertheless, the combination of the aforementioned barrier effect and faster isotropic diffusion at the interphase was not sufficient to be able to fit experimental results in all three directions with a single set of parameters. Such a fit could only be found by making the interphase diffusivity orthotropic with a higher value in the direction parallel to the fibers.

REFERENCES

[1] I. B. C. M. Rocha, S. Raijmaekers, F. P. van der Meer, R. P. L. Nijssen, H. R. Fischer, and L. J. Sluys, *Combined experimental/numerical investigation of directional moisture diffusion in glass/epoxy composites,* Composites Science and Technology **151**, 16 (2017).

[2] H. S. Choi, K. J. Ahn, J.-D. Nam, and H. J. Chun, *Hygroscopic aspects of epoxy/carbon fiber composite laminates in aircraft environments,* Composites: Part A **32**, 709 (2001).

[3] Y. Joliff, W. Rekik, L. Belec, and J. F. Chailan, *Study of the moisture/stress effects on glass fibre/epoxy composite and the impact of the interphase area,* Composite Structures **108**, 876 (2014).

[4] *Technical data sheet - EPIKOTE resin MGS RIMR 135 and EPIKURE curing agent MGS RIMH 134-RIMH 137*, Tech. Rep. (Momentive, 2006).

[5] *Technical data sheet - PPG fiber glass: Hybon 2002 roving*, Tech. Rep. (PPG, 2010).

[6] S. A. Grammatikos, B. Zafari, M. C. Evernden, J. T. Mottram, and J. M. Mitchels, *Moisture uptake characteristics of a pultruded fibre reinforced polymer flat sheet subjected to hot/wet aging,* Polymer Degradation and Stability **121**, 407 (2015).

[7] G. M. Odegard and A. Bandyopadhyay, *Physical aging of epoxy polymers and their composites,* Journal of Polymer Science: Part B **49**, 1695 (2011).

[8] T. C. Wong and L. J. Broutman, *Water in epoxy resins part II. diffusion mechanism,* Polymer Engineering and Science **25**, 529 (1985).

[9] B. Dewimille and A. R. Bunsell, *Accelerated ageing of a glass fibre-reinforced epoxy resin in water,* Composites , 35 (1983).

[10] R. Häßler and E. Mühlen, *An introduction to µta(tm) and its application to the study of interfaces,* **361**, 113 (2000).

[11] G. Van Assche and B. Van Mele, *Interphase formation in model composites studied by micro-thermal analysis,* Polymer **43**, 4605 (2002).

[12] M. S. Tillman, B. S. Hayes, and J. C. Seferis, *Examination of interphase thermal property variance in glass fiber composites,* **392-393**, 299 (2002).

[13] S. Mallarino, J. F. Chailan, and J. L. Vernet, *Interphase investigation in glass fibre composites by micro-thermal analysis,* Composites: Part A **36**, 1300 (2005).

[14] H. R. Fischer, *Calibration of micro-thermal analysis for the detection of glass transition temperatures and melting points - repeatability and reproducibility,* Journal of Thermal Analysis and Calorimetry **92**, 625 (2008).

[15] F. P. van der Meer, *Micromechanical validation of a mesomodel for plasticity in composites,* European Journal of Mechanics - A/Solids **60**, 58 (2016).

[16] I. Özdemir, W. A. M. Brekelmans, and M. G. D. Geers, *Computational homogenization for heat conduction in heterogeneous solids,* International Journal for Numerical Methods in Engineering **73**, 185 (2008).

[17] K. Terada and M. Kurumatani, *Two-scale diffusion-deformation coupling model for material deterioration involving micro-crack propagation,* International Journal for Numerical Methods in Engineering **83**, 426 (2010).

[18] J. Kim, M. Sham, and J. Wu, *Nanoscale characterisation of interphase in silane treated glass fibre composites,* Composites: Part A **38**, 607 (2001).

[19] L. S. Faraji, *Nanoscale carbon fiber-matrix interphase characterization with atomic force microscopy indentation* (PhD thesis, Oklahoma State University, 2014).

[20] I. B. C. M. Rocha, S. Raijmaekers, R. P. L. Nijssen, F. P. van der Meer, and L. J. Sluys, *Hygrothermal ageing behaviour of a glass/epoxy composite used in wind turbine blades,* Composite Structures **174**, 110 (2017).

[21] M. Malagù, A. Lyulin, E. Benvenuti, and A. Simone, *A molecular-dynamics study of size and chirality effects on glass-transition temperature and ordering in carbon nanotube-polymer composites,* Macromol Theory Simul **25**, 571 (2016).

[22] P. Davies, F. Pomies, and L. A. Carlsson, *Influence of water and accelerated aging on the shear fracture properties of glass/epoxy composite,* Applied Composite Materials **3**, 71 (1996).

[23] Y. J. Weitsman, *Anomalous fluid sorption in polymeric composites and its relation to fluid-induced damage,* Composites: Part A **37**, 617 (2006).

4

A MULTISCALE/MULTIPHYSICS FRAMEWORK FOR HYGROTHERMAL AGING

One's ideas must be as broad as nature
if they are to interpret nature.

Arthur Conan Doyle, *A Study in Scarlet*

4.1. INTRODUCTION

In this chapter, knowledge on aging mechanisms (Chapter 2) and moisture diffusion (Chapter 3) will be used as the basis of a multiphysics and multiscale numerical framework for modeling hygrothermal aging in composites. A diffusion model at the macroscale is coupled with a computational (FE^2) homogenization scheme in order to model swelling and material degradation at both the micro- and macroscales. At the microscale, failure is modeled in a representative volume element (RVE) of the material by using an elasto-plastic epoxy model with damage [2] combined with cohesive interfaces around every fiber [3]. A model for concentration-dependent mechanical properties with a single degradation factor is proposed. At every time step, the spatial scales are coupled by passing the local strain and water concentration to micromodels embedded at every material point, from which stress and tangent stiffness are in turn obtained. The model formulations and the calibration of the epoxy model using experimental results are shown in detail. A study on the required RVE size is performed and the framework is demonstrated by modeling aging in a unidirectional short-beam shear test specimen immersed in water.

Apart from minor changes to its introductory section, this chapter was integrally extracted from [1].

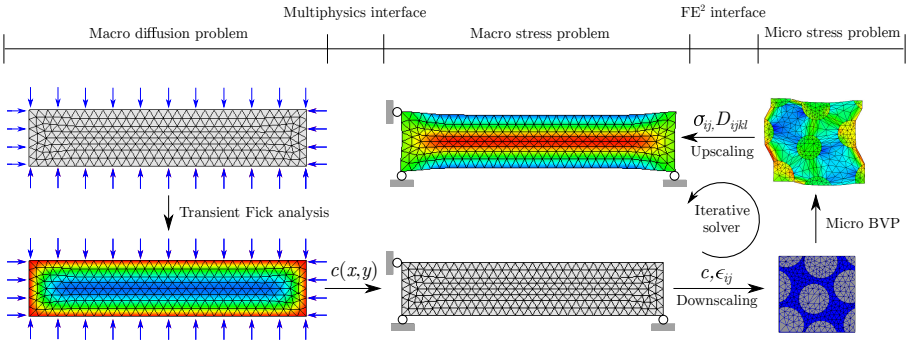

Figure 4.1: Schematic representation of the multiphysics/multiscale model for hygrothermal aging

4.2. MODEL FORMULATION

4.2.1. MATHEMATICAL NOTATION

In this work, both index notation and matrix notation will be used to represent tensors and vectors. When index notation is used, the indices i, j, k, l range from one to the number of spatial dimensions of the problem being solved. In products between two entities in index notation, summation over repeated indices is implied. In matrix notation, vectors are represented by boldfaced lower-case symbols while matrices are given by boldfaced upper-case symbols. When representing stresses and strains in matrix notation, the use of Voigt notation is implied.

As the formulations presented here span multiple spatial scales, the superscripts M and m will be used to represent macroscopic and microscopic entities, respectively. For the sake of generality, all formulations will be presented considering three-dimensional macro- and micromodels.

4.2.2. MACROSCALE PROBLEM

In order to simulate the aging process at the macroscopic scale, a coupled multiphysics problem is solved involving water diffusion and mechanical stresses (Figure 4.1). At a given point in time, the water concentration field c^{M} is given by Fick's second law of diffusion:

$$\dot{c}^{\mathrm{M}} + \frac{\partial j_i^{\mathrm{M}}}{\partial x_i^{\mathrm{M}}} = 0 \tag{4.1}$$

where j_i^{M} are the water flux components, given by:

$$j_i^{\mathrm{M}} = -D_{ij}^{\mathrm{M}} \frac{\partial c}{\partial x_j^{\mathrm{M}}} \tag{4.2}$$

and D_{ij}^{M} is a diffusivity tensor. The water movement is therefore modeled as a smooth molecular motion driven by concentration gradients.

It is worth mentioning that the water uptake model of Eq. (4.1) is suitable for resin systems featuring one-phase Fickian diffusion behavior, which is the case for the epoxy

system used to calibrate the present formulations [4] and systems studied by multiple other authors [5–8]. For systems that display a two-phase behavior, the model must be expanded into a diffusion-reaction scheme, which entails the inclusion of a reaction term into Eq. (4.1). Details of such procedure can be found in [9].

An increase in water concentration will cause the macroscopic specimen to swell. If the specimen is constrained or if the concentration field is not constant at every point in space, swelling stresses will be generated. Stress equilibrium is enforced by:

$$\frac{\partial \sigma^{\mathrm{M}}_{ji}}{\partial x^{\mathrm{M}}_{j}} + b_i = 0 \tag{4.3}$$

where b_i are body forces. In stress analysis, it is also necessary to define the relationship between the strain and displacement fields. Here, the small strain tensor is used:

$$\varepsilon^{\mathrm{M}}_{ij} = \frac{1}{2}\Big(\frac{\partial u^{\mathrm{M}}_{i}}{\partial x^{\mathrm{M}}_{j}} + \frac{\partial u^{\mathrm{M}}_{j}}{\partial x^{\mathrm{M}}_{i}}\Big) \tag{4.4}$$

For the rest of this section, matrix notation will be adopted and the superscript M will be dropped to keep the notation compact. In order to solve the multiphysics problem with the Finite Element Method (FEM), the macroscopic volume Ω is discretised in elements and both concentration and displacement fields are interpolated using the nodal values $\overline{\mathbf{c}}$ and $\overline{\mathbf{u}}$:

$$c = \mathbf{N}_c \overline{\mathbf{c}} \qquad \mathbf{u} = \mathbf{N}_u \overline{\mathbf{u}} \tag{4.5}$$

where $\mathbf{N}_c$ and $\mathbf{N}_u$ are shape functions for concentration and displacements, respectively.

Substituting the discretized fields of Eq. (4.5) into Eqs. (4.1) and (4.3) and solving them in their weak form, the global moisture and stress equilibrium equations are obtained:

$$\mathbf{K}_c \overline{\mathbf{c}} + \mathbf{C}\dot{\overline{\mathbf{c}}} = \mathbf{f}_{\mathrm{j}} \qquad \mathbf{K}_u \overline{\mathbf{u}} = \mathbf{f}_{\mathrm{ext}} \tag{4.6}$$

with $\dot{\overline{\mathbf{c}}}$ being the nodal values of the time derivative of the concentration, $\mathbf{K}_c$, $\mathbf{C}$ and $\mathbf{f}_j$ are the diffusion matrix, the water capacity matrix and the external flux vector, respectively, given by:

$$\mathbf{K}_c = \int_\Omega \mathbf{B}_c^{\mathrm{T}} \mathbf{D}_c \mathbf{B}_c \, d\Omega \qquad \mathbf{C} = \int_\Omega \mathbf{N}_c^{\mathrm{T}} \mathbf{N}_c \, d\Omega \qquad \mathbf{f}_j = \int_{\Gamma_j} \mathbf{N}_c^{\mathrm{T}} \mathbf{j}_\Gamma \, d\Gamma \tag{4.7}$$

and $\mathbf{K}_u$ and $\mathbf{f}_{\mathrm{ext}}$ are the stiffness matrix and the external force vector, respectively:

$$\mathbf{K}_u = \int_\Omega \mathbf{B}_u^{\mathrm{T}} \mathbf{D}_u \mathbf{B}_u \, d\Omega \qquad \mathbf{f}_{\mathrm{ext}} = \int_\Omega \mathbf{N}_u^{\mathrm{T}} \mathbf{b} \, d\Omega + \int_{\Gamma_\sigma} \mathbf{N}_u^{\mathrm{T}} \boldsymbol{\sigma}_\Gamma \, d\Gamma \tag{4.8}$$

where Γ denotes surfaces with prescribed water flux or stresses and integrals in the macroscopic domain Ω imply element-wise integration followed by an assembly procedure.

In Eqs. (4.7) and (4.8), $\mathbf{B}$ contains spatial derivatives of the shape functions and $\mathbf{D}_c$ is the diffusivity tensor of Eq. (4.2). In this work, the diffusivity is considered independent of the water concentration and is thus constant throughout the analysis. Finally, $\mathbf{D}_u$ is

the tangent material stiffness matrix. In contrast with the diffusivity behavior, a constitutive model for strains is not assumed *a priori* but is instead substituted by embedded micromodels at every integration point. Each micromodel receives the strain from the macromodel and returns the associated stress tensor and tangent stiffness. The down- and upscaling procedures involved in this process are shown in Section 4.2.4.

As can be seen in Figure 4.1, a one-way coupling exists between the diffusion and stress models. The diffusion analysis is not affected by the stress state of the material and the interaction between the two problems shown in Eq. (4.6) does not need to be solved iteratively. Instead, the diffusion model is solved first and the resultant concentration field is passed to the stress model. This type of staggered operator-split strategy was also adopted by other authors [10, 11].

4.2.3. MICROSCALE PROBLEM

The micromodel considered in this work consists in a Representative Volume Element (RVE) of unidirectional fibers surrounded by resin, with interface elements around every fiber, allowing for the modeling of fiber-matrix interface debonding. The difference in length scales between macro- and micromodels is considered large enough for the principle of separation of scales [12] to be applied. Thus, the macroscopic strains and water concentration are considered uniform over the microscopic domain and only the stress equilibrium problem is considered:

$$\frac{\partial \sigma^{\mathrm{m}}_{ji}}{\partial x^{\mathrm{m}}_{j}} = 0 \qquad \varepsilon^{\mathrm{m}}_{ij} = \frac{1}{2}\Big(\frac{\partial u^{\mathrm{m}}_{i}}{\partial x^{\mathrm{m}}_{j}} + \frac{\partial u^{\mathrm{m}}_{j}}{\partial x^{\mathrm{m}}_{i}}\Big) \tag{4.9}$$

where the body forces b_i are neglected. The reasoning behind considering that the water concentration is constant over the entire micro domain is presented in Section 4.2.4. Solving the problem using FEM involves solving a system of equations similar to the second expression of Eq. (4.6) but now the integrations are performed over the microscopic volume ω. Additionally, since the micromodel includes interface elements around every fiber, the displacement jumps along them are also interpolated and their contribution to the global stiffness matrix is obtained via:

$$[\![\mathbf{u}]\!] = \mathbf{N}_{[\![\mathrm{u}]\!]}\overline{\mathbf{u}} \qquad \Rightarrow \qquad \mathbf{K}_{[\![\mathrm{u}]\!]} = \int_{\gamma_{\mathrm{i}}} \mathbf{N}^{\mathrm{T}}_{[\![\mathrm{u}]\!]}\mathbf{T}\mathbf{N}_{[\![\mathrm{u}]\!]}\, d\gamma_{\mathrm{i}} \tag{4.10}$$

where $\mathbf{N}_{[\![\mathrm{u}]\!]}$ is the shape function matrix for displacement jumps, γ_{i} are the interface surfaces and $\mathbf{T}$ is the tangent constitutive matrix for the interface elements.

At the microscale, the constitutive model of each material component is assumed *a priori* and is used to compute the stresses $\boldsymbol{\sigma} = \boldsymbol{\sigma}(\boldsymbol{\varepsilon})$, the tractions $\mathbf{t} = \mathbf{t}([\![\mathbf{u}]\!])$ and provide the tangent constitutive matrices:

$$\mathbf{D}_u = \frac{\partial \boldsymbol{\sigma}}{\partial \boldsymbol{\varepsilon}} \qquad \mathbf{T} = \frac{\partial \mathbf{t}}{\partial [\![\mathbf{u}]\!]} \tag{4.11}$$

Since water affects each material component (fiber, matrix, interface) differently, suitable constitutive models have to be chosen in order to capture the essential degradation and failure processes that can occur during aging. The fibers are modeled as linear-elastic and their failure is not considered. In the subsequent sections, the models for the epoxy and fiber-matrix interface behaviors are presented in detail.

EPOXY MODEL

The epoxy resin is modeled as elasto-plastic with damage, using the model formulated by Melro *et al.* [2] and incorporating improvements proposed by Van der Meer [13]. The model is composed of a linear-elastic portion followed by plastic hardening and transitioning to damage with exponential softening after the fracture strength is reached.

The model starts as elasto-plastic, with a stress-strain relationship given by:

$$\sigma_{ij} = D^{\mathrm{e}}_{ijkl}\left(\varepsilon_{kl} - \varepsilon^{\mathrm{p}}_{kl}\right) \tag{4.12}$$

where only the elastic part of the strains is considered and the elastic stiffness D_{ijkl} can be written as:

$$D_{ijkl} = G(\delta_{ij}\delta_{kl} + \delta_{il}\delta_{jk}) + \left(K - \frac{2}{3}G\right)\delta_{ij}\delta_{kl} \tag{4.13}$$

with K being the bulk modulus for the resin and G its shear modulus. Plastic strains develop when the yield surface is reached. A paraboloidal surface is considered:

$$\phi^{\mathrm{p}}(\boldsymbol{\sigma}, \sigma_{\mathrm{c}}, \sigma_{\mathrm{t}}) = 6J_2 + 2I_1(\sigma_{\mathrm{c}} - \sigma_{\mathrm{t}}) - 2\sigma_{\mathrm{c}}\sigma_{\mathrm{t}} \leq 0 \tag{4.14}$$

where σ_{c} and σ_{t} are the compression and tension yield stresses, respectively, J_2 is the second invariant of the deviatoric stress tensor and I_1 is the first stress invariant. This yield surface consists of the classic von Mises surface augmented with the pressure-dependent term $2I_1(\sigma_{\mathrm{c}} - \sigma_{\mathrm{t}})$.

The evolution of the yield surface due to hardening is dictated by the evolution of σ_{c} and σ_{t} with the equivalent plastic strain $\varepsilon^{\mathrm{p}}_{\mathrm{eq}}$. At each time step, the variation of the equivalent plastic strain is given by:

$$\Delta\varepsilon^{\mathrm{p}}_{\mathrm{eq}} = \sqrt{k\Delta\varepsilon^{\mathrm{p}}_{ij}\Delta\varepsilon^{\mathrm{p}}_{ij}} \;\Rightarrow\; \sigma_{\mathrm{c}} = \sigma_{\mathrm{c}}(\varepsilon^{\mathrm{p}}_{\mathrm{eq}}),\ \sigma_{\mathrm{t}} = \sigma_{\mathrm{t}}(\varepsilon^{\mathrm{p}}_{\mathrm{eq}}) \tag{4.15}$$

and the variation of the plastic strains is computed through a non-associative flow rule given by:

$$\Delta\varepsilon^{\mathrm{p}}_{ij} = \Delta\gamma\left(3S_{ij} + \frac{2}{9}\alpha I_1\delta_{ij}\right) \tag{4.16}$$

where S_{ij} is the deviatoric stress tensor and α depends on the plastic Poisson ratio ν_{p}:

$$\alpha = \frac{9}{2}\frac{1 - 2\nu_{\mathrm{p}}}{1 + \nu_{\mathrm{p}}} \tag{4.17}$$

In order to determine the plastic multiplier increment $\Delta\gamma$, an iterative elastic predictor/return mapping algorithm is used until the computed stress state stops violating the yield surface (*i.e.* until $\phi^{\mathrm{p}} = 0$). Details on the return mapping algorithm and on computing the consistent tangent matrix are left out of the present discussion for the sake of compactness and can be found in [13].

When the material fracture strength is reached, the model switches to a continuum damage formulation with secant unloading. After such point, the stress-strain relationship is given by:

$$\varepsilon^{\mathrm{e}}_{ij} = \varepsilon_{ij} - \varepsilon^{\mathrm{p}}_{ij} = \frac{1 + \nu}{E(1 - d_{\mathrm{m}})}\sigma_{ij} - \frac{\nu d_{\mathrm{m}}}{E(1 - d_{\mathrm{m}})}\sigma_{ij}\delta_{ij} - \frac{\nu}{E}\sigma_{kk}\delta_{ij} \tag{4.18}$$

where the plastic strain is still subtracted from the total strain but stops evolving after damage starts developing. A single damage variable d_{m} is adopted and its evolution is dictated by the fracture surface defined as:

$$\phi^{\mathrm{d}}(\widetilde{\boldsymbol{\sigma}}, r) = 6\widetilde{J}_2 + 2\widetilde{I}_1(X_{\mathrm{c}} - X_{\mathrm{t}}) - 2rX_{\mathrm{c}}X_{\mathrm{t}} \leq 0 \tag{4.19}$$

which is similar to Eq. (4.14) but with yield stresses substituted by the fracture strengths (X_{c}, X_{t}) and the invariants are now computed with the effective stresses, calculated using the undamaged stiffness tensor of Eq. (4.13).

In order to ensure that the stress state does not violate the fracture surface, the internal variable r at time step t_n is:

$$r^{t_n} = \max\left\{1, \max_{0\leq t\leq t_n}\left\{\frac{3\widetilde{J}_2^t}{X_{\mathrm{c}}X_{\mathrm{t}}} + \frac{\widetilde{I}_1^t(X_{\mathrm{c}} - X_{\mathrm{t}})}{X_{\mathrm{c}}X_{\mathrm{t}}}\right\}\right\} \tag{4.20}$$

and is related to the damage parameter d_{m} by:

$$d_{\mathrm{m}} = 1 - \frac{e^{A\left(3-\sqrt{7+2r^2}\right)}}{\sqrt{7+2r^2}-2} \tag{4.21}$$

where the parameter A is computed through the classic Crack Band model by regularising the dissipated energy with respect to the fracture toughness G_c and the characteristic length of the finite element l_{e}:

$$f(A) = \int_1^{\infty} \frac{\partial U}{\partial d_{\mathrm{m}}}\frac{\partial d_{\mathrm{m}}}{\partial r}dr = \frac{G_c}{l_{\mathrm{e}}} \tag{4.22}$$

with l_{e} computed as:

$$l_{\mathrm{e}}^{\mathrm{2D}} = \frac{6}{\pi\sqrt[4]{3}}\sqrt{\gamma_{\mathrm{e}}} \qquad l_{\mathrm{e}}^{\mathrm{3D}} = \sqrt[3]{\omega_{\mathrm{e}}} \tag{4.23}$$

and γ_{e} and ω_{e} are the element area and volume, respectively. The consistent tangent matrix is obtained through linearisation of the secant stress-strain expression of Eq. (4.18). Further details on the linearisation process can be found in [2].

COHESIVE INTERFACE MODEL

The occurrence of fiber-matrix interface debonding is simulated by incorporating a cohesive zone damage model to interface elements generated around every fiber of the RVE. The chosen model is a mixed-mode damage law developed by Turon *et al.* [3], with later improvements proposed by Van der Meer and Sluys [14]. In the local frame of the interface element, the traction-separation law can be written as:

$$\mathbf{t} = [\mathbf{I} - d_{\mathrm{i}}\mathbf{P}]K_{\mathrm{d}}[\![\mathbf{u}]\!] \tag{4.24}$$

where K_{d} is an initial stiffness, d_{i} is the damage variable associated with the model and the matrix $\mathbf{P}$ prevents the development of cohesive tractions in compression by applying the operator $\langle x\rangle = (x + |x|)/2$:

$$\mathbf{P} = \begin{bmatrix} \frac{\langle [\![u]\!]_n \rangle}{[\![u]\!]_n} & 0 & 0 \\ 0 & 1 & 0 \\ 0 & 0 & 1 \end{bmatrix} \tag{4.25}$$

where $[\![u]\!]_n$ is the displacement jump in the direction normal to the interface surfaces.

The damage variable d_i is given by:

$$d_\mathrm{i}^{t_n} = \max_{0\le t\le t_n} \begin{cases} 0, & [\![u]\!]_\mathrm{eq} \le [\![u]\!]_\mathrm{eq}^0 \\ \frac{[\![u]\!]_\mathrm{eq}^\mathrm{f}([\![u]\!]_\mathrm{eq}-[\![u]\!]_\mathrm{eq}^0)}{[\![u]\!]_\mathrm{eq}([\![u]\!]_\mathrm{eq}^\mathrm{f}-[\![u]\!]_\mathrm{eq}^0)}, & [\![u]\!]_\mathrm{eq}^0 < [\![u]\!]_\mathrm{eq} < [\![u]\!]_\mathrm{eq}^\mathrm{f} \\ 1, & [\![u]\!]_\mathrm{eq} \ge [\![u]\!]_\mathrm{eq}^\mathrm{f} \end{cases} \tag{4.26}$$

where the equivalent displacement jump ($[\![u]\!]_\mathrm{eq}$), the displacement jump at the onset of damage ($[\![u]\!]_\mathrm{eq}^0$) and the jump after damage has completely developed ($[\![u]\!]_\mathrm{eq}^\mathrm{f}$) are given by:

$$[\![u]\!]_\mathrm{eq} = \sqrt{\langle [\![u]\!]_n\rangle^2 + [\![u]\!]_\mathrm{sh}^2} \qquad [\![u]\!]_\mathrm{sh}^2 = [\![u]\!]_s^2 + [\![u]\!]_t^2 \tag{4.27}$$

$$[\![u]\!]_\mathrm{eq}^0 = \sqrt{([\![u]\!]_n^0)^2 + \chi^\eta \left[([\![u]\!]_s^0)^2 - ([\![u]\!]_n^0)^2\right]} \tag{4.28}$$

$$[\![u]\!]_\mathrm{eq}^\mathrm{f} = \frac{[\![u]\!]_n^0[\![u]\!]_n^\mathrm{f} + \chi^\eta \left[[\![u]\!]_s^0[\![u]\!]_s^\mathrm{f} - [\![u]\!]_n^0[\![u]\!]_n^\mathrm{f}\right]}{[\![u]\!]_\mathrm{eq}^0} \tag{4.29}$$

where η is the Benzeggagh-Kenane mode interaction parameter [15] and χ is the ratio between the shear energy dissipation and the total dissipation:

$$\chi = \frac{[\![u]\!]_\mathrm{sh}^2}{[\![u]\!]_\mathrm{sh}^2 + \langle [\![u]\!]_n\rangle^2} \tag{4.30}$$

Finally, the single-mode displacement jumps at damage onset depend on the fracture strength of the interface while the final interface openings depend on its fracture toughness:

$$[\![u]\!]_n^0 = \frac{X_n}{K_\mathrm{d}} \qquad [\![u]\!]_s^0 = \frac{X_s}{K_\mathrm{d}} \qquad [\![u]\!]_n^\mathrm{f} = \frac{2G_{Ic}}{X_n} \qquad [\![u]\!]_s^\mathrm{f} = \frac{2G_{IIc}}{X_s} \tag{4.31}$$

The formulation is completed with the definition of the material tangent stiffness matrix $\mathbf{T}$ of Eq. (4.11) through consistent linearisation of the traction-separation law of Eq. (4.24). Details of the linearisation procedure can be found in [14].

LOADS AND BOUNDARY CONDITIONS

In the present model, periodic boundary conditions are adopted in the micromodel in order to represent the behavior of a macroscopic bulk material point. Figure 4.2 shows a schematic representation of the node groups involved in enforcing the boundary conditions. The origin of the RVE coordinate system is fixed at node 0 and its displacement is fixed:

$$\mathbf{u}_0 = \mathbf{0} \tag{4.32}$$

The corner nodes with displacements given by $\mathbf{u}_j^c$, where j ranges from 1 to the number of spatial dimensions of the RVE, will be prescribed based on the macroscopic strain values at the point according to the scale transitions discussed in Section 4.2.4. Finally, the displacements of nodes on opposing boundary surfaces are related by:

$$\mathbf{u}^{\gamma_j^+} = \mathbf{u}^{\gamma_j^-} + \mathbf{u}_j^c \tag{4.33}$$

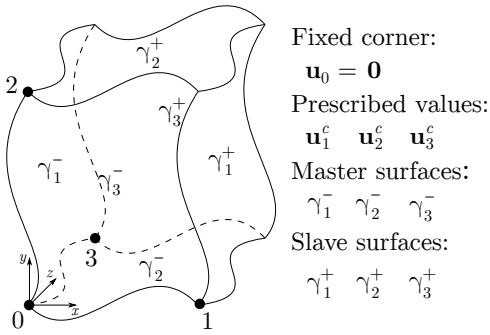

Figure 4.2: Periodic RVE with controlling nodes and boundary surfaces.

where the constraints are handled using the master-slave method, which means that the degrees of freedom of the slave nodes will be condensed out of the microscopic global stiffness matrix.

Resin elements are allowed to swell based on the current water concentration of the micromodel. The swelling is applied as a strain contribution at each material point:

$$\varepsilon_{ij}^{\text{total}} = \varepsilon_{ij} - c\alpha_{\text{sw}}\delta_{ij} \tag{4.34}$$

where α_{sw} is the swelling coefficient of the resin. Since the fibers do not take water and are therefore not allowed to swell, differential swelling stresses will be generated. If the RVE is free to swell, the volume average of such stresses will be zero. However, the presence of prescribed macroscopic strains on the RVE implies that the micromodel cannot swell freely, and the resultant modified stress field may bring changes to its failure behavior.

CONCENTRATION-DEPENDENT PROPERTIES

Experimental evidence shows a significant drop in mechanical properties of the resin and interface after water uptake [16, 17]. In order to realistically predict the effects of the aging process, such degradation caused by plasticization and interfacial bond weakening must be incorporated in the micromodel. Here, resin and interface properties are linearly dependent on the water concentration of the micromodel using a single degradation factor:

$$d_{\text{w}} = \frac{d_{\text{w}}^{\infty}}{c_{\infty}} c \tag{4.35}$$

where c_{∞} and d_{w}^{∞} are respectively the water concentration and associated material degradation at saturation, obtained experimentally.

With the definition of the degradation factor, the resin properties are modified as:

$$E^{\text{w}} = (1-d_{\text{w}})E, \quad \sigma_{\text{c}}^{\text{w}} = (1-d_{\text{w}})\sigma_{\text{c}}, \quad \sigma_{\text{t}}^{\text{w}} = (1-d_{\text{w}})\sigma_{\text{t}} \tag{4.36}$$

$$X_{\text{c}}^{\text{w}} = (1-d_{\text{w}})X_{\text{c}}, \quad X_{\text{t}}^{\text{w}} = (1-d_{\text{w}})X_{\text{t}}, \quad G_c^{\text{w}} = (1-d_{\text{w}})^2 G_c \tag{4.37}$$

and the interface properties as:

$$X_n^{\text{w}} = (1-d_{\text{w}})X_n, \quad X_s^{\text{w}} = (1-d_{\text{w}})X_s, \quad G_{Ic}^{\text{w}} = (1-d_{\text{w}})^2 G_{Ic}, \quad G_{IIc}^{\text{w}} = (1-d_{\text{w}})^2 G_{IIc} \tag{4.38}$$

It is important to note that applying the degradation factor to the yield stresses σ_c and σ_t implies a degradation of the hardening curve for every value of equivalent plastic strain. For fracture toughness, the squared degradation factor was adopted for the sake of numerical stability and implies reductions in both the strength and the strain (or displacement jump) level at which the softening is completely developed.

4.2.4. SCALE TRANSITIONS

With the formulations of the models in both macro- and microscales, it is necessary to define the interaction between scales. Following the scheme presented in Figure 4.1, such interactions comprise a macro-to-micro downscaling procedure, where strain and water concentration are passed to the micromodels, and a micro-to-macro upscaling procedure, with the recovery of the macroscopic stress and tangent stiffness.

Starting with the downscaling procedure, the displacement field of the micromodel can be decomposed in a linear displacement field related to the macroscopic strain and a fluctuation field $\tilde{u}$ caused by microscopic inhomogeneities:

$$u_i^{\mathrm{m}} = \varepsilon_{ij}^{\mathrm{M}} x_j^{\mathrm{m}} + \tilde{u}_i^{\mathrm{m}} \tag{4.39}$$

It is important to note that such linear dependency on the macroscopic strain is only allowed because the principle of separation of scales mentioned in Section 4.2.3 is considered valid. For water concentration, since it is directly linked to strains through swelling (Equation 4.34), bringing concentration gradients to the microscale would make it necessary to also bring strain gradients. This approach is not followed here and the concentration is therefore considered constant over the entire microscopic domain, a hypothesis also adopted by Terada and Kurumatani [11]:

$$c^{\mathrm{m}} = c^{\mathrm{M}}(\mathbf{x}^{\mathrm{M}}) \tag{4.40}$$

When making the transition to the microscale, the volume average of the microscopic strain must be equal to the macroscopic strain at a particular material point:

$$\varepsilon_{ij}^{\mathrm{M}}(\mathbf{x}^{\mathrm{M}}) = \frac{1}{|\omega|}\int_{\omega} \varepsilon_{ij}^{\mathrm{m}}(\mathbf{x}^{\mathrm{m}})\, d\omega = \frac{1}{|\omega|}\int_{\gamma} (u_i^{\mathrm{m}} n_j + u_j^{\mathrm{m}} n_i)\, d\gamma \tag{4.41}$$

where the volume integral was substituted by one in the RVE surface γ using the Gauss theorem and $\mathbf{n}$ is the vector normal to γ. Substituting Eq. (4.39), we obtain:

$$\frac{1}{|\omega|}\int_{\gamma} (\tilde{u}_i^{\mathrm{m}} n_j + \tilde{u}_j^{\mathrm{m}} n_i)\, d\gamma = 0 \quad \Rightarrow \quad \varepsilon_{ij}^{\mathrm{M}} = \frac{1}{|\omega|}\int_{\omega} \varepsilon_{ij}^{\mathrm{m}}\, d\omega \tag{4.42}$$

which dictates that the strain averaging is only satisfied if the fluctuation displacement field cancels at the RVE boundary.

After solving the microscopic boundary value problem, the macroscopic stress tensor must be recovered from the micro solution. For this part of the upscaling procedure, the Hill-Mandel principle is applied:

$$\sigma_{ij}^{\mathrm{M}} \dot{\varepsilon}_{ij}^{\mathrm{M}} = \frac{1}{|\omega|}\int_{\omega} \sigma_{ij}^{\mathrm{m}} \dot{\varepsilon}_{ij}^{\mathrm{m}}\, d\omega = \frac{1}{|\omega|}\int_{\gamma} t_i^{\mathrm{m}} \dot{u}_i^{\mathrm{m}}\, d\gamma \tag{4.43}$$

The principle postulates that the macroscopic stress power must be equal to the volume average of the microscopic one. The volume integral can be substituted by a boundary integral of the product between the traction and the variation of the displacement field. Substituting Eq. (4.39), we obtain a result similar to the one in Eq. (4.42):

$$\frac{1}{|\omega|}\int_{\gamma} t_i^{\mathrm{m}}\dot{\tilde{u}}_i^{\mathrm{m}}d\gamma = 0 \quad \Rightarrow \quad \sigma_{ij}^{\mathrm{M}} = \frac{1}{|\omega|}\int_{\omega}\sigma_{ij}^{\mathrm{m}}d\omega \tag{4.44}$$

which means that the microscopic fluctuation field must have zero resultant work at the boundaries.

Considering the periodic boundary conditions shown in the previous section and imposing the additional requirement that the geometry of the RVE must be symmetric, it can be shown that:

$$\tilde{u}_i^{\mathrm{m}+} = \tilde{u}_i^{\mathrm{m}-} \qquad n_i^{+} = -n_i^{-} \qquad t_i^{\mathrm{m}+} = -t_i^{\mathrm{m}-} \tag{4.45}$$

from which the following equalities arise:

$$\int_{\gamma^-}(\tilde{u}_i^{\mathrm{m}-}n_j^{-} + \tilde{u}_j^{\mathrm{m}-}n_i^{-})d\gamma = -\int_{\gamma^+}(\tilde{u}_i^{\mathrm{m}+}n_j^{+} + \tilde{u}_j^{\mathrm{m}+}n_i^{+})d\gamma \tag{4.46}$$

$$\int_{\gamma^-}\dot{\tilde{u}}_i^{\mathrm{m}-}t_i^{\mathrm{m}-}d\gamma = -\int_{\gamma^+}\dot{\tilde{u}}_i^{\mathrm{m}+}t_i^{\mathrm{m}+}d\gamma \tag{4.47}$$

Substituting Eqs. (4.46) and (4.47) into Eqs. (4.42) and (4.41), it can be seen that both requirements for the fluctuation field are satisfied.

Finally, the scale transitions can be formulated in Voigt notation for ease of implementation. For a given macroscopic strain tensor $\boldsymbol{\varepsilon}^{\mathrm{M}}$, the displacements $\mathbf{u}_j^c$ of the controlling nodes shown in Figure 4.2 are computed as:

$$\mathbf{u}_j^c = \mathbf{H}_j^{\mathrm{T}}\boldsymbol{\varepsilon}^{\mathrm{M}}, \qquad \mathbf{H}_j = \frac{1}{2}\begin{bmatrix} 2x & 0 & 0 \\ 0 & 2y & 0 \\ 0 & 0 & 2z \\ y & x & 0 \\ 0 & z & y \\ z & 0 & x \end{bmatrix}_j, \boldsymbol{\varepsilon}^{\mathrm{M}} = \begin{bmatrix} \varepsilon_{xx}^{\mathrm{M}} \\ \varepsilon_{yy}^{\mathrm{M}} \\ \varepsilon_{zz}^{\mathrm{M}} \\ 2\varepsilon_{xy}^{\mathrm{M}} \\ 2\varepsilon_{yz}^{\mathrm{M}} \\ 2\varepsilon_{xz}^{\mathrm{M}} \end{bmatrix} \tag{4.48}$$

where the matrix $\mathbf{H}$ is filled with the coordinates of each controlling node. After solving the microscopic equilibrium equations and obtaining the internal forces at the controlling nodes, the macroscopic stresses are recovered:

$$\boldsymbol{\sigma}^{\mathrm{M}} = \frac{1}{|\omega|}\begin{bmatrix}\mathbf{H}_1 & \mathbf{H}_2 & \mathbf{H}_3\end{bmatrix}\begin{bmatrix}\mathbf{f}_1^{\mathrm{m}} \\ \mathbf{f}_2^{\mathrm{m}} \\ \mathbf{f}_3^{\mathrm{m}}\end{bmatrix} = \frac{1}{|\omega|}\mathbf{H}\mathbf{f}_{\mathrm{c}}^{\mathrm{m}} \tag{4.49}$$

The final step in the upscaling procedure is to compute the tangent macroscopic stiffness matrix $\delta\boldsymbol{\sigma}^{\mathrm{M}} = \mathbf{D}_u^{\mathrm{M}}\delta\boldsymbol{\varepsilon}^{\mathrm{M}}$ from Eq. (4.8). Here, the procedure follows the formulation presented by Nguyen *et al.* [18] but is rewritten for the case of homogenization

towards a bulk macroscopic point. The procedure starts by partitioning the global stiffness matrix of the micromodel as follows:

$$\begin{bmatrix} \mathbf{K}^{\mathrm{m}}_{\mathrm{ii}} & \mathbf{K}^{\mathrm{m}}_{\mathrm{id}} \\ \mathbf{K}^{\mathrm{m}}_{\mathrm{di}} & \mathbf{K}^{\mathrm{m}}_{\mathrm{dd}} \end{bmatrix} \begin{bmatrix} \delta\mathbf{u}^{\mathrm{m}}_{\mathrm{i}} \\ \delta\mathbf{u}^{\mathrm{m}}_{\mathrm{d}} \end{bmatrix} = \begin{bmatrix} \mathbf{r}^{\mathrm{m}}_{\mathrm{i}} \\ \mathbf{r}^{\mathrm{m}}_{\mathrm{d}} \end{bmatrix} \tag{4.50}$$

with d representing the dependent nodes from the slave surfaces (Figure 4.2) and i the remaining ones, including the controlling corner nodes. Representing the constraints by a coefficient matrix $\mathbf{C}$, the displacement vector is given by:

$$\begin{bmatrix} \delta\mathbf{u}^{\mathrm{m}}_{\mathrm{i}} \\ \delta\mathbf{u}^{\mathrm{m}}_{\mathrm{d}} \end{bmatrix} = \begin{bmatrix} \mathbf{I} \\ \mathbf{C} \end{bmatrix} \delta\mathbf{u}^{\mathrm{m}}_{\mathrm{i}} = \mathbf{T}\delta\mathbf{u}^{\mathrm{m}}_{\mathrm{i}} \tag{4.51}$$

Pre-multiplying both sides of Eq. (4.50) by $\mathbf{T}^{\mathrm{T}}$ and substituting the displacement vector by the one in Eq. (4.51), the dependent displacements are condensed out and a reduced system is obtained:

$$\begin{bmatrix} \overline{\mathbf{K}}^{\mathrm{m}} & \mathbf{0} \\ \mathbf{0} & \mathbf{I} \end{bmatrix} \begin{bmatrix} \delta\mathbf{u}^{\mathrm{m}}_{\mathrm{i}} \\ \delta\mathbf{u}^{\mathrm{m}}_{\mathrm{d}} \end{bmatrix} = \begin{bmatrix} \overline{\mathbf{r}}^{\mathrm{m}} \\ \delta\mathbf{u}^{\mathrm{m}}_{\mathrm{d}} \end{bmatrix}, \qquad \overline{\mathbf{K}}^{\mathrm{m}} = \mathbf{T}^{\mathrm{T}}\mathbf{K}^{\mathrm{m}}\mathbf{T}, \qquad \overline{\mathbf{r}}^{\mathrm{m}} = \mathbf{T}^{\mathrm{T}}\mathbf{r}^{\mathrm{m}} \tag{4.52}$$

The system is further partitioned by separating the controlling nodes (c) from the rest (a):

$$\begin{bmatrix} \overline{\mathbf{K}}^{\mathrm{m}}_{\mathrm{aa}} & \overline{\mathbf{K}}^{\mathrm{m}}_{\mathrm{ac}} \\ \overline{\mathbf{K}}^{\mathrm{m}}_{\mathrm{ca}} & \overline{\mathbf{K}}^{\mathrm{m}}_{\mathrm{cc}} \end{bmatrix} \begin{bmatrix} \delta\mathbf{u}^{\mathrm{m}}_{\mathrm{a}} \\ \delta\mathbf{u}^{\mathrm{m}}_{\mathrm{c}} \end{bmatrix} = \begin{bmatrix} \mathbf{0} \\ \delta\mathbf{f}^{\mathrm{m}}_{\mathrm{c}} \end{bmatrix} \tag{4.53}$$

where the variation of the external force on the controlling nodes used in the stress upscaling of Eq. (4.49) now appears in the right-hand side. From this reduced system, the macroscopic tangent stiffness matrix can be evaluated in a columnwise manner by using a probing technique:

$$\mathbf{D}^{\mathrm{M}}_{u} = \left[\mathbf{D}^{\mathrm{M}}_{1} \quad \mathbf{D}^{\mathrm{M}}_{2} \cdots \mathbf{D}^{\mathrm{M}}_{n}\right], \qquad \mathbf{D}^{\mathrm{M}}_{j} = \frac{1}{|\omega|}\mathbf{H}(\boldsymbol{\xi} - \boldsymbol{\lambda}) \tag{4.54}$$

where each column $j = 1, \ldots, n$ gives the stiffness contribution of one of the n strain components. The matrix $\mathbf{H}$ is given in Eq. (4.48) and the vectors $\boldsymbol{\xi}$ and $\boldsymbol{\lambda}$ are given by a sequence of matrix-vector multiplications:

$$\boldsymbol{\xi} = \overline{\mathbf{K}}^{\mathrm{m}}_{\mathrm{cc}}\boldsymbol{\beta}, \qquad \boldsymbol{\beta} = \mathbf{H}\mathbf{e}_{j}, \qquad \boldsymbol{\lambda} = \overline{\mathbf{K}}^{\mathrm{m}}_{\mathrm{ca}}\boldsymbol{\kappa}, \tag{4.55}$$

with $\mathbf{e}_j$ being the j-th row of an identity matrix of size n and $\boldsymbol{\lambda}$ is obtained by solving the linear system:

$$\begin{bmatrix} \overline{\mathbf{K}}^{\mathrm{m}}_{\mathrm{aa}} & \overline{\mathbf{K}}^{\mathrm{m}}_{\mathrm{ac}} \\ \overline{\mathbf{K}}^{\mathrm{m}}_{\mathrm{ca}} & \overline{\mathbf{K}}^{\mathrm{m}}_{\mathrm{cc}} \end{bmatrix} \begin{bmatrix} \boldsymbol{\kappa} \\ \mathbf{0} \end{bmatrix} = \begin{bmatrix} \overline{\mathbf{K}}^{\mathrm{m}}_{\mathrm{ac}}\boldsymbol{\beta} \\ \mathbf{0} \end{bmatrix} \tag{4.56}$$

which completes the definition of the macroscopic tangent stiffness without the need to invert the microscopic global stiffness matrix.

4.2.5. SOLUTION METHODS

Using the multiphysics/multiscale numerical framework presented in the previous sections requires robust and efficient solution methods. For the diffusion analysis, a time stepping procedure is necessary, while a non-linear path-following method has to be used in the FE^2 stress analysis.

To solve the transient diffusion problem, the linear 3-step method developed by Park [19] is used. The water concentration field at time t is computed as [20]:

$$\mathbf{c}_t = h_\beta \dot{\mathbf{c}}_t + \mathbf{h}_t \tag{4.57}$$

where h_β is the scaled time step and $\mathbf{h}$ is a history vector that depends on the concentration fields of the three previous steps.

For the stress analysis, a Newton-Raphson solver is applied. During the aging process, the non-linear equilibrium problem is solved for each time step and a path-following algorithm is not needed. For every macroscopic iteration, the microscopic equilibrium problem has to be solved at every material point. Since the points are independent from one another, they are solved in parallel in a shared-memory environment. For material points close to the surfaces exposed to water, saturation happens in one time step, which can make convergence difficult. In order to mitigate this issue, the substepping algorithm proposed by Sommer *et al.* [21] is applied. Here, the method is modified by splitting not only the macroscopic strains but also the water concentration in two consecutive substeps. If no convergence is obtained for any of the substeps, the process is repeated recursively.

At the end of the aging process, it is interesting to assess the strength degradation caused by water immersion by loading each material point to failure and obtaining their failure envelopes. For this type of analysis, the dissipation-based arclength method developed by Gutiérrez is used [22]. The method constrains the dissipated energy during one time step by imposing the constraint:

$$\frac{1}{2}\left(\lambda_0 \Delta\overline{\mathbf{u}}^{\mathrm{T}}\mathbf{q} - \Delta\lambda\overline{\mathbf{u}}_0^{\mathrm{T}}\mathbf{q} + \Delta\overline{\mathbf{u}}^{\mathrm{T}}\mathbf{f}_0^*\right) = \Delta U \tag{4.58}$$

where λ is the load factor, $\mathbf{q}$ is the unit load vector and the subscript 0 indicates values from the last converged time step. The term $\Delta\overline{\mathbf{u}}^{\mathrm{T}}\mathbf{f}_0^*$ was proposed by Van der Meer *et al.* [23] and accounts for the presence of permanent plastic deformations and swelling strains. The dissipated energy ΔU is adjusted during the analysis by an efficient adaptive stepping algorithm [24].

Since a continuum damage model regularised using the Crack Band method is used for the epoxy at the microscale, additional convergence problems arise as the Newton-Raphson solver struggles to identify which band of elements is damaging and gets trapped in an oscillatory response. To restore convergence in such cases, the modified Newton-Raphson scheme proposed by Van der Meer [24] is used, in which the oscillating points are identified and their secant stiffness is used instead of the consistent tangent one. After the residual decreases for a certain number of consecutive steps, the algorithm switches back to using the consistent tangent.

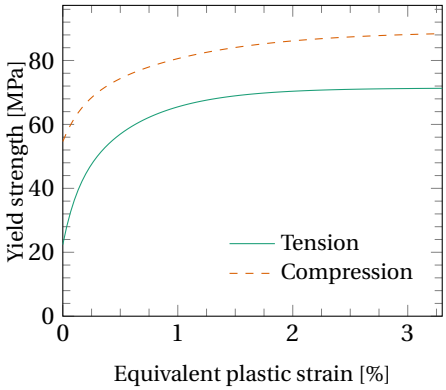

Figure 4.3: Input hardening data for the epoxy model.

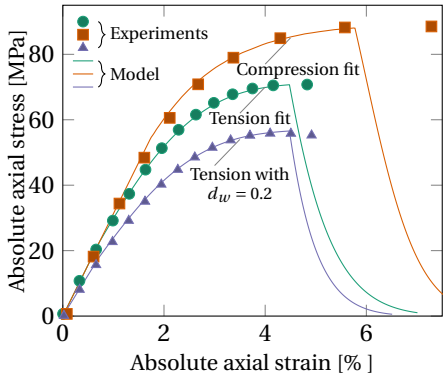

Figure 4.4: Experimental validation of the epoxy model.

4.3. RESULTS

The presented numerical framework is used to model the hygrothermal aging behavior of unidirectional composite laminates. In the examples presented in this section, a glass/epoxy material system used in wind turbine design (EPIKOTE RIMR135/1366 resin and PPG Hybon 2002 glass fiber rovings) is considered. The material properties for each of the constituents (fiber, matrix and interface) are shown in Table 5.1.

For the resin, most properties were obtained experimentally on neat resin specimens tested in tension and compression. The resultant stress-strain curves were also used to extract the plastic hardening curves, shown in Figure 4.3. Properties for the glass fiber and fiber/matrix interface were obtained from literature. The maximum uptake c_∞ and diffusivity (D) for the unidirectional composite material were obtained through an immersion experiment in water at 50°C, with weight measurements performed periodically [25]. Finally, the maximum property degradation at saturation (d_w^∞) was obtained from mechanical tests on saturated tension specimens.

The proposed model for concentration dependency of Section 4.2.3 was validated

using experimental results on saturated epoxy. Figure 4.4 shows results of 1-element models, where the purple and red curves were obtained using the hardening curves extracted from compression and tension tests on dry resin specimens, respectively. For these two cases, a good agreement between experiments and models is expected since the original curves were used to calibrate the model. The blue curve was obtained by degrading the dry model using $d_w = 0.2$. The good agreement with the experimental curve of a saturated specimen shows that using a single degradation factor for stiffness, yield stress and strength is effective for describing the degradation in the material response, although no conclusion can be drawn about the adopted fracture toughness degradation due to the sudden failure behavior of the specimens.

4.3.1. RVE STUDY

In applying the proposed formulation, it is important to choose a suitable RVE size. In order to be representative, the RVE should be large enough to ensure that the micromodel response does not change considerably if the size is further increased. In this work, two-dimensional micromodels with random fiber distributions are used. Simplification of the presented three-dimensional formulations of Section 5.2 for a 2D analysis is trivial and will not be presented.

The models were generated using the discrete element package HADES, starting with a regular grid of circles representing the fibers, bounded by a periodic box. A pseudo-random velocity vector is assigned to each circle and a contact model is executed, letting the circles get rearranged as they collide, while the bounding box shrinks over time. The process is stopped when the desired fiber volume fraction is reached. The resultant geometry is then meshed with triangular finite elements using Gmsh [26]. Based on loss-on-ignition measurements and microscopic observations on the adopted material system, the fiber diameter was randomly generated between $13\,\mu m$ and $16\,\mu m$ and a target volume fraction of 0.6 was adopted. Interface elements are generated at runtime around every fiber.

Figure 4.5a shows homogenised stiffness values for micromodels with a number of fibers ranging from 4 (2 x 2) to 49 (7 x 7), including a unit cell with one fiber and surrounding matrix. Values for both dry and saturated micromodels are shown and each point shows the average and standard deviation obtained using 30 different micromodels (with the exception of unit cell values).

As the size of the RVE is increased, average stiffness values for both dry and wet models tend to decrease. The standard deviation also decreases, although significant scatter is still observed even for the largest RVE size considered, which is partly due to fluctuations in the obtained fiber volume fraction after the discrete element contact analysis.

It is interesting to note that the difference between wet and dry stiffness values increases as the RVE grows in size, with a 17% reduction obtained for the unit cell model and a 23% one for 7 x 7 models, on average. The difference in the rate of stiffness reduction with RVE size is caused by failure events driven by the combination of swelling and degradation of the resin and interface properties. These failure events are not fully captured in smaller micromodels, making the convergence to a stable stiffness value slower when compared to dry micromodels.

The micromodels were also loaded in transverse tension (σ_{22}), with changes in strength

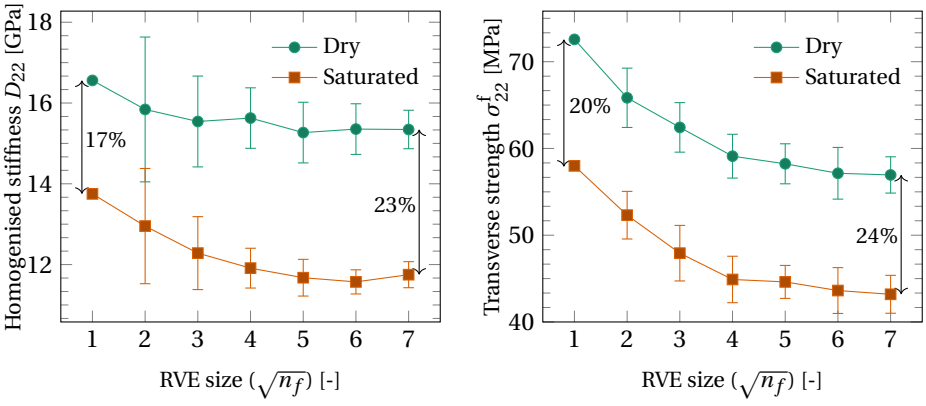

(a) Stiffness.

(b) Strength

Figure 4.5: Changes in computed transverse tension stiffness and strength with RVE size.

as the RVE size increases shown in Figure 4.5b. A behavior similar to the one obtained for stiffness is observed, with a decrease in strength as the RVE size increases, although the convergence rate is now similar for both dry and wet micromodels. In general, a representive initial stiffness can be achieved with a relatively small RVE size, while correctly representing its failure behavior both in terms of distributed and localised damage requires larger RVE sizes. Nevertheless, since significant scatter is still present for both stiffness and strength even for the largest RVE size considered in the present study, it cannot be claimed that a truly representative micromodel was found.

It is also interesting to investigate changes in failure behavior after aging for stress states other than uniaxial transverse tension. Figure 4.6 shows biaxial failure envelopes in both dry and wet conditions of a 7 x 7 RVE. Each point in the envelope was obtained by applying a horizontal load of $\lambda \cos\theta$ to controlling node 1 and a vertical load of $\lambda \sin\theta$ to controlling node 2 (see Figure 4.2), with θ ranging from 0° to 345° in steps of 15°. The load scale factor λ is resolved in every time step using the arc length method. For each direction, the strength was identified as the point that maximises $\sqrt{\sigma_{22}^2 + \sigma_{33}^2}$.

Comparing the obtained envelopes, it is interesting to note the differences in the wet material behavior in tension and compression. For tension, a strength reduction of approximately 27% was obtained after aging. In compression, however, the strength reduction falls to 15% due to the effect of differential swelling. This effect is particularly relevant for the case of biaxial compression ($\theta = 225°$), for which the wet strength is actually higher than the dry one, in spite of the weakening effect caused by plasticization and interface weakening. The resultant change in envelope shape after aging can therefore be interpreted as the combination of shrinkage caused by water degradation and a shift caused by differential swelling.

It can therefore be concluded that in order to realistically model the hygrothermal aging phenomenon in composites, it is important to take into account the contributions of both differential swelling and physical/chemical degradation. In isolation, neither

Epoxy		Interface		Fibre		Diffusion	
E [MPa] [a]	3130	K_d [MPa] [b]	$5 \cdot 10^7$	E [MPa] [27]	73000	c_∞ [%] [a]	3.4
ν [-] [a]	0.37	X_n [MPa] [28]	60.0	ν [-] [27]	0.22	D [$\mu m^2/s$] [a]	0.500
ν_p [-] [a]	0.32	X_s [MPa] [28]	60.0				
X_t [MPa] [a]	70.7	G_{Ic} [N/mm] [28]	0.87				
X_c [MPa] [a]	88.5	G_{IIc} [N/mm] [28]	1.72				
G_c [N/mm] [2]	0.09	η [-] [b]	1.0				
α_{sw} [$\%^{-1}$] [a]	0.002	d_w^∞ [-] [b]	0.2				
d_w^∞ [-] [a]	0.2						

[a] Values experimentally obtained by the authors.
[b] Assumed values.

Table 4.1: Material Properties used in the examples.

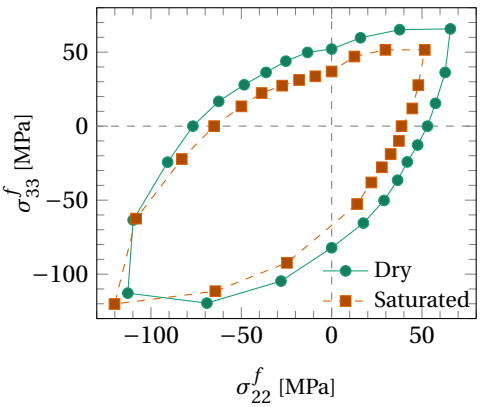

Figure 4.6: Biaxial failure envelopes for a 7 x 7 RVE, both dry and saturated.

mechanism is enough to represent the complex changes in failure behavior after aging.

4.3.2. AGING EXAMPLE

The numerical framework presented in this work is demonstrated by simulating the hygrothermal aging process in a unidirectional glass/epoxy composite specimen immersed in water at 50°C. The specimen dimensions and fiber direction are shown in Figure 4.7a, consisting in a short-beam typically used to evaluate the interlaminar shear strength of unidirectional composites in a three-point bending setup. Here, the virtual specimen is not mechanically loaded, and only the material degradation caused by the hygrothermal conditioning is simulated.

Figure 4.7b shows an idealised model of the aging problem, where only the transverse plane of the specimen is modeled in plane strain and symmetry along the x and y axes is exploited in order to reduce the computational effort. With this modeling ap-

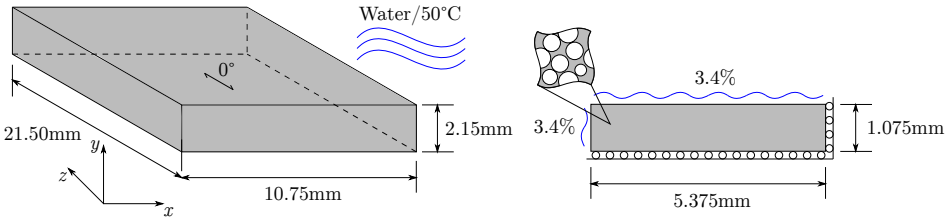

(a) Immersion problem (b) Modelling approach

Figure 4.7: Modeling hygrothermal aging in a unidirectional composite short-beam.

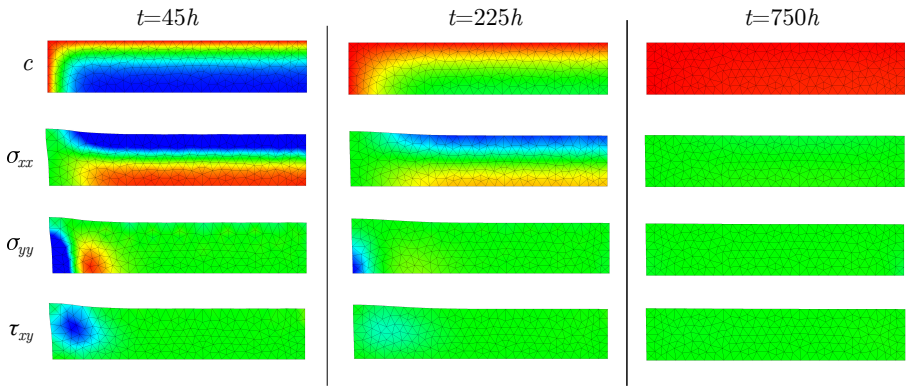

Figure 4.8: Evolution of macroscopic displacements and stresses during aging.

proach, it is assumed that diffusion and swelling do not occur along the z-axis. The latter assumption is reasonable since the specimen is significantly stiffer in the fiber direction, while the former leads to an underestimation of the water concentration field at any given time step, which is an acceptable drawback in exchange for computational efficiency. The specimen is initially dry and the immersion environment is simulated by prescribing the water concentration of pure resin at saturation to the top and left edges, while the bottom and right edges are mechanically constrained. A 5 x 5 RVE with strength response close to the average shown in Figure 4.5b was chosen to represent the material microscopic response.

The transient FE^2 problem is solved from $t = 0$ h to $t = 750$ h, when saturation occurs, with a time step $h = 15$ h. Figure 4.8 shows concentration and stress fields of the macromodel at three different time steps. The full field solution can be recovered from the symmetric model through mirroring along the x and y axes.

As expected, water concentration gradients along the specimen create transient tension, compression and shear stresses. These stresses attain peak values of 5 MPa in shear, 9 MPa in tension and 17 MPa in compression. The stress fields are consistent with the ones experimentally observed by Pitarresi *et al.* [8]. As diffusion progresses and the concentration gradients decrease, start to subside, vanishing upon saturation, as expected.

The effect of transient swelling in the microscopic material state can be visualised by

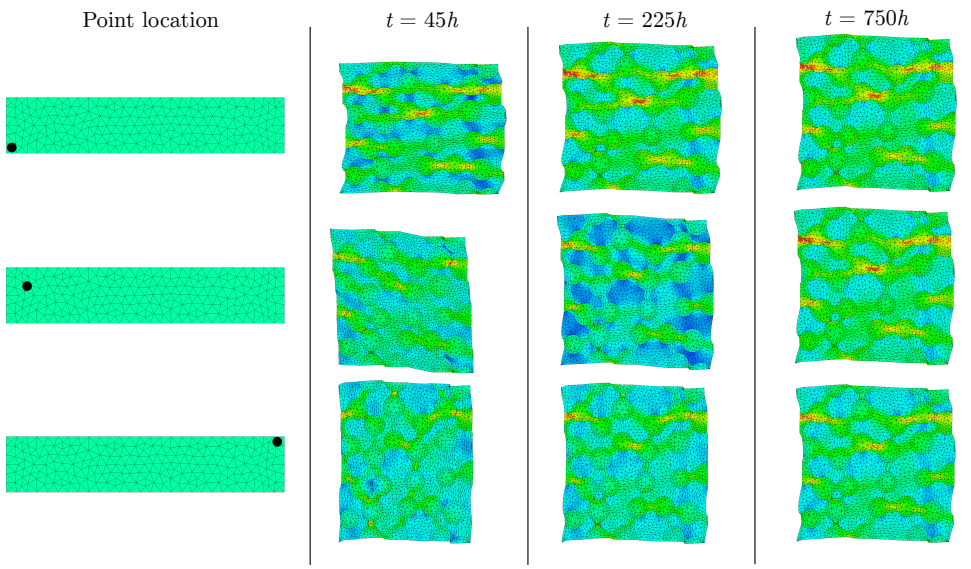

Figure 4.9: Evolution of microscopic displacements and transverse stresses for three different integration points.

tracking microscopic deformations throughout the aging process. Figure 4.9 shows displacements and transverse stress fields (σ_{22}) of three distinct material points at three different time steps. Since the points are located close to the specimen surface, near-instant saturation is expected. However, the micromodels are constrained by the macroscopic compatibility requirement: Points 1 and 3 are constrained by neighboring dry points and can therefore only swell in one direction, while point 2 undergoes a combination of shear and swelling. At longer immersion times (750 h), the macroscopic stresses vanish and the points attain a similar deformed shape. However, because of the distinct strain history, equally saturated points can have different residual stress fields due to differences in local material state, as shown in Figure 4.10.

Besides tracking the material state during the aging process in terms of stiffness degradation and distributed failure phenomena, it is also interesting to assess the strength degradation caused by exposure to water by mechanically loading the macroscopic specimen to failure. However, such analysis involves a number of incompatibilities with the presented numerical framework. Firstly, as the micromodel starts to exhibit global softening due to strain localisation, it can be proven that an RVE ceases to exist and the material response becomes more brittle as the micromodel size is increased [29]. Secondly, the periodic boundary conditions applied to the micromodels may impose additional constraints in the formation of a strain localisation band, depending on the direction of the external loading.

In this work, a simplified approach is taken in order to circumvent such incompatibilities. After the aging analysis is completed (*i.e.* after the macromodel saturates), the displacement fields and material history of the micromodels are saved and used as the starting point of new analyses where mechanical loads are applied to the controlling

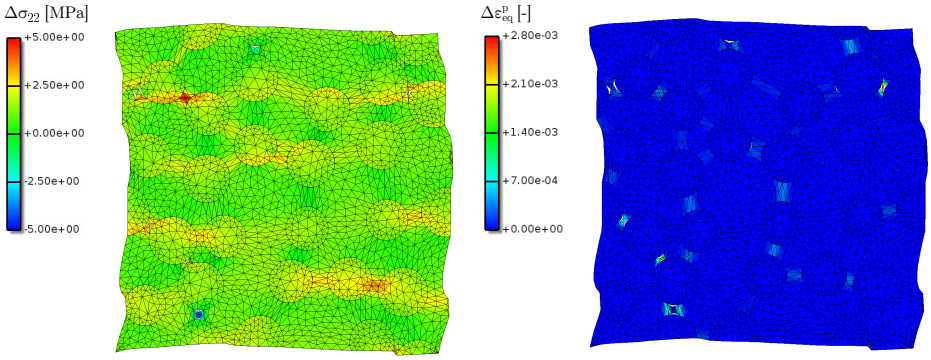

Figure 4.10: Difference fields obtained by superimposing the stress and plastic strain fields of two different saturated points.

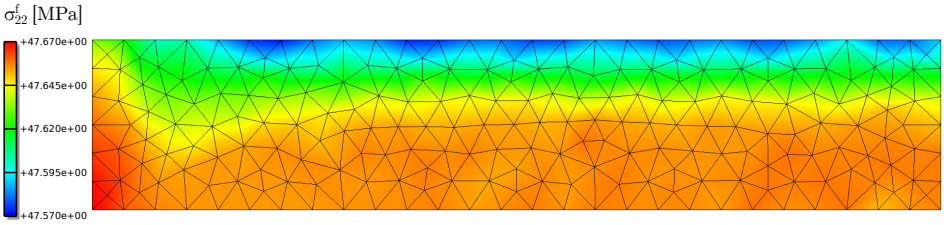

Figure 4.11: Spatial distribution of transverse tension strength in the macro specimen after aging.

nodes and the models are loaded until failure. Since an arc length method is used instead of resorting to displacement control, biaxial stress states can be simulated while keeping stress ratios constant. Stress values are then computed by averaging the nodal forces along the edges of the RVE. Since only the maximum stress is of interest, incompatibilities of the strain localisation band direction with the applied periodic boundary conditions have limited influence.

Such analysis approach can be used to obtain the spatial strength distribution of the macroscopic specimen after aging, as can be seen in Figure 4.11 for uniaxial transverse tension σ_{22}. During aging, the additional constraints imposed by transient swelling stresses and the consequent differences in development of distributed resin and interface failures create a non-uniform strength distribution. Although the difference in strength between the weakest and strongest points is small (approximately 200 kPa), the transient swelling effectively creates weak spots where damage is likely to initiate and propagate from. Such effect can only be captured by combining macroscopic diffusion with a fully-coupled multiscale mechanical analysis.

4.4. CONCLUSIONS

This work presented a coupled multiscale/multiphysics numerical analysis framework suitable for modeling of hygrothermal aging in laminated composites. The proposed model consists of a macroscopic transient diffusion analysis coupled with a multiscale

(FE^2) mechanical model in order to account for microscopic degradation mechanisms and failure events.

At the macroscale, diffusion is considered isotropic with constant diffusivity, while no mechanical constitutive model is explicitly defined. The mechanical response is instead obtained through homogenization of the microscopic material response. At the microscale, diffusion is modeled as steady-state with constant water concentration. An elasto-plastic epoxy model with damage is combined with cohesive zones at the fiber/matrix interfaces in order to model failure caused by swelling, plasticization and interface weakening after water ingression. Detailed formulations for every constituent of the framework were presented.

While properties for the interfaces were obtained from literature, the calibration of the epoxy model has been performed based on experimental investigations in both dry and saturated pure resin specimens. It was shown that the water degradation model with a single degradation factor was capable of correctly predicting the experimental stress-strain material response after aging.

An RVE size study was conducted, ranging from a unit cell model with a single fiber to 7 x 7 fibers micromodels with random fiber distribution. While the mean dry stiffness response stabilised with relatively small RVE sizes, the saturated stiffness and both dry and wet transverse strengths required larger sizes. Nevertheless, an RVE with representative behavior could not be obtained in the investigated size range, since significant scatter was still present for both stiffness and strength. Biaxial transverse failure envelopes of both dry and saturated micromodels were also compared. After aging, the failure envelope tends to shrink due to plasticization and interface weakening as well as shift towards the compression bisector due to differential swelling.

The capabilities of the model were demonstrated through the simulation of the hygrothermal aging process of a unidirectional composite short-beam immersed in water at 50°C. Transient swelling stresses due to water concentration gradients were correctly predicted. Through the FE^2 scale coupling, the macroscopic compatibility requirement acted as constraints to the micromodels and influenced their final homogenised stiffness and strength. Although such transient effects were found to bring limited impact to the final material stiffness and strength, they effectively create weak spots where damage can initiate and propagate from.

REFERENCES

[1] I. B. C. M. Rocha, F. P. van der Meer, R. P. L. Nijssen, and L. J. Sluys, *A multiscale and multiphysics numerical framework for modelling of hygrothermal ageing in laminated composites,* International Journal for Numerical Methods in Engineering **112**, 360 (2017).

[2] A. R. Melro, P. P. Camanho, F. M. Andrade Pires, and S. T. Pinho, *Micromechanical analysis of polymer composites reinforced by unidirectional fibres: Part I - Constitutive modelling,* International Journal of Solids and Structures **50**, 1897 (2013).

[3] A. Turon, P. P. Camanho, J. Costa, and C. G. Dávila, *A damage model for the simulation of delamination in advanced composites under variable-mode loading,* Mechanics of Materials **38**, 1072 (2006).

[4] I. B. C. M. Rocha, S. Raijmaekers, R. P. L. Nijssen, and F. van der Meer, *Hydrothermal ageing of glass/epoxy composites for wind turbine blades,* in *In: Procedures of the 20th International Conference on Composite Materials* (2015).

[5] Y. Joliff, W. Rekik, L. Belec, and J. F. Chailan, *Study of the moisture/stress effects on glass fibre/epoxy composite and the impact of the interphase area,* Composite Structures **108**, 876 (2014).

[6] S. A. Grammatikos, B. Zafari, M. C. Evernden, J. T. Mottram, and J. M. Mitchels, *Moisture uptake characteristics of a pultruded fibre reinforced polymer flat sheet subjected to hot/wet aging,* Polymer Degradation and Stability **121**, 407 (2015).

[7] L. Gautier, B. Mortaigne, and B. V., *Interface damage study of hydrothermally aged glass-fibre-reinforced polyester composites,* Composites Science and Technology **59**, 2329 (1999).

[8] G. Pitarresi, M. Scafidi, S. Alessi, M. Di Filippo, C. Billaud, and G. Spadaro, *Absorption kinetics and swelling stresses in hydrothermally aged epoxies investigated by photoelastic image analysis,* Polymer Degradation and Stability **111**, 55 (2015).

[9] J. El Yagoubi, G. Lubineau, F. Roger, and J. Verdu, *A fully coupled diffusion-reaction scheme for moisture sorption-desorption in an anhydride-cured epoxy resin,* Polymer **53**, 5582 (2012).

[10] I. Özdemir, W. A. M. Brekelmans, and M. G. D. Geers, *FE^2 computational homogenization for the thermo-mechanical analysis of heterogeneous solids,* Computer Methods in Applied Mechanics and Engineering **198**, 602 (2008).

[11] K. Terada and M. Kurumatani, *Two-scale diffusion-deformation coupling model for material deterioration involving micro-crack propagation,* International Journal for Numerical Methods in Engineering **83**, 426 (2010).

[12] M. G. D. Geers, V. G. Kouznetsova, and W. A. M. Brekelmans, *Multi-scale computational homogenization: Trends and challenges,* Journal of Computational and Applied Mathematics **234**, 2175 (2010).

[13] F. P. van der Meer, *Micromechanical validation of a mesomodel for plasticity in composites,* European Journal of Mechanics - A/Solids **60**, 58 (2016).

[14] F. P. van der Meer and L. J. Sluys, *Mesh-independent modeling of both distributed and discrete matrix cracking in interaction with delamination in composites,* Engineering Fracture Mechanics **77**, 719 (2010).

[15] M. L. Benzeggagh and M. Kenane, *Measurement of mixed-mode delamination fracture toughness of unidirectional glass/epoxy composites with mixed mode bending apparatus,* Composites Science and Technology **56**, 439 (1996).

[16] F. Naya, C. González, C. S. Lopes, S. van der Veen, and F. Pons, *Computational micromechanics of the transverse and shear behaviour of unidirectional fiber reinforced polymers including environmental effects,* Composites: Part A (2016).

[17] P. Davies, F. Mazéas, and P. Casari, *Sea water aging of glass reinforced composites: Shear behaviour and damage modelling,* Journal of Composite Materials **35**, 1343 (2000).

[18] V. P. Nguyen, O. Lloberas-Valls, M. Stroeven, and L. J. Sluys, *Computational homogenization for multiscale crack modelling. implementation and computational aspects,* International Journal for Numerical Methods in Engineering **89**, 192 (2012).

[19] K. C. Park, *An improved stiffly stable method for direct integration of nonlinear structural dynamic equations,* Journal of Applied Mechanics **42**, 464 (1975).

[20] J. Remmers, *Mode-jumping simulations using the new implicit time integrator in b2000,* in *2nd B2000/MEMCOM workshop* (1998).

[21] D. D. Sommer, E. A. de Souza Neto, W. G. Dettmer, and D. Perić, *A sub-stepping scheme for multi-scale analysis of solids,* Computer Methods in Applied Mechanics and Engineering **198**, 1006 (2009).

[22] M. A. Gutiérrez, *Energy release control for numerical simulations of failure in quasi-brittle solids,* Communications in Numerical Methods in Engineering **20**, 19 (2004).

[23] F. P. van der Meer, C. Oliver, and L. J. Sluys, *Computational analysis of progressive failure in a notched laminate including shear nonlinearity and fiber failure,* Composites Science and Technology **70**, 692 (2010).

[24] F. P. van der Meer, *Mesolevel modeling of failure in composite laminates: Constitutive, kinematic and algorithmic aspects,* Archives of Computational Methods in Engineering **19**, 381 (2012).

[25] I. B. C. M. Rocha, S. Raijmaekers, R. P. L. Nijssen, F. P. van der Meer, and L. J. Sluys, *Experimental/numerical study of anisotropic water diffusion in glass/epoxy composites,* IOP Conference Series: Materials Science and Engineering **139**, 1 (2016).

[26] C. Geuzaine and J.-F. Remacle, *Gmsh: A three-dimensional finite element mesh generator with built-in pre- and post-processing facilities,* International Journal for Numerical Methods in Engineering **79**, 1309 (2009).

[27] C. Qian, T. Westphal, and R. P. L. Nijssen, *Micro-mechanical fatigue modelling of unidirectional glass fibre reinforced polymer composites,* Computational Materials Science **69**, 62 (2013).

[28] M. Li, *Temperature and moisture effects on composite materials for wind turbine blades* (MSc thesis, Montana State University-Bozeman, 2000).

[29] V. P. Nguyen, O. Lloberas Valls, M. Stroeven, and L. J. Sluys, *On the existence of representative volumes for softening quasi-brittle materials - a failure zone averaging scheme,* Computer Methods in Applied Mechanics and Engineering **199**, 45 (2010).

5

A VISCOELASTIC, VISCOPLASTIC, DAMAGE MODEL FOR EPOXY

I prepared myself for a multitude of reverses; my operations might be incessantly baffled, and at last my work be imperfect, yet when I considered the improvement which every day takes place in science and mechanics, I was encouraged to hope my present attempts would at least lay the foundations of future success.

Mary Shelley, *Frankenstein*

5.1. INTRODUCTION

In Chapter 4, an elastoplastic model with damage was used to represent the microscopic mechanical behavior of the epoxy resin considered in this thesis. Such an inviscid model, although suitable for a number of loading scenarios, is not capable of taking into account the strain rate-dependent response of the resin. This is of particular importance given the fact that hygrothermal aging is, for most practical applications, a significantly slower process than the mechanical loads applied, for instance, during the mechanical test of a pre-conditioned specimen. A correct representation of the epoxy resin behavior across time scales is therefore an important extension to the framework, and the subject of the present chapter.

Accurate constitutive modeling of epoxies and other polymers is complicated by the fact that their mechanical behavior is time- and temperature-dependent. Such viscous effects give rise to phenomena such as strain rate dependency [2], ratcheting [3] and stress relaxation [4]. Additionally, polymers are known to develop permanent strains

This chapter is based on [1]. Text from the appendices has been moved back into the main text and the introductory section has been shortened.

through pressure-dependent plastic yielding [5] and, in the particular case of crosslinked thermosets, undergo rate-dependent brittle failure at relatively low strain levels [6, 7]. Finally, all of these material features are sensitive to physical and chemical effects caused by water absorption [8, 9], physical aging [10], oxidation [11], among others. Therefore, despite the already large amount of literature on the subject, experimental and numerical efforts on polymer characterization often ignore such complex material aspects.

A number of authors opt for elastoplastic constitutive models with pressure-dependent yielding [12, 13] calibrated using experiments with fixed strain rate and temperature and therefore ignoring the aforementioned viscous material features. The use of such models to describe material failure in fatigue or during aging may therefore be unrealistic. Phenomenological corrections have been proposed in order to introduce such dependencies by scaling a reference yield surface depending on rate and temperature [14]. However, this approach becomes unsuitable in loading situations with continuously changing strain rate or in non-isothermal conditions.

A second class of models attempts to introduce a time scale to the plastic flow rate while keeping the original inviscid yield surface [7, 9, 15–17]. This approach is interesting for finite element implementation since it can build upon previously implemented inviscid models. However, the temperature dependence is still not captured.

A third option in which temperature dependency is also addressed involves using Eyring-type rate equations [18], which consider yielding as a thermomechanically activated process [2, 19–21]. This is usually combined with a hyperelastic model in order to capture orientation hardening at high strains [2].

Finally, a number of physically-based macromolecular constitutive models have been devised which take into account changes in polymer chain orientation after yielding [6, 22–30]. In these approaches, both strain and temperature dependencies as well as orientation hardening are captured and arise as a consequence of underlying macromolecular mechanisms, providing a strong physical basis for the models. However, a number of drawbacks remain for application of these models in the numerical analysis of highly cross-linked thermosetting polymers. Firstly, most of the models are constructed with thermoplastic polymers in mind, which are capable to attain significantly higher strain levels. Consequently, the models are seldom concerned with material failure through fracture, while for highly cross-linked epoxies fracture is indeed observed at relatively low strain levels. Secondly, the models usually assume that no plastic deformation occurs before the peak stress, while experiments in epoxy show the occurrence of pre-peak plasticity (see [6] for an adapted macromolecular model). Thirdly, the models are often formulated in terms of principal stretches and seldom provide tangent stiffness operator expressions (notable exceptions are [30, 31]), making their finite element implementation and use for micromechanical modeling of complex stress states a difficult task.

Regarding modeling of the cyclic response of polymers, multiple works are limited to accurately describing the stress-strain behavior after a small number of loading-unloading cycles [7, 8, 17]. In those works, the viscoelastic-viscoplastic material behavior is taken into account but no attempt is made to model material failure in fatigue. At the other end of the spectrum, a number of works focus on high-cycle fatigue failure by phenomenologically imposing the evolution of a continuum damage internal variable with the num-

ber of fatigue cycles while ignoring viscous contributions [32, 33]. However, experimental results by multiple authors [3, 4, 28] emphasize the occurrence of fatigue failure with little to no change in stiffness, particularly in the high-cycle regime, which invalidates the use of a damage variable. It is important to note that modulus measurements in fatigue are affected by viscoelastic contributions that relax over time and might be erroneously interpreted as modulus degradation, in particular for tests in the low-cycle regime. For materials showing such type of fatigue failure behavior, appropriate definitions for the onset and evolution of damage are needed while maintaining a correct description of their viscous behavior.

5.1.1. EXPERIMENTAL MOTIVATION

Figure 5.1 illustrates the shortcomings of using state-of-the-art elastoplastic-damage (E-P-D) formulations to model the cyclic behavior of the epoxy resin considered here. In a preliminary study, a material sample was subjected to a number of loading-unloading cycles at 1 mm/min with increasing displacement amplitudes until failure occurred. The resultant load-displacement curve can be seen in Figure 5.1a, while the expected material response using either the inviscid model by Melro *et al.* [12] or its rate-dependent variation proposed by Bai *et al.* [14] is shown in Figure 5.1b.

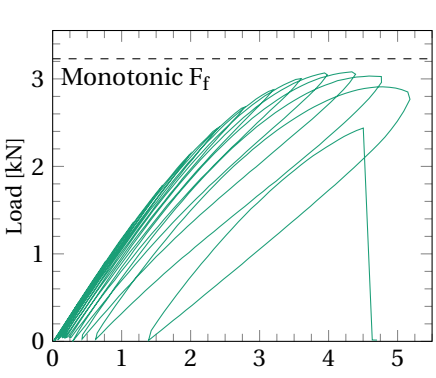

(a) Experimental response

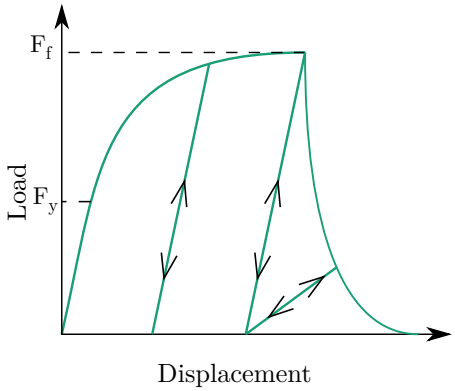

(b) Prediction using an E-P-D model

Figure 5.1: Material response in a loading-unloading scenario with increasing amplitude.

According to the model, the material behaves elastically up until the yield point F_y after which a hardening regime is observed until the fracture load F_f is reached. The model unloads and reloads elastically along the same path with a slope equal to the initial stiffness until damage is activated, at which point plasticity stops evolving and the stiffness gradually decreases until final failure. During reloading, the curve always meets its respective unloading point and the response returns to the curve for monotonic loading even if a rate-dependent yield surface is used [14], since the strain rate does not change throughout the test.

On the other hand, experimental unloading and reloading branches are nonlinear and do not follow the same path, with significant hysteresis (viscoelasticity). Upon reload-

ing, the curve does not meet its original unloading point and further plastic strain develops (viscoplasticity). Finally, the specimen fails without ever reaching the monotonic failure load and without a gradual stiffness reduction, suggesting that fracture initiation is driven by plastic strain development and rapid crack propagation leading to brittle failure. Furthermore, subjecting the material to fatigue loads in the high-cycle regime leads to failure without any measurable loss of stiffness and after stabilization of ratcheting, suggesting that fracture initiation is not only affected by plastic strain development but also by phenomena occurring in the elastic regime.

Based on these preliminary investigations, a number of additional model ingredients may be proposed in order to improve the performance of conventional elastoplastic-damage models when dealing with time-dependent mechanical behavior while keeping as many of their original components as possible. Firstly, the observed hysteresis behavior can be captured by adding a time-dependent stiffness contribution to the existing elasticity formulation. Secondly, since permanent strains develop gradually under cyclic loading, plastic strain development must be retarded by allowing stresses to temporarily surpass the original yield surface. Finally, the existing damage formulation must be adjusted in order to allow for fracture initiation at load levels lower than the original fracture load by introducing a fracture surface shrink driven by both viscoelastic and viscoplastic mechanisms.

5.1.2. OUTLINE OF THE STUDY

In this chapter, the state-of-the-art pressure-dependent elastoplastic formulation presented by Melro *et al.* [12] is expanded into a viscoelastic-viscoplastic-damage (VE-VP-D) model. The modified model can in turn be used in isolation or to provide more realistic predictions of the mechanical behaviour of composite materials subjected to monotonic or cyclic loadings through micromechanical modeling.

Viscoelasticity is incorporated through a series of springs and dashpots. Viscoplasticity is modeled through a Perzyna-type formulation. Fracture is modeled by a thermodynamically consistent damage model with linear softening and a fracture surface that shrinks as energy is dissipated. Finally, the mechanical model is complemented by a damage model with a single degradation factor in order to take into account changes in polymer behavior after moisture absorption. The formulations are presented in a way that facilitates their implementation in a finite element framework. The model is calibrated using an original series of monotonic and cyclic experiments on pure resin specimens both dry and after being saturated in water at 50 °C. After calibration, the model is used to predict the rate-dependent response of the water-saturated polymer and its behavior during loading-unloading and fatigue tests. The model performance is assessed by comparing these predictions with validation experiments.

5.2. MODEL FORMULATION

5.2.1. MATHEMATICAL NOTATION

In this work, both index notation and matrix notation will be used to represent tensors and vectors. When index notation is used, the indices i, j, k, l range from one to the number of spatial dimensions of the problem being solved. In products between two

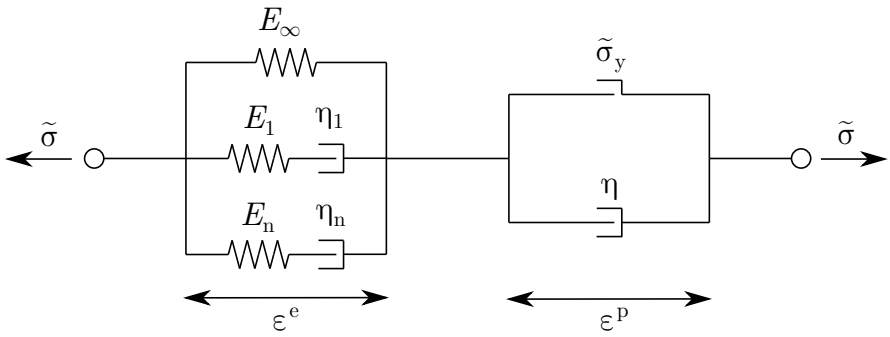

Figure 5.2: Schematic representation of the VE/VP/D model.

entities in index notation, summation over repeated indices is implied. In matrix notation, vectors are represented by boldfaced lower-case symbols while matrices are given by boldfaced upper-case symbols. When representing stresses and strains in matrix notation, the use of Voigt notation is implied.

5.2.2. RHEOLOGICAL MODEL

The present model can be schematically represented by the rheological model of Figure 5.2. For a given applied stress, the strain response is decomposed into elastic and plastic parts. The elastic behavior is represented by a parallel chain of Maxwell elements with springs and dashpots to which a long-term spring is added. The plastic behavior is represented by a sliding element on which the stress cannot be higher than the yield stress σ_y. By adding a dashpot element in parallel with the sliding element, an overstress is allowed to develop resulting in viscoplastic behavior. Finally, damage is enforced by degrading the resultant effective stress $\tilde{\sigma}$.

In the following sections, each model component will be formulated and expressions for stress update and tangent stiffness will be provided in order to facilitate their implementation in general finite element codes.

5.2.3. VISCOELASTICITY

In the model, an additive decomposition of strain in elastic and plastic parts is considered:

$$\varepsilon_{ij} = \varepsilon^{\mathrm{e}}_{ij} + \varepsilon^{\mathrm{p}}_{ij} \tag{5.1}$$

The viscoelastic stress is computed in integral form by applying the Boltzmann superposition principle [15]:

$$\sigma_{ij}(t) = D^{\infty}_{ijkl}\varepsilon^{\mathrm{e}}_{kl}(t) + \int_0^t D^{\mathrm{ve}}_{ijkl}(t-\tilde{t})\frac{\partial \varepsilon^{\mathrm{e}}_{kl}(\tilde{t})}{\partial \tilde{t}}d\tilde{t} \tag{5.2}$$

where the long-term and viscous contributions are explicitly separated. The long-term elastic stiffness D^{∞}_{ijkl} is given by:

$$D^{\infty}_{ijkl} = G_\infty(\delta_{ij}\delta_{kl} + \delta_{il}\delta_{jk}) + \left(K_\infty - \frac{2}{3}G_\infty\right)\delta_{ij}\delta_{kl} \tag{5.3}$$

where G_∞ and K_∞ are the long term shear and bulk modulus, respectively. It is important to note that the response of this back-bone elastic solid is time-independent and is therefore taken out of the integral of Eq. (5.2).

The viscoelastic contribution has a similar form but is now composed of time-dependent stiffnesses:

$$D^{\text{ve}}_{ijkl}(t) = G_{\text{ve}}(t)(\delta_{ij}\delta_{kl} + \delta_{il}\delta_{jk}) + \Big(K_{\text{ve}}(t) - \frac{2}{3}G_{\text{ve}}(t)\Big)\delta_{ij}\delta_{kl} \tag{5.4}$$

where G_{ve} and K_{ve} are the stiffnesses of the Maxwell elements of Figure 5.2 and can be expressed as a Prony series of n_r bulk elements and n_s shear elements:

$$K_{\text{ve}}(t) = \sum_{r=1}^{n_r} K_r \exp\Big(-\frac{t}{k_r}\Big) \qquad G_{\text{ve}}(t) = \sum_{s=1}^{n_s} G_s \exp\Big(-\frac{t}{g_s}\Big) \tag{5.5}$$

where K_r, G_s, k_r and g_s are bulk and shear stiffnesses and relaxation times, respectively.

In order to avoid performing the time integration of Eq. (5.2) at every time step and thus having to store the whole strain history of every material point, the stress update can be represented in a time discrete manner. Following the development in Haouala and Doghri [15], Eq. (5.2) becomes:

$$\sigma_{ij}(t_{n+1}) = D^{\infty}_{ijkl}\varepsilon^{\text{e}}_{kl}(t_{n+1}) + \sum_{r=1}^{n_r} p^{\text{ve}}_r(t_{n+1})\delta_{ij} + \sum_{s=1}^{n_s} S^{\text{ve}}_{ij,s}(t_{n+1}) \tag{5.6}$$

where the deviatoric and hydrostatic viscoelastic stress contributions S^{ve}_{ij} and p^{ve} of each Prony element are given by:

$$p^{\text{ve}}_r(t_{n+1}) = \exp\Big(\frac{-\Delta t}{k_r}\Big)p^{\text{ve}}_r(t_n) + K_r\Big[1 - \exp\Big(\frac{-\Delta t}{k_r}\Big)\Big]\frac{k_r}{\Delta t}\big(\varepsilon^{\text{e}}_{\text{v}}(t_{n+1}) - \varepsilon^{\text{e}}_{\text{v}}(t_n)\big) \tag{5.7}$$

$$S^{\text{ve}}_{ij,s}(t_{n+1}) = \exp\Big(\frac{-\Delta t}{g_s}\Big)S^{\text{ve}}_{ij,s}(t_n) + 2G_s\Big[1 - \exp\Big(\frac{-\Delta t}{g_s}\Big)\Big]\frac{g_s}{\Delta t}\big(\varepsilon^{\text{e}}_{ij,\text{d}}(t_{n+1}) - \varepsilon^{\text{e}}_{ij,\text{d}}(t_n)\big) \tag{5.8}$$

where $\Delta t = t_{n+1} - t_n$ is the time step, $\varepsilon_{\text{v}} = \varepsilon_{kk}$ is the volumetric part of the strain and $\varepsilon_{ij,\text{d}} = \varepsilon_{ij} - 1/3\varepsilon_{\text{v}}\delta_{ij}$ is the deviatoric part. In discrete form, only information about the previous converged time step t_n has to be stored. Finally, the total elastic stiffness can be found by substituting Eqs. (5.7) and (5.8) into Eq. (5.6):

$$D^{\text{e}}_{ijkl}(t_{n+1}) = D^{\infty}_{ijkl} + D^{\text{ve}}_{ijkl}(\Delta t) \tag{5.9}$$

5.2.4. VISCOPLASTICITY

In contrast with the stress update for viscoelasticity, an iterative procedure is necessary in order to compute the stresses in the viscoplastic regime. At first, it is assumed that the increment of strain is viscoelastic and a trial stress is computed. By explicitly isolating historical terms from terms that operate on the current strain increment in Eq. (5.6), the trial stress is computed as:

$$\sigma^{\text{tr}}_{ij} = D^{\infty}_{ijkl}\big(\varepsilon_{kl}(t_{n+1}) - \varepsilon^{\text{p}}_{kl}(t_n)\big) + D^{\text{ve}}_{ijkl}\big(\varepsilon_{kl}(t_{n+1}) - \varepsilon^{\text{p}}_{kl}(t_n) - \varepsilon^{\text{e}}_{kl}(t_n)\big) + \sigma^{\text{hist}}_{ij}(t_n) \tag{5.10}$$

If no further plastic strain is developed, the computed trial stress is correct and the update is completed by updating the historical stresses of Eqs. (5.7) and (5.8). However, if the amount of plastic strain changes, the stresses must be corrected:

$$\sigma_{ij} = \sigma^{\text{tr}}_{ij} - (D^{\infty}_{ijkl} + D^{\text{ve}}_{ijkl})\Delta\varepsilon^{\text{p}}_{kl} \tag{5.11}$$

and the historical stresses must be updated using the correct value for the elastic strain.

The yield surface adopted in this model is the one proposed by Melro et al. [12]:

$$f_{\text{p}}(\boldsymbol{\sigma}, \varepsilon^{\text{p}}_{\text{eq}}) = 6J_2 + 2I_1(\sigma_c - \sigma_t) - 2\sigma_c\sigma_t \tag{5.12}$$

where σ_t and σ_c are the yield stresses in tension and compression, respectively, $I_1 = \sigma_{kk}$ is the first stress invariant and $J_2 = \frac{1}{2}S_{ij}S_{ij}$ is the second invariant of the deviatoric stress.

The hardening behavior is a consequence of the evolution of the yield stresses σ_t and σ_c, which are functions of the equivalent plastic strain:

$$\Delta\varepsilon^{\text{p}}_{\text{eq}} = \sqrt{\frac{1}{1+2\nu^2_{\text{p}}}\Delta\varepsilon^{\text{p}}_{ij}\Delta\varepsilon^{\text{p}}_{ij}} \;\Rightarrow\; \sigma_t = \sigma_t(\varepsilon^{\text{p}}_{\text{eq}}),\, \sigma_c = \sigma_c(\varepsilon^{\text{p}}_{\text{eq}}) \tag{5.13}$$

where ν_p is the plastic Poisson ratio and the yield stresses are given by functions of equivalent plastic strain that can take any form. The variation in plastic strains is computed through a non-associative flow rule:

$$\Delta\varepsilon^{p}_{ij} = \Delta\gamma\left(3S_{ij} + \frac{2}{9}\alpha I_1\delta_{ij}\right) \tag{5.14}$$

where γ is the plastic multiplier, the expression in parentheses is the plastic flow direction, and α is:

$$\alpha = \frac{9}{2}\frac{1-2\nu_p}{1+\nu_p} \tag{5.15}$$

The choice for non-associative plasticity is related to the pressure dependency of the model and is done in order to avoid the occurrence of spurious volumetric plastic strains [12].

A viscous time scale is introduced in the model by relaxing the classic Kuhn-Tucker conditions on the yield function and allowing it to attain positive values. This effectively delays the development of plastic strains and allows for the development of an overstress above the yield surface. In this work, the Perzyna-type formulation used in [15] is modified for the yield surface of Eq. (5.12) and dictates the evolution of the plastic multiplier:

$$\Delta\gamma = \begin{cases} \frac{\Delta t}{\eta_{\text{p}}}\left(\frac{f_{\text{p}}}{\sigma^0_{\text{t}}\sigma^0_{\text{c}}}\right)^{m_{\text{p}}}, & \text{if} f > 0 \\ 0, & \text{if} f \leq 0 \end{cases} \tag{5.16}$$

where the time discrete expression is obtained through a backward Euler scheme [15], the superscript 0 indicates yield stress values for $\varepsilon^{\text{p}}_{\text{eq}} = 0$, and η_{p} and m_{p} are the viscoplastic modulus and exponent, respectively.

With the definition of the flow rule, the stresses of Eq. (5.11) may be written as:

$$\sigma_{ij} = \frac{S^{\text{tr}}_{ij}}{\zeta_s} + \frac{I^{\text{tr}}_1\delta_{ij}}{3\zeta_p} \tag{5.17}$$

where the factors ζ_s and ζ_p are:

$$\zeta_s = 1 + 6\big(G_\infty + G_{\text{ve}}(\Delta t)\big)\Delta\gamma \;\Rightarrow \zeta_s = 1 + 6\widehat{G}\Delta\gamma \tag{5.18}$$

$$\zeta_p = 1 + 2\big(K_\infty + K_{\text{ve}}(\Delta t)\big)\alpha\Delta\gamma \;\Rightarrow \zeta_p = 1 + 2\widehat{K}\alpha\Delta\gamma \tag{5.19}$$

Substituting Eq. (5.17) into the equivalent plastic strain expression of Eq. (5.13) through Eq. 5.14 and into the yield surface of Eq. (5.12), Eq. (5.16) becomes a function of $\Delta\gamma$ only and can be solved iteratively using Newton's method:

$$\Phi(\Delta\gamma) = \frac{\Delta t}{\eta_{\text{p}}}(\Delta\gamma)\Big(\frac{f_{\text{p}}}{\sigma_{\text{t}}^0\sigma_{\text{c}}^0}\Big)^{m_{\text{p}}} - \Delta\gamma = 0 \tag{5.20}$$

In order to accelerate convergence, it is necessary to compute the derivative of Eq. (5.20) with respect to $\Delta\gamma$:

$$\frac{\partial\Phi}{\partial\Delta\gamma} = \frac{m_{\text{p}}\Delta t}{\eta_{\text{p}}\sigma_{\text{t}}^0\sigma_{\text{c}}^0}\Big(\frac{f_{\text{p}}}{\sigma_{\text{t}}^0\sigma_{\text{c}}^0}\Big)^{m_{\text{p}}-1}\frac{\partial f_{\text{p}}}{\partial\Delta\gamma} - 1 = \widehat{V}\frac{\partial f_{\text{p}}}{\partial\Delta\gamma} - 1 \tag{5.21}$$

where $\partial f/\partial\Delta\gamma$ is:

$$\frac{\partial f_{\text{p}}}{\partial\Delta\gamma} = -\frac{72\widehat{G}}{\zeta_s^3}J_2^{\text{tr}} - \frac{4\widehat{K}\alpha I_1^{\text{tr}}}{\zeta_p^2}(\sigma_c - \sigma_t) + \frac{\partial f_{\text{p}}}{\partial\varepsilon_{\text{eq}}^{\text{p}}}\frac{\partial\Delta\varepsilon_{\text{eq}}^p}{\partial\Delta\gamma} \tag{5.22}$$

and $\partial f_{\text{p}}/\partial\varepsilon_{\text{eq}}^{\text{p}}$ is:

$$\frac{\partial f_{\text{p}}}{\partial\varepsilon_{\text{eq}}^{\text{p}}} = \frac{2I_1^{\text{tr}}}{\zeta_p}(H_c - H_t) - 2(\sigma_c H_t + \sigma_t H_c) = \widehat{H} \tag{5.23}$$

where H_c and H_t are derivatives of σ_c and σ_t with respect to $\varepsilon_{\text{eq}}^p$ and representing the compressive and tensile hardening moduli, respectively.

The only remaining term to compute in Eq. 5.22 is $\partial\Delta\varepsilon_{\text{eq}}^p/\partial\Delta\gamma$. Substituting Eq. (5.14) in Eq. (5.13) and applying the trial stress conversion of Eq. (5.17), the variation of equivalent plastic strain becomes:

$$\Delta\varepsilon_{\text{eq}}^p = \Delta\gamma\sqrt{\frac{\frac{18}{\zeta_s^2}J_2^{\text{tr}} + \frac{4\alpha^2}{27\zeta_p^2}(I_1^{\text{tr}})^2}{1 + 2\nu_p^2}} = \Delta\gamma\sqrt{\frac{\widehat{A}}{1 + 2\nu_p^2}} \tag{5.24}$$

and its derivative with respect to $\Delta\gamma$ is:

$$\frac{\partial\Delta\varepsilon_{\text{eq}}^{\text{p}}}{\partial\Delta\gamma} = \sqrt{\frac{1}{1 + 2\nu_{\text{p}}^2}}\Big[\sqrt{\widehat{A}} - \frac{\Delta\gamma}{2\sqrt{\widehat{A}}}\Big(\frac{216\widehat{G}J_2^{\text{tr}}}{\zeta_s^3} + \frac{16\alpha^3\widehat{K}(I_1^{\text{tr}})^2}{27\zeta_p^3}\Big)\Big] \tag{5.25}$$

The last step in the formulation is to obtain the consistent tangent stiffness matrix. Because of the time scale introduced by the viscous plastic multiplier of Eq. (5.16), there is no strict relationship between variations of stress and strain. However, since the stress

update is performed in a time discrete manner, it is still possible to define an algorithmic tangent matrix by differentiating Eq. (5.17) with respect to strain:

$$\frac{\partial \sigma_{ij}}{\partial \varepsilon_{kl}} = \frac{1}{\zeta_s}\frac{\partial S^{\mathrm{tr}}_{ij}}{\partial \varepsilon_{kl}} - \frac{6\widehat{G}}{\zeta_s^2} S^{\mathrm{tr}}_{ij}\frac{\partial \Delta\gamma}{\partial \varepsilon_{kl}} + \frac{1}{3\zeta_p}\delta_{ij}\frac{\partial I_1^{\mathrm{tr}}}{\partial \varepsilon_{kl}} - \frac{2\widehat{K}\alpha I_1^{\mathrm{tr}}}{3\zeta_p^2}\delta_{ij}\frac{\partial \Delta\gamma}{\partial \varepsilon_{kl}} \tag{5.26}$$

The derivatives of the deviatoric stress and first stress invariant can be readily computed:

$$\frac{\partial S^{\mathrm{tr}}_{ij}}{\partial \varepsilon_{kl}} = \widehat{G}\Big(\delta_{ik}\delta_{jl} + \delta_{il}\delta_{jk} - \frac{2}{3}\delta_{ij}\delta_{kl}\Big) \tag{5.27}$$

$$\frac{\partial I_1^{\mathrm{tr}}}{\partial \varepsilon_{kl}} = 3\widehat{K}\delta_{kl} \tag{5.28}$$

while the variation of the plastic multiplier with respect to strain is derived from differentiation of the viscoplastic consistency condition of Eq. (5.17) [34]:

$$\delta\Phi = \frac{\partial \Phi}{\partial \varepsilon_{kl}}\delta\varepsilon_{kl} + \frac{\partial \Phi}{\partial \Delta\gamma}\delta\Delta\gamma = 0 \quad \Rightarrow \quad \frac{\partial \Delta\gamma}{\partial \varepsilon_{kl}} = \frac{1}{\mu}\frac{\partial \Phi}{\partial \varepsilon_{kl}} \tag{5.29}$$

where μ is the negative of the derivative of Eq. (5.21):

$$\mu = -\frac{\partial \Phi}{\partial \Delta\gamma} \tag{5.30}$$

Differentiation of Φ with respect to strain takes a similar form as Eq. (5.21):

$$\frac{\partial \Phi}{\partial \varepsilon_{kl}} = \widehat{V}\frac{\partial f_{\mathrm{p}}}{\partial \varepsilon_{kl}} \tag{5.31}$$

and $\partial f_{\mathrm{p}}/\partial \varepsilon_{kl}$ in terms of trial stresses is given by:

$$\frac{\partial f_{\mathrm{p}}}{\partial \varepsilon_{kl}} = \frac{6}{\zeta_s^2}\frac{\partial J_2^{\mathrm{tr}}}{\partial \varepsilon_{kl}} + \frac{2(\sigma_c - \sigma_t)}{\zeta_p}\frac{\partial I_1^{\mathrm{tr}}}{\partial \varepsilon_{kl}} + \widehat{H}\frac{\partial \varepsilon^{\mathrm{p}}_{\mathrm{eq}}}{\partial \varepsilon_{kl}} \tag{5.32}$$

The derivative of the first invariant is shown in Eq. (5.28), while the derivative of J_2^{tr} is given by:

$$\frac{\partial J_2^{\mathrm{tr}}}{\partial \varepsilon_{kl}} = S^{\mathrm{tr}}_{ij}\frac{\partial S^{\mathrm{tr}}_{ij}}{\partial \varepsilon_{kl}} = 2\widehat{G}S^{\mathrm{tr}}_{kl} \tag{5.33}$$

The last term of Eq. (5.32) takes into account variations in yield stress with strain through the consequent variation in equivalent plastic strain [34]. The factor $\widehat{H}$ is given in Eq. (5.23), and $\partial \varepsilon^{\mathrm{p}}_{\mathrm{eq}}/\partial \varepsilon_{kl}$ is obtained from Eqs. (5.13) and (5.14):

$$\begin{aligned}\frac{\partial \varepsilon^{\mathrm{p}}_{\mathrm{eq}}}{\partial \varepsilon_{kl}} = &\frac{1}{1+2\nu_p^2}\frac{(\Delta\gamma)^2}{\Delta\varepsilon^{\mathrm{p}}_{\mathrm{eq}}}\Big(\frac{3S^{\mathrm{tr}}_{ij}}{\zeta_s} + \frac{2\alpha I_1^{\mathrm{tr}}\delta_{ij}}{9\zeta_p}\Big)\cdot \\ &\cdot\Big(\frac{\widehat{G}}{\zeta_s}\big(3(\delta_{ik}\delta_{jl} + \delta_{il}\delta_{jk}) - 2\delta_{ij}\delta_{kl}\big) + \frac{2\widehat{K}\alpha}{3\zeta_p}\delta_{ij}\delta_{kl}\Big) = \widehat{E}_{kl}\end{aligned} \tag{5.34}$$

Substitution of Eqs. (5.27), (5.28) and (5.29) in the tangent tensor of Eq. (5.26) yields:

$$\begin{aligned}\frac{\partial\sigma_{ij}}{\partial\varepsilon_{kl}} = &\frac{\widehat{G}}{\zeta_s}\Big(\delta_{ik}\delta_{jl}+\delta_{il}\delta_{jk}-\frac{2}{3}\delta_{ij}\delta_{kl}\Big)+\frac{\widehat{K}}{\zeta_p}\delta_{ij}\delta_{kl}\\ &-\frac{72\widehat{V}\widehat{G}^2}{\mu\zeta_s^4}S_{ij}^{\mathrm{tr}}S_{kl}^{\mathrm{tr}}-\frac{36(\sigma_c-\sigma_t)\widehat{V}\widehat{K}\widehat{G}}{\mu\zeta_p\zeta_s^2}S_{ij}^{\mathrm{tr}}\delta_{kl}\\ &-\frac{8\alpha I_1^{\mathrm{tr}}\widehat{V}\widehat{K}\widehat{G}}{\mu\zeta_p^2\zeta_s^2}\delta_{ij}S_{kl}^{\mathrm{tr}}-\frac{4\alpha I_1^{\mathrm{tr}}(\sigma_c-\sigma_t)\widehat{V}\widehat{K}^2}{\mu\zeta_p^3}\delta_{ij}\delta_{kl}\\ &-\frac{6\widehat{V}\widehat{G}\widehat{H}}{\mu\zeta_s^2}S_{ij}^{\mathrm{tr}}\widehat{E}_{kl}-\frac{2\alpha I_1^{\mathrm{tr}}\widehat{V}\widehat{K}\widehat{H}}{3\mu\zeta_p^2}\delta_{ij}\widehat{E}_{kl}\end{aligned} \tag{5.35}$$

which can be cast in the notation adopted by Melro *et al.* [12] and later by Van der Meer [34]:

$$\frac{\partial\boldsymbol{\sigma}}{\partial\boldsymbol{\varepsilon}} = \beta\mathbf{I}_4^s+\Big(\phi-\frac{\beta}{3}\Big)\mathbf{II}-\rho\mathbf{S}^{\mathrm{tr}}\mathbf{I}-\chi\mathbf{S}^{\mathrm{tr}}\mathbf{S}^{\mathrm{tr}}-\psi\mathbf{I}\mathbf{S}^{\mathrm{tr}}-\omega\mathbf{S}^{\mathrm{tr}}\mathbf{E}-\xi\mathbf{I}\mathbf{E} \tag{5.36}$$

where $\mathbf{I}_4^s = 1/2(\delta_{ik}\delta_{jl}+\delta_{il}\delta_{jk})$ and the coefficients are given by:

$$\beta = \frac{2\widehat{G}}{\zeta_s} \qquad \phi = \frac{\widehat{K}}{\zeta_p}-\frac{4\alpha I_1^{\mathrm{tr}}(\sigma_c-\sigma_t)\widehat{V}\widehat{K}^2}{\mu\zeta_p^3} \tag{5.37}$$

$$\rho = \frac{36(\sigma_c-\sigma_t)\widehat{V}\widehat{K}\widehat{G}}{\mu\zeta_p\zeta_s^2} \qquad \chi = \frac{72\widehat{V}\widehat{G}^2}{\mu\zeta_s^4} \tag{5.38}$$

$$\psi = \frac{8\alpha I_1^{\mathrm{tr}}\widehat{V}\widehat{K}\widehat{G}}{\mu\zeta_p^2\zeta_s^2} \qquad \omega = \frac{6\widehat{V}\widehat{G}\widehat{H}}{\mu\zeta_s^2} \qquad \xi = \frac{2\alpha I_1^{\mathrm{tr}}\widehat{V}\widehat{K}\widehat{H}}{3\mu\zeta_p^2} \tag{5.39}$$

5.2.5. DAMAGE

The formulation for the damage model starts with the definition of a measure of material free energy [7, 35]:

$$\Psi = (1-d)\Big[\frac{1}{2}\int_0^t\int_0^t\frac{\partial\varepsilon_{ij}^{\mathrm{e}}(\tilde{t})}{\partial\tilde{t}}D_{ijkl}^{\mathrm{e}}(2t-\bar{t}-\tilde{t})\frac{\partial\varepsilon_{kl}^{\mathrm{e}}(\tilde{t})}{\partial\tilde{t}}d\bar{t}d\tilde{t}\Big]+\Psi^{\mathrm{h}} \tag{5.40}$$

where $0\leq d\leq 1$ is the single damage variable adopted in this work and the plastic harderning energy contribution Ψ^{h} has been ommited for compactness. It is worth mentioning that damage evolution is not linked to the development of plastic strains, as adopted by Krairi and Doghri [7], but rather evolves independently, similar to the approach adopted by Simo and Ju [35] and Melro *et al.* [12].

For this particular definition of free energy, the term within brackets can be readily identified as the thermodynamic force $Y = -\partial\Psi/\partial d$, and Eq. (5.40) may be rewritten as:

$$\Psi = (1-d)Y+\Psi^{\mathrm{h}} \tag{5.41}$$

In order to impose the second law of thermodynamics and assure that damage is an energetically irreversible process, the Clausius-Duhem inequality for the isothermal case is imposed:

$$\Xi = \sigma_{ij}\dot{\varepsilon}_{ij}-\dot{\Psi}\geq 0 \tag{5.42}$$

where Ξ is the mechanical energy dissipation. Following the derivation by Krairi and Doghri [7], the total derivative of the energy can be given by:

$$\dot{\Psi} = (1-d)\Big[\frac{1}{2}\int_0^t\int_0^t \frac{\partial \varepsilon^{\mathrm{e}}_{ij}(\bar{t})}{\partial \bar{t}}\frac{\partial D^{\mathrm{e}}_{ijkl}(2t-\bar{t}-\tilde{t})}{\partial t}\frac{\partial \varepsilon^{\mathrm{e}}_{kl}(\tilde{t})}{\partial \tilde{t}}d\bar{t}d\tilde{t} + \frac{\partial \varepsilon^{\mathrm{e}}_{ij}}{\partial t}\int_0^t D^{\mathrm{e}}_{ijkl}(t-\tilde{t})\frac{\partial \varepsilon^{\mathrm{e}}_{kl}(\tilde{t})}{\partial \tilde{t}}d\tilde{t}\Big] - Y\dot{d} + \dot{\Psi}^{\mathrm{h}} \tag{5.43}$$

Substituting Eq. (5.43) into the inequality of Eq. (5.42) and splitting the strains in elastic and plastic parts as shown in Eq. (5.1), the damaged stress-strain relationship is recovered:

$$\sigma_{ij} = (1-d)\int_0^t D^{\mathrm{e}}_{ijkl}(t-\tilde{t})\frac{\partial \varepsilon^{\mathrm{e}}_{kl}(\tilde{t})}{\partial \tilde{t}}d\tilde{t} \tag{5.44}$$

and the dissipation now reads:

$$\Xi = Y\dot{d} + (1-d)\Xi^{\mathrm{ve}} + \Xi^{\mathrm{p}} \tag{5.45}$$

where Ξ^{p} is the plastic dissipation:

$$\Xi^{\mathrm{p}} = \sigma_{ij}\dot{\varepsilon}^{\mathrm{p}}_{ij} - \dot{\Psi}^{\mathrm{h}} \tag{5.46}$$

and Ξ^{ve} is the viscoelastic dissipation, given by:

$$\Xi^{\mathrm{ve}} = -\frac{1}{2}\int_0^t\int_0^t \frac{\partial \varepsilon^{\mathrm{e}}_{ij}(\bar{t})}{\partial \bar{t}}\frac{\partial D^{\mathrm{e}}_{ijkl}(2t-\bar{t}-\tilde{t})}{\partial t}\frac{\partial \varepsilon^{\mathrm{e}}_{kl}(\tilde{t})}{\partial \tilde{t}}d\bar{t}d\tilde{t} \tag{5.47}$$

Adopting the concept of effective stress proposed by Simo and Ju [35], stresses in the undamaged portion of the material can be written as:

$$\widetilde{\sigma}_{ij} = \frac{\sigma_{ij}}{1-d} \tag{5.48}$$

Using this definition and Eqs. (5.6) and (5.44), the thermodynamic force and viscoelastic dissipation can be expressed in terms of effective stress as [7]:

$$Y = \frac{\widetilde{S}^{\infty}_{ij}\widetilde{S}^{\infty}_{ij}}{4G_{\infty}} + \frac{(\tilde{p}^{\infty})^2}{2K_{\infty}} + \sum_{s=1}^{n_s}\frac{\widetilde{S}^{\mathrm{ve}}_{ij,s}\widetilde{S}^{\mathrm{ve}}_{ij,s}}{4G_s} + \sum_{r=1}^{n_r}\frac{(\tilde{p}^{\mathrm{ve}}_r)^2}{2K_r} \tag{5.49}$$

$$\Xi^{\mathrm{ve}} = \sum_{s=1}^{n_s}\frac{\widetilde{S}^{\mathrm{ve}}_{ij,s}\widetilde{S}^{\mathrm{ve}}_{ij,s}}{2G_s g_s} + \sum_{r=1}^{n_r}\frac{(\tilde{p}^{\mathrm{ve}}_r)^2}{K_r k_r} \tag{5.50}$$

For numerical simulation purposes, the stress update of Eq. (5.44) is done in a time discrete manner in the same way as done in Eq. (5.6). The deviatoric and hydrostatic stresses used to compute Y and Ξ^{ve} are therefore the ones at time t_{n+1}.

In order to control the evolution of damage, an internal variable $r \in [1,\infty]$ is adopted to represent the size of a pressure-dependent paraboloidal fracture surface in effective stress space:

$$f_{\mathrm{d}}(\widetilde{\boldsymbol{\sigma}}, r) = \frac{3\widetilde{J}_2}{X_{\mathrm{c}}X_{\mathrm{t}}} + \frac{\widetilde{I}_1(X_{\mathrm{c}}-X_{\mathrm{t}})}{X_{\mathrm{c}}X_{\mathrm{t}}} - r \quad \Rightarrow \quad f_{\mathrm{d}}(\widetilde{\boldsymbol{\sigma}}, r) = \Lambda - r \tag{5.51}$$

which is similar to the yield surface of Eq. (5.12) but with the yield stresses substituted by the fracture strengths X_c and X_t.

In order to allow for rate-dependent damage initiation, the viscosity already included in the preceding viscoelastic/viscoplastic formulation is exploited by making the fracture surfaces X_t and X_c general functions of an accumulated energy measure Υ which allows them to shrink as the material dissipates energy:

$$X_t = X_t(\Upsilon) \qquad X_c = X_c(\Upsilon) \tag{5.52}$$

where Υ includes the dissipated energy and the energy stored by hardening:

$$\Upsilon(t) = \int_{\tau=0}^{t} \left[\Xi^{ve}(\tau) + \sigma_{ij}(\tau)\dot{\varepsilon}^{p}_{ij}(\tau) \right] \mathrm{d}\tau \tag{5.53}$$

which allows for damage initiation both in a quasi-static or low-cycle fatigue scenarios (dominated by Ξ^{p}) as well as in the high-cycle fatigue regime (dominated by Ξ^{ve}).

As this shrink is driven by both VE and VP contributions, the present formulation is a departure from the classic Chaboche-Lemaitre coupled plasticity-damage models that explicitly consider damage as a function of plastic strain [7, 36]. The advantage of the proposed approach lies in allowing for fracture initiation even after the backbone plastic yield surface is reached, for instance after ratcheting stabilizes during a fatigue test [3]. Such a link between damage activation and dissipated energy has also been put forward in literature both for quasi-static loading [7] and for fatigue [3, 4]. After damage initiates, the fracture surface is kept constant in order to control the amount of energy that is dissipated during damage development.

Using the classic loading-unloading conditions $\dot{r} \geq 0$; $f_d \leq 0$; $\dot{r} f_d = 0$, the value of r can be explicitly obtained:

$$r_{t_{n+1}} = \max\left\{1, \max_{0 \leq t \leq t_{n+1}} \Lambda_t\right\} \tag{5.54}$$

It is worth mentioning that, in contrast with the plasticity-coupled damage evolution models used by Krairi and Doghri [7] and Zhu and Sun [17], damage and plasticity evolve independently in the present formulation.

Having defined an evolution law for the internal variable r, it is necessary to relate it to damage variable d. Since it is often difficult to experimentally obtain fracture properties using axially loaded specimens due to structural instabilities such as necking [6] and kinetic energy dissipation due to rapid crack propagation, a damage evolution law with linear softening based on an uniaxial tensile test is adopted for simplicity [37]:

$$d = \begin{cases} \dfrac{\widetilde{\sigma}_f(\widetilde{\sigma}_{eq} - \widetilde{\sigma}_0)}{\widetilde{\sigma}_{eq}(\widetilde{\sigma}_f - \widetilde{\sigma}_0)}, & \widetilde{\sigma}_{eq} \leq \widetilde{\sigma}_f \\ 1, & \widetilde{\sigma}_{eq} > \widetilde{\sigma}_f \end{cases} \tag{5.55}$$

where $\widetilde{\sigma}_0$ and $\widetilde{\sigma}_f$ are the effective stress levels at the onset of damage and at complete failure, respectively:

$$\widetilde{\sigma}_0 = X_t \qquad \widetilde{\sigma}_f = \frac{2G^* \widehat{E}}{l_e X_t} \tag{5.56}$$

with $\widetilde{\sigma}_{\text{eq}}$ being an equivalent stress measure that allows the treatment of multiaxial stress states, $\widehat{E}$ the instantaneous Young's modulus computed from $\widehat{K}$ and $\widehat{G}$ and G^* an energy parameter related to the fracture energy G_{c} which is regularized using the finite element characteristic length l_{e} according to Bažant's crack band model [38]. Depending on the element type, l_{e} can be computed as:

$$l_{\text{e}}^{\text{2D}} = \frac{6}{\pi\sqrt[4]{3}}\sqrt{A_{\text{e}}} \qquad l_{\text{e}}^{\text{3D}} = \sqrt[3]{V_{\text{e}}} \tag{5.57}$$

where A_{e} and V_{e} are the element area and volume, respectively. These are computed as the sum of the integration weights of each element in a mesh, yielding the area in case the element is 2D or the volume in case a 3D element is used. Finally, the expression for $\widetilde{\sigma}_{\text{eq}}$ can be found by evaluating $\widetilde{I}_1$ and $\widetilde{J}_2$ for an uniaxial stress state, inserting them into Eq. (5.51) and imposing the loading condition $f_{\text{d}} = 0$:

$$\widetilde{\sigma}_{\text{eq}} = \frac{X_{\text{t}} - X_{\text{c}} + \sqrt{(X_{\text{t}} - X_{\text{c}})^2 + 4X_{\text{c}}X_{\text{t}}r}}{2} \tag{5.58}$$

It is important to acknowledge that adopting the free energy measure of Eq. (5.40) implicitly assumes that the Poisson's ratio will remain unchanged, leading to the aforementioned discrepancy between G^* and G_{c}. Furthermore, keeping a constant ratio may lead to undesired spurious hardening when a band of elements is softening while being constrained by bands of elastically unloading elements. For a non-viscous model that accounts for this effect, the reader is referred to [37]. Similar to the model by Melro *et al.* [12], plasticity is deactivated after initiation of damage in order to guarantee that the energy dissipated during the whole fracture process (*i.e.* up until the damage reaches $d = 1$) is equal to the input fracture toughness G^*

After updating r, the damage variable d and the stresses can be computed using Eqs. (5.55) and (5.44), respectively. In a numerical analysis context, it is also important to compute the algorithmic tangent stiffness matrix. Since plasticity is deactivated after damage starts, the total strain rate is fully elastic (*i.e.* $\dot{\varepsilon}_{kl} = \dot{\varepsilon}^{\text{e}}_{kl}$) and differentiation of Eq. (5.48) yields:

$$\frac{\partial \sigma_{ij}}{\partial \varepsilon_{kl}} = (1-d)\frac{\partial \widetilde{\sigma}_{ij}}{\partial \varepsilon^{\text{e}}_{kl}} - \frac{\partial d}{\partial r}\widetilde{\sigma}_{ij}\frac{\partial r}{\partial \varepsilon^{\text{e}}_{kl}} \tag{5.59}$$

which can be cast in a form similar to Eq. (5.36):

$$\frac{\partial \boldsymbol{\sigma}}{\partial \boldsymbol{\varepsilon}} = \beta \mathbf{I}_4^s + \left(\phi - \frac{\beta}{3}\right)\mathbf{II} - \rho\widetilde{\mathbf{S}}\mathbf{I} - \chi\widetilde{\mathbf{S}}\widetilde{\mathbf{S}} - \psi\mathbf{I}\widetilde{\mathbf{S}} \tag{5.60}$$

with coefficients:

$$\beta = 2(1-d)\widehat{G} \qquad \phi = (1-d)\widehat{K} - \frac{\widehat{D}\widehat{K}\widetilde{I}_1(X_{\text{c}} - X_{\text{t}})}{X_{\text{c}}X_{\text{t}}} \tag{5.61}$$

$$\rho = \frac{3\widehat{D}\widehat{K}(X_{\text{c}} - X_{\text{t}})}{X_{\text{c}}X_{\text{t}}} \qquad \chi = \frac{6\widehat{D}\widehat{G}}{X_{\text{c}}X_{\text{t}}} \qquad \psi = \frac{2\widehat{D}\widehat{G}\widetilde{I}_1}{X_{\text{c}}X_{\text{t}}} \tag{5.62}$$

where $\widehat{K} = K_\infty + K_{\text{ve}}(\Delta t)$, $\widehat{G} = G_\infty + G_{\text{ve}}(\Delta t)$ and $\widehat{D} = \partial d/\partial r$.

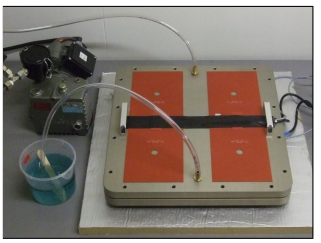
(a) Manufacturing


(b) Conditioning

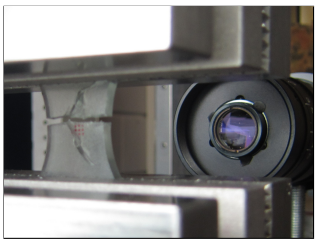
(c) Testing

Figure 5.3: Experimental procedure workflow.

5.2.6. WATER CONCENTRATION DEPENDENCY

In this work, the mechanical models of the preceding sections are complemented by a simple model for representing the effects of plasticization after water absorption on the mechanical properties of epoxy resins. This is of particular importance when accurate predictions of long-term material performance during service are sought. Experimental evidence suggests that physical processes such as plasticization promote significant changes in stiffness and strength after water absorption [9, 13, 39]. In the present formulation, such changes are represented by a single degradation factor d_{w}:

$$d_{\mathrm{w}} = \frac{d_{\mathrm{w}}^{\infty}}{c_{\infty}} c \tag{5.63}$$

where a linear dependency on the water concentration c is assumed and c_{∞} and d_{w}^{∞} are the concentration and the degradation level at saturation, respectively.

The degradation factor is then used to modify the properties as follows:

$$\widehat{K}_{\mathrm{w}} = (1-d_{\mathrm{w}})\widehat{K}, \quad \widehat{G}_{\mathrm{w}} = (1-d_{\mathrm{w}})\widehat{G} \tag{5.64}$$

$$\sigma_{\mathrm{c}}^{\mathrm{w}} = (1-d_{\mathrm{w}})\sigma_{\mathrm{c}}, \quad \sigma_{\mathrm{t}}^{\mathrm{w}} = (1-d_{\mathrm{w}})\sigma_{\mathrm{t}} \tag{5.65}$$

$$X_{\mathrm{c}}^{\mathrm{w}} = (1-d_{\mathrm{w}})X_{\mathrm{c}}, \quad X_{\mathrm{t}}^{\mathrm{w}} = (1-d_{\mathrm{w}})X_{\mathrm{t}}, \quad G_{\mathrm{w}}^{*} = (1-d_{\mathrm{w}})^2 G^{*} \tag{5.66}$$

where the viscoelastic relaxation times and the viscoplastic modulus and exponent are assumed to remain constant. The validity of such simplifications will be assessed in the next section. It is important to note that, in contrast with the damage formulation introduced in Section 5.2.5, the evolution of d_{w} is not irreversible and complete property recovery can be achieved through drying.

5.3. EXPERIMENTS

5.3.1. MANUFACTURING AND CONDITIONING

The epoxy resin considered in this work is the Momentive EPIKOTE RIMR 135 / EPIKURE RIMH 1366, with a ratio between monomer and hardener of 100:30 in weight. Panels with a thickness of 3 mm were manufactured through vaccuum infusion molding (Figure 5.3a), with a curing cycle consisting of 2 h at 30°C, 5 h at 50°C and 10 h at 70°C.

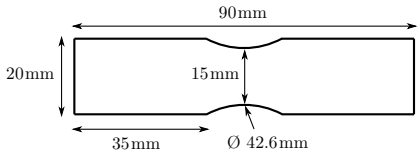

Figure 5.4: Planar dimensions of the specimens used for tension experiments (thickness is 3 mm).

Specimens were cut from the panels using a CNC milling machine in a custom-tailored short dog-bone shape that induces a stress concentration at a single point at mid-length (Fig. 5.4). Inducing strain localization at the center of the specimen in contrast to having a longer gauge length reduces the influence of material imperfections on the fracture behavior of the material and limits the influence of necking on its yield behavior by hindering its formation and propagation along the length. It is important to note that necking (in tension) and barreling (in compression) are structural instabilities which do not represent intrinsic material behavior and therefore do not generate useful data for model calibration [6]. Beam-shaped specimens used for Dynamic Mechanical Analysis (DMA) tests were also extracted from the panels.

After cutting, part of the specimens was kept in a desiccator at 50°C in vacuum until the time of testing in order to guarantee a moisture-free material state and achieve stabilization of molecular relaxation processes (physical aging) and post-curing [10], effectively creating a baseline material state with which results in aged samples will be compared. Another set of specimens was conditioned in demineralized water at 50°C (20°C lower than the saturated T_g) and tested after saturation at a concentration level of 3.2%. The conditioning setups are shown in Figure 5.3b.

5.3.2. MECHANICAL TESTS

For calibration of the viscoelastic moduli and relaxation times, DMA tests were conducted using a Netzsch DMA 242 E Artemis apparatus. Dry and saturated prismatic samples ($55 \times 10 \times 3\ mm^3$) were loaded in three-point bending with a deflection amplitude of 100 μm at multiple frequencies ranging from 0.1 Hz to 25 Hz, resulting in storage (E') and loss (E') moduli values as a function of frequency. The reported DMA results and calibrated viscoelastic properties were obtained using averaged measurements from two specimens.

Dry and saturated dog-bone specimens were tested in tension in an MTS universal test frame in displacement control at three different nominal rates (0.1 mm/min, 1 mm/min and 36 mm/min). Furthermore, dry specimens were tested in tension until failure with intermediate unloading branches and in stress-controlled fatigue with an R ratio of 0.1. For quasi-static and loading-unloading tests, two specimens were tested for each condition. For fatigue, four different stress levels were considered with 3 specimens being tested for each level. All tests were conducted at standard laboratory conditions (23°C, 50%RH). The dependency of resin properties on temperature will therefore not be treated in this work. For relevant investigations on the matter, the reader is referred to [6, 9].

Strain in the longitudinal direction was measured through micro video-extensometry

by stamping an array of dots covering an area of 1.8 x 1.8 mm^2 at the center of the specimens and tracking their positions throughout the test using a camera equipped with a microscope lens (Figure 5.3c). Each frame from the resultant videos was then assigned a time stamp in sync with the load and displacement signals from the test frame. Finally, the relative distances between the dots at the edges of the tracked area were used to compute the engineering strain ε_x. Since the constitutive features of interest are located in the low strain regime and measurements after global softening (strain localization) occurs are not used for calibration, the use of engineering strains was considered a reasonable approach.

5.3.3. MODEL CALIBRATION

VISCOELASTICITY AND MOISTURE DEPENDENCY

Calibration of viscoelastic properties was performed following Miled [40]. The dynamic moduli obtained through DMA can be expressed as a function of the oscillatory frequency ω and the Prony moduli and relaxation times:

$$E'(\omega) = E_\infty + \sum_{i=1}^{n_i} \frac{E_i \omega^2}{\frac{1}{\tau_i^2} + \omega^2} \tag{5.67}$$

$$E''(\omega) = \sum_{i=1}^{n_i} \frac{E_i \frac{\omega}{\tau_i}}{\frac{1}{\tau_i^2} + \omega^2} \tag{5.68}$$

The value for E_∞ and for the viscoelastic moduli E_i and relaxation times τ_i were fit to the data through a nonlinear least squares procedure. Finally, bulk and shear values were obtained under the assumption of a constant Poisson's ratio [7, 15, 40]:

$$G_\infty = \frac{E_\infty}{2(1+\nu)} \qquad G_i = \frac{E_i}{2(1+\nu)} \qquad g_i = \frac{\tau_i E_i}{G_i} \tag{5.69}$$

$$K_\infty = \frac{E_\infty}{3(1-2\nu)} \qquad K_i = \frac{E_i}{3(1-2\nu)} \qquad k_i = \frac{\tau_i E_i}{K_i} \tag{5.70}$$

with $\nu = 0.37$ obtained in previous experiments on the same material system [41].

Figure 5.5a shows the obtained values for storage (E') and loss (E") moduli of dry DMA samples, with the lines representing the best attained fit. The resultant properties, comprising 4 Prony elements, are shown in Table 5.1. Since the value for E_∞ was also obtained from the same fitting procedure, the resultant optimization problem features a large number of local minima. Therefore, the least squares procedure was performed multiple times starting from random values for the moduli and relaxation times until a final fit was chosen which featured good agreement in terms of loss modulus without significantly sacrificing precision in terms of storage modulus. The fitted model can describe the viscoelastic behavior reasonably well, with small deviations in storage modulus for frequencies between 0.1 Hz and 1 Hz and in loss modulus between 1 Hz and 4 Hz. The fitting procedure was also performed with a higher number of Prony elements, but the quality of the fit did not improve further.

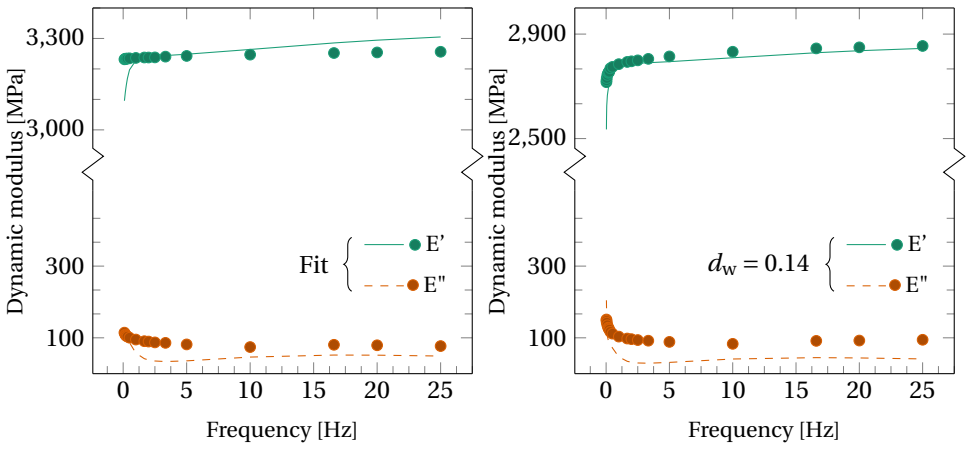

(a) Fitted dry response

(b) Degraded wet response

Figure 5.5: DMA results for dry and wet samples.

With this set of dry VE properties, another fitting procedure was performed in order to determine the moisture degradation factor d_w^∞ using DMA results from saturated samples. The results can be seen in Figure 5.5b. For the present material system, a value of $d_w^\infty = 0.14$ was found to correctly represent the material behavior after saturation without having to obtain another complete set of VE properties. It can be seen, however, that differences in loss moduli are slightly higher than for the dry case, suggesting that plasticization not only promotes stiffness degradation but also lead to a slightly more pronounced viscoelastic behavior. With the obtained degradation factor, no additional calibration is necessary in order to describe the behavior of the saturated resin.

VISCOPLASTICITY

For calibration of the viscoplastic properties, the model of Section 5.2 was implemented in an in-house finite element code using the Jem/Jive C++ library [42]. In order to obtain an accurate stress value at the center of the specimen from the force signal of the load cell, the complete geometry of the dog-bone was modeled and a stress concentration factor (K_σ) was computed in order to account for concentrations arising from the specimen geometry and the presence of grips:

$$K_\sigma = \frac{\sigma_y^{\text{num}} A}{F^{\text{num}}} \tag{5.71}$$

where A is the cross-sectional area at the center of the specimen and σ_y^{num} is the longitudinal stress at the same point resulting from the FE analysis when a prescribed displacement is applied to the top of the dog-bone and generates an internal force F_{num}. The experimental stress can then be estimated as:

$$\sigma_y^{\text{exp}} = K_\sigma \frac{F^{\text{exp}}}{A} \tag{5.72}$$

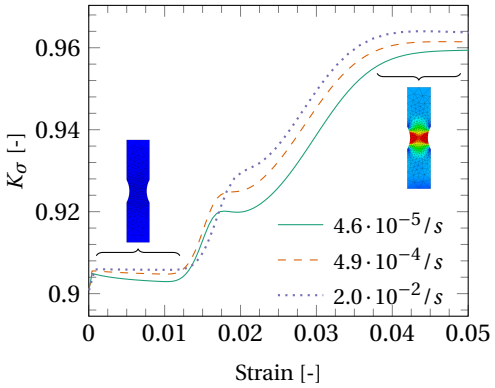

Figure 5.6: Evolution of stress concentration factor K_σ with strain for three different strain rates.

where F_{exp} is the force value measured by the load cell in the test frame.

The full dog-bone model was then substituted by a single-element model of the region where strain was measured. The experimental strain in the longitudinal direction was applied as a prescribed displacement and the fitting problem was cast as the minimization of the function:

$$f = \sum_t [\sigma_y^{\text{exp}}(t) - \sigma_y^{\text{num}}(t)]^2 \tag{5.73}$$

and solved using a nonlinear optimization algorithm.

In order to take into account the difference in yield behavior in tension and compression, a constant σ_c/σ_t ratio of 1.25 was considered based on previously obtained experimental results (Section 4.3). Furthermore, since only longitudinal strains were used in the current calibration procedure, the value for $\nu_p = 0.32$ was also adopted from Chapter 4.

It is important to note that, due to the development of plastic strains at different rates for different parts of the specimen, K_σ is not constant but rather depends on the shape of the yield surfaces, the test speed and the current strain at the center of the specimen. Therefore, an iterative fitting procedure was performed: The experimental stresses were first obtained under the assumption of purely viscoelastic behavior. With the resultant VP properties, two additional calibration rounds were performed while updating the factors between each of them. Figure 5.6 shows the final stress concentration curves for the three different strain rates used for VP calibration as a function of strain at the center of the specimen.

Figure 5.7a shows the stress-strain curves obtained experimentally for each strain rate. Curves from different specimens tested in the same conditions exhibit low variability, similar to previous observations in the same system (Section 2.3) and suggesting that the performed tests have an acceptable degree of reproducibility. The portions of the curves depicted in gray refer to stress-train data obtained after the experimental load peak and were therefore not used for calibration since they may not represent the intrinsic constitutive behavior of the material [6]. As expected, the present epoxy system features nonlinear stress-strain behavior, in particular at strains higher than 0.02,

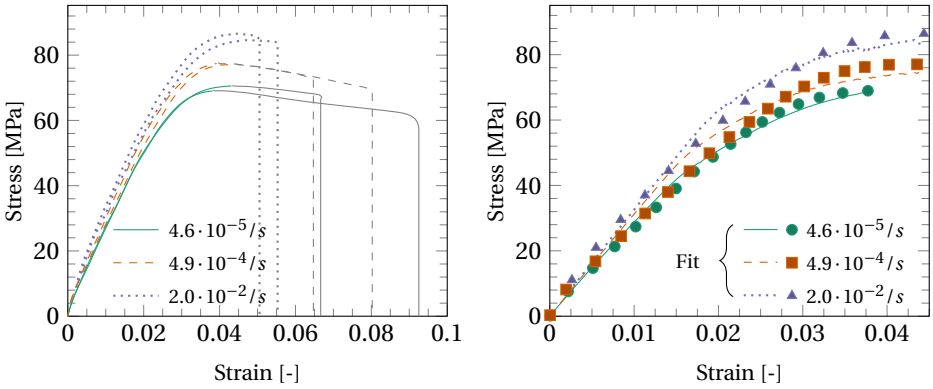

(a) Experimental results

(b) Fitted model

Figure 5.7: Results for dry quasi-static tension in three different strain rates. Grayed lines indicate the reponse after strain localization and marks represent experimental results.

exhibits strain-rate dependency and fractures at relatively low strain levels, with higher failure strains observed for slower tests.

Using a single curve for each strain rate, an exponential yield surface was fitted by determining the coefficients c_1 to c_5 in:

$$\sigma_t = c_1 + c_2 e^{\varepsilon_{eq}^p / c_3} + c_4 e^{\varepsilon_{eq}^p / c_5} \tag{5.74}$$

as well as the VP parameters η_p and m_p, with the resultant properties shown in Table 5.1. Figure 5.7b shows the fitted curves together with their experimental counterparts. It can be seen that a good agreement was obtained for all rates, with only small deviations noted for the intermediate rate test at low strains.

FRACTURE

The first step in calibrating the damage model was fixing an upper bound for X_t, since rate dependency arises naturally as the material dissipates energy and the fracture surface shrinks. In view of the available test data, a pragmatic choice would be the peak load for the highest rate test (83.8 MPa). Naturally, bounding X_t in this manner will result in early failure for the highest strain rate test since the energy dissipation at the peak load would not be accounted for. Nevertheless, since failure occurs after the peak load for all strain rates, energy dissipation at the onset of fracture is not well defined and thus the practical choice of $X_t = 83.8$ MPa was adopted.

With a value for X_t, the fracture energy $G^* = 1.9$ N/mm was computed using Eq. (5.56), leading to a vertical softening branch for $l_e = 1.8\,mm$ failing at the upper bound of X_t. It is important to note that the sudden failure observed in the experiments is in fact a dynamic event for which part of the energy will be dissipated as kinetic energy. Since inertia effects are not taken into account in the energy expression of Eq. (5.40), the calibrated value of G^* should be interpreted with caution and cannot be seen as a fracture energy measurement.

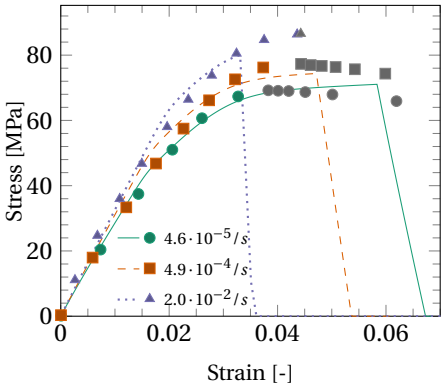

Figure 5.8: Model response of the dry material in tension including damage. Marks represent experimental results and gray marks indicate the response after strain localization.

The last step in the calibration process was the definition of X_t as a function of the accumulated dissipated energy measure Υ. As previously mentioned, the energy dissipation at failure is not well defined in quasi-static tests since it takes place after the global peak load and is therefore potentially influenced by strain localization and necking. The dissipation was therefore obtained from the stress-controlled fatigue test with the highest peak load (and thus the shortest duration). Since only one condition was used for calibration, a linear X_t decay was adopted:

$$X_t = 83.8 - a\Upsilon \qquad \text{with} \qquad a = \frac{83.8 - \sigma_{max}}{\Upsilon_{break}} \tag{5.75}$$

where σ_{max} = 74.9 MPa for the highest tested fatigue load and Υ_{break} was obtained by running the model for a number of load cycles equal to the average cycles at break obtained for the 3 specimens tested at this stress level.

The stress-strain response of the calibrated damage model can be seen in Figure 5.8. As expected, the failure strain for the curve with the highest strain rate was not correctly captured, which also caused the peak load to be slightly (approximately 2 MPa) lower. Failure for the other two strain rates occurred at higher strain levels, following the trend observed experimentally. It is interesting to note that since the adopted rheological model couples VE and VP (σ_{ij}^{hist} helps drive plastic strain development), the test with the highest strain ratio actually features a higher amount of plastic strain than the slower ones, leading to a higher energy dissipation and consequently to failure at a lower strain level.

5.3.4. MODEL PREDICTIONS

In this section, the model is used to predict material behavior in loading scenarios not used for calibration, including quasi-static tensile tests of saturated specimens at different strain rates, loading-unloading tests with increasing strain amplitudes and stress-controlled fatigue tests. The predictions are compared with further experimental results and the model performance is discussed.

Viscoelasticity				
K_∞ [MPa]	3205			
G_∞ [MPa]	912			
K_r [MPa]	125	182	625	143
G_s [MPa]	36	52	178	41
k_r [s]	$4.16 \cdot 10^{-2}$	$2.30 \cdot 10^{0}$	$4.22 \cdot 10^{1}$	$3.11 \cdot 10^{4}$
g_s [s]	$1.46 \cdot 10^{-1}$	$8.08 \cdot 10^{0}$	$1.48 \cdot 10^{2}$	$1.09 \cdot 10^{5}$
Viscoplasticity				
σ_t [MPa]	$64.80 - 33.6\mathrm{e}^{-\epsilon^\mathrm{p}_\mathrm{eq}/0.003407} - 10.21\mathrm{e}^{-\epsilon^p_\mathrm{eq}/0.06493}$			
σ_c [MPa]	$81.0 - 42.0\mathrm{e}^{-\epsilon^\mathrm{p}_\mathrm{eq}/0.003407} - 12.77\mathrm{e}^{-\epsilon^p_\mathrm{eq}/0.06493}$			
η_p [s]	$3.49 \cdot 10^{12}$			
m_p [-]	7.305			
ν_p [-]	0.32			
Damage				
X_t [MPa]	$83.8 - 5.99\,\Upsilon$			
X_c [MPa]	$104.7 - 7.48\,\Upsilon$			
G^* [N/mm]	1.9			
Hygrothermal aging				
d_w^∞ [-]	0.14			
c_∞ [%]	3.2			

Table 5.1: Calibrated material properties.

WATER CONCENTRATION INFLUENCE

Figure 5.9a shows quasi-static tensile test results for specimens saturated in water at 50°C. Similar to dry specimens, results for all strain rates featured low scatter both in the elastic and plastic regimes as well as in the failure strain. Once again tests with the highest rate failed at higher stresses but lower strains, with only limited strain localization. Plasticization due to interaction with water molecules resulted in lower peak stresses for all rates. Interestingly enough, the failure strains remained similar to the ones from dry specimens, although it is difficult to determine the exact stress or strain at failure due to the occurrence of strain localization.

Using the dry VE/VP properties and the value for d_w^∞ calibrated from DMA tests, the saturated VE/VP response was predicted and is shown together with the experimental pre-peak curves in Figure 5.9b. The model shows excellent agreement with experiments for all strain rates, suggesting that the simple degradation model of Section 5.2.6 can effectively describe the behavior of the saturated resin in both VE and VP regimes, even though the viscoplastic parameters remain intact and only the backbone yield surface

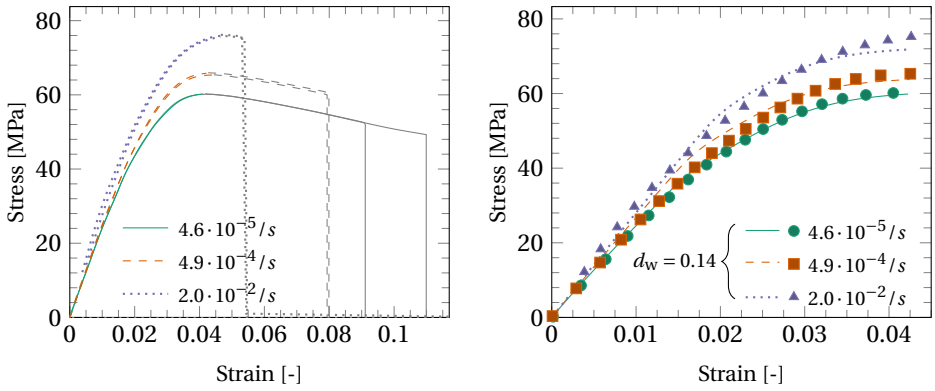

(a) Experimental results

(b) Degraded model.

Figure 5.9: Results for saturated quasi-static tension specimens. Gray lines indicate the response after strain localization. Marks represent experimental results on saturated specimens.

is degraded. Nevertheless, the present results are limited to quasi-static loading and further tests need to be performed in order to assess the performance of the model in predicting the fatigue behavior of saturated specimens.

LOADING-UNLOADING TESTS

The next loading scenario is a revisit of the loading-unloading test of Figure 5.1. Specimens were loaded in displacement control at 1 mm/min (strain rate of $4.9 \cdot 10^{-4}$/s) and unloaded at intermediate steps. A special test frame control procedure was then used in order to trigger a new loading phase when the force reached zero. Each loading cycle stopped at a linearly increasing maximum strain value until final failure. The resultant stress-strain curve can be seen in Figure 5.10a and the model prediction in Figure 5.10b.

From the numerical response, it can be seen that all time-dependent phenomena mentioned in Section 5.1.1 are now present: Non-linear reloading branches that do not meet the original curve, hysteresis during unloading and failure at slightly lower strain and stress when compared to the monotonic response.

However, comparing the model prediction with the experimental curve makes an important shortcoming of the model evident. Even though the stresses at the unloading points are similar for the two curves, the model grossly overestimates the amount of plastic strain at the points of zero stress. The source of this discrepancy lies in the way by which the nonlinear part of the stress-strain response is modeled. While the load-displacement response of Figure 5.1 suggests the presence of significant pre-localization plastic strains, Figure 5.10a suggests that the greater part of the nonlinearity is in fact viscoelastic. This observation also helps to explain the differences in hysteresis area between model and experiments.

In order to confirm the existence of pre-localization plastic strains and rule out the possibility of a purely viscoelastic response, the same test was repeated but including rest periods of one minute at zero stress before reloading. Figure 5.11 shows the strain response obtained during one such rest period. Despite the presence of measurement

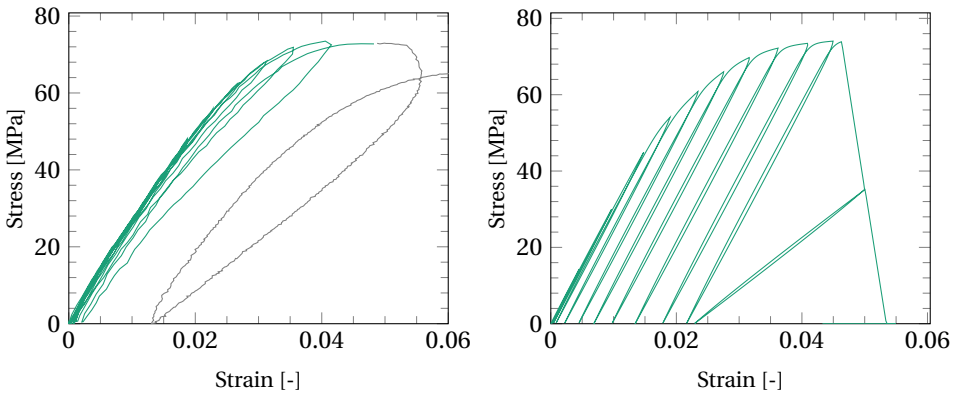

(a) Experimental results (b) Numerical prediction

Figure 5.10: Loading-unloading test with increasing amplitude (dry). Gray lines indicate the response after strain localization.

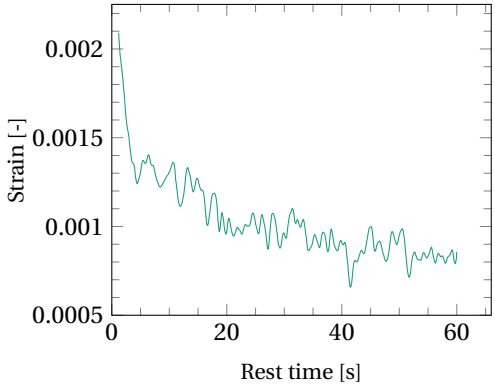

Figure 5.11: Strain relaxation after unloading from $\epsilon_{\text{amp}} = 0.035$, indicating the presence of permanent strains.

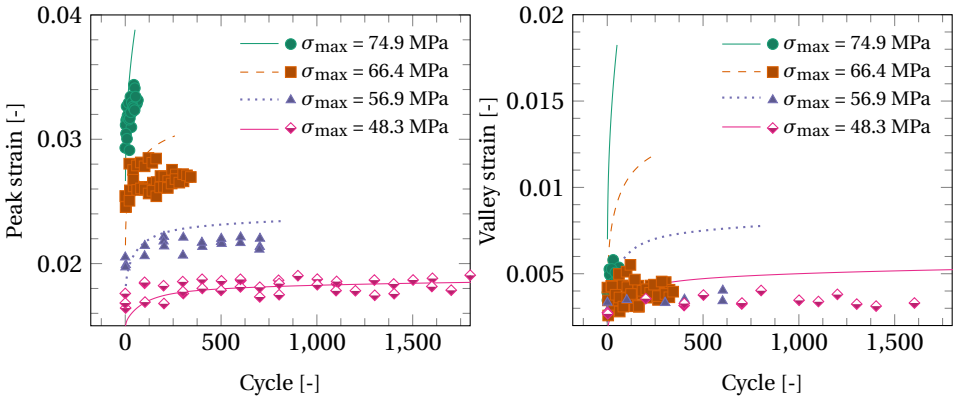

(a) Peak strains (b) Valley strains

Figure 5.12: Experimental (marks) and numerical (lines) strains for different load levels (dry).

5

noise, an asymptotic relaxation process towards a non-zero strain value can be clearly identified. It is concluded that the nonlinear behavior consists of a complex combination of nonlinear viscoelasticity and viscoplasticity.

It is important to note that either a purely VE model like the one proposed by Xia *et al.* [43] or the present VE/VP model are able to reproduce the quasi-static curves from the previous section, and the complex constitutive nature of the resin would be overlooked if no loading-unloading tests were performed. It is also interesting to note that even though the hysteresis area is underestimated by the model, the added plastic dissipation helps to diminish the difference in total dissipation and the damage part is activated at the same strain level at which localization starts in the experiments. Nevertheless, the inclusion of nonlinear viscoelasticity [9, 43] would improve the predictive capabilities of the present model.

FATIGUE TESTS

The last loading scenario consists of stress-controlled fatigue tests at four different stress levels with an R-ratio ($\sigma_{min}/\sigma_{max}$) of 0.1 and a nominal strain rate of $2.0 \cdot 10^{-2}$/s. Since stress is controlled, VE creep and VP evolution become manifest in the form of ratcheting (*i.e.* strain accumulation with fatigue cycles). It is therefore interesting to track the evolution of strains at the peak and valley loads with the number of cycles. Figures 5.12a and 5.12b show strains at peak and valley stress, respectively, for the four stress levels, with lines representing model predictions. Since the model does not take into account the nonlinear viscoelastic behavior exhibited by the material, both peak and valley strains were overestimated. This overestimation is particularly significant for valley strains, similar to the mismatch in permanent strain observed in the loading-unloading tests. As σ_{max} decreases, the model predictions become more accurate because less plastic strain develops.

Figures 5.13a and 5.13b show experimental and numerical curves for a complete fatigue test with σ_{max} = 74.9 MPa. The experimental response showed failure with no no-

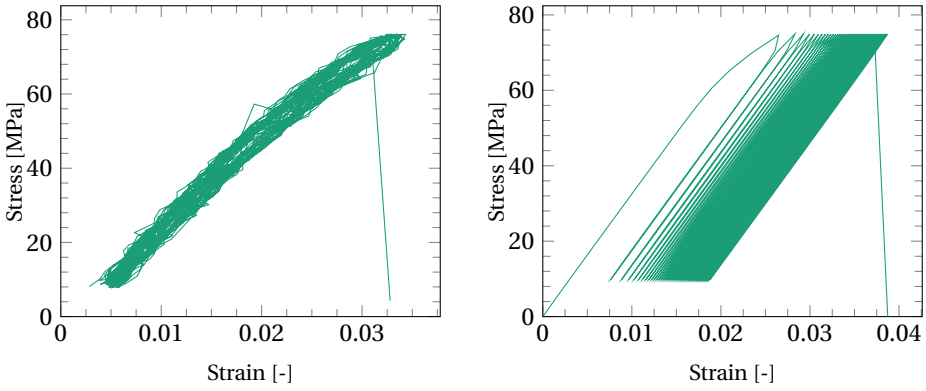

(a) Experimental response

(b) Model prediction

Figure 5.13: Fatigue stress-strain curves for σ_{max} = 74.9MPa (dry).

ticeable loss of stiffness and featured a large hysteresis area that is partly obscured by the ratcheting strain that develops with the number of cycles. The numerical response showed a significantly larger ratcheting strain, as the model relies on plastic strains in order to correctly represent the nonlinear stress-strain response.

Such differences in energy dissipation can be clearly seen in Figure 5.14, which shows stress-strain snapshots of a fatigue test at σ_{max} = 48.3 MPa after 1300 load cycles, when the material is close to breaking. A large hysteresis loop can be seen in the experimental curve, while the numerically predicted area is significantly smaller. On the other hand, the model features a larger amount of viscoplastic dissipation, as evidenced by the higher valley strain. If the hypothesis that energy dissipation promotes initiation of fracture is valid, it is reasonable to suppose that the erroneous viscoelastic dissipation predicted by the model will in part be compensated by its overestimated viscoplastic dissipation.

Using the fracture surface degradation calibrated with the tests at σ_{max} = 74.9 MPa, the model was used to predict fatigue life at the three other stress levels, with results shown in Figure 5.15. The model gives reasonable estimates for the number of cycles to failure for all stress levels, suggesting that the dissipation-driven fracture initiation hypothesis is a valid approach for the high- to medium-cycle fatigue regimes. A loss of accuracy can be expected for lower stress levels as the viscoelastic dissipation will tend to dominate the material response and the present model is not able to reproduce this in a satisfactory manner. Furthermore, the role of dissipative mechanisms on fracture initiation might change in the high-cycle regime. More experimental data and model development are therefore necessary.

5.4. CONCLUSIONS

Based on preliminary experiments on an epoxy resin, a number of time-dependent phenomena were identified which are not taken into account by conventional elastoplastic models but may nevertheless play an important role in the long-term mechanical re-

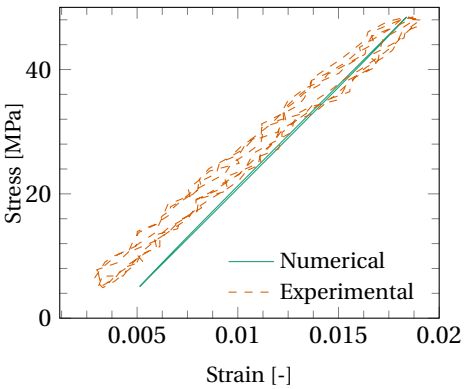

Figure 5.14: Dry material response after 1300 cycles with $\sigma_{max} = 48.3$MPa.

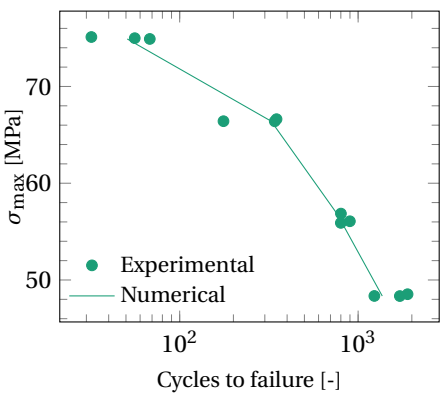

Figure 5.15: Experimental S/N curve and model prediction for dry specimens.

sponse of epoxy resins, such as hysteresis and strain-rate dependency. In this work, a viscoelastic/viscoplastic model with continuum damage was developed that can reproduce such phenomena.

The model consists of a parallel array of elastic Maxwell elements arranged in series with a pressure-dependent viscoplastic element. The integral viscoelastic stress update was presented in a time-discrete manner suitable for finite element implementation. For viscoplasticity, a Perzyna-type function was included in a non-associative plasticity model with general-shape yield functions. A pressure-dependent continuum damage model was developed for which the fracture surfaces are made to shrink as the material dissipates energy. Finally, a simple degradation model was presented for polymer degradation through plasticization.

The viscoelastic and viscoplastic properties were calibrated using DMA tests in bending and quasi-static monotonic tests in tension at different strain rates. The damage model was calibrated using static tests at a single strain rate and a short cyclic test with controlled stress. The calibrated model was able to accurately reproduce the rate-dependent material response both in plasticity and fracture, with good predictions for failure strain and maximum stress. The response of the water-saturated material at different rates was also predicted with excellent accuracy. For cyclic tests, the model was found inadequate in its representation of the observed nonlinear stress-strain response which was modeled as plastic but is in fact a combination of plasticity and nonlinear viscoelasticity.

REFERENCES

[1] I. B. C. M. Rocha, F. P. van der Meer, S. Raijmaekers, F. Lahuerta, R. P. L. Nijssen, and L. J. Sluys, *Numerical/experimental study of the monotonic and cyclic viscoelastic/viscoplastic/fracture behavior of an epoxy resin,* Under Review (2019).

[2] E. Kontou, *Viscoplastic deformation of an epoxy resin at elevated temperatures,* Journal of Applied Polymer Science **101**, 2027 (2006).

[3] G. Tao and Z. Xia, *Ratcheting behavior of an epoxy polymer and its effect on fatigue life,* Polymer Testing **26**, 451 (2007).

[4] G. Tao and Z. Xia, *Mean stress/strain effect on fatigue behavior of an epoxy resin,* International Journal of Fatigue **29**, 2180 (2007).

[5] B. Fiedler, M. Hojo, S. Ochiai, K. Schulte, and M. Ando, *Failure behavior of an epoxy matrix under different kinds of static loading,* Composites Science and Technology **61**, 1615 (2001).

[6] X. Poulain, A. A. Benzerga, and R. K. Goldberg, *Finite-strain elasto-viscoplastic behavior of an epoxy resin: Experiments and modeling in the glassy regime,* International Journal of Plasticity **62**, 138 (2014).

[7] A. Krairi and I. Doghri, *A thermodynamically-based constitutive model for thermoplastic polymers coupling viscoelasticity, viscoplasticity and ductile damage,* International Journal of Plasticity **60**, 163 (2014).

[8] M. N. Silberstein and M. C. Boyce, *Constitutive modeling of the rate, temperature, and hydration dependent deformation response of nafion to monotonic and cyclic loading,* **195**, 5692 (2010).

[9] C. Yu, G. Kang, and K. Chen, *A hygro-thermal-mechanical coupled cyclic constitutive model for polymers with considering glass transition,* International Journal of Plasticity **89**, 29 (2017).

[10] G. M. Odegard and A. Bandyopadhyay, *Physical aging of epoxy polymers and their composites,* Journal of Polymer Science: Part B **49**, 1695 (2011).

[11] R. Polanský, V. Mantlík, P. Prosr, and J. Sušír, *Influence of thermal treatment on the glass transition temperature of thermosetting epoxy laminate,* Polymer Testing **28**, 428 (2009).

[12] A. R. Melro, P. P. Camanho, F. M. Andrade Pires, and S. T. Pinho, *Micromechanical analysis of polymer composites reinforced by unidirectional fibres: Part I - Constitutive modelling,* International Journal of Solids and Structures **50**, 1897 (2013).

[13] F. Naya, C. González, C. S. Lopes, S. van der Veen, and F. Pons, *Computational micromechanics of the transverse and shear behaviour of unidirectional fiber reinforced polymers including environmental effects,* Composites: Part A (2016).

[14] X. Bai, M. A. Bessa, A. R. Melro, P. P. Camanho, L. Guo, and W. K. Liu, *High-fidelity micro-scale modeling of the thermo-visco-plastic behavior of carbon fiber polymer matrix composites,* Composite Structures **134**, 132 (2015).

[15] S. Haouala and I. Doghri, *Modeling and algorithms for two-scale time homogenization of viscoelastic-viscoplastic solids under large numbers of cycles,* International Journal of Plasticity **70**, 98 (2015).

[16] C. Yu, G. Kang, F. Lu, Y. Zhu, and C. K., *Viscoelastic-viscoplastic cyclic deformation of polycarbonate polymer: experiment and constitutive model,* Journal of Applied Mechanics **83**, 1 (2016).

[17] H. Zhu and L. Sun, *A viscoelastic-viscoplastic damage constitutive model for asphalt mixtures based on thermodynamics,* International Journal of Plasticity **40**, 81 (2002).

[18] H. J. Eyring, *Viscosity, plasticity, and diffusion as examples of absolute reaction rates,* The Journal of Chemical Physics **4**, 283 (1936).

[19] T. A. Tervoort, E. T. J. Klompen, and L. E. Govaert, *A constitutive equation for the elasto-viscoplastic deformation of glassy polymers,* **40**, 779 (1996).

[20] T. A. Tervoort, R. J. M. Smit, W. A. M. Brekelmans, and L. E. Govaert, *A constitutive equation for the elasto-viscoplastic deformation of glassy polymers,* Mechanics of Time-Dependent Materials **1**, 269 (1998).

[21] L. E. Govaert, H. J. Schellens, H. J. M. Thomassen, R. J. M. Smit, L. Terzoli, and T. Peijs, *A micromechanical approach to time-dependent failure in off-axis loaded polymer composites,* Composites: Part A **32**, 1697 (2001).

[22] A. S. Argon, *A theory for the low-temperature plastic deformation of glassy polymers,* Philosophical Magazine **28**, 839 (1973).

[23] M. C. Boyce and E. M. Arruda, *Constitutive models of rubber elasticity: A review,* Rubber Chemistry and Technology **73**, 504 (2000).

[24] E. van der Giessen, *Localized plastic deformations in glassy polymers,* European Journal of Mechanics - A/Solids **16**, 87,106 (1997).

[25] L. Anand, N. M. Ames, V. Srivastava, and S. A. Chester, *A thermo-mechanically coupled theory for large deformations of amorphous polymers. Part I: Formulation,* International Journal of Plasticity **25**, 1474 (2009).

[26] J. L. Bouvard, D. K. Francis, M. A. Tschopp, E. B. Marin, D. J. Bammann, and M. F. Horstemeyer, *An internal state variable material model for predicting the time, thermomechanical, and stress state dependence of amorphous glassy polymers under large deformation,* International Journal of Plasticity **42**, 168 (2013).

[27] A. D. Drozdov and J. C. Christiansen, *Viscoelasticity and viscoplasticity of semicrystalline polymers: Structure-property relations for high-density polyethylene,* Computational Materials Science **39**, 729 (2007).

[28] A. D. Drozdov, *Cyclic viscoelastoplasticity and low-cycle fatigue of polymer composites,* International Journal of Solids and Structures **48**, 2026,2040 (2011).

[29] A. D. Drozdov, *Multi-cycle viscoplastic deformation of polypropylene,* Computational Materials Science **50**, 1991 (2011).

[30] C. Miehe, S. Göktepe, and J. Méndez Diez, *Finite viscoplasticity of amorphous glassy polymers in the logarithmic strain space,* International Journal of Solids and Structures **46**, 181 (2009).

[31] S. Kweon and A. A. Benzerga, *Finite element implementation of a macromolecular viscoplastic polymer model,* International Journal for Numerical Methods in Engineering **94**, 895 (2013).

[32] C. Oskay and J. Fish, *Fatigue life prediction using 2-scale temporal asymptotic homogenization,* International Journal for Numerical Methods in Engineering **61**, 329 (2004).

[33] R. Crouch, C. Oskay, and J. Fish, *Multiple spatio-temporal scale modeling of composites subjected to cyclic loading,* Computational Mechanics **51**, 93 (2013).

[34] F. P. van der Meer, *Micromechanical validation of a mesomodel for plasticity in composites,* European Journal of Mechanics - A/Solids **60**, 58 (2016).

[35] J. C. Simo and J. W. Ju, *Strain- and stress-based continuum damage models - I. Formulation,* International Journal of Solids and Structures **23**, 821 (1987).

[36] J. Lemaitre, *Coupled elasto-plasticity and damage constituive equations,* Computer Methods in Applied Mechanics and Engineering **51**, 31 (1985).

[37] A. Arefi, F. P. van der Meer, M. R. Forouzan, and M. Silani, *Formulation of a consistent pressure-dependent damage model with fracture energy as input,* Composite Structures **201**, 208 (2018).

[38] Z. P. Bažant and B. Oh, *Crack band theory for fracture of concrete,* Matériaux et Construction **16**, 155 (1983).

[39] P. Davies, F. Mazéas, and P. Casari, *Sea water aging of glass reinforced composites: Shear behaviour and damage modelling,* Journal of Composite Materials **35**, 1343 (2000).

[40] B. Miled, *Coupled viscoelastic-viscoplastic modeling of homogeneous and reinforced thermoplastic polymers* (PhD thesis, Université Catholique de Louvain, 2011).

[41] I. B. C. M. Rocha, S. Raijmaekers, R. P. L. Nijssen, F. P. van der Meer, and L. J. Sluys, *Hygrothermal ageing behaviour of a glass/epoxy composite used in wind turbine blades,* Composite Structures **174**, 110 (2017).

[42] Jive - Software development kit for advanced numerical simulations, http://jive.dynaflow.com, accessed: 04-03-2018.

[43] Z. Xia, Y. Hu, and F. Ellyin, *Deformation behavior of an epoxy resin subject to multiaxial loadings. Part ii: Constitutive modeling and predictions,* Polymer Engineering and Science **43**, 734 (2003).

6

ACCELERATION TECHNIQUES FOR CYCLIC MICROMECHANICAL ANALYSIS

'Wait', he says.
Do I look like a waiter?

Kefka, *Final Fantasy VI*

6.1. INTRODUCTION

The multiscale/multiphysics numerical framework of Chapter 4 involves solving an independent microscopic mesh for each integration point of the macroscopic model. This results in an exceedingly high computational cost, in particular if large micromodels with dense finite element meshes are employed or cyclic loads are treated. To make matters worse, using material models with time-discrete response such as the one formulated in Chapter 5 at the microscale requires small time steps in order to be accurate. In order to arrive at a framework suitable for predicting material behavior after long-term environmental exposure combined with cyclic mechanical loads, it is thus necessary to seek techniques to accelerate the solution of these microscopic boundary-value problems without sacrificing the accuracy of the homogenized material response needed at the macroscale analysis.

One approach for acceleration is based on recognizing that prediction of the cyclic behavior in polymers is a multiscale problem in time [2–4]. This multiscale problem can

Apart from minor changes to its introductory section, this chapter was integrally extracted from [1].

be solved efficiently through a so-called Time Homogenization process by explicitly separating the fast response inside a load cycle from the long-term material response and solving the problem for each time scale in isolation. Another approach relies on constructing Reduced-Order Models (ROM) from the original high-fidelity model. The most popular reduction technique involves representing the solution of the equilibrium problem in terms of a lower-dimensional solution basis, similar to the Ritz method [5]. Such reduced basis is constructed by gathering snapshots of the high-fidelity model response and applying a dimensionality reduction technique such as the Proper Orthogonal Decomposition (POD) [6–8]. This reduction in the size of the global equilibrium equations can be coupled with a so-called *hyper-reduction* technique in order to minimize the number of constitutive model evaluations, such as the Discrete Empirical Interpolation Method (DEIM) [9], the Missing Point Estimation Method [10], Gappy Data reconstruction [11] and Empirical Cubature Method [12–14]. Other reduction strategies can also be found in literature, such as self-consistent clustering [15], wavelet-based reduction [16], nonuniform transformation field analysis [17, 18], which attempt to overcome the drawbacks of classic reduction by projection. Lastly, a number of adaptive strategies have been proposed that expand upon the classic POD by adding new basis vectors or performing corrections to the reduced basis during the analysis [6] as well as employing domain decomposition techniques to fully solve the equilibrium problem only in strain localization zones while the rest of the domain is solved in a reduced space [19, 20].

In this chapter, a number of acceleration techniques are explored and applied to the micromechanical analysis of fiber-reinforced composites. The micromodels consist of linear-elastic fibers and a viscoelastic/viscoplastic resin. Time Homogenization (TH) is used to decompose the original equilibrium problem into macro- and microchronological parts. A modified return mapping algorithm incorporating time averaging is proposed in order to compute the plastic strain increment after a complete load cycle. Proper Orthogonal Decomposition (POD) is used to reduce the number of degrees of freedom of the problem and a hyper-reduction step based on the Empirical Cubature Method (ECM) is performed. A novel adaptive analysis scheme combining features of TH and POD is proposed which avoids the need for an offline training phase. Lastly, an efficient technique for recovering stresses and material history at all integration points is proposed by combining a Gappy Data least-squares reconstruction with a clustering algorithm typically used in machine learning and data mining applications. The performance of each acceleration ingredient is assessed in terms of speed-up and accuracy of the approximated solutions and an adaptive analysis scheme combining both reduced and unreduced steps is proposed.

6.1.1. MATHEMATICAL NOTATION

In this chapter, both index notation and matrix notation are used to represent tensors and vectors. When index notation is used, the indices i, j, k, l range from one to the number of spatial dimensions of the problem being solved. In products between two entities in index notation, summation over repeated indices is implied. In matrix notation, vectors are represented by boldfaced lower-case symbols while matrices are given by boldfaced upper-case symbols. When representing stresses and strains in matrix notation, the use of Voigt notation is implied.

6.2. MICROMECHANICAL PROBLEM

This chapter focuses on the micromechanical modeling of fiber-reinforced polymer composites. The material microstructure consists of unidirectional fibers and surrounding resin. The fibers are modeled as linear elastic and the resin as a viscoelastic/viscoplastic solid. In this section, the constitutive model for the resin will be briefly presented in its original form in preparation for applying the time homogenization strategy of Section 6.3.

6.2.1. VISCOELASTICITY

In the present model, an additive decomposition of the total strain ε_{ij} in viscoelastic (VE) and viscoplastic (VP) parts is adopted:

$$\varepsilon_{ij} = \varepsilon^{\mathrm{e}}_{ij} + \varepsilon^{\mathrm{p}}_{ij} \tag{6.1}$$

where the superscripts e and p refer to elastic and plastic contributions, respectively. The stresses σ_{ij} at time t_n are computed from the viscoelastic strains in an integral form through the Boltzmann superposition principle:

$$\sigma_{ij}(t_n) = D^{\infty}_{ijkl}\varepsilon^{\mathrm{e}}_{kl}(t_n) + \sum_{u=1}^{n_u} p^{\mathrm{ve}}_u(t_n)\delta_{ij} + \sum_{v=1}^{n_v} s^{\mathrm{ve}}_{v,ij}(t_n) \tag{6.2}$$

where D^{∞}_{ijkl} is the long-term stiffness tensor and p^{ve} and $s^{\mathrm{ve}}_{s,ij}$ are respectively the hydrostatic and deviatoric viscous stress contributions of a Prony series of Maxwell elements comprising n_u bulk elements and n_v shear elements. The long-term stiffness can be written as:

$$D^{\infty}_{ijkl} = G_{\infty}(\delta_{ij}\delta_{kl} + \delta_{il}\delta_{jk}) + \Big(K_{\infty} - \frac{2}{3}G_{\infty}\Big)\delta_{ij}\delta_{kl} \tag{6.3}$$

with G_{∞} and K_{∞} being the long-term shear and bulk moduli, respectively. The viscoelastic contributions of each Prony element are computed in a time-discrete form as:

$$p^{\mathrm{ve}}_u(t_n) = \exp\Big(\frac{-\Delta t}{k_u}\Big)p^{\mathrm{ve}}_u(t_{n-1}) + K_u\Big[1 - \exp\Big(\frac{-\Delta t}{k_u}\Big)\Big]\frac{k_u}{\Delta t}\big(\varepsilon^{\mathrm{e}}_{\mathrm{v}}(t_n) - \varepsilon^{\mathrm{e}}_{\mathrm{v}}(t_{n-1})\big) \tag{6.4}$$

$$s^{\mathrm{ve}}_{v,ij}(t_n) = \exp\Big(\frac{-\Delta t}{g_v}\Big)s^{\mathrm{ve}}_{v,ij}(t_{n-1}) + 2G_v\Big[1 - \exp\Big(\frac{-\Delta t}{g_v}\Big)\Big]\frac{g_v}{\Delta t}\big(\varepsilon^{\mathrm{e}}_{ij,\mathrm{d}}(t_n) - \varepsilon^{\mathrm{e}}_{ij,\mathrm{d}}(t_{n-1})\big) \tag{6.5}$$

where $\Delta t = t_n - t_{n-1}$, K_u and G_v are the bulk and shear stiffness contributions for each Prony element, k_u and g_v are the associated relaxation times and $\varepsilon^{\mathrm{e}}_{\mathrm{v}}$ and $\varepsilon^{\mathrm{e}}_{ij,\mathrm{d}}$ are the volumetric and deviatoric components of the elastic strain, respectively.

The resultant stiffness is the combination of the long-term and viscous contributions:

$$D_{ijkl} = D^{\infty}_{ijkl} + D^{\mathrm{ve}}_{ijkl} \tag{6.6}$$

where D^{ve}_{ijkl} has a similar structure to the long-term stiffness of Eq. (6.3):

$$D^{\mathrm{ve}}_{ijkl}(t) = G_{\mathrm{ve}}(t)(\delta_{ij}\delta_{kl} + \delta_{il}\delta_{jk}) + \Big(K_{\mathrm{ve}}(t) - \frac{2}{3}G_{\mathrm{ve}}(t)\Big)\delta_{ij}\delta_{kl} \tag{6.7}$$

and the time-dependent bulk and shear moduli are written as:

$$K_{\mathrm{ve}}(t) = \sum_{u=1}^{n_u} K_u\Big[1 - \exp\Big(\frac{-\Delta t}{k_u}\Big)\Big]\frac{k_u}{\Delta t} \qquad G_{\mathrm{ve}}(t) = \sum_{v=1}^{n_v} G_v\Big[1 - \exp\Big(\frac{-\Delta t}{g_v}\Big)\Big]\frac{g_v}{\Delta t} \tag{6.8}$$

6.2.2. VISCOPLASTICITY

At the beginning of each time step, a trial stress $\sigma_{ij}^{\mathrm{tr}}$ is computed, supposing that the stress update is purely viscoelastic and given by Eq. (6.2). If the trial stress state lies outside the yield surface, it is corrected by removing the plastic strain contribution:

$$\sigma_{ij} = \sigma_{ij}^{\mathrm{tr}} - (D_{ijkl}^{\infty} + D_{ijkl}^{\mathrm{ve}})\Delta\varepsilon_{kl}^{\mathrm{p}} \tag{6.9}$$

A paraboloidal yield surface with pressure-dependent hardening [21] is adopted:

$$f\left(\boldsymbol{\sigma}, \varepsilon_{\mathrm{eq}}^{\mathrm{p}}\right) = 6J_2 + 2I_1\left(\sigma_c - \sigma_t\right) - 2\sigma_c\sigma_t \tag{6.10}$$

where I_1 and J_2 are the first stress invariant and the second invariant of the deviatoric stresses, respectively, and the tension (σ_{t}) and compression (σ_{c}) yield stresses are a function of the equivalent plastic strain $\varepsilon_{\mathrm{eq}}^{\mathrm{p}}$:

$$\Delta\varepsilon_{\mathrm{eq}}^{\mathrm{p}} = \sqrt{\frac{1}{1+2\nu_{\mathrm{p}}^2}\Delta\varepsilon_{ij}^{\mathrm{p}}\Delta\varepsilon_{ij}^{\mathrm{p}}} \;\Rightarrow\; \sigma_t = \sigma_t(\varepsilon_{\mathrm{eq}}^{\mathrm{p}}),\, \sigma_c = \sigma_c(\varepsilon_{\mathrm{eq}}^{\mathrm{p}}) \tag{6.11}$$

with ν_{p} being the plastic Poisson's ratio.

Plastic flow is dictated by a non-associative flow rule:

$$\Delta\varepsilon_{ij}^{p} = \Delta\gamma\left(3s_{ij} + \frac{2}{9}\alpha I_1\delta_{ij}\right) \equiv \Delta\gamma m_{ij} \tag{6.12}$$

where γ is the plastic multiplier, m_{ij} is the direction of the plastic flow and α is given by:

$$\alpha = \frac{9}{2}\frac{1-2\nu_p}{1+\nu_p} \tag{6.13}$$

In an inviscid plasticity model, $\Delta\gamma$ would be computed in order to keep the final stress state on top of the yield surface (*i.e.* $f = 0$). However, in order to capture rate-dependent plasticity, a rheological modification of the plasticity model is performed by adding a dashpot element which takes part of the overstress resulting from crossing the yield surface. In this work, a Perzyna-type viscoplastic formulation is used and the evolution of the plastic multiplier is prescribed as:

$$\Delta\gamma = \begin{cases} \dfrac{\Delta t}{\eta_{\mathrm{p}}}\left(\dfrac{f}{\sigma_{\mathrm{t}}^{\mathrm{i}}\sigma_{\mathrm{c}}^{\mathrm{i}}}\right)^{m_{\mathrm{p}}} \equiv g\Delta t, & \text{if } f > 0 \\ 0, & \text{if } f \le 0 \end{cases} \tag{6.14}$$

where $g = g(f)$ is the viscoplastic function, η_{p} and m_{p} are the viscoplastic modulus and exponent, respectively, and $\sigma_{\mathrm{c}}^{\mathrm{i}}$ and $\sigma_{\mathrm{t}}^{\mathrm{i}}$ are the initial yield stress values (for $\varepsilon_{\mathrm{eq}}^{\mathrm{p}} = 0$).

By substituting Eq. (6.12) into Eq. (6.9), the corrected stresses can be expressed as a function of the trial stresses and $\Delta\gamma$. Substitution into Eq. (7.10) leads to a nonlinear expression for $\Delta\gamma$ which is solved iteratively. The conventional return mapping procedure with 7 unknowns (6 stress components and the plastic multiplier) is then substituted by the simpler problem of determining only $\Delta\gamma$ since $\sigma_{ij}^{\mathrm{tr}}$ and σ_{ij} have the same direction. Since this property is lost after applying time homogenization, further details on the return mapping procedure and the resultant tangent stiffness matrix are omitted in the current development. The interested reader is instead referred to [22] for an inviscid description of the algorithm.

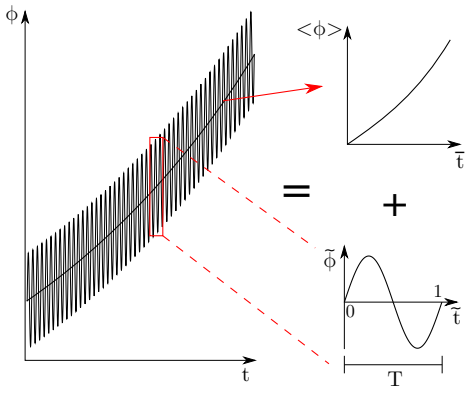

Figure 6.1: Separation of time scales.

6.3. TIME HOMOGENIZATION

Running a viscoelastic/viscoplastic micromodel for a large number of time steps requires significant computational effort, especially when a multiscale technique such as FE^2 [23] is employed. Eqs. (6.4), (6.5) and (6.8) are obtained from time discretization, which implies that the use of larger time steps is detrimental to the accuracy of the viscoelastic solution. In this regard, a time homogenization strategy can be applied in order to reduce the number of computationally heavy viscoplastic stress updates to a single one per load cycle while maintaining a high accuracy for the viscoelastic part. In this section, the homogenization strategy proposed by Yu and Fish [4] and later adopted by Haouala and Doghri [2] is applied to the present pressure-dependent VE/VP material model. The formulation proposed in [2] is expanded to include a return-mapping algorithm suitable for multi-point time integration of multiaxial stress states.

The homogenization process is based on the definition of two distinct time scales (Fig. 6.1). The first time scale ($\bar{t}$) describes the long-term loading and material response, while the second ($\tilde{t}$) describes rapid variations caused by a cyclic load of period T. The physical time t is then the combination of these slow and fast time scales:

$$t = \bar{t} + T\tilde{t} \tag{6.15}$$

where $\tilde{t} \in [0,1]$ is parametrized inside a single load cycle. Using the chain rule, the total time derivative of a general response field ϕ is given by:

$$\dot{\phi} = \frac{\partial \phi}{\partial \bar{t}} + \frac{1}{T}\frac{\partial \phi}{\partial \tilde{t}} \tag{6.16}$$

In order to obtain separate boundary-value problems in the slow and fast time coordinates, the model response fields are asymptotically expanded in powers of T:

$$\phi(\bar{t},\tilde{t}) = \sum_{i=0}^{\infty} T^i \phi_i(\bar{t},\tilde{t}) \tag{6.17}$$

where ϕ_i are periodic functions of decreasing amplitude. Adopting a first-order expansion, the stress update of Eq. (6.2) can be rewritten as:

$$\sigma_{0,ij} + T\sigma_{1,ij} = D^{\infty}_{ijkl}(\varepsilon^{\mathrm{e}}_{0,kl} + T\varepsilon^{\mathrm{e}}_{1,kl}) + \sum_{u=1}^{n_u}(p^{\mathrm{ve}}_{0,u} + Tp^{\mathrm{ve}}_{1,u})\delta_{ij} + \sum_{v=1}^{n_v}(s^{\mathrm{ve}}_{0,v,ij} + Ts^{\mathrm{ve}}_{1,v,ij}) \quad (6.18)$$

and the evolution of plastic strains and plastic multiplier can be given by:

$$\dot{\varepsilon}^{\mathrm{p}}_{0,ij} + T\dot{\varepsilon}^{\mathrm{p}}_{1,ij} = B_{0,ij} + T\Big(\frac{\partial B_{0,ij}}{\partial \sigma_{0,ij}}\sigma_{1,ij} + \frac{\partial B_{0,ij}}{\partial \gamma_0}\gamma_1\Big) \quad (6.19)$$

$$\dot{\gamma}_0 + T\dot{\gamma}_1 = C_0 + T\Big(\frac{\partial C_0}{\partial \sigma_{0,ij}}\sigma_{1,ij} + \frac{\partial C_0}{\partial \gamma_0}\gamma_1\Big) \quad (6.20)$$

where $B_{0,ij}$ and C_0 are the viscoplastic operators shown in Eqs. (6.12) and (7.10), respectively, evaluated at $(\sigma_{0,ij}, \gamma_0)$.

Applying the total time derivative of Eq. (6.16) to the variations of plastic strain and plastic multiplier and grouping terms of the same order of T, the following problems are obtained:

$$O(-1): \begin{cases} \dfrac{\partial \varepsilon^{\mathrm{p}}_{0,ij}}{\partial \bar{t}} = 0 \\ \dfrac{\partial \gamma_0}{\partial \bar{t}} = 0 \end{cases} \quad (6.21)$$

$$O(0): \begin{cases} \sigma_{0,ij} = D^{\infty}_{ijkl}\varepsilon^{\mathrm{e}}_{0,kl} + \displaystyle\sum_{u=1}^{n_u} p^{\mathrm{ve}}_{0,u}\delta_{ij} + \sum_{v=1}^{n_v} s^{\mathrm{ve}}_{0,v,ij} \\ \dfrac{\partial \varepsilon^{\mathrm{p}}_{0,ij}}{\partial \bar{t}} = B_{0,ij} \\ \dfrac{\partial \gamma_0}{\partial \bar{t}} = C^0 \end{cases} \quad (6.22)$$

$$O(1): \begin{cases} \sigma_{1,ij} = D^{\infty}_{ijkl}\varepsilon^{\mathrm{e}}_{1,kl} + \displaystyle\sum_{u=1}^{n_u} p^{\mathrm{ve}}_{1,u}\delta_{ij} + \sum_{v=1}^{n_v} s^{\mathrm{ve}}_{1,v,ij} \\ \dfrac{\partial \varepsilon^{\mathrm{p}}_{1,ij}}{\partial \bar{t}} = \dfrac{\partial B_{0,ij}}{\partial \sigma_{0,ij}}\sigma_{1,ij} + \dfrac{\partial B_{0,ij}}{\partial \gamma_0}\gamma_1 \\ \dfrac{\partial \gamma_1}{\partial \bar{t}} = \dfrac{\partial C_0}{\partial \sigma_{0,ij}}\sigma_{1,ij} + \dfrac{\partial C_0}{\partial \gamma_0}\gamma_1 \end{cases} \quad (6.23)$$

From the $O(-1)$ problem, it can be seen that the variation of the zero-order plastic strain with the fast time coordinate is zero. Therefore, by solving only the $O(0)$ problem, the fact that viscoplasticity only evolves with slow time $\bar{t}$ can be exploited in order to accelerate the analysis. Naturally, ignoring the higher-order problems introduces an error in the prediction of the response fields ϕ.

Following the time decomposition of Eq. (6.15), the response fields are also decomposed in slow and fast parts:

$$\phi = \langle \phi \rangle + \widetilde{\phi} \quad (6.24)$$

where $\langle\phi\rangle$ is defined as the average response within a load cycle:

$$\langle\phi\rangle = \int_0^1 \phi(\bar{t},\widetilde{t})\, d\widetilde{t} \tag{6.25}$$

With such definitions, the original boundary-value problem can be decomposed into microchronological and macrochronological parts. Since only the $O(0)$ problem is being solved, the subscript 0 will be dropped from now on for notational simplicity.

6.3.1. MICROCHRONOLOGICAL PROBLEM

At the fast time scale, the boundary-value problem involves the fluctuations of applied displacements or forces:

$$\widetilde{u}_i\big|_{\Gamma_\mathrm{u}} = \widetilde{u}_i^\Gamma \qquad (\widetilde{\sigma}_{ij} n_j)\big|_{\Gamma_\sigma} = \widetilde{f}_i^\Gamma \tag{6.26}$$

where Γ_u and Γ_σ refer to Dirichlet and Neumann surfaces, respectively, and the superscript Γ indicates a prescribed value. Since the evolution of viscoplasticity is blocked, the stress update is purely viscoelastic:

$$\widetilde{\sigma}_{ij} = D^\infty_{ijkl}\widetilde{\varepsilon}^\mathrm{e}_{kl} + \sum_{u=1}^{n_u} \widetilde{p}^\mathrm{ve}_u \delta_{ij} + \sum_{v=1}^{n_v} \widetilde{s}^\mathrm{ve}_{v,ij} \tag{6.27}$$

and the variations of plastic strain and plastic multiplier are trivially determined:

$$\Delta\widetilde{\varepsilon}^\mathrm{p}_{ij} = 0 \qquad \Delta\widetilde{\gamma} = 0 \tag{6.28}$$

Since only a viscoelastic problem needs to be solved, the analysis is accelerated by skipping the viscoplastic return mapping algorithm and by solving the global system of equations using a linear solver.

6.3.2. MACROCHRONOLOGICAL PROBLEM

At the macroscale, the time-averaged values for the applied forces or displacements are used:

$$\langle u\rangle_i\big|_{\Gamma_\mathrm{u}} = \langle u\rangle_i^\Gamma \qquad (\langle\sigma\rangle_{ij} n_j)\big|_{\Gamma_\sigma} = \langle f\rangle_i^\Gamma \tag{6.29}$$

and the stress update can be written as:

$$\langle\sigma\rangle_{ij} = D^\infty_{ijkl}\langle\varepsilon\rangle^\mathrm{e}_{kl} + \sum_{u=1}^{n_u} \langle p\rangle^\mathrm{ve}_u \delta_{ij} + \sum_{v=1}^{n_v} \langle s\rangle^\mathrm{ve}_{v,ij} \tag{6.30}$$

It is important to note that the hereditary stresses of Eqs. (6.27) and (6.30) evolve independently and therefore need to be separately stored. Finally, the plastic strain and plastic multiplier rates are defined as time averages of the nonlinear operators B_{ij} and C:

$$\Delta\langle\varepsilon\rangle^\mathrm{p}_{ij} = \langle B\rangle_{ij} \qquad \Delta\langle\gamma\rangle = \langle C\rangle\Delta\bar{t} \tag{6.31}$$

Recalling from Eqs. (6.19) and (6.20) that the viscoplastic operators must be evaluated using the total stresses $\sigma_{ij} = \langle\sigma\rangle_{ij} + \widetilde{\sigma}_{ij}$, the one-way coupling between time scales

becomes evident: For each macro time step, the microchronological problem is solved and the resultant stresses are used in combination with the macroscopic ones in order to compute the viscoplastic operator averages. Since the stress updates on both scales are time-discrete, these averages are computed through numerical integration:

$$\Delta\langle\gamma\rangle = \langle g\rangle\Delta\bar{t} \approx \sum_{\tau}^{n_{\mathrm{ip}}} \frac{\Delta\bar{t}}{\eta_{\mathrm{p}}}\left(\frac{f\left(\langle\sigma\rangle_{ij,\tau}+\widetilde{\sigma}_{ij,\tau}\right)}{\sigma_{\mathrm{t}}^{\mathrm{i}}\sigma_{\mathrm{c}}^{\mathrm{i}}}\right)^{\mathrm{m_p}}\beta_\tau\omega_\tau \tag{6.32}$$

$$\Delta\langle\varepsilon\rangle_{ij}^{\mathrm{p}} = \Delta\langle\gamma\rangle\langle m\rangle_{ij} \approx \Delta\langle\gamma\rangle\sum_{\tau}^{n_{\mathrm{ip}}} m_{ij}\left(\langle\sigma\rangle_{ij,\tau}+\widetilde{\sigma}_{ij,\tau}\right)\beta_\tau\omega_\tau \tag{6.33}$$

where ω_τ is the integration weight at $\widetilde{t}=\tau$ and β_τ is a factor used to account for the discontinuous nature of the viscoplastic operators: $\beta_\tau = 1$ if the yield function is crossed at point τ and $\beta_\tau = 0$ otherwise.

VISCOPLASTIC RETURN MAPPING

Since the flow direction $\langle m\rangle_{ij}$ does not depend only on $\langle\sigma\rangle_{ij}$ but rather on the total stress σ_{ij}, the simple return mapping algorithm with a single unknown presented in [22] cannot be employed here. The resultant system of equations with seven unknowns in matrix notation is given by:

$$\begin{cases}\mathbf{r}^{\sigma} = \langle\boldsymbol{\sigma}\rangle - \langle\boldsymbol{\sigma}\rangle^{\mathrm{tr}} + \Delta\langle\gamma\rangle\mathbf{D}\langle\mathbf{m}\rangle = \mathbf{0}\\ r^{\gamma} = \langle g\rangle\Delta\bar{t} - \Delta\langle\gamma\rangle = 0\end{cases} \tag{6.34}$$

which is solved iteratively using the Newton-Raphson method:

$$\begin{pmatrix}\langle\boldsymbol{\sigma}\rangle\\ \Delta\langle\gamma\rangle\end{pmatrix}_{\mathrm{n}} = \begin{pmatrix}\langle\boldsymbol{\sigma}\rangle\\ \Delta\langle\gamma\rangle\end{pmatrix}_{\mathrm{o}} - \begin{bmatrix}\dfrac{\partial\mathbf{r}^{\sigma}}{\partial\langle\boldsymbol{\sigma}\rangle} & \dfrac{\partial\mathbf{r}^{\sigma}}{\partial\Delta\langle\gamma\rangle}\\ \dfrac{\partial r^{\gamma}}{\partial\langle\boldsymbol{\sigma}\rangle} & \dfrac{\partial r^{\gamma}}{\partial\langle\gamma\rangle}\end{bmatrix}_{\mathrm{o}}^{-1}\begin{pmatrix}\mathbf{r}^{\sigma}\\ r^{\gamma}\end{pmatrix}_{\mathrm{o}} \tag{6.35}$$

where the subscripts n and o indicate values from the current and previous iterations, respectively. Elaborating the residual derivatives gives:

$$\frac{\partial\mathbf{r}^{\sigma}}{\partial\langle\boldsymbol{\sigma}\rangle} = \mathbf{I} + \Delta\langle\gamma\rangle\mathbf{D}\frac{\partial\langle\mathbf{m}\rangle}{\partial\langle\boldsymbol{\sigma}\rangle} \tag{6.36}$$

$$\frac{\partial\mathbf{r}^{\sigma}}{\partial\Delta\langle\gamma\rangle} = \mathbf{D}\langle\mathbf{m}\rangle \tag{6.37}$$

$$\frac{\partial r^{\gamma}}{\partial\langle\boldsymbol{\sigma}\rangle} = \frac{\partial\langle g\rangle}{\partial\langle\boldsymbol{\sigma}\rangle}\Delta\bar{t} \tag{6.38}$$

$$\frac{\partial r^{\gamma}}{\partial\Delta\langle\gamma\rangle} = \frac{\partial\langle g\rangle}{\partial\Delta\langle\gamma\rangle}\Delta\bar{t} - 1 \tag{6.39}$$

where $\mathbf{I}$ is the identity matrix. The derivatives of the numerically integrated time averages of $\mathbf{m}$ and g are given by:

$$\frac{\partial\langle\mathbf{m}\rangle}{\partial\langle\boldsymbol{\sigma}\rangle} = \sum_{\tau}^{n_{\mathrm{ip}}}\left[3\mathbf{I} + \left(\frac{2}{9}\alpha - 1\right)\mathbf{I}_2\right]\beta_\tau\omega_\tau \tag{6.40}$$

$$\frac{\partial \langle g \rangle}{\partial \langle \boldsymbol{\sigma} \rangle} = \frac{m_\mathrm{p}}{\eta_\mathrm{p} (\sigma_\mathrm{t}^\mathrm{i} \sigma_\mathrm{c}^\mathrm{i})^{m_\mathrm{p}}} \sum_\tau^{n_\mathrm{ip}} f_\tau^{m_\mathrm{p}-1} \frac{\partial f_\tau}{\partial \langle \boldsymbol{\sigma} \rangle} \beta_\tau \omega_\tau \tag{6.41}$$

$$\frac{\partial \langle g \rangle}{\partial \Delta \langle \gamma \rangle} = \frac{m_\mathrm{p}}{\eta_\mathrm{p} (\sigma_\mathrm{t}^\mathrm{i} \sigma_\mathrm{c}^\mathrm{i})^{m_\mathrm{p}}} \sum_\tau^{n_\mathrm{ip}} f_\tau^{m_\mathrm{p}-1} \frac{\partial f_\tau}{\partial \Delta \langle \gamma \rangle} \beta_\tau \omega_\tau \tag{6.42}$$

where $\mathbf{I}_2$ is the Voigt representation of the tensor $\delta_{ij}\delta_{kl}$. The derivatives of the yield function with respect to stress and plastic multiplier at $\widetilde{t} = \tau$ are computed as:

$$\frac{\partial f_\tau}{\partial \langle \boldsymbol{\sigma} \rangle} = 6 \left(\langle \mathbf{s} \rangle + \widetilde{\mathbf{s}}^\tau \right)^\mathrm{T} \left(\mathbf{I} - \frac{1}{3} \mathbf{I}_2 \right) + 2(\sigma_\mathrm{c} - \sigma_\mathrm{t}) \mathbf{i}_1 + \frac{\partial f_\tau}{\partial \langle \varepsilon \rangle_\mathrm{eq}^\mathrm{p}} \frac{\partial \Delta \langle \varepsilon \rangle_\mathrm{eq}^\mathrm{p}}{\partial \langle \boldsymbol{\sigma} \rangle} \tag{6.43}$$

$$\frac{\partial f_\tau}{\partial \Delta \langle \gamma \rangle} = \frac{\partial f_\tau}{\partial \langle \varepsilon \rangle_\mathrm{eq}^\mathrm{p}} \frac{\partial \Delta \langle \varepsilon \rangle_\mathrm{eq}^\mathrm{p}}{\partial \Delta \langle \gamma \rangle} \tag{6.44}$$

where $\mathbf{i}_1$ is the Voigt representation of the matrix δ_{ij}. In the previous expressions, the derivative of f with respect to equivalent plastic strain is the tangent pressure-dependent hardening modulus:

$$\frac{\partial f_\tau}{\partial \langle \varepsilon \rangle_\mathrm{eq}^\mathrm{p}} = 2(\langle I_1 \rangle + \widetilde{I}_1^\tau)(H_\mathrm{c} - H_\mathrm{t}) - 2(\sigma_\mathrm{c} H_\mathrm{t} + \sigma_\mathrm{t} H_\mathrm{c}) \tag{6.45}$$

with H_c and H_t being the hardening moduli in compression and tension, respectively. The formulation is completed by defining the variations of equivalent plastic strain with stresses and plastic multiplier:

$$\frac{\partial \Delta \langle \varepsilon \rangle_\mathrm{eq}^\mathrm{p}}{\partial \langle \boldsymbol{\sigma} \rangle} = \frac{(\Delta \langle \gamma \rangle)^2 k}{\Delta \langle \varepsilon \rangle_\mathrm{eq}^\mathrm{p}} \langle \mathbf{m} \rangle \frac{\partial \langle \mathbf{m} \rangle}{\partial \langle \boldsymbol{\sigma} \rangle} \qquad \frac{\partial \Delta \langle \varepsilon \rangle_\mathrm{eq}^\mathrm{p}}{\partial \Delta \langle \gamma \rangle} = \sqrt{k \langle \mathbf{m} \rangle \langle \mathbf{m} \rangle} \tag{6.46}$$

where $k = 1/(1 + 2\nu_\mathrm{p})$ is the plastic contraction factor from Eq. (6.11). It is important to note that the present algorithm is suitable for multiaxial load cases, thus expanding upon the multi-point integration return mapping proposed by Haouala and Doghri [2] for uniaxial loading.

ALGORITHMIC TANGENT STIFFNESS

The last step in the time-homogenized viscoplastic discretization is the definition of the algorithmic tangent stiffness matrix. Taking the full derivative of $\mathbf{r}^\sigma$ yields:

$$\delta \langle \boldsymbol{\sigma} \rangle = \mathbf{D} \delta \langle \boldsymbol{\varepsilon} \rangle - \mathbf{D} \langle \mathbf{M} \rangle \delta \Delta \langle \gamma \rangle - \Delta \langle \gamma \rangle \mathbf{D} \frac{\partial \langle \mathbf{m} \rangle}{\partial \langle \boldsymbol{\sigma} \rangle} \delta \langle \boldsymbol{\sigma} \rangle - \Delta \langle \gamma \rangle \mathbf{D} \frac{\partial \langle \mathbf{m} \rangle}{\partial \Delta \langle \gamma \rangle} \delta \Delta \langle \gamma \rangle \tag{6.47}$$

where the last term evaluates to zero since $\langle \mathbf{m} \rangle$ does not depend on the plastic multiplier. In order to obtain an expression for $\delta \Delta \langle \gamma \rangle$, the full derivative of r^γ is rearranged into:

$$\delta \Delta \langle \gamma \rangle = \frac{1}{\mu} \frac{\partial \langle g \rangle}{\partial \langle \boldsymbol{\sigma} \rangle} \Delta \bar{t} \, \delta \langle \boldsymbol{\sigma} \rangle \tag{6.48}$$

with μ given by:

$$\mu = 1 - \frac{\partial \langle g \rangle}{\partial \Delta \langle \gamma \rangle} \Delta \bar{t} \tag{6.49}$$

Finally, substitution of Eq. (6.48) into Eq. (6.47) yields an expression for the tangent stiffness matrix:

$$\delta\langle\boldsymbol{\sigma}\rangle = \mathbf{H}^{-1}\mathbf{D}\delta\langle\boldsymbol{\varepsilon}\rangle \tag{6.50}$$

where the matrix $\mathbf{H}$ is:

$$\mathbf{H} = \mathbf{I} + \frac{\Delta\bar{t}}{\mu}\mathbf{D}\langle\mathbf{m}\rangle\frac{\partial\langle g\rangle}{\partial\langle\boldsymbol{\sigma}\rangle} + \Delta\langle\gamma\rangle\mathbf{D}\frac{\partial\langle\mathbf{m}\rangle}{\partial\langle\boldsymbol{\sigma}\rangle} \tag{6.51}$$

6.4. REDUCED-ORDER MODELING

Although promoting gains in execution time, both micro- and macrochronological problems of Section 6.3 are still conventional finite element problems often featuring dense meshes and a large number of degrees of freedom. In this section, an additional set of numerical techniques used to reduce the complexity of a finite element problem is presented.

6.4.1. FULL-ORDER FE PROBLEM

In the current development, a stress equilibrium problem is solved using the Finite Element (FE) method. The domain Ω is subdivided in a number of discrete elements connected by nodes, with a total of N degrees of freedom. The global equilibrium problem is therefore solved iteratively (*e.g.* with a Newton-Raphson solver) in its weak form:

$$\mathbf{r} = \mathbf{f}^{\Gamma} - \mathbf{f}^{\Omega}(\mathbf{u}) = \mathbf{0} \tag{6.52}$$

where $\mathbf{r} \in \mathbb{R}^N$ is a residual vector that vanishes at equilibrium, $\mathbf{f}^{\Gamma} \in \mathbb{R}^N$ is an external force vector representing a set of Neumann boundary conditions acting on surfaces Γ_f and $\mathbf{f}^{\Omega} \in \mathbb{R}^N$ is the internal force vector which is a function of the nodal displacements $\mathbf{u} \in \mathbb{R}^N$. In Eq. (6.52), Dirichlet constraints of the form $\mathbf{u}\big|_{\Gamma_\mathrm{u}} = \mathbf{u}^{\Gamma}$ are implicitly applied ($\Gamma_\mathrm{f} \cap \Gamma_\mathrm{u} = \varnothing$).

Solution of Eq. (6.52) involves iteratively correcting the displacement vector as follows:

$$\Delta\mathbf{u} = \mathbf{u}_\mathrm{n} - \mathbf{u}_\mathrm{o} = -\mathbf{K}_\mathrm{o}^{-1}\mathbf{r}_\mathrm{o} \tag{6.53}$$

where the subscripts o and n refer to values from the old and new analysis increments, respectively, $\mathbf{K} \in \mathbb{R}^{N\times N}$ is the global tangent stiffness matrix:

$$\mathbf{K} = \frac{\partial\mathbf{f}^{\Omega}}{\partial\mathbf{u}} \tag{6.54}$$

and the global internal force vector is obtained by a volume integral:

$$\mathbf{f}^{\Omega} = \int_{\Omega}\mathbf{f}\,d\Omega \approx \sum_{i}^{M}\mathbf{f}(\mathbf{x}_i)\,w_i \tag{6.55}$$

where $\mathbf{f} \in \mathbb{R}^N$ is the sparse internal force vector at a given material point obtained after an assembly procedure that relates the local degrees of freedom of a given element with their global counterparts. The integral is computed numerically by evaluating the integrand $\mathbf{f}$ at M integration points with integration weights $\mathbf{w} \in \mathbb{R}^M$.

Two main complexity reduction avenues can be identified. Firstly, reducing the number of degrees of freedom N accelerates the solution of the nonlinear equilibrium problem of Eq. (6.52). Section 6.4.2 presents a strategy of reduction by projection that aims to address this part of the complexity. Secondly, solving the problem for $n \ll N$ degrees of freedom still requires the volume integration of $\mathbf{f}$, which in turn depends on the size of the full problem. Section 6.4.3 presents a modified numerical integration technique that drastically reduces the number of integration points to $m \ll M$ in Eq. (6.55).

After these two reduction procedures, the constitutive response of most of the original integration points is never computed, causing loss of information in terms of stresses and material history. If stresses and history at every material point are required *online* (*e.g.* an adaptive reduction scheme involving sporadic execution of a full analysis), an efficient recovery procedure becomes necessary. Section 6.4.4 presents a combination of techniques that use information at the reduced integration points to retrieve stresses and history at all other points in the mesh. Finally, an adaptive reduction scheme which avoids the need of an *offline* training phase is presented in Section 6.4.5

6.4.2. PROPER ORTHOGONAL DECOMPOSITION (POD)

The full model response $\mathbf{u}$ may be approximated by the linear combination of $n \ll N$ displacement modes $\boldsymbol{\phi}_i \in \mathbb{R}^N$ (also called Ritz vectors [6]). By arranging such modes in a matrix $\boldsymbol{\Phi} \in \mathbb{R}^{N \times n}$:

$$\boldsymbol{\Phi} = \begin{bmatrix} \boldsymbol{\phi}_1 & \boldsymbol{\phi}_2 & \cdots & \boldsymbol{\phi}_n \end{bmatrix} \tag{6.56}$$

the original problem can now be expressed in terms of relative contributions α_i of each mode:

$$\mathbf{u} = \boldsymbol{\Phi}\boldsymbol{\alpha} \tag{6.57}$$

with $\boldsymbol{\alpha} \in \mathbb{R}^n$ being the reduced vector of degrees of freedom.

With this definition, the problem of Eq. (6.52) can be solved in the reduced space by enforcing the Galerkin projection constraint $\boldsymbol{\Phi}^{\mathrm{T}}\mathbf{r} = \mathbf{0}$. The force vectors and stiffness matrix are then given by:

$$\mathbf{f}_{\mathrm{r}}^{\Omega} = \boldsymbol{\Phi}^{\mathrm{T}}\mathbf{f}^{\Omega} \qquad \mathbf{f}_{\mathrm{r}}^{\Gamma} = \boldsymbol{\Phi}^{\mathrm{T}}\mathbf{f}^{\Gamma} \qquad \mathbf{K}_{\mathrm{r}} = \boldsymbol{\Phi}^{\mathrm{T}}\mathbf{K}\boldsymbol{\Phi} \tag{6.58}$$

and Dirichlet boundary conditions can be imposed on $\boldsymbol{\alpha}$ by selecting the terms of the basis vectors corresponding to the original constraints:

$$\mathbf{u}^{\Gamma} = \boldsymbol{\Phi}\big|_{\Gamma_{\mathrm{u}}}\boldsymbol{\alpha} \tag{6.59}$$

The basis matrix $\boldsymbol{\Phi}$ is obtained in the so-called *offline* or *training* phase by first running the full model and collecting displacement snapshots for each configuration (time step or loading type), resulting in a snapshot matrix $\mathbf{X} \in \mathbb{R}^{N \times P}$. In the classic Proper Orthogonal Decomposition (POD) method, the basis matrix is obtained through the Singular Value Decomposition (SVD) of $\mathbf{X}$:

$$\mathbf{X} = \boldsymbol{\Phi}\mathbf{S}\mathbf{V}^{\mathrm{T}} \tag{6.60}$$

where $\boldsymbol{\Phi}$ is the left-singular matrix of orthonormal basis vectors, $\mathbf{V}$ is the right-singular basis matrix and $\mathbf{S}$ is a diagonal matrix of singular values.

In the present development, this procedure is complemented by the elastic-inelastic decompostion proposed by Hernández *et al.* [24]. First, the snapshot matrix is decomposed into elastic ($\mathbf{X}_\mathrm{e}$) and inelastic ($\mathbf{X}_\mathrm{i}$) parts:

$$\mathbf{X} = \begin{bmatrix} \mathbf{X}_\mathrm{e} & \mathbf{X}_\mathrm{i} \end{bmatrix} \tag{6.61}$$

Then, an orthogonal basis matrix $\mathbf{Y} \in \mathbb{R}^{N \times n_\mathrm{e}}$ for the n_e first elastic modes of $\mathbf{X}_\mathrm{e}$ is computed and the full $\mathbf{X}$ is projected into it:

$$\overline{\mathbf{X}}_\mathrm{e} = \mathbf{Y}(\mathbf{Y}^\mathrm{T}\mathbf{X}) \tag{6.62}$$

yielding a modified elastic snapshot matrix. Finally, the inelastic part is obtained by subtracting it from the original $\mathbf{X}$:

$$\overline{\mathbf{X}}_\mathrm{i} = \mathbf{X} - \overline{\mathbf{X}}_\mathbf{e} \tag{6.63}$$

With the modified versions of $\mathbf{X}_\mathrm{e}$ and $\mathbf{X}_\mathrm{i}$, the SVD is applied separately to each of them and the resulting left-singular matrices are truncated to n_e elastic modes and n_i inelastic modes:

$$\overline{\mathbf{X}}_\mathrm{e} \approx \overline{\mathbf{U}}_\mathrm{e}\overline{\mathbf{S}}_\mathrm{e}\overline{\mathbf{V}}_\mathrm{e}^\mathrm{T} \qquad \overline{\mathbf{X}}_\mathrm{i} \approx \overline{\mathbf{U}}_\mathrm{i}\overline{\mathbf{S}}_\mathrm{i}\overline{\mathbf{V}}_\mathrm{i}^\mathrm{T} \tag{6.64}$$

with $\overline{\mathbf{U}}_\mathrm{e} \in \mathbb{R}^{N \times n_\mathrm{e}}$, $\overline{\mathbf{U}}_\mathrm{i} \in \mathbb{R}^{N \times n_\mathrm{i}}$ and $n = n_\mathrm{e} + n_\mathrm{i}$. Finally, the basis is the combination of elastic and inelastic contributions:

$$\mathbf{\Phi} = \begin{bmatrix} \overline{\mathbf{U}}_\mathrm{e} & \overline{\mathbf{U}}_\mathrm{i} \end{bmatrix} \tag{6.65}$$

6.4.3. EMPIRICAL CUBATURE METHOD (ECM)

In addition to reducing the complexity of the global equilibrium equations of Eq. (6.52), further acceleration is possible by reducing the number of material points used to compute the internal force vector from M to $m \ll M$ (the subscript r is omitted for compactness):

$$\mathbf{f}^\Omega = \int_\Omega \mathbf{f} d\Omega \approx \sum_{i=1}^{m} \mathbf{f}(\mathbf{x}_i)\varpi_i \tag{6.66}$$

where ϖ_i are modified integration weights. The result of combining this strategy with POD is a so-called hyper-reduced model. The Empirical Cubature Method (ECM) proposed by Hernández *et al.* [12] is chosen in order to determine an optimized combination of points and weights. The method is summarized here in order to keep the work self-contained, but without motivating every formulation choice. For further details, the interested reader is referred to the original works by Hernández *et al.* [12] and An *et al.* [13].

The optimization problem involved in determining the set $\boldsymbol{\zeta}$ of m integration points and their respective weights $\boldsymbol{\varpi}$ consists in minimizing the integration error for all P training configurations:

$$(\boldsymbol{\varpi}, \boldsymbol{\zeta}) = \underset{\boldsymbol{\varpi} \in \mathbb{R}^m, \boldsymbol{\zeta} \in \mathbb{N}^m}{\arg\min} \; \|\mathbf{E}\| \tag{6.67}$$

where the matrix $\mathbf{E} \in \mathbb{R}^{n \times P}$ consists of error vectors $\mathbf{e}_j \in \mathbb{R}^n$ for each training configuration j:

$$\mathbf{e}_j = \sum_i^m \mathbf{f}_j(\mathbf{x}_i)\varpi_i - \int_\Omega \mathbf{f}_j d\Omega \tag{6.68}$$

and the operator $\|\cdot\|$ applied to a matrix is its Frobenius norm:

$$\|\mathbf{E}\| = \sqrt{\sum_{i}^{n}\sum_{j}^{P} E_{ij}^2} \tag{6.69}$$

Solving Eq. (6.67) for all training configurations P can be burdensome, especially if a large number of time steps is considered (which is commonly the case for VE/VP models). Alternatively, $\mathbf{f}_j$ can be approximated by a set of basis functions Λ_k and coefficients $\mathbf{c}_j^k$ that reasonably approximate its value for all P training configurations. Since only the coefficients change with j, the error vector may be rewritten as:

$$\mathbf{f}_j \approx \sum_{k=1}^{p} \Lambda_k \mathbf{c}_j^k \Rightarrow \mathbf{e}_j = \left[\sum_{i=1}^{m}\left(\sum_{k=1}^{p}\Lambda_k(\mathbf{x}_i)\right)\varpi_i - \int_\Omega \left(\sum_{k=1}^{p}\Lambda_k\right)\mathrm{d}\Omega\right]\mathbf{c}_j \tag{6.70}$$

which reduces the size of the optimization problem from P to p, with $p \ll P$. Based on this idea but using a basis matrix $\mathbf{\Lambda}$ instead of basis functions, Eq. (6.67) can be recast as:

$$(\boldsymbol{\alpha}, \boldsymbol{\zeta}) = \underset{\overline{\alpha}\geq\mathbf{0},\overline{\boldsymbol{\zeta}}}{\arg\min} \left\| \mathbf{J}_{\overline{\boldsymbol{\zeta}}}\overline{\boldsymbol{\alpha}} - \mathbf{b}\right\|^2 \tag{6.71}$$

with the weights:

$$\varpi_i = \sqrt{w_i}\alpha_i \tag{6.72}$$

and the terms $\mathbf{J}_{\boldsymbol{\zeta}}$ and $\mathbf{b}$:

$$\mathbf{J}_{\boldsymbol{\zeta}} = \begin{bmatrix}\mathbf{\Lambda}_{\boldsymbol{\zeta}} & \sqrt{\mathbf{w}_{\boldsymbol{\zeta}}}\end{bmatrix}^{\mathrm{T}} \qquad \mathbf{b} = \begin{bmatrix}\mathbf{0} & \Omega\end{bmatrix}^{\mathrm{T}} \tag{6.73}$$

where $\mathbf{\Lambda}_{\boldsymbol{\zeta}} \in \mathbb{R}^{m\times p}$ is a block matrix extracted from $\mathbf{\Lambda} \in \mathbb{R}^{M\times p}$ corresponding to the reduced set of m integration points $\boldsymbol{\zeta} \subset \{1,2,...,M\}$. Inclusion of the original integration weights $\mathbf{w}$ and the domain volume Ω in the problem guarantees that the reduced points and weights will integrate the domain volume exactly and eliminates the ill-posedness of the optimization problem if $\mathbf{f}_j^\Omega = \mathbf{0}, \forall\, j$ (*e.g.* when only Dirichlet boundary conditions are used).

In order to obtain the basis matrix $\mathbf{\Lambda}$ for the internal forces, the stress-based approach presented in Hernández *et al.* [12] is adopted in combination with the elastic-inelastic decomposition presented in Section 6.4.2. The POD-reduced model is executed for all P training configurations and the stresses at every integration point are gathered as:

$$\mathbf{X}^\sigma = \begin{bmatrix} \boldsymbol{\sigma}^1(\mathbf{x}_1) & \boldsymbol{\sigma}^2(\mathbf{x}_1) & \cdots & \boldsymbol{\sigma}^P(\mathbf{x}_1) \\ \boldsymbol{\sigma}^1(\mathbf{x}_2) & \boldsymbol{\sigma}^2(\mathbf{x}_2) & \cdots & \boldsymbol{\sigma}^P(\mathbf{x}_2) \\ \vdots & \vdots & \ddots & \vdots \\ \boldsymbol{\sigma}^1(\mathbf{x}_M) & \boldsymbol{\sigma}^2(\mathbf{x}_M) & \cdots & \boldsymbol{\sigma}^P(\mathbf{x}_M) \end{bmatrix} \tag{6.74}$$

with $\boldsymbol{\sigma} \in \mathbb{R}^s$, with s being the number of stress components. Applying the elastic-inelastic decomposition procedure, a basis matrix for stresses $\mathbf{\Psi} \in \mathbb{R}^{sM\times q}$ and its corresponding singular values $\boldsymbol{\lambda} \in \mathbb{R}^q$ are obtained:

$$\mathbf{\Psi} = \begin{bmatrix}\overline{\mathbf{U}}_{\mathrm{e}}^\sigma & \overline{\mathbf{U}}_{\mathrm{i}}^\sigma\end{bmatrix} \qquad \boldsymbol{\lambda} = \begin{bmatrix}\bar{\mathbf{s}}_{\mathrm{e}} & \bar{\mathbf{s}}_{\mathrm{i}}\end{bmatrix} \tag{6.75}$$

The basis matrix is then obtained by combining the projected internal force vector $\widehat{\mathscr{F}}_j \in \mathbb{R}^{M\times n}$ for each column of $\boldsymbol{\Psi}$:

$$\boldsymbol{\Lambda} = \begin{bmatrix} \widehat{\mathscr{F}}_1 & \widehat{\mathscr{F}}_2 & \cdots & \widehat{\mathscr{F}}_q \end{bmatrix} \tag{6.76}$$

where the contribution of each mode is given by:

$$\widehat{\mathscr{F}}_j = \begin{bmatrix} \sqrt{w_1}\left(\mathbf{f}_j(\mathbf{x}_1) - \frac{1}{\Omega}\mathbf{f}_j^{\Omega}\right) \\ \sqrt{w_2}\left(\mathbf{f}_j(\mathbf{x}_2) - \frac{1}{\Omega}\mathbf{f}_j^{\Omega}\right) \\ \vdots \\ \sqrt{w_M}\left(\mathbf{f}_j(\mathbf{x}_M) - \frac{1}{\Omega}\mathbf{f}_j^{\Omega}\right) \end{bmatrix} \tag{6.77}$$

and the internal force is computed from the stress snapshots as:

$$\mathbf{f}_j = \boldsymbol{\Phi}^{\mathrm{T}}\mathbf{B}^{\mathrm{T}}\lambda_j\boldsymbol{\psi}_j \tag{6.78}$$

where $\boldsymbol{\psi}_j \in \mathbb{R}^s$ is a block extracted from $\boldsymbol{\Psi}$ corresponding with the j-th stress snapshot and $\mathbf{B} \in \mathbb{R}^{s\times N}$ is the strain-displacement matrix expanded to global size by a conventional FE assembly procedure. It can be seen from Eqs. (6.76) and (6.77) that, for such stress-based strategy, the number of columns p of $\boldsymbol{\Lambda}$ is qn.

The optimization problem of Eq. (6.71) is solved using Algorithm 1, a modified version of the classic active set algorithm developed by Lawson and Hanson [25] incorporating changes proposed by An *et al.* [13] and Hernández *et al.* [12].

6.4.4. STRESS AND HISTORY RECONSTRUCTION

Employing an ECM-reduced model leads to loss of information in terms of stress and material history at most integration points. In order to circumvent this drawback, an efficient recovery procedure is proposed that combines the so-called Gappy Data reconstruction [11, 12] with a k-means clustering algorithm inspired by the work of Liu *et al.* [15]. Gappy data reconstruction consists in approximating a vector using values at a small number of sampling points through a least-squares procedure based on previously obtained snapshots of the full vector. The method is the basis for hyper-reduction methods such as the Discrete Empirical Interpolation Method (DEIM) [9] and has also been employed by Hernández *et al.* [12] for stress recovery.

The efficiency of the recovery procedure can be further improved by using a k-means clustering algorithm, a method originally employed in machine learning, data mining and image compression applications, which involves grouping entities in k clusters based on how similar each entity is to the mean value of each cluster. The method was used in a mechanical analysis context by Liu *et al.* to cluster material points based on their mechanical response and solve a reduced equilibrium problem [15]. Here, the two methods are combined, resulting in a compressed version of the classical Gappy data reconstruction. First, a history snapshot matrix similar to the one from Eq. (6.74) is assembled:

$$\mathbf{X}^{\mathrm{hist}} = \begin{bmatrix} \mathbf{h}^1(\mathbf{x}_1) & \mathbf{h}^2(\mathbf{x}_1) & \cdots & \mathbf{h}^P(\mathbf{x}_1) \\ \mathbf{h}^1(\mathbf{x}_2) & \mathbf{h}^2(\mathbf{x}_2) & \cdots & \mathbf{h}^P(\mathbf{x}_2) \\ \vdots & \vdots & \ddots & \vdots \\ \mathbf{h}^1(\mathbf{x}_M) & \mathbf{h}^2(\mathbf{x}_M) & \cdots & \mathbf{h}^P(\mathbf{x}_M) \end{bmatrix} \tag{6.79}$$

Input: $\mathbf{J} = \begin{bmatrix} \mathbf{\Lambda} & \sqrt{\mathbf{w}} \end{bmatrix}^{\mathrm{T}}$, $\mathbf{b} = \begin{bmatrix} \mathbf{0} & \Omega \end{bmatrix}^{\mathrm{T}}$, m, $i_{\max}$, tol
Output: Reduced point set $\boldsymbol{\zeta}$, Modified integration weights $\boldsymbol{\varpi}$
Initialization: $\boldsymbol{\zeta} = \varnothing$, $\mathbf{y} = \{1, 2, ..., M\}$, $\boldsymbol{\alpha} = \mathbf{0}$, $\boldsymbol{\alpha}^{\mathrm{old}} = \mathbf{0}$, $\mathbf{r} = \mathbf{b}$;
while size($\boldsymbol{\zeta}$) $\leq m$ **and** $i \leq i_{\max}$ **and** $\frac{\mathbf{r}}{\|\mathbf{r}\|} >$ tol **do**
  compute next index $j = \arg\max_{\bar{j} \in \mathbf{y}} \left(\frac{\mathbf{J}_{\bar{j}}}{\|\mathbf{J}_{\bar{j}}\|} \right)^{\mathrm{T}} \left(\frac{\mathbf{r}}{\|\mathbf{r}\|} \right)$;
  move j from $\mathbf{y}$ to $\boldsymbol{\zeta}$;
  update integration weights $\boldsymbol{\alpha}_{\boldsymbol{\zeta}} = (\mathbf{J}_{\boldsymbol{\zeta}}^{\mathrm{T}} \mathbf{J}_{\boldsymbol{\zeta}})^{-1} \mathbf{J}_{\boldsymbol{\zeta}}^{\mathrm{T}} \mathbf{b}$, $\boldsymbol{\alpha}_{\mathbf{y}} = \mathbf{0}$;
  while any element of $\boldsymbol{\alpha}_{\boldsymbol{\zeta}} < 0$ **do**
    compute return amplitude $c = \min \left(\frac{\boldsymbol{\alpha}_{\boldsymbol{\zeta}}^{\mathrm{old}}}{\boldsymbol{\alpha}_{\boldsymbol{\zeta}}^{\mathrm{old}} - \boldsymbol{\alpha}_{\boldsymbol{\zeta}}} \right)$;
    correct integration weights $\boldsymbol{\alpha}_{\boldsymbol{\zeta}} = \boldsymbol{\alpha}_{\boldsymbol{\zeta}}^{\mathrm{old}} + c(\boldsymbol{\alpha}_{\boldsymbol{\zeta}} - \boldsymbol{\alpha}_{\boldsymbol{\zeta}}^{\mathrm{old}})$;
    move to $\mathbf{y}$ all indices j from $\boldsymbol{\zeta}$ for which $\alpha_{\boldsymbol{\zeta},j} = 0$;
    update integration weights $\boldsymbol{\alpha}_{\boldsymbol{\zeta}} = (\mathbf{J}_{\boldsymbol{\zeta}}^{\mathrm{T}} \mathbf{J}_{\boldsymbol{\zeta}})^{-1} \mathbf{J}_{\boldsymbol{\zeta}}^{\mathrm{T}} \mathbf{b}$, $\boldsymbol{\alpha}_{\mathbf{y}} = \mathbf{0}$;
  end
  update $\boldsymbol{\alpha}_{\boldsymbol{\zeta}}^{\mathrm{old}} = \boldsymbol{\alpha}_{\boldsymbol{\zeta}}$, $\mathbf{r} = (\mathbf{b} - \mathbf{J}_{\boldsymbol{\zeta}} \boldsymbol{\alpha}_{\boldsymbol{\zeta}})$;
end
compute the final weights $\varpi_j = \sqrt{w_j} \alpha_{\boldsymbol{\zeta},j}$;

Algorithm 1: Nonnegative least-squares algorithm for ECM.

with $\mathbf{X}^{\mathrm{hist}} \in \mathbb{R}^{hM \times P}$ and h is the size of the history vector which may also include the stresses. In that case, the remaining history terms may be added to the already stored $\mathbf{X}^{\sigma}$ for efficiency.

The SVD is then applied to $\mathbf{X}^{\mathrm{hist}}$ in order to obtain a truncated orthonormal basis matrix $\boldsymbol{\Upsilon} \in \mathbb{R}^{hM \times p}$ for history:

$$\mathbf{X}^{\mathrm{hist}} \approx \boldsymbol{\Upsilon} \mathbf{S} \mathbf{V}^{\mathrm{T}} \tag{6.80}$$

which can be divided in a block corresponding to the reduced integration points ($\boldsymbol{\Upsilon}_{\boldsymbol{\zeta}}$) and a block corresponding to the remaining points for which history is unknown ($\boldsymbol{\Upsilon}_{\mathbf{y}}$). If only stresses are being recovered, the basis matrix $\boldsymbol{\Psi}$ of Eq. (6.75) can be used directly without performing another SVD.

After gathering the history data computed at the reduced integration point set $\boldsymbol{\zeta}$ in a vector, history at the remaining points is obtained via Gappy Data reconstruction as follows:

$$\mathbf{h}_{\mathbf{y}} = \boldsymbol{\Upsilon}_{\mathbf{y}} \left(\boldsymbol{\Upsilon}_{\boldsymbol{\zeta}}^{\mathrm{T}} \boldsymbol{\Upsilon}_{\boldsymbol{\zeta}} \right)^{-1} \boldsymbol{\Upsilon}_{\boldsymbol{\zeta}}^{\mathrm{T}} \mathbf{h}_{\boldsymbol{\zeta}} \tag{6.81}$$

with $\mathbf{h}_{\mathbf{y}} \in \mathbb{R}^{h(M-m)}$ and $\mathbf{h}_{\boldsymbol{\zeta}} \in \mathbb{R}^{hm}$. Although all right-hand side terms aside from $\mathbf{h}_{\boldsymbol{\zeta}}$ can be pre-computed, this recovery approach is still dependent on the full size of the mesh (since $m \ll M$) and may become inefficient if h is large — which incidentally is the case for a VE/VP material with multiple Prony elements for which hereditary stresses have to be stored.

An alternative to improve the efficiency of the recovery procedure consists in dividing the points in $\mathbf{y}$ into k clusters, where $k \ll (M-m)$, and assuming that all points inside

a given cluster have the same history. The recovery problem is therefore reduced to determining $\mathbf{h}$ for each cluster:

$$\mathbf{h}_{\mathscr{C}} = \boldsymbol{\Upsilon}_{\mathscr{C}} \left(\boldsymbol{\Upsilon}_{\boldsymbol{\zeta}}^{\mathrm{T}} \boldsymbol{\Upsilon}_{\boldsymbol{\zeta}} \right)^{-1} \boldsymbol{\Upsilon}_{\boldsymbol{\zeta}}^{\mathrm{T}} \mathbf{h}_{\boldsymbol{\zeta}} \tag{6.82}$$

where $\mathbf{h}_{\mathscr{C}} \in \mathbb{R}^{hk}$ and $\boldsymbol{\Upsilon}_{\mathscr{C}} \in \mathbb{R}^{hk \times p}$ is a compressed version of $\boldsymbol{\Upsilon}_{\mathbf{y}}$ now containing the average cluster response for each loading scenario.

In the present approach, instead of building clusters using the Euclidean distance between points (*e.g.* a Voronoi diagram), the Frobenius norm of the difference between the basis matrix of a point and the cluster average is used as objective function in an optimization procedure:

$$(\mathscr{C}, \boldsymbol{\Upsilon}_{\mathscr{C}}) = \underset{\overline{\mathscr{C}}}{\arg\min} \sum_{i=1}^{k} \sum_{j \in \mathbf{c}^i} \left\| \boldsymbol{\Upsilon}_j - \boldsymbol{\Upsilon}_{\mathscr{C}}^i \right\|^2 \tag{6.83}$$

where $\mathscr{C}$ is a matrix containing the indices of points inside the k clusters $\mathbf{c}^i$:

$$\mathscr{C} = \begin{bmatrix} \mathbf{c}^1 & \mathbf{c}^2 & \cdots & \mathbf{c}^k \end{bmatrix} \tag{6.84}$$

$\boldsymbol{\Upsilon}_j \in \mathbb{R}^{h \times q}$ is a block matrix corresponding to integration point j extracted from $\boldsymbol{\Upsilon}_{\mathbf{y}}$ and $\boldsymbol{\Upsilon}_{\mathscr{C}}^i \in \mathbb{R}^{h \times q}$ is the centroid of the i-th cluster. The clustering procedure is performed using the classical Lloyd's algorithm [26], the steps of which are presented in Algorithm 2 for completeness.

Input: Basis matrix of non-ECM points $\boldsymbol{\Upsilon}_{\mathbf{y}}$, number of clusters k
Output: Cluster set $\mathscr{C}$, compressed basis $\boldsymbol{\Upsilon}_{\mathscr{C}}$
Initialization: Select k random points from $\mathbf{y}$ as centroids;
while $\mathscr{C}^{\mathrm{old}} \neq \mathscr{C}$ **do**
  $\mathscr{C}^{\mathrm{old}} = \mathscr{C}$;
  for each j in $\mathbf{y}$ **do**
    move point to cluster $i = \underset{\bar{i}}{\arg\min} \left\| \boldsymbol{\Upsilon}_j - \boldsymbol{\Upsilon}_{\mathscr{C}}^{\bar{i}} \right\|^2$;
  end
  for each $\mathbf{c}^i$ in $\mathscr{C}$ **do**
    update centroid $\boldsymbol{\Upsilon}_{\mathscr{C}}^i = \dfrac{1}{N_i} \sum_{j \in \mathbf{c}^i} \boldsymbol{\Upsilon}_j$;
  end
end

Algorithm 2: k-means clustering procedure for history recovery.

6.4.5. ADAPTIVE POD

One last analysis strategy combining Time Homogenization and POD is proposed. Since TH guarantees that the microchronological cycles are purely VE, it follows that a POD

basis which correctly represents the structure's behavior at the beginning of a micro cycle will maintain its accuracy during at least the entirety of the cycle.

This observation motivates the use of an adaptive reduction scheme: The analysis starts unreduced until the first macrochronological point is reached. The obtained snapshots are then gathered and the SVD is performed in order to obtain a POD basis. From this point on, all micro steps are reduced and all macro steps are unreduced. After each macro step, the model is checked for plastic strain development. If this is detected, the current POD basis is updated to include the latest full model response. The macrochronological displacement field $\mathbf{u}$ is projected on the current base by means of a Gram-Schmidt process:

$$\mathbf{v} = \mathbf{u} - \sum_{i=1}^{n} \boldsymbol{\phi}_i^{\mathrm{T}} \mathbf{u} \boldsymbol{\phi}_i \tag{6.85}$$

and the resulting mode is included in the basis. If the number of snapshots exceeds a user-determined limit, the oldest live snapshot is removed. Such a scheme exploits features of both TH and POD and requires no *offline* training, being useful in situations for which the loading path is not known *a priori*. Although the examples in this work are confined to a scheme that updates the POD basis every time further plastic strain is developed, variations of the method can be developed in which updating is performed less frequently. Due to this high update frequency, which would imply the execution of Algorithm 1 at every macrochronological step, ECM is not included in the present adaptive scheme.

6.5. RESULTS AND DISCUSSION

The numerical techniques presented in Sections 6.3 and 7.4.3 were implemented in in-house Finite Element software built using the open-source Jem/Jive C++ numerical analysis library [27]. In this section, each of the techniques is applied to the solution of microscopic boundary-value problems in laminate composites and their performance is assessed in terms of acceleration and retention of accuracy. The material properties used in all examples are shown in Table 6.1. The micromodels consist of unidirectional fibers embedded in resin in plane strain conditions. Periodic geometries with pseudo-random fiber arrangements were generated using the discrete element package HADES [22] and meshed with Gmsh [28]. Micromodel sizes ranging from a unit cell with a single fiber to domains with 7×7 fibers are used in the examples.

First-order (3-node) triangular elements are used in all micromechanical examples. It should be noted in passing that using first-order elements, especially in coarse meshes, may lead to irregular stress distributions that can influence plastic strain development. This issue is, however, left out of the scope of the present work, which instead focuses on the additional losses in accuracy caused by the acceleration techniques of Sections 6.3 and 7.4.3. In using these methods, it is therefore assumed that the full-order model used as basis for constructing the faster reduced models has an adequate level of fidelity.

When cyclic loads are treated, the following general load characteristic is adopted:

$$at + b(t) \sin\left(\frac{2\pi t}{T}\right) + c \tag{6.86}$$

Linear-elastic glass fibers ([29])				
K [MPa]	43452			
G [MPa]	29918			
Viscoelastic/viscoplastic epoxy resin (5)				
K_∞ [MPa]	3205			
G_∞ [MPa]	912			
K_u [MPa]	125	182	625	143
G_ν [MPa]	36	52	178	41
k_u [s]	$4.16\cdot10^{-2}$	$2.30\cdot10^{0}$	$4.22\cdot10^{1}$	$3.11\cdot10^{4}$
g_ν [s]	$1.46\cdot10^{-1}$	$8.08\cdot10^{0}$	$1.48\cdot10^{2}$	$1.09\cdot10^{5}$
σ_t [MPa]	$64.80-33.6\mathrm{e}^{-\epsilon^\mathrm{p}_\mathrm{eq}/0.003407}-10.21\mathrm{e}^{-\epsilon^p_\mathrm{eq}/0.06493}$			
σ_c [MPa]	$81.0-42.0\mathrm{e}^{-\epsilon^\mathrm{p}_\mathrm{eq}/0.003407}-12.77\mathrm{e}^{-\epsilon^p_\mathrm{eq}/0.06493}$			
η_p [s]	$3.49\cdot10^{12}$			
m_p [-]	7.305			
ν_p [-]	0.32			

Table 6.1: Material properties used in the numerical examples.

where T is the load period and the coefficients a, b and c vary in the examples. Loads are applied as prescribed displacements to the corner nodes of the micromodel and represent a macroscopic strain value that is constant inside the micro domain. Periodic boundary conditions are applied to the edges of the micromodel in order to simulate the behavior of a macroscopic material point [22]. The results presented here are therefore representative of using these acceleration techniques in an FE^2 context. All examples are executed on a single core of a Core i7-7500U processor on a machine with 8GB RAM running Ubuntu 16.04.3. The reported speed-ups are the average of three executions.

6.5.1. TIME HOMOGENIZATION

Before applying the time homogenization (TH) technique to a micromodel, it is first used in a one-element mesh. Since time homogenization is applied directly at the constitutive model level, a one-element model can be used to obtain knowledge on its advantages and drawbacks.

First, time-step dependency of a full VE/VP model is illustrated. A cyclic strain ε_{xx} with shape $a = 0$, $b = 1.125\times10^{-2}$, $c = 1.375\times10^{-2}$ and period $T = 0.01$ s is applied and the full model (TH deactivated) was executed until $t = 40$ s, for a total of 4000 cycles. The model is executed with different numbers of steps per cycle (*i.e.* with Δt ranging from 0.01 s to 0.0005 s). Fig. 6.2 shows the evolution of stresses in the last load cycle.

It is interesting to note that the one-step curve essentially models the cyclic strain as a relaxation test, with a significant plastic strain overshoot (8.3 % lower stress). The retardation effect caused by cycling the strain instead of holding it is lost. As more points are added, better predictions of the plastic strain are obtained. This illustrates the importance of using appropriately sized time steps for time-dependent materials. The po-

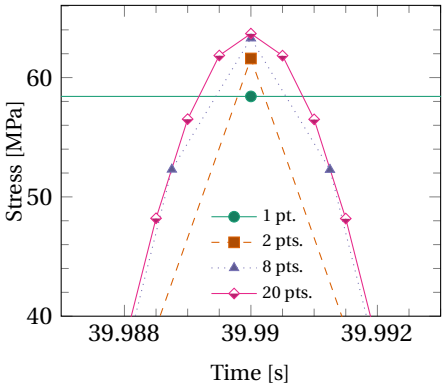

Figure 6.2: Full model performance with varying number of steps per cycle.

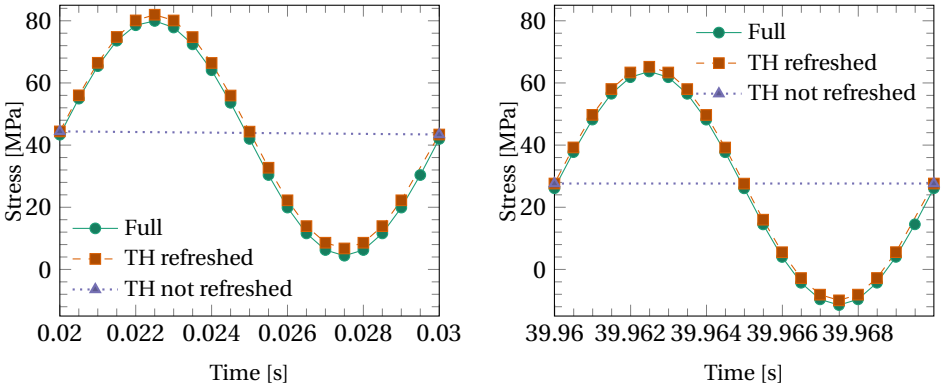

Figure 6.3: Comparison between full and TH responses.

tential of TH lies in reducing the computational effort of the analysis while maintaining the original number of time steps.

The same example is also run with time homogenization. Since the amplitude of the microscopic loading does not change with time, it is possible to both run the microchronological steps for every load cycle (*TH refreshed*) or alternatively compute the microscopic stresses only once and skip refreshing their values for the rest of the analysis (*TH not refreshed*). In Fig. 6.3, the graph on the left shows the response during the second load cycle while the one on the right shows the response during the last cycle. As expected, VE/VP relaxation leads to drops in peak and valley stresses even though the load has constant mean and amplitude. Use of TH results in differences in stress of approximately 1.5 MPa and a relative error of approximately 2.3 % with respect to the full solution. This difference is constant throughout the analysis, in contrast with the observations made by Haouala and Doghri [2] who obtained significantly higher differences during the first cycles. This may be due to the choice of numerical time integration (1-point Gauss in [2] versus trapezoidal integration here). Skipping all microchronolog-

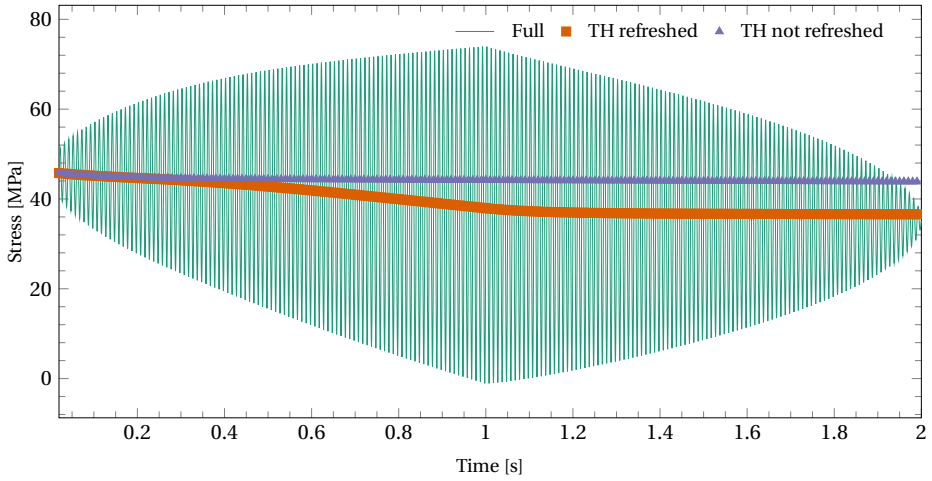

Figure 6.4: Time homogenization of variable-amplitude loading: Effect of refreshing $\tilde{\boldsymbol{\sigma}}$.

ical cycles except the first one results in the same solution but requires significantly less equilibrium steps. In this case, only the solution is only computed for the macrochronological steps, but the original homogenized curve would be readily recovered by adding the stored values of $\tilde{\boldsymbol{\sigma}}$.

Although computing the microchronological part of the loading only once leads to higher speed-ups (≈ 18 versus 1.3 when refreshing $\tilde{\boldsymbol{\sigma}}$ every cycle), this strategy becomes unsuitable for cases when the microscopic loading depends on the macroscopic time (*e.g.* variable-amplitude loading). In order to illustrate this effect, the applied strain is modified by making $b = 1.125 \times 10^{-2}\sqrt{t}$ for $0\,\mathrm{s} \leq t \leq 1\,\mathrm{s}$ and $b = 1.125 \times 10^{-2}\sqrt{2-t}$ for $1\,\mathrm{s} \leq t \leq 2\,\mathrm{s}$. The results can be seen in Fig. 6.4, where TH responses shown as $\langle \sigma_{xx} \rangle$ to avoid clutter. For this loading scenario, keeping the $\tilde{\boldsymbol{\sigma}}$ values for the first cycle throughout the analysis leads to a significant overshoot in stress response, while refreshing it leads to better predictions.

Finally, TH is applied to a micromodel with 2×2 fibers to which a horizontal cyclic displacement with increasing mean is applied to its bottom-right corner node ($a = 5 \times 10^{-4}$, $b = 5.625 \times 10^{-5}$, $c = 6.875 \times 10^{-5}$). The resultant load is obtained by summing up the horizontal internal force components at the right edge of the micromodel. Fig. 6.5 shows the obtained results. Both *Refreshed* and *Not refreshed* responses are found to be accurate, with a difference of approximately 1.1 % with respect to the full response. It is interesting to note that, even though the mean displacement is increasing, the microchronological cycle is constant and computing it only once for the complete analysis does not bring additional loss of accuracy.

6.5.2. REDUCED-ORDER MODELING

PROPER ORTHOGONAL DECOMPOSITION (POD)

First, the performance of POD in isolation is assessed. A 2×2-fibers micromodel is subjected to uniaxial tension with a linearly-increasing deformation ε_{xx} ($a = 5 \times 10^{-2}$, $b =$

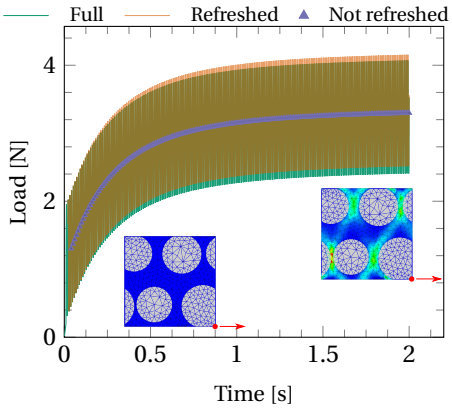

Figure 6.5: Time homogenization applied to a micromodel. Full and homogenized responses.

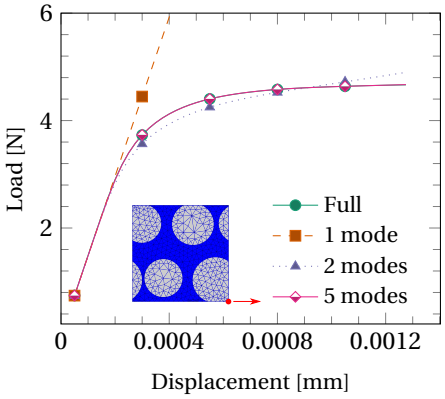

Figure 6.6: Reduced model response after POD-reduction

$c = 0$) until plastic strain starts to localize in bands and the global response is perfectly-plastic. Applying the SVD to the collected displacement snapshots, a series of reduced models with increasing number of modes is obtained. Fig. 6.6 shows the full model response along with the reduced response with 1, 2 and 5 modes. Using the elastic/inelastic decomposition of Eq. (6.56), the elastic response of the model is always exactly captured with a single mode. As expected, this single mode loses precision as plastic strain develops, requiring the presence of additional modes. For this micromodel and loading type, using 5 modes (1 elastic and 4 inelastic) yields a maximum relative error of 0.44 % with respect to the full solution. Fig. 6.7a shows the evolution of the error as additional modes are added.

Keeping a constant number of modes (1 elastic and 4 inelastic), the resultant acceleration caused by reducing the size of the global equilibrium problem for different micromodel sizes ranging from a unit cell (1×1) to a micromodel with 49 fibers (7×7) is shown in Fig. 6.7b. As expected, the acceleration increases with micromodel size as the number

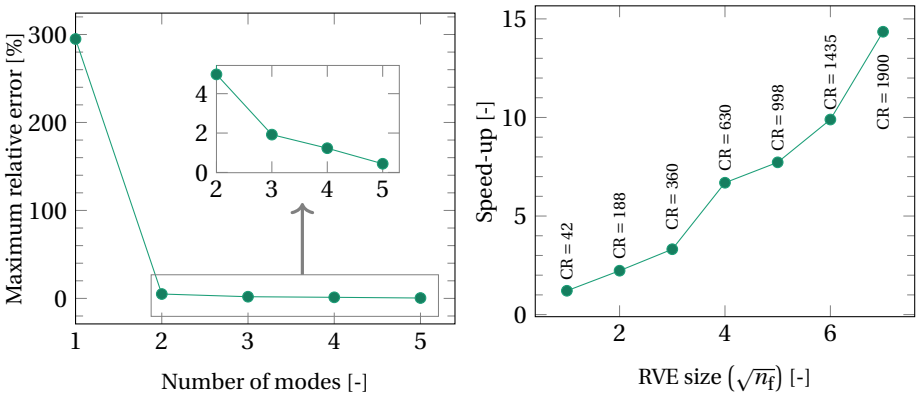

(a) Error with number of modes

(b) Speed-up with RVE size

Figure 6.7: Precision and acceleration of a POD-reduced model.

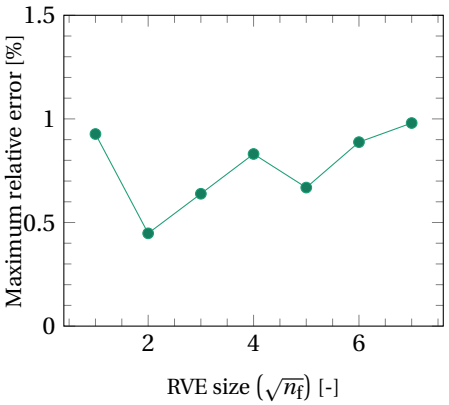

Figure 6.8: Precision of the POD-reduced model for increasingly large micromodels.

of degrees of freedom increases but the number of modes is kept constant (resulting in a higher compression ratio CR = $\frac{N}{n}$). With an acceleration of up to 15 times, the POD speed-ups obtained in the current study are significantly higher than the ones reported by Hernández *et al.* [12], who report a speed-up of 2 for a model with $N = 92326$ and CR = 9217. Finally, the maximum relative error in load-displacement behavior for $n = 5$ and different micromodel sizes are plotted in Fig. 6.8. It is observed that the error caused by the POD reduction remains small irrespective of the RVE size. Since POD modes are constructed with the global displacement field of the micromodel, the precision of the method does not depend on N. In practice, this allows for increasing the size of the microdomain — which largely determines its ability to correctly represent a macroscopic material point — without sacrificing accuracy or efficiency.

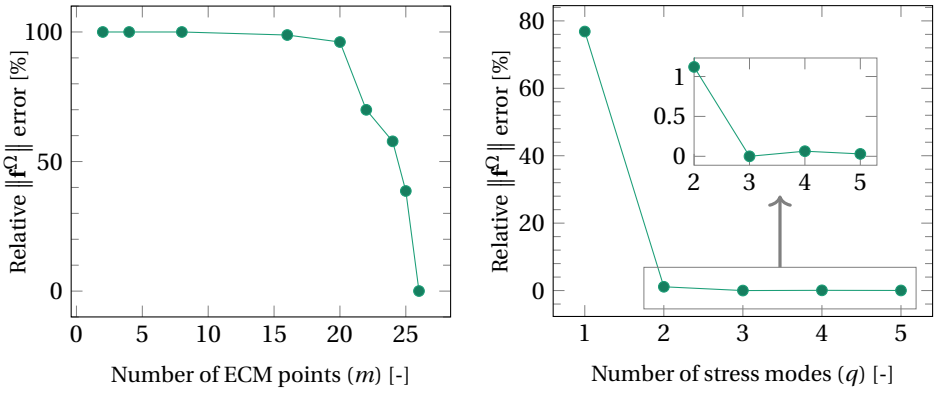

(a) Number of points m

(b) Number of stress modes q ($m = nq + 1$)

Figure 6.9: Precision of the ECM-reduced model with the number of points and stress modes.

EMPIRICAL CUBATURE METHOD (ECM)

Moving to the hyper-reduced model based on the ECM approach of Section 6.4.3, the first investigation considers the performance of the nonnegative least squares procedure of Algorithm 1. Using the same micromodel as the one of Fig. 6.6, the $n = 5$ POD model is used as a first reduction phase, and $q = 5$ stress modes are used in the SVD of Eq. (6.75), resulting in a $\mathbf{J}$ matrix with 26 columns. The selection algorithm is truncated at different values of m. The resultant hyper-reduced model is run and the relative error in the global internal force vector at the last analysis step is computed as $\frac{\|\mathbf{f}^{\Omega}_{\text{ECM}} - \mathbf{f}^{\Omega}_{\text{POD}}\|}{\|\mathbf{f}^{\Omega}_{\text{POD}}\|}$. Results are shown in Fig. 6.9a. The point selection algorithm progressively reduces the integration error, reducing to 0.03 % when 26 ($nq+1$) points are selected, at which point $\mathbf{J}_{\zeta}$ becomes a square matrix and the mesh volume is exactly integrated. Although such low integration error effectively guarantees an excellent approximation for the reduced internal force vector, the convergence behavior of the selection algorithm shows a departure from the asymptotic convergence observed by Hernández *et al.* [12]. Assuming the selection algorithm was correctly implemented, this difference may indicate that the performance of a truncated ECM-reduced model is problem-dependent.

The number of stress modes q also impacts the quality of the approximated integral. Fig. 6.9b shows the resultant integration error for different values of q while maintaining $nq + 1$ ECM points. As expected, if only a single (elastic) stress mode is used, the hyper-reduced approximation of the internal force vector is inaccurate. This error quickly moves to zero as more modes are added.

Keeping $n = q = 5$ (resulting in 26 integration points), the obtained analysis speed-up as the micromodel size increases is shown in Fig. 6.10a. Once again the speed-up increases with micromodel size as the number of integration points M increases together with the compression ratio $\text{CR} = \frac{M}{m}$, with a value as high as 120 for a 7×7 micromodel.

One last interesting aspect that drives ECM performance is the number of loading scenarios included in the training set. The importance of including additional loading cases when training both POD and ECM is illustrated in Fig. 6.11. The equivalent plas-

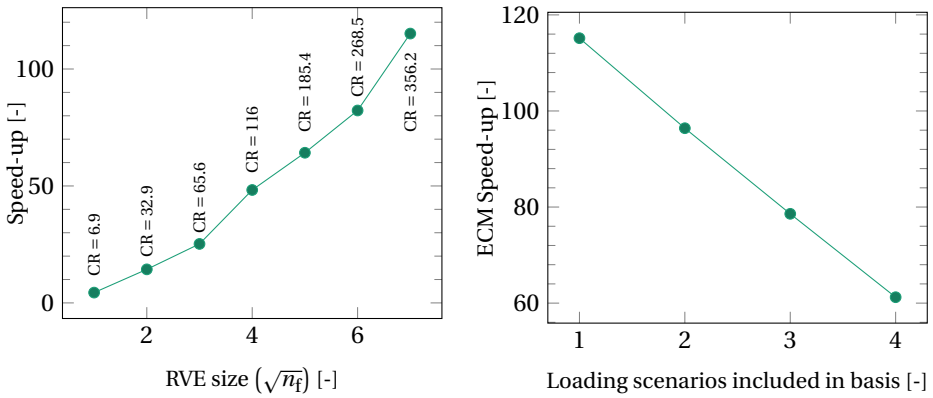

(a) One loading scenario, different RVE sizes. (b) 7 x 7 RVE, different no. of loading scenarios.

Figure 6.10: ECM speed-ups for different micromodel sizes and number of loading scenarios in basis.

tic strain field on the left was obtained by running the full model of a 5×5 micromodel subjected to biaxial tension loading indicated by the red arrows. Including both horizontal and vertical load cases in the reduced basis ($n = 10$) and running the resultant POD-reduced model yields the erroneous field shown on the right. Even though the initial linear behavior is correctly captured by the snapshots of both longitudinal load cases in isolation, a spurious strain localization behavior is obtained at higher strains.

For most practical applications, it is therefore necessary to include a large number of loading scenarios when training a reduced model, which leads to an increased number of reduced DOFs n and consequently to a higher number of integration points m. Fig. 6.10b shows that the resultant speed-up is significantly impacted by such extended training. This highlights the importance of developing adaptive reduction methods which can improve their predictions on-the-fly [6, 7, 19, 20].

GAPPY DATA AND K-MEANS CLUSTERING

The investigation moves to the history recovery procedure based on the Gappy Data reconstruction and the k-means clustering method. Fig. 6.12 shows the result of the clustering process in a 5×5 micromodel with different values of k and a history vector of size 30 (including stresses, strains, plastic strains, equivalent plastic strain and hereditary stresses). The history snapshots are stored together with the stress snapshots used for ECM training, in this case for a longitudinal tensile loading. Similar to the ones obtained by Liu *et al.* [15], the clusters are irregular and disconnected.

Using the compressed Gappy Data process to reconstruct the equivalent plastic strain field of a longitudinal tensile test yields the fields shown in Fig. 6.14. This post-localization field is especially challenging for reconstruction, as the clustered micromodel has difficulty to reproduce the observed localization bands. Instead, a diffuse distribution of strain is predicted for models with low k. For 100 clusters, the band patterns start to be correctly reproduced, although some diffusion is still noted. The clustering procedure produces better results if the original field also exhibits a diffuse behavior, as seen

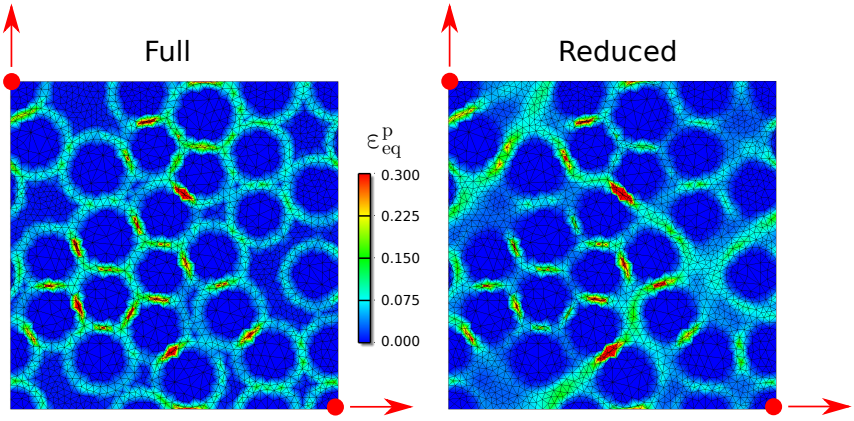

Figure 6.11: Erroneous post-localization response of a reduced model with incomplete basis.

in Fig. 6.15 for the plastic strain field prior to localization. However, even for localized bands, an increase of the number of clusters leads to better reconstructions. Using the same compressed Gappy Data matrix, the stresses in the resin are also reconstructed (Fig. 6.16).

Finally, Fig. 6.13 shows the additional time spent with history reconstruction as the number of clusters increases. Using the original Gappy Data reconstruction approach without the clustering leads to a increase of 200 % in execution time due to the very large matrix operations involved in the reconstruction process. This effectively negates a significant part of the speed-up obtained through POD and ECM. On the other hand, compressing the reconstruction matrix through clustering makes the reconstruction operation significantly more efficient, with up to only 15 % increase in execution time for 100 clusters. Here, the compression ratio is given by $\mathrm{CR} = \frac{k}{M-m}$.

ADAPTIVE POD

The performance of the adaptive POD scheme of Section 6.4.5 is assessed by returning to the final example of Section 6.5.1. The results of the adaptive method (*A-POD*) are compared with the ones obtained with TH in isolation and by solving the micro cycles with a POD model ($n = 2$) trained *online* with data from the first micro cycle but not updated as the analysis progressed. For the adaptive model, a limit of 1 elastic mode and 1 adaptive mode is adopted. The curves for the first 0.25 s of loading are shown in Fig. 6.17.

As expected, the non-refreshed POD model loses precision as the analysis progresses. The incorrect displacement modes used during the micro cycles also degrade the solution quality of the fully-solved macro steps (indicated by markers). On the other hand, the adaptive model yields exactly the same solution as the TH model.

6.5.3. COMBINING THE METHODS

After establishing the capabilities of time homogenization and reduced order modeling separately, they are now combined in solving a practical case of micromechanical analy-

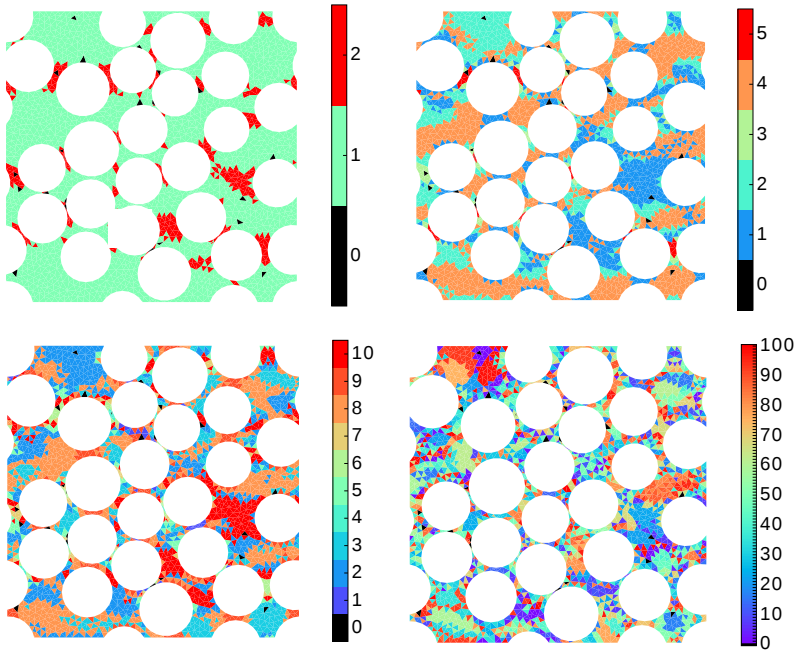

Figure 6.12: Clustering of a 5×5 RVE with $k = 2, 5, 10, 100$. ECM points are shown in black as cluster 0.

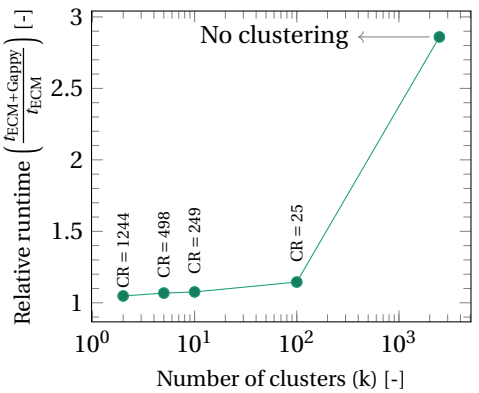

Figure 6.13: Additional runtime required for history reconstruction with different k values (5×5 RVE).

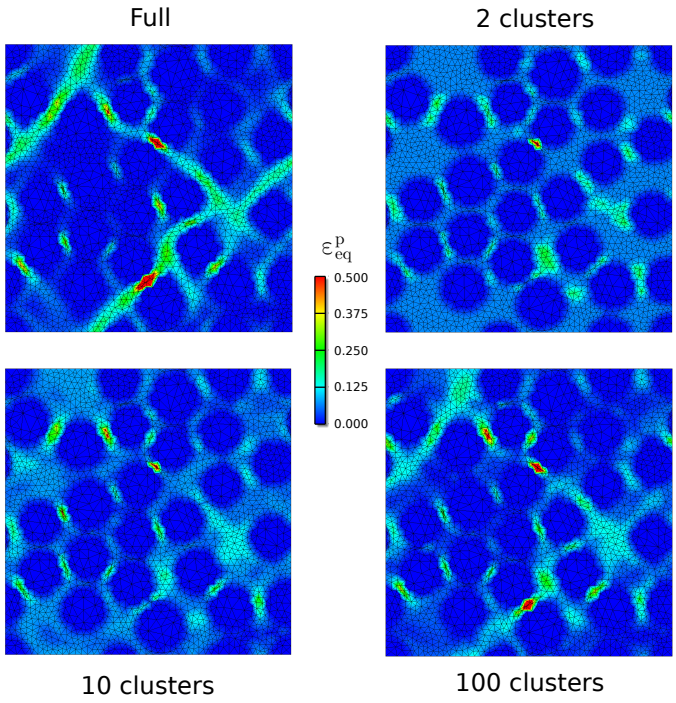

Figure 6.14: Equivalent plastic strain response at localization for different values of k.

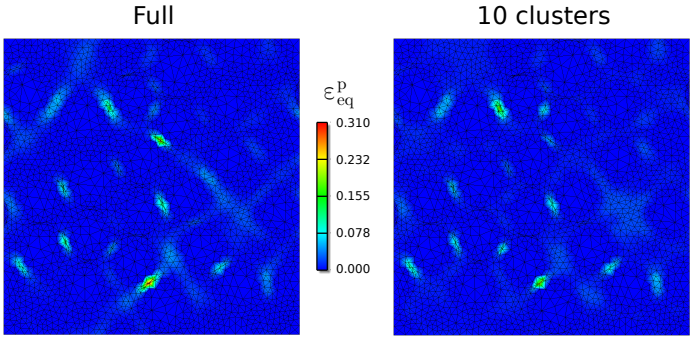

Figure 6.15: Equivalent plastic strain response prior to localization for $k = 10$.

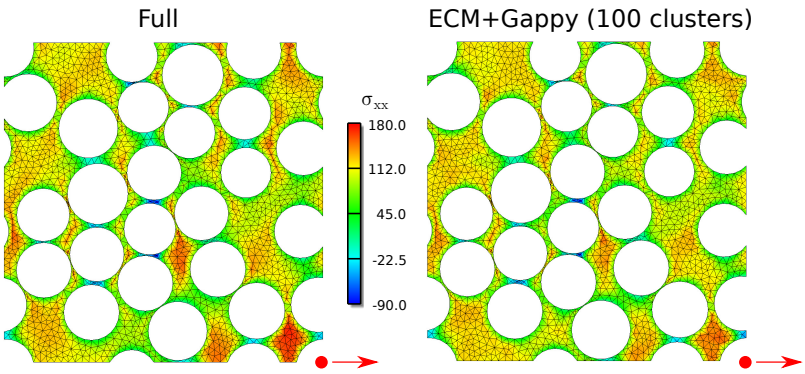

Figure 6.16: Stresses in the resin at localization: Full and ECM ($k = 100$) responses.

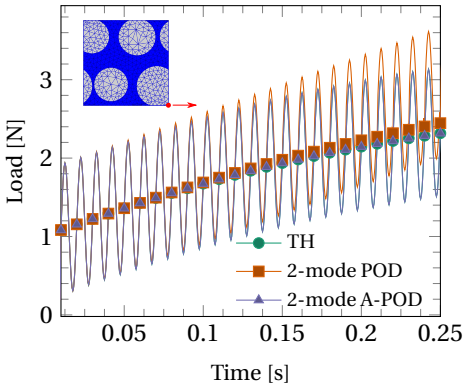

Figure 6.17: Adaptive POD response compared to TH response.

sis of a micromodel subjected to cyclic loads. The problem involves the analysis of a 7×7 micromodel subjected to a horizontal tensile cyclic displacement described by Eq. (6.86) with $a = 5 \times 10^{-4}$, $b = 5.625 \times 10^{-5}$, $c = 6.875 \times 10^{-5}$ and $T = 0.01$ s, identical in shape to the one used in Fig. 6.5. The analysis is stopped when a time $t = 5$ s is reached.

Method	Recovery	Refreshed $\widetilde{\boldsymbol{\sigma}}$	Error [%]	Runtime [s]	Speedup [-]
Full	N/A	N/A	-	19440	1.0
TH	N/A	Yes	0.68[a]	6538	2.97
Adaptive POD	N/A	N/A	0.68[a]	3691	5.27
TH	N/A	No	0.68[a]	3144	6.18
TH + POD	N/A	Yes	1.19[a]	974	19.9
TH + POD + ECM	Unclustered	Yes	0.25[b]	604	32.2
TH + POD	N/A	No	1.19[a]	452	42.9
TH + POD + ECM	$k = 100$	Yes	0.25[b]	134	145.0
TH + POD + ECM	None	Yes	0.25[b]	111	174.9
TH + POD + ECM	$k = 100$	No	0.25[b]	17.9	1086.4
TH + POD + ECM	None	No	0.25[b]	16.6	1167.8

[a]Error computed from the load-displacement behavior with the full solution as reference.
[b]Additional error computed from the reduced $\mathbf{f}^{\Omega}$ vector with the POD solution as reference

Table 6.2: Runtimes obtained using different combinations of techniques.

Table 6.2 shows the obtained execution times for the problem at hand by using different combinations of TH, POD, ECM and clustering. All models that required training are trained by subjecting the micromodel to a monotonically increasing horizontal tensile loading until a perfectly plastic response is obtained. History recovery is performed both with $k = 100$ and through unclustered Gappy Data. Since the accuracy of the methods was already investigated in the previous sections, this example is only concerned with speed-ups.

It is interesting to note that, for this specific load case, only time homogenization in isolation, with a speed-up of approximately 3, allowed for larger time savings than for the cases considered in Section 6.5.1. The speed-up is related to the fact that, as the mean load increases, all microchronological stress points actually lie above the yield surface, which results in a large number of Newton-Raphson iterations in the full analysis. The TH model, on the other hand, solves a purely VE problem for every microchronological time step which does not need any iterations. The adaptive POD strategy takes longer to run than a non-refreshed TH model without ROM. It should be noted, however, that the adaptive POD would prove advantageous if a variable-amplitude loading was considered. Furthermore, the adaptive strategy requires no offline training and still provides reasonable acceleration without additional sources of error.

Combining POD with the time homogenized model increases the speed-up to 20 and 42 for the cases with refreshed and not refreshed microscale stresses, respectively. The effect of precomputing $\widetilde{\boldsymbol{\sigma}}$ brings an additional speed-up of approximately 2, in contrast with the additional acceleration of about 14 obtained in the one-element tests of

Section 6.5.1. In this case, the large number of iterations required for each macro step dominates the execution time, making the influence of the linear micro steps less pronounced.

Very large speed-ups are obtained by also adding ECM, with combined speed-ups that exceed a factor 1000. Interestingly, the additional acceleration obtained by skipping microchronological steps is higher again for this case, with a factor of almost 7. Since ECM speed-ups are proportional to the computational cost of the constitutive model, it is less effective in reducing the computational effort of the already inexpensive microchronological steps. These consequently account for a significant portion of the total execution time, making the choice for precomputation more effective.

Due to the large number of history variables, performing an unclustered Gappy Data procedure negates most of the speed-up offered by ECM and makes history recovery at every step impractical. On the other hand, the additional time required for history reconstruction with $k = 100$ falls in line with the results reported in Fig. 6.13.

It is concluded that combining the different acceleration techniques drastically improves the feasibility of having fast and accurate predictions of material behavior even when complex time-dependent material models are used and a large number of load cycles is simulated. The results are also promising in mitigating the high computational demands of concurrent multiscale analysis (FE^2). However, the limitations of each acceleration technique must be kept in mind in order to avoid introducing additional approximation errors:

- For time homogenization, the loading must be periodic (Eq. (6.17)) and the separation of time scales principle should hold (Eq. (6.15). The computation of the microchronological cycle can only be skipped if the micro loads do not change with time.

- For POD and ECM, it is important to include all relevant load cases in the training process, and special care must be taken if the analysis moves into the strain localization regime. In this regard, adaptive techniques such as the *Adaptive POD* proposed here, the domain partition strategy proposed by Kerfriden *et al.* [20] or the machine learning techniques presented by Ghavamian *et al.* [7] may be used.

6.6. CONCLUSIONS

This chapter explored a number of techniques used to accelerate the solution of an FE stress equilibrium problem when large numbers of load cycles are considered. The techniques of Time Homogenization (TH), Proper Orthogonal Decomposition (POD) and Empirical Cubature Method (ECM) were presented and analyzed. An efficient material history recovery technique was developed combining Gappy Data reconstruction with a k-means clustering algorithm. An adaptive ROM strategy was proposed combining the advantages of TH and POD which avoids the need to train the reduced model before the analysis.

Time homogenization allows for the plastic strain evolution to be computed only once per load cycle. Furthermore, if the microchronological cycle does not change throughout the analysis, it may be computed only once at the beginning of the analysis, leading

to further acceleration. For the load scenarios considered in the examples, the loss of accuracy after homogenization was very limited (between 1.1 % and 2.3 %). The resultant speed-up is highly dependent on the number of microchronological points that cross the yield surface, with values as high as 3.0 obtained for a 7×7 micromodel loaded in transverse tension with increasing mean.

Reduction by projection (POD) was also found to correctly reproduce the behavior of the full model, if enough basis vectors are used. The number of necessary displacement modes increases when the micromodel reaches a plastic strain localization regime. Moreover, the shape of the strain localization bands is highly dependent on the load shape. Failure to include a certain load combination in the basis can lead to erroneous plastic strain distributions at higher strains, even if all load directions are included in isolation. Employing POD in isolation, speed-ups as high as 15 were found for 7×7 micromodels.

The hyper-reduction strategy based on the Empirical Cubature method offers accurate approximations of the global internal force vector using only a small fraction of the integration points, with errors as low as 0.03 % and speed-ups as high as 120. Live reconstruction of the history variables through Gappy Data and *k*-means clustering yields promising results, even though a relatively large number of clusters was necessary to correctly reproduce localized plastic strain patterns. For a case where the microchronological response could be precomputed, the combination of time homogenization with hyper-reduction and the proposed history recovery method resulted in speed-up values higher than 1000.

REFERENCES

[1] I. B. C. M. Rocha, F. P. van der Meer, and L. J. Sluys, *Efficient micromechanical analysis of fiber-reinforced composites subjected to cyclic loading through time homogenization and reduced-order modeling,* Computer Methods in Applied Mechanics and Engineering **345**, 644 (2019).

[2] S. Haouala and I. Doghri, *Modeling and algorithms for two-scale time homogenization of viscoelastic-viscoplastic solids under large numbers of cycles,* International Journal of Plasticity **70**, 98 (2015).

[3] C. Oskay and J. Fish, *Fatigue life prediction using 2-scale temporal asymptotic homogenization,* International Journal for Numerical Methods in Engineering **61**, 329 (2004).

[4] Q. Yu and J. Fish, *Temporal homogenization of viscoelastic and viscoplastic solids subjected to locally periodic loading,* Computational Mechanics **29**, 199 (2002).

[5] R. D. Cook, D. S. Malkus, M. E. Plesha, and R. J. Witt, *Concepts and applications of finite element analysis* (John Wiley and Sons, 2001).

[6] P. Kerfriden, P. Gosselet, S. Adhikari, and S. P. A. Bordas, *Bridging proper orthogonal decomposition methods and augmented newton-krylov algorithms: An adaptive model order reduction for highly nonlinear mechanical problems,* Computer Methods in Applied Mechanics and Engineering **200**, 850 (2011).

[7] F. Ghavamian, P. Tiso, and A. Simone, *POD-DEIM model order reduction for strain-softening viscoplasticity,* Computer Methods in Applied Mechanics and Engineering **317**, 458 (2017).

[8] R. A. van Tuijl, J. J. C. Remmers, and M. G. D. Geers, *Integration efficiency for model reduction in micro-mechanical analyses,* Computational Mechanics , 1 (2017).

[9] S. Chaturantabut and D. C. Sorensen, *Nonlinear model reduction via discrete empirical interpolation,* SIAM Journal on Scientific Computing **32**, 2737 (2010).

[10] P. Astrid, S. Weiland, K. Willcox, and T. Backx, *Missing point estimation in models described by proper orthogonal decomposition,* IEEE Transactions on Automatic Control **53**, 2237 (2008).

[11] R. Everson and L. Sirovich, *Karhunen-Loeve procedure for gappy data,* Journal of the Optical Society of America A **12**, 1567 (1996).

[12] J. A. Hernández, M. A. Caicedo, and A. Ferrer, *Dimensional hyper-reduction of nonlinear finite element models via empirical cubature,* Computer Methods in Applied Mechanics and Engineering **313**, 687 (2017).

[13] S. An, T. Kim, and D. James, *Optimizing cubature for efficient integration of subspace deformations,* ACM Transactions on Graphics **27**, 165 (2009).

[14] C. Farhat, P. Avery, T. Chapman, and J. Cortial, *Dimensional reduction of nonlinear finite element dynamic models with finite rotations and energy-based mesh sampling and weighting for computational efficiency,* International Journal for Numerical Methods in Engineering **98**, 625 (2014).

[15] Z. Liu, M. Bessa, and W. K. Liu, *Self-consistent clustering analysis: An efficient multi-scale scheme for inelastic heterogeneous materials,* Computer Methods in Applied Mechanics and Engineering **306**, 319 (2016).

[16] H. Flórez and M. Argáez, *A model-order reduction method based on wavelets and pod to solve nonlinear transient and steady-state continuation problems,* Applied Mathematical Modelling **53**, 12 (2018).

[17] R. Crouch, C. Oskay, and J. Fish, *Multiple spatio-temporal scale modeling of composites subjected to cyclic loading,* Computational Mechanics **51**, 93 (2013).

[18] C. Oskay and J. Fish, *Eigendeformation-based reduced order homogenization for failure analysis of heterogeneous materials,* Computer Methods in Applied Mechanics and Engineering **196**, 1216 (2007).

[19] P. Kerfriden, J. C. Passieux, and S. P. A. Bordas, *Local/global model order reduction strategy for the simulation of quasi-brittle failure,* International Journal for Numerical Methods in Engineering **89**, 154 (2012).

[20] P. Kerfriden, O. Goury, T. Rabczuk, and S. P. A. Bordas, *A partitioned model order reduction approach to rationalise computational expenses in nonlinear fracture mechanics,* Computer Methods in Applied Mechanics and Engineering **256**, 169 (2013).

[21] A. R. Melro, P. P. Camanho, F. M. Andrade Pires, and S. T. Pinho, *Micromechanical analysis of polymer composites reinforced by unidirectional fibres: Part I - Constitutive modelling,* International Journal of Solids and Structures **50**, 1897 (2013).

[22] F. P. van der Meer, *Micromechanical validation of a mesomodel for plasticity in composites,* European Journal of Mechanics - A/Solids **60**, 58 (2016).

[23] C. Miehe, J. Schotte, and J. Schröder, *Computational micro-macro transitions and overall moduli in the analysis of polycrystals at large strains,* Computational Materials Science **16**, 372 (1999).

[24] J. A. Hernández, J. Oliver, A. Huespe, M. Caicedo, and J. Cante, *High-performance model reduction techniques in computational multiscale homogenization,* Computer Methods in Applied Mechanics and Engineering **276**, 149 (2014).

[25] C. L. Lawson and R. J. Hanson, *Solving Least Squares Problems* (SIAM, 1974).

[26] S. P. Lloyd, *Least squares quantization in pcm,* IEEE Transactions on Information Theory **28**, 129 (1982).

[27] Jive - Software development kit for advanced numerical simulations, http://jive.dynaflow.com, accessed: 04-03-2018.

[28] C. Geuzaine and J.-F. Remacle, *Gmsh: A three-dimensional finite element mesh generator with built-in pre- and post-processing facilities,* International Journal for Numerical Methods in Engineering **79**, 1309 (2009).

[29] C. Qian, T. Westphal, and R. P. L. Nijssen, *Micro-mechanical fatigue modelling of unidirectional glass fibre reinforced polymer composites,* Computational Materials Science **69**, 62 (2013).

7

VALIDATION OF THE FRAMEWORK

Do you know, Poole, that you and I are about
to place ourselves in a position of some peril?

Robert Louis Stevenson, *The Strange Case of Dr. Jekyll and Mr. Hyde*

7.1. INTRODUCTION

In this chapter, the framework of Chapter 4 is used to predict hygrothermal degradation in unidirectional short beams tested in three-point bending. As improvements to the original framework, a slightly modified version of the viscoelastic/viscoplastic material with damage formulated in Chapter 5 is employed, friction stresses are included in the cohesive-zone model formulated in Chapter 4 and the full-order microscopic boundary-value problems are substituted by a hyper-reduced model using the techniques of Chapter 6. The fiber-matrix interface properties are estimated through single fiber fragmentation tests and a new set of interlaminar shear experiments with additional redried tests is presented. In order to gain further insight in the aging process, fractographic analysis of specimens aged at two different temperatures (50 °C and 65 °C) is performed through X-ray 3D computed tomography. The modified framework is used in an attempt to reproduce the experimentally obtained interlaminar shear stress behavior.

7.2. MECHANICAL TESTS

In this section, the effects of hygrothermal aging in a glass/epoxy material system are investigated through mechanical tests. More specifically, this chapter focuses on mechanical performance degradation of composite specimens subjected to interlaminar

Apart from its introductory section and slight changes to Section 7.4, this chapter was integrally extracted from [1].

shear and of the fiber-matrix interface adhesion as measured by single-fiber fragmentation tests (SFFT). The results obtained from the micromechanical tests are used as input for the multiscale modeling framework of Section 7.4 while results from the macroscopic tests are used to assess model performance.

7.2.1. MANUFACTURING AND CONDITIONING

The material system used in this chapter is a combination of the EPIKOTE RIMR 135/EPIKURE RIMH 1366 epoxy resin reinforced with unidirectional (UD) E-Glass fiber fabrics composed of PPG Hybon 2002 fiber rovings. In order to obtain purely UD laminates, the 90° stability roving layers originally included in the commercial UD fabric were manually removed.

Dog-bone shaped single-fiber fragmentation specimens with 16 mm gauge length, 2 mm gauge width, 6.45 mm tab width and 2 mm thickness were manufactured by extracting single fibers from a fabric and positioning them in latex molds into which resin was poured and cured. For interlaminar shear strength (ILSS) tests, a 3-ply 320 mm × 320 mm × 2.15 mm panel was manufactured through vacuum infusion molding and short-beams with 21.5 mm length, 10.75 mm width and 2.15 mm thickness (ISO 14130 [2]) were cut from it using a CNC milling machine. The curing cycle for both specimen types consisted of 2 h at 30 °C, 5 h at 50 °C and 10 h at 70 °C.

After manufacturing, the specimens were kept in an evacuated desiccator at 50 °C and periodically weighed until a moisture-free state was reached. Sets of specimens were tested in this dry reference state. The remaining specimens were immersed in demineralized water at 50 °C for different durations before being removed for testing. ILSS specimens were immersed for periods varying from 250 h to 2000 h, during which water uptake measurements through weighing were periodically conducted. Single-fiber fragmentation specimens were immersed until saturation (approximately 500 h), after which weight measurements performed on two consecutive days were used to confirm that saturation had been reached. Finally, sets of ILSS samples immersed for 500 h and 1000 h were redried in the evacuated desiccator before being tested. Weight measurements performed on two consecutive days were used to confirm that a stable dry state had been reached.

7.2.2. TESTING

After conditioning, 10 single-fiber fragmentation specimens (5 dry, 5 saturated) were tested in an MTS test frame with 1 kN load cell using a custom tensile fixture suitable for small dog-bone specimens. The specimen was tested in displacement control at a rate of $0.5\,\mathrm{mm\,min^{-1}}$ until failure. A microscope camera equipped with polarized light filters was used to record the development of fiber breaks.

Sets of 10 ILSS specimens for each condition were tested in three-point bending at $1\,\mathrm{mm\,min^{-1}}$. The bending span was fixed at 11.4 mm and steel cylinders with diameters measuring 3.14 mm and 6 mm were used as supports and loading nose, respectively.

7.2.3. RESULTS AND DISCUSSION

SINGLE-FIBER FRAGMENTATION TESTS

An attempt is made at estimating the fiber-matrix interface properties through a combination of optic measurements around broken fiber fragments, the recent shear-lag model proposed by Sørensen [3] and a finite element model of the fragmentation process. Interface decohesion is modeled through a cohesive zone model with friction (Section 7.4.1) and is characterized by a decohesion strength X_{sh}, a fracture toughness G_{IIc} and a friction coefficient μ.

Fig. 7.1a shows a zoomed-in view of a single fiber break during a fragmentation test. Three quantities of interest are identified: The debonded length l_{d}, which delimits the region where interface adhesion is completely lost and only a constant friction stress between fiber and matrix remains, the length l_{cz} of the cohesive zone in which debonding is taking place [4], and the distance l_{p} between the brightest light spots in the fragment, which can be reliably measured even at lower magnifications and used to derive l_{d}.

For each fiber break, the debonded length l_{d} is plotted against the strain of the gauge section of the dog-bone ε, measured through videoextensometry with 10 mm gauge length. A straight line is then fitted through the data points:

$$\varepsilon = \varepsilon_0 + \frac{d\,\varepsilon}{d\,(l_{\mathrm{d}}/r_{\mathrm{f}})}\frac{l_{\mathrm{d}}}{r_{\mathrm{f}}} \tag{7.1}$$

where ε_0 is an intercept parameter and r_{f} is the fiber radius. Care is taken to select fragments which grow with no other fragments nearby and for strain values before plastic localization occurs, two situations that violate assumptions made in the shear-lag model for data reduction [3]. Assuming a constant friction stress τ_{sh} along the debonded zone, the shear-lag model allows to evaluate its value from measured strain and debond length as:

$$\tau_{\mathrm{sh}} = \frac{1}{2}\frac{d\,\varepsilon}{d\,(l_{\mathrm{d}}/r_{\mathrm{f}})}E_{\mathrm{f}} \tag{7.2}$$

where E_{f} is the Young's modulus of the fiber. In order to compute the fracture toughness, a residual strain $\varepsilon_{\mathrm{res}}$ used to compute the strain at the fiber surface is estimated from the combined actions of curing (shrinking) and water swelling (expansion). Assuming that resin hardening takes place during the 50 °C curing step and that chemical shrinkage due to crosslinking reactions is negligible for the present multi-step curing cycle [5], a differential strain $\varepsilon_{\mathrm{res}}^{\mathrm{dry}} = 0.0015$ is obtained. For saturated specimens, the swelling contribution is subtracted leading to $\varepsilon_{\mathrm{res}}^{\mathrm{wet}} = -0.0049$. With these values, the fracture toughness is computed as [3]:

$$G_{\mathrm{IIc}} = \frac{1}{4}E_{\mathrm{f}}r_{\mathrm{f}}(\varepsilon_0 - \varepsilon_{\mathrm{res}})^2 \tag{7.3}$$

With values for τ_{sh}, G_{IIc} and the cohesive zone length l_{cz}, the interface strength X_{sh} can be estimated through a finite element model with a one-dimensional fiber with slip degrees of freedom embedded in a periodic resin slice (the reader is referred to [6] for details on the model formulation). From Fig. 7.1b, features with the same shapes as the ones seen through birefringence in the experiments can be observed. The cohesive strength X_{sh} used as input in the model has a direct influence on the resultant cohesive zone length l_{cz}. This means that an estimate for X_{sh} can be obtained by fixing the other parameters that also influence l_{cz}, namely the frictional stress τ_{sh} and the fracture energy

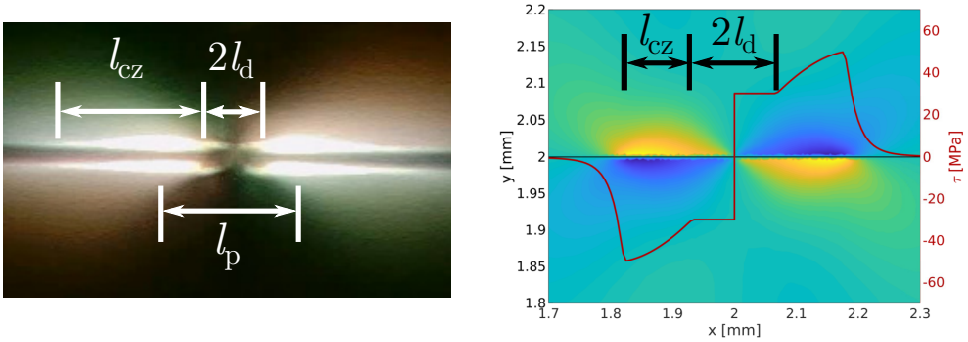

(a) Experiment (b) Simulation

Figure 7.1: A fiber break as observed during an experiment and through numerical simulation, showing the quantities of interest for property estimation.

G_{IIc}, and adjusting the input strength until the numerical l_{cz} matches the experimentally measured one. Since neither the analytical nor the numerical model take radial stresses into account, it is not possible to estimate the friction coefficient μ. For the present, the value $\mu = 0.4$, found by Naya *et al.* [7] to give the best fit with experimental data for carbon/epoxy composites, is adopted.

Measurement results are presented in Figs. 7.2a and 7.2b, showing adimensionalized debonded lengths (l_d/r_f) versus fiber strain ($\varepsilon - \varepsilon_{res}$) for 4 dry fragments and 12 wet fragments. In the plots, the different colors and point markers represent measurements on individual fragments. The reason for the lower number of dry fragments stems from the relatively low failure strain of the present epoxy resin, which caused global failure to happen in many of the tested specimens before useful debond measurements could be made. For saturated specimens, in contrast, plasticization and differential swelling promote earlier fragment development.

The averages and standard deviations of the obtained properties are shown in Table 7.1, computed with $l_{cz} = 0.15$ mm, considered constant throughout the test. Due to the indirect nature of the estimation procedure, a lack of literature consensus on the definition of a debonded region with constant shear stress [3, 4], uncertainties related to the amount of thermal and chemical residual strains and the large scatter observed between fragments, these values only provide a rough estimate of interface performance. Further experiments and model development are therefore necessary. Nevertheless, results indicate loss of friction and degraded adhesion properties after aging, as expected.

	Dry	Saturated
τ_{sh} [MPa]	46.27 ± 16.37	27.31 ± 13.22
G_{IIc} [N/mm]	0.093 ± 0.056	0.067 ± 0.031
X_{sh} [MPa]	52.0	30.0

Table 7.1: Interface properties estimated through single-fiber fragmentation tests.

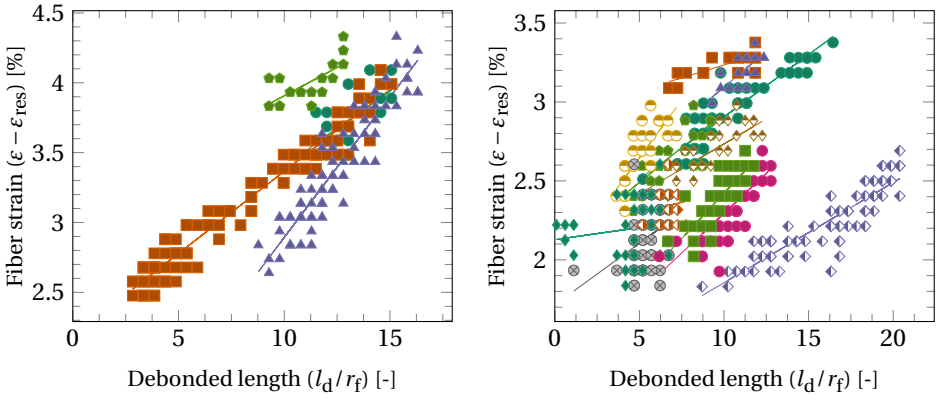

(a) Dry specimens

(b) Saturated specimens

Figure 7.2: Results from Single-Fiber Fragmentation Tests (SFFT).

INTERLAMINAR SHEAR TESTS

For the macromechanical part of this study, hygrothermal degradation is measured in unidirectional short beams tested in three-point bending. A measure of the transverse shear stress at the center of the short-beam specimens is obtained from the force signal F of the test frame [2]:

$$\tau_{\text{ILSS}} = \frac{3}{4}\frac{F}{bh} \tag{7.4}$$

where b and h are the specimen width and thickness, respectively, measured after conditioning. Fig. 7.3a plots the thus computed shear stress versus crosshead displacement for different aging times. To avoid clutter, only one representative specimen for each condition is shown. Average values of the maximum attained stress (interlaminar shear strength) for each condition are presented in Table 7.2.

In order to relate changes in strength to the water concentration in the specimens, the water uptake is computed as:

$$w_{\%}(t) = 100\frac{m(t) - m_{\text{dry}}}{m_{\text{dry}}} \tag{7.5}$$

where $m(t)$ is the specimen mass at time t and m_{dry} is a reference mass measured before aging. Water uptake and average interlaminar shear strength values (wet and redried) are plotted against time in Fig. 7.3b. It is important to note that unsaturated samples have a non-uniform water concentration field. The associated $w_{\%}$ values for these samples are therefore the volume averages of the concentration and do not represent the exact amount of water at material regions where interlaminar failure occurs.

The results point to a gradual strength decrease as the specimens absorb water, with up to 50 % degradation after 1000 h, a point in time when the diffusion process subsides and the specimen is saturated with water. A clear correlation can therefore be identified between the amount of water in the specimen and its interlaminar shear performance.

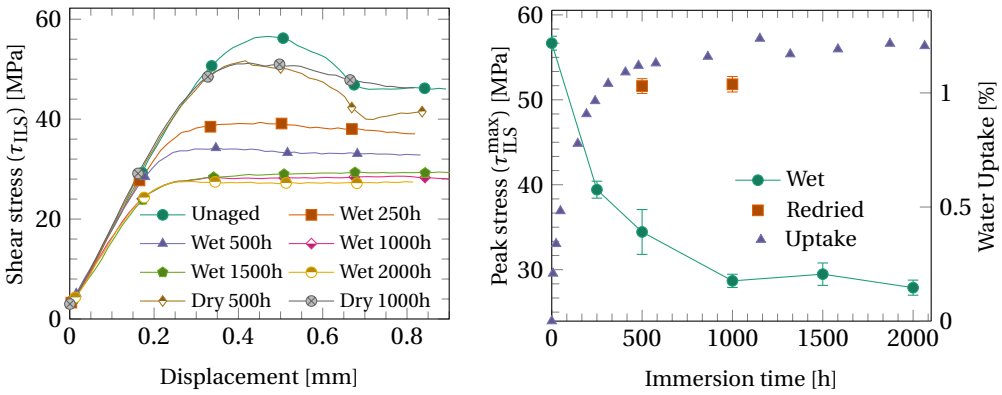

(a) Representative curves

(b) Peak stresses and uptake

Figure 7.3: Results from ILSS tests on wet and redried specimens.

After reaching a stable value at saturation, the strength and uptake remain approximately constant between 1000 h and 2000 h, suggesting that long-term chemical degradation of the interface, as observed in the results of Chapter 2, is negligible for the short aging durations considered here. Nevertheless, a small part of the degradation is irreversible, as evidenced by the redried tests performed after 500 h and 1000 h of immersion. The numerical models of Section 7.4 will help elucidate if this permanent degradation arises from swelling-induced microscopic failure events or if it is instead caused by a fast chemical degradation process taking place at the same time scale as that of the diffusion phenomenon.

	Unaged	250h	500h	1000h	1500h	2000h
Tested wet						
τ_{ILS}^{max} [MPa]	-	39.4 ± 1.0	34.4 ± 2.6	28.7 ± 0.9	29.5 ± 1.3	27.9 ± 0.9
Tested dry						
τ_{ILS}^{max} [MPa]	56.7 ± 0.8	-	51.6 ± 0.9	51.8 ± 0.9	-	-

Table 7.2: ILSS values for short-beam specimens.

7.3. X-RAY COMPUTED TOMOGRAPHY

Results from mechanical tests point to the occurrence of material damage after hygrothermal aging. It is therefore interesting to employ microscopic observation techniques in an attempt to observe degradation events in specimens after aging but before being mechanically tested.

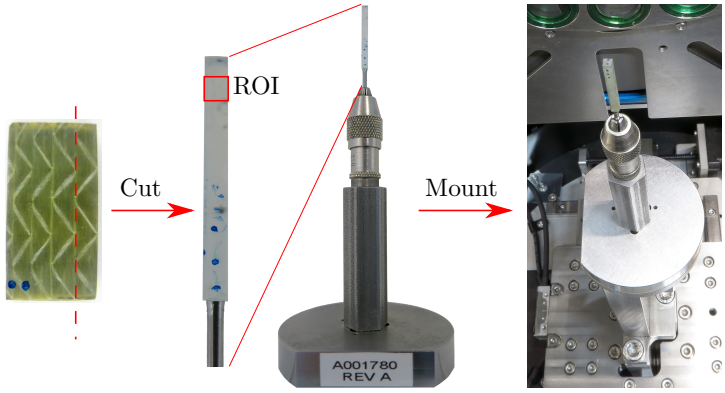

Figure 7.4: Specimen preparation and scanning procedure, showing the Region of Interest (ROI) for the scans.

7.3.1. CONDITIONING

For this part of the study, one additional short-beam specimen was conditioned at 50 °C for the longer period of 5000 h in order to investigate both short- and long-term hygrothermal degradation. Furthermore, a specimen was conditioned at 65 °C for 500 h so that degradation at two different temperatures can be compared. Observations on an unaged specimen are also performed for comparison.

7.3.2. SCANNING

Three-dimensional X-ray computed tomography scans of the specimens are performed using a Zeiss Xradia Versa 520 scanner. Strip specimens with nominal dimensions 2.15 mm × 2.15 mm × 21.5 mm are cut from the short-beams and glued to an aluminum pin which is then attached to a special mount and positioned in the scanning chamber between an X-ray source and a detector (Fig. 7.4). A motorized x-y-z stage is used to align the scanning Region of Interest (ROI) with the source and suitable source-sample and sample-detector distances are chosen in order to obtain the desired scanning Field of View (FoV). During the scans, tomographic projections of the ROI are taken as the sample holder is gradually rotated. As a post-processing step, the projections are combined to form three-dimensional reconstructions of the scanned volumes.

As scanning resolution is inversely proportional to the size of the scanned volume but the study involves searching for relatively small features (*e.g.* interfacial debonding cracks on single fibers), a sequential scanning strategy is adopted. First, a large field of view (*LFoV*) scan is performed and regions of interest close to the center and surface of the specimens are chosen for small field of view scans (*SFoV*). Parameters for both scan types are shown in Table 7.3.

7.3.3. RESULTS AND DISCUSSION

Fig. 7.5 shows the reconstructed cylindrical volume resulting from the LFoV scan of an unaged specimen. The locations of the fiber bundles and resin rich regions along the

Parameter	LFoV	SFoV
Magnification [-]	4.0x	20.0x
Beam voltage [keV]	30	45
Beam power [W]	2	3.5
Exposure time [s]	13-18	40
No. of projections [-]	5201-5801	3801
Field of view [μm]	2500	500
Scanning time [h/scan]	32	45

Table 7.3: Scanning parameters for small and large field of view scans.

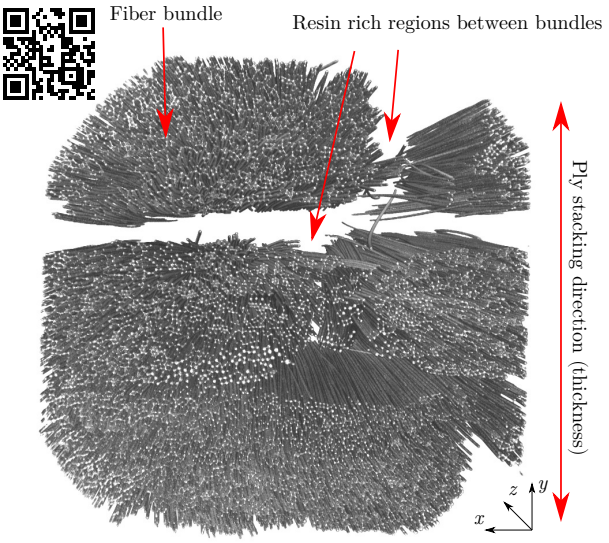

Figure 7.5: Reconstructed scanned volume of a dry specimen (LFoV).

three plies that make up the specimen can be clearly identified. Fig. 7.6 shows SFoV scans of the same specimen. No visible failure can be identified for this condition.

More interesting features are observed on the specimen aged at 65 °C. The LFoV scan of Fig. 7.7 shows a region of extensive interface debonding close to the specimen surface. By moving along the specimen length (z-axis), it is possible to observe the crack and its associated fracture process zone. Similar failure loci can also be observed at multiple other points close to the specimen surface. The SFoV scan of Fig. 7.8a shows one of these locations, with interface debonding both in isolated fibers and propagating among groups of fibers. In contrast, a zoomed-in scan close to the center of the specimen reveals only barely visible debonding cracks (Fig. 7.8b).

For the specimen aged at 50 °C, only minor failure events can be observed, both in the LFoV and SFoV scans (Fig. 7.9). Material degradation is therefore markedly worse for specimens aged at 65 °C. Furthermore, the new spaces formed by crack opening pro-

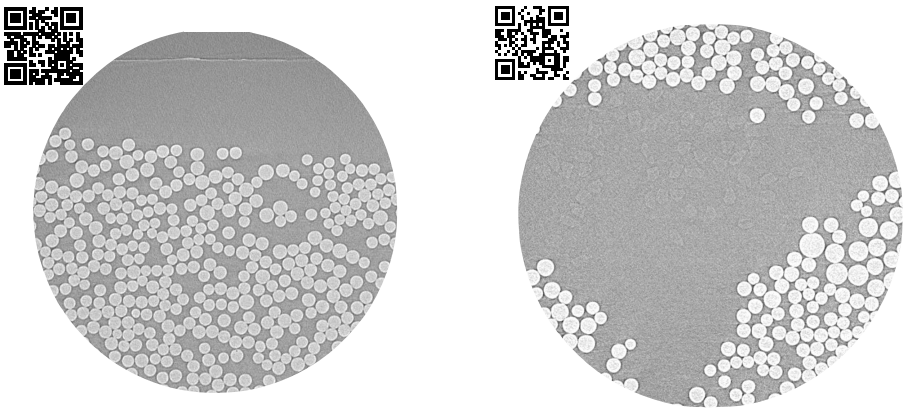

(a) Specimen surface (b) Specimen center

Figure 7.6: Small field of view scans of a reference specimen.

mote additional water uptake, with a moisture content of 1.5 % measured after 500 h of immersion at 65 °C, higher than the observed saturation level of 1.2 % for 50 °C specimens (Fig. 7.3b). Similar uptake behavior has been observed in Chapter 2 and in other studies [8–10].

Based on their proximity to the surface and on the large openings between crack faces, it can be hypothesized that such debonding cracks, initiated through differential swelling, propagate aided by an osmotic process that leads to accelerated water uptake and hydrostatic pressure between crack faces. This is similar to the behavior reported for glass/polyester composites by Gautier *et al.* [9] and would imply that hydrolytic chemical reactions take place involving either the interface sizing or the glass fibers, creating leachates that drive the ensuing osmosis.

Activation of such osmotic mechanism would therefore depend on the differences in speed between diffusion, chemical reaction and leaching. For specimens aged at 50 °C, it is reasonable to suppose that diffusion and reaction are slow enough to allow for reaction products to be leached before significant osmosis takes place. Nevertheless, hydrolytic reactions would permanently degrade interface performance, which corresponds with the measured strength loss in the redried specimens of Section 7.2.3.

7.4. NUMERICAL MODELING

The aging process followed by mechanical testing is numerically simulated using the Finite Element Method in order to reproduce the experimentally observed material degradation. Since aging affects each material constituent differently, a micromechanical modeling strategy is adopted. In order to realistically simulate tests on specimens with non-homogeneous water concentration fields, a multiscale approach is used to model both micro and macroscales concurrently. In this section, the resultant numerical framework, which builds upon the one presented in Chapter 4, is briefly summarized in order to keep this chapter self-contained.

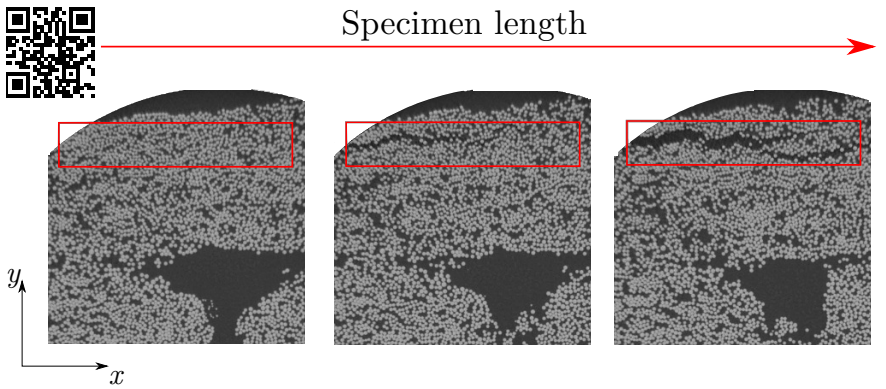

Figure 7.7: Large field of view scan of a specimen aged at 65 °C showing a large debonding crack.

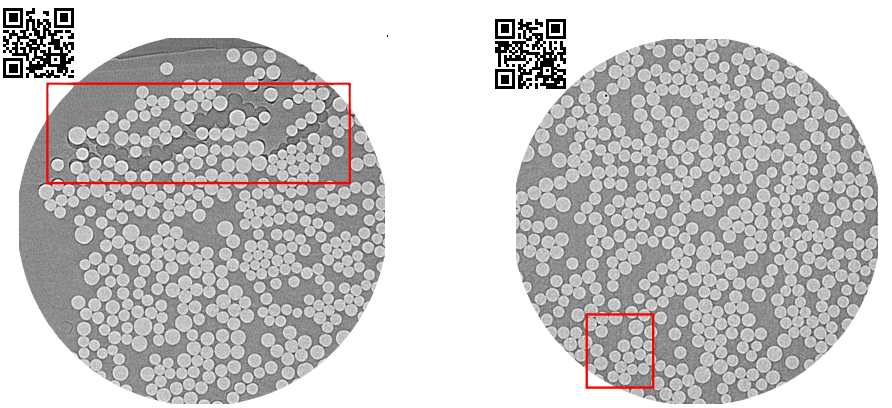

(a) Specimen surface (b) Specimen center

Figure 7.8: Small field of view scans of a specimen aged at 65 °C, with cracks marked in red.

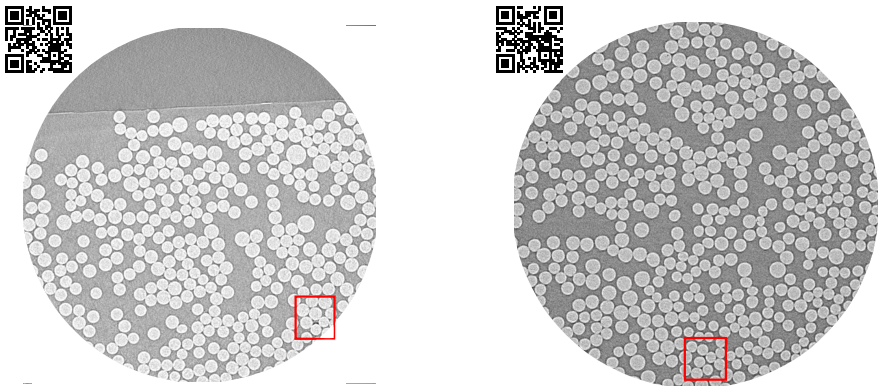

(a) Specimen surface (b) Specimen center

Figure 7.9: Small field of view scans of a specimen aged at 50 °C, with small debonding cracks marked in red.

7.4.1. MICROSCOPIC MATERIAL MODELS

VISCOELASTIC-VISCOPLASTIC-DAMAGE EPOXY

An epoxy model with viscoelastic, viscoplastic and damage components is adopted in order to take into account rate-dependent plasticity and damage activation. The present development is based on the model of Chapter 5 but features a modified damage component inspired by the work of Arefi *et al.* [11].

The model is based on an additive strain decomposition in elastic, plastic, thermal and swelling parts:

$$\boldsymbol{\varepsilon} = \boldsymbol{\varepsilon}^{\mathrm{e}} + \boldsymbol{\varepsilon}^{\mathrm{p}} + \boldsymbol{\varepsilon}^{\mathrm{th}} + \boldsymbol{\varepsilon}^{\mathrm{sw}} \tag{7.6}$$

where the thermal and swelling contributions are given by:

$$\boldsymbol{\varepsilon}^{\mathrm{th}} = \alpha_{\mathrm{t}}\,(T - T_0)\,\mathbf{I} \quad \boldsymbol{\varepsilon}^{\mathrm{sw}} = \alpha_{\mathrm{sw}}\, c\,\mathbf{I} \tag{7.7}$$

with α_{t} and α_{sw} being the thermal and swelling expansion coefficients, respectively, $\mathbf{I}$ being the identity matrix, c being the water concentration and T and T_0 the actual temperature and the temperature at which resin hardening took place, respectively.

The elastic strains are used to compute the stresses by integrating the complete strain time history through the use of a time variable $\tilde{t}$:

$$\tilde{\boldsymbol{\sigma}}(t) = \mathbf{D}^{\infty}\boldsymbol{\varepsilon}^{\mathrm{e}}(t) + \int_0^t \mathbf{D}^{\mathrm{ve}}(t-\tilde{t})\,\frac{\partial \boldsymbol{\varepsilon}^{\mathrm{e}}(\tilde{t})}{\partial \tilde{t}}\,d\tilde{t} \tag{7.8}$$

The stresses are composed of an inviscid contribution related to the long-term stiffness $\mathbf{D}^{\infty}$ and a viscous contribution driven by the time-dependent viscoelastic stiffness $\mathbf{D}^{\mathrm{ve}}$. This viscous contribution is represented by a Prony series of bulk and shear stiffness elements arranged in parallel, with stiffnesses K_u and G_v and relaxation times k_u and g_v, respectively.

Plastic strain develops when a pressure-dependent paraboloidal yield surface is reached:

$$f_{\mathrm{p}}(\boldsymbol{\sigma}, \varepsilon^{\mathrm{p}}_{\mathrm{eq}}) = 6J_2 + 2I_1\left(\sigma_c(\varepsilon^{\mathrm{p}}_{\mathrm{eq}}) - \sigma_t(\varepsilon^{\mathrm{p}}_{\mathrm{eq}})\right) - 2\sigma_c(\varepsilon^{\mathrm{p}}_{\mathrm{eq}})\sigma_t(\varepsilon^{\mathrm{p}}_{\mathrm{eq}}) \tag{7.9}$$

where J_2 and I_1 are the second invariant of the deviatoric stress tensor and the first invariant of the stress tensor, respectively, and σ_c and σ_t are the yield stresses in compression and tension, respectively. Hardening is taken into account through the dependency of the yield stresses on the equivalent plastic strain ε_{eq}^p. The non-associative plastic flow $\Delta\boldsymbol{\varepsilon}^p$ is dictated by the plastic multiplier γ which in turn evolves in a viscous manner:

$$\Delta\boldsymbol{\varepsilon}^p = \Delta\gamma\left(3\mathbf{S} + \frac{2}{9}\alpha I_1\mathbf{I}\right) \quad \Delta\gamma = \begin{cases} \frac{\Delta t}{\eta_p}\left(\frac{f_p}{\sigma_t^0\sigma_c^0}\right)^{m_p}, & \text{if} f_p > 0 \\ 0, & \text{if} f_p \leq 0 \end{cases} \tag{7.10}$$

where $\mathbf{S}$ is the deviatoric stress tensor, α is a factor related to the plastic Poisson's ratio ν_p, η_p and m_p are the viscoplastic modulus and exponent, respectively, σ_t^0 and σ_c^0 are the initial yield stresses, and Δt is a time step.

A continuum damage model is adopted in order to model resin fracture. A damage variable d_m is adopted and the damaged stresses are computed as:

$$\boldsymbol{\sigma} = \mathbf{D}^s\mathbf{H}_0\tilde{\boldsymbol{\sigma}} \tag{7.11}$$

where $\tilde{\boldsymbol{\sigma}}$ and $\mathbf{H}_0$ are the stresses and compliance matrix computed for the pristine material (*i.e.* with $d_m = 0$) and $\mathbf{D}^s$ is a secant stiffness matrix written as:

$$\mathbf{D}^s = \begin{bmatrix} \kappa & \beta & \beta & 0 & 0 & 0 \\ \beta & \kappa & \beta & 0 & 0 & 0 \\ \beta & \beta & \kappa & 0 & 0 & 0 \\ 0 & 0 & 0 & \widehat{G}(1-d_m) & 0 & 0 \\ 0 & 0 & 0 & 0 & \widehat{G}(1-d_m) & 0 \\ 0 & 0 & 0 & 0 & 0 & \widehat{G}(1-d_m) \end{bmatrix} \tag{7.12}$$

and the factors κ and β are given by:

$$\kappa = \frac{\widehat{E}(1-d_m)(1-\widehat{\nu}(1-d_m))}{(1+\widehat{\nu}(1-d_m))(1-2\widehat{\nu}(1-d_m))} \quad \beta = \frac{\widehat{E}\widehat{\nu}(1-d_m)^2}{(1+\widehat{\nu}(1-d_m))(1-2\widehat{\nu}(1-d_m))} \tag{7.13}$$

with $\widehat{G}$ being the viscoelastic shear modulus and $\widehat{E}$ and $\widehat{\nu}$ the viscoelastic Young's modulus and Poisson's ratio, computed as:

$$\widehat{E} = 2\widehat{G}(1+\widehat{\nu}) \quad \widehat{\nu} = \frac{3\widehat{K}-2\widehat{G}}{2\widehat{G}+6\widehat{K}} \tag{7.14}$$

This definition of the secant stiffness deviates from the model of Chapter 5 by also applying a degradation to $\widehat{\nu}$. This makes the model more suitable for use in dense finite element meshes by avoiding spurious hardening on damaged elements constrained by bands of elements undergoing elastic unloading.

A pressure-dependent paraboloidal fracture surface is adopted:

$$f_d(\tilde{\boldsymbol{\sigma}}, r) = \frac{3\widetilde{J}_2}{X_c X_t} + \frac{\widetilde{I}_1(X_c - X_t)}{X_c X_t} - r \quad \Rightarrow \quad f_d(\tilde{\boldsymbol{\sigma}}, r) = \Lambda - r \tag{7.15}$$

where r is an internal variable which controls damage evolution and $X_c = X_c(\Upsilon)$ and $X_t = X_t(\Upsilon)$ are the fracture strengths in compression and tension, respectively, which

are functions of the cumulative dissipated energy $\Upsilon = \Upsilon_{ve} + \Upsilon_{vp}$, as shown in Chapter 5. Through a shrink in the fracture surfaces as energy dissipates, rate-dependent damage activation is taken into account.

At each time step, the variable r is explicitly updated as:

$$r_{t_{n+1}} = \max\left\{1, \max_{0 \le t \le t_{n+1}} \Lambda_t\right\} \tag{7.16}$$

and the damage variable is computed based on the linear softening law proposed by Arefi *et al.* [11]:

$$d_m = \begin{cases} \dfrac{\varepsilon_f(\varepsilon_{eq} - \varepsilon_0)}{\varepsilon_{eq}(\varepsilon_f - \varepsilon_0)}, & \varepsilon_{eq} \le \varepsilon_f \\ 1, & \varepsilon_{eq} > \varepsilon_f \end{cases} \tag{7.17}$$

where the strains at the beginning (ε_0) and end (ε_f) of the softening regime are determined based on an uniaxial tensile test:

$$\varepsilon_0 = X_t \qquad \varepsilon_f = \frac{2G_c\widehat{E}}{l_e X_t} \tag{7.18}$$

with G_c being the resin fracture toughness and l_e the characteristic finite element length [12]. Finally, ε_{eq} is a scalar measure of the strain state:

$$\varepsilon_{eq} = \frac{-q + \sqrt{q^2 - 4pu}}{2p} \tag{7.19}$$

and the parameters q, p and u are given by:

$$\begin{gathered} q = 2a(1-a)b\varepsilon_f + (1+2a)c \quad u = b(a\varepsilon_f)^2 - 2ac\varepsilon_f - rX_tX_c \\ p = b(1-a)^2 \quad a = \frac{\widehat{\nu}X_t}{\widehat{E}(\varepsilon_f - \varepsilon_0)} \\ b = \left(\frac{\widehat{E}}{1+\widehat{\nu}}\right)^2 \quad c = \left(\frac{\widehat{E}}{1-2\widehat{\nu}}\right)(X_c - X_t) \end{gathered} \tag{7.20}$$

COHESIVE INTERFACES WITH FRICTION

Fiber-matrix interface debonding is modeled using interface elements with softening behavior dictated by a cohesive-zone model. The model used in this chapter is based on the one presented in Chapter 4 but is modified to include a friction component, following the formulation by Alfano and Sacco [13]. The displacement jump is additively split into elastic and friction contributions:

$$[\![\mathbf{u}]\!] = [\![\mathbf{u}]\!]^e + [\![\mathbf{u}]\!]^\mu \tag{7.21}$$

and a friction traction contribution $\mathbf{t}^\mu$ is added to the original cohesive traction:

$$\mathbf{t} = (1 - d_i)\, K [\![\mathbf{u}]\!] + d_i \mathbf{t}^\mu \tag{7.22}$$

where K is an initial stiffness, $\mathbf{t}^\mu = K([\![\mathbf{u}]\!] - [\![\mathbf{u}]\!]^\mu)$, and d_i is a damage variable which represents the degree of interface debonding.

The evolution of d_i with the total displacement jump $[\![\mathbf{u}]\!]$ remains unchanged from the one of Chapter 4. Friction evolves in a way analogous to non-associative plasticity. The displacement jump $[\![\mathbf{u}]\!]^\mu$ is updated when a Coulomb friction surface is reached:

$$f_\mu(\mathbf{t}^\mu) = \mu\langle t_\mathrm{n}^\mu\rangle_- + t_\mathrm{sh}^\mu \tag{7.23}$$

where the $\langle\cdot\rangle_-$ operator returns the negative part of its operand and $t_\mathrm{sh}^\mu = \sqrt{(t_\mathrm{s}^\mu)^2 + (t_\mathrm{t}^\mu)^2}$ is the normalized shear traction. Finally, the friction flow rule is given by:

$$\Delta[\![\mathbf{u}]\!]^\mu = \Delta\lambda \begin{bmatrix} 0 \\ t_\mathrm{sh}^\mu \\ \hline |t_\mathrm{sh}^\mu| \end{bmatrix} \quad \Delta\lambda = \frac{f_\mu}{K} \tag{7.24}$$

which is complemented by the Kuhn-Tucker conditions $\dot\lambda \geq 0$, $f_\mu \leq 0$, $\dot\lambda f_\mu = 0$.

HYGROTHERMAL AGING

Plasticization and fiber-matrix interface weakening are modeled with an additional degradation variable d_w which is a function of the water concentration c of the material point:

$$d_\mathrm{w} = \frac{d_\mathrm{w}^\infty}{c_\infty} c \tag{7.25}$$

where c_∞ and d_w^∞ are the water concentration and material degradation at saturation, respectively. Since only tests at dry and saturated states are available for resin (Section 5.3.4) and interface (Section 7.2.3), a linear evolution of d_w is adopted. The degradation variable is then used to modify the resin properties as follows:

$$\widehat{E}_\mathrm{w} = (1 - d_\mathrm{w})\widehat{E} \tag{7.26}$$

$$\sigma_\mathrm{c}^\mathrm{w} = (1 - d_\mathrm{w})\sigma_\mathrm{c}, \quad \sigma_\mathrm{t}^\mathrm{w} = (1 - d_\mathrm{w})\sigma_\mathrm{t} \tag{7.27}$$

$$X_\mathrm{c}^\mathrm{w} = (1 - d_\mathrm{w})X_\mathrm{c}, \quad X_\mathrm{t}^\mathrm{w} = (1 - d_\mathrm{w})X_\mathrm{t}, \quad G_\mathrm{c}^\mathrm{w} = (1 - d_\mathrm{w})^2 G_\mathrm{c} \tag{7.28}$$

where the squared toughness degradation is adopted for the sake of numerical stability, since no reliable measurements of saturated fracture toughness on the present resin system are available and only an estimation of its value based on the tensile tests of Section 5.3.3 is adopted.

For the fiber-matrix interface, a similar degradation approach is adopted, but the change in fracture toughness is modified in order to reflect the results obtained on the fragmentation tests of Section 7.2.3:

$$X_\mathrm{n}^\mathrm{w} = (1 - d_\mathrm{w})X_\mathrm{n} \quad X_\mathrm{sh}^\mathrm{w} = (1 - d_\mathrm{w})X_\mathrm{sh} \quad G_\mathrm{Ic}^\mathrm{w} = \sqrt{1 - d_\mathrm{w}}G_\mathrm{Ic} \quad G_\mathrm{IIc}^\mathrm{w} = \sqrt{1 - d_\mathrm{w}}G_\mathrm{IIc} \tag{7.29}$$

where X_n, G_Ic, X_sh and G_IIc are the interface strength and fracture toughness in mode I and modes II and III, respectively. Since only mode II properties are available for the present material system (Table 7.1), they are also used to describe decohesion in mode I in the present study.

The experiments on neat resin from Chapter 2 point to complete stiffness and strength recovery after a single immersion-redrying cycle at 50 °C. Hygrothermal degradation of the resin is therefore modeled as a reversible process. Due to the lack of experimental data on redried fragmentation specimens, interface degradation is also modeled as reversible.

7.4.2. MULTISCALE/MULTIPHYSICS FRAMEWORK

The microscopic material models of Section 7.4.1 are used in conjunction with a multiscale/multiphysics framework in order to predict the behavior of macroscopic material specimens subjected to aging followed by mechanical loads. The main features of the framework, presented in detail in Chapter 4, will be briefly summarized in the following.

DIFFUSION MODEL

A Fickian diffusion model is used to predict the evolution of the macroscopic water concentration field with aging time. The changes in concentration and the resultant mass flux **j** are computed by:

$$\dot{c}^{\Omega} + \frac{\partial}{\partial \mathbf{x}^{\Omega}} \cdot \mathbf{j}^{\Omega} = 0 \quad \mathbf{j}^{\Omega} = -\mathbf{D}^{\Omega} \frac{\partial c}{\partial \mathbf{x}^{\Omega}} \tag{7.30}$$

where **D** is an orthotropic diffusivity matrix and the superscript Ω indicates macroscopic quantities. The water concentration at each material point is downscaled to an embedded micromodel (FE^2) and is considered constant inside the microdomain. This solution implicitly assumes that water diffusion in the resin is well represented by a one-phase Fick solution. The anisotropic diffusivity parameters from Chapter 3 are used and considered constant throughout the analysis, leading to a linear transient diffusion problem.

STRESS MODEL

The nonlinear stress problem is solved iteratively using a Newton-Raphson solver and takes place after the water concentration field is updated (staggered coupling). An equilibrium problem is solved at both scales:

$$\frac{\partial}{\partial \mathbf{x}^{\Omega}} \cdot \boldsymbol{\sigma}^{\Omega} = \mathbf{0} \quad \frac{\partial}{\partial \mathbf{x}^{\omega}} \cdot \boldsymbol{\sigma}^{\omega} = \mathbf{0} \tag{7.31}$$

where the superscript ω indicates microscopic quantities. No assumptions are made regarding the constitutive behavior of the macroscopic material. Instead, stresses and stiffnesses are obtained through homogenization of the microscopic response: Strains are applied as prescribed displacements at the corners of the embedded micromodels, the micro boundary value problems are solved and volume averages of stiffnesses and stresses are upscaled.

7.4.3. REDUCED-ORDER MODELING

The multiscale/multiphysics framework of Section 7.4.2 involves solving a microscopic boundary value problem for each macroscopic integration point on every iteration of every time step. In turn, solving each micromodel involves solving a nonlinear finite element equilibrium problem featuring dense meshes and complex material models. The resultant computational effort is, therefore, exceedingly high. In this section, the two model order reduction techniques presented in detail in Chapter 6 will be used to efficiently solving the microscopic equilibrium problems with minimum loss of accuracy.

PROPER ORTHOGONAL DECOMPOSITION (POD)

Instead of solving for the full micro displacement field $\mathbf{u}^{\omega}$ with N unknowns, one can instead choose a number $n \ll N$ of displacement modes arranged in a matrix $\boldsymbol{\Phi} \in \mathbb{R}^{N \times n}$

and solve for their relative contributions $\boldsymbol{\alpha}$, which reduces the size of the equilibrium system to n unknowns. The original displacement field is the linear combination of the n modes:

$$\mathbf{u} = \boldsymbol{\Phi}\boldsymbol{\alpha} \tag{7.32}$$

which leads to reduced versions of the global internal force and tangent stiffness:

$$\mathbf{f}_{\mathrm{r}}^{\omega} = \boldsymbol{\Phi}^{\mathrm{T}}\mathbf{f}^{\omega} \quad \mathbf{K}_{\mathrm{r}}^{\omega} = \boldsymbol{\Phi}^{\mathrm{T}}\mathbf{K}^{\omega}\boldsymbol{\Phi} \tag{7.33}$$

where a subscript r denotes a reduced entity. The displacement modes are computed before the multiscale analysis by subjecting the micromodel to representative loading situations and applying a truncated Singular Value Decomposition (SVD) process to the obtained displacement snapshots (Section 6.4.2).

EMPIRICAL CUBATURE METHOD (ECM)

Although POD reduces the size of the global equilibrium equation, computing $\mathbf{f}^{\omega}$ and $\mathbf{K}^{\omega}$ still involves computing complex constitutive models for all M integration points of the microscopic domain ω. Further acceleration (so-called *hyper-reduction*) can be achieved by choosing a number $m \ll M$ of integration points and computing modified integration weights $\boldsymbol{\varpi}$ in order to obtain a good approximation of the reduced global internal force vector with only a small fraction of the effort:

$$\mathbf{f}^{\omega} = \int_{\omega} \mathbf{f}\, d\omega \approx \sum_{i=1}^{m} \mathbf{f}\left(\mathbf{x}_i^{\omega}\right) \varpi_i \tag{7.34}$$

The reduced set of points and weights is chosen by minimizing the error between the original and approximated versions of $\mathbf{f}_{\mathrm{r}}^{\omega}$ using the least-squares point selection algorithm of Section 6.4.3.

7.4.4. RESULTS AND DISCUSSION

The preceding numerical framework was implemented in an in-house Finite Element code built using the open-source *Jem/Jive* C++ library [14]. The analyses are executed on a workstation equipped with an Intel Xeon E5-2650 processor and 64 Gb of RAM. Evaluation of the micromodels during concurrent multiscale analyses is performed in parallel. The microscopic domain is represented by a periodic microcell with 16 fibers. Based on the RVE study of Section 4.3.1, this microdomain size is considered to represent the macroscopic behavior of the unidirectional composite material with reasonable accuracy. The micromodel is discretized with 3198 wedge finite elements and 337 interface elements around the fibers. The fibers are modeled as linear-elastic, while the material models of Section 7.4.1 are used for the resin and interfaces. The adopted microscopic material properties are shown in Table 7.4.

In order to employ the micromodel in a macroscopic simulation of an ILSS test, a reduced-order model is first trained to accurately represent the elastic, plastic and fracture response of a micromodel subjected to a combination of interlaminar shear, hygrothermal aging and residual stresses. The load cases used in the training process are shown in Fig. 7.10. A strain rate $\dot{\varepsilon} = 5 \times 10^{-2}\,\mathrm{s}^{-1}$ is adopted for all cases with mechanical loads. For cases including water concentration, it is applied in steps from an initially dry

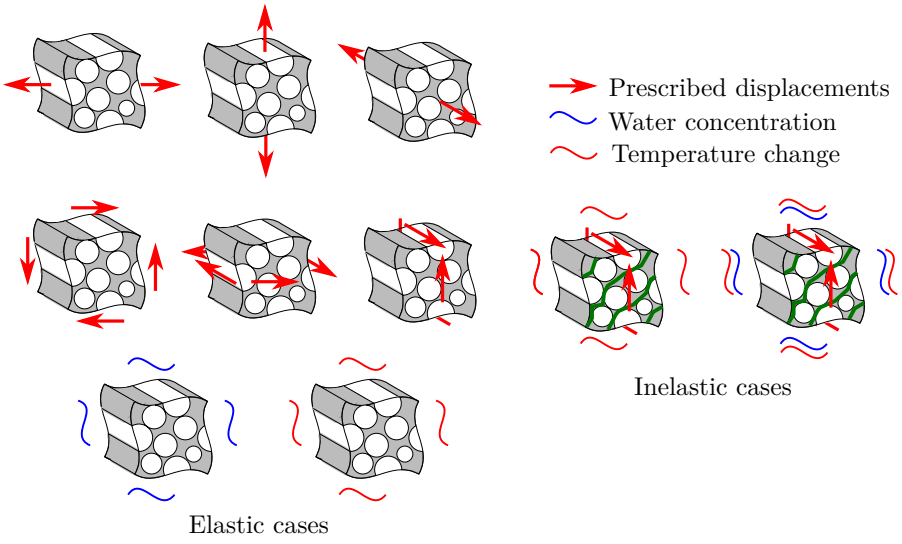

Figure 7.10: Load cases used for training the reduced-order model.

state to a concentration value of 3.2 %, corresponding to the saturation level of the epoxy resin. For residual stresses, a temperature variation $\Delta T = -27\,°C$ is applied in steps. For cases combining environmental loads with mechanical strains, water is applied first, followed by temperature and finally by prescribed displacements. Each elastic case is run for three steps in order to provide the reduced model with information on the decay of viscoelastic stresses. The inelastic cases are run until a stress drop is observed, indicating strain localization. Since failure occurs due to transverse shear, it manifests as a single horizontal localization band which runs between the left and right boundaries of the RVE.

The original model is reduced from $N = 12\,138$ to $n = 21$ degrees of freedom in a first reduction stage (POD). This reduced model is then subjected to a second training stage in order to select a reduced set of integration points, with a reduction from $M = 4546$ to $m = 589$ integration points. Fig. 7.11 shows the homogenized stress-strain responses for both the dry and saturated conditions of the full micromodel and its POD-reduced counterpart (after the first reduction phase). The reduced model is able to accurately represent the full response of the cases used for training, although the prediction of the softening response of the saturated material is relatively less accurate due to the sharp softening branch caused by the influence of displacement modes obtained from the dry test. Comparing the reduced internal force vectors for the POD-reduced and ECM-reduced models, the additional error caused by hyper-reduction is approximately 1.9 %. The resultant speed-ups of the POD-reduced and ECM-reduced models with respect to the full-order model are 51 and 302, respectively.

Before using the reduced model in a multiscale analysis, it is interesting to assess its performance for non-trained load cases. Full and POD-reduced micromodels loaded in transverse shear at intermediate water concentration values are executed and their

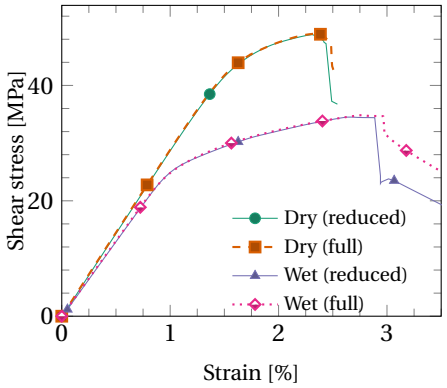

Figure 7.11: Reduced RVE model response for the inelastic training cases.

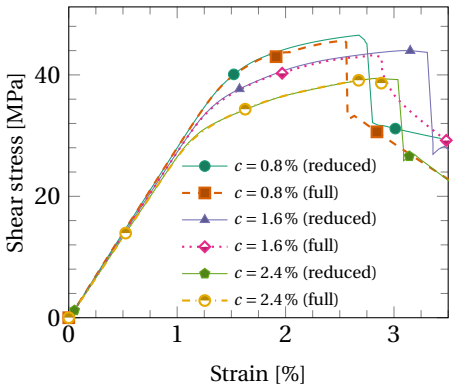

Figure 7.12: Reduced RVE model response for untrained scenarios of mechanical tests at different levels of saturation.

homogenized responses are compared in Fig. 7.12. The reduced model is capable of interpolating from the trained cases and correctly predicting material behavior for all concentration values, with only small overshoots in failure strain. The largest overshoot occurs for a concentration of 1.6 %, a case that requires the largest amount of interpolation from either the dry or saturated states used for training. Influenced by the displacement modes at failure obtained from the training cases, failure strains are overestimated and steep load drops are obtained for all intermediate concentration values. It is interesting to note that, due to the smaller number of degrees of freedom, the reduced model features improved numerical robustness. This can be observed, for instance, in the $c = 2.4\,\%$ curve, a case on which the full analysis is terminated due to lack of convergence as soon as the softening branch of the equilibrium path is reached while the reduced model maintains the convergence behavior observed during the training cases.

For the next test, the POD-reduced model is assessed on its ability to represent loading at different strain rates. The full and reduced responses of a micromodel subjected

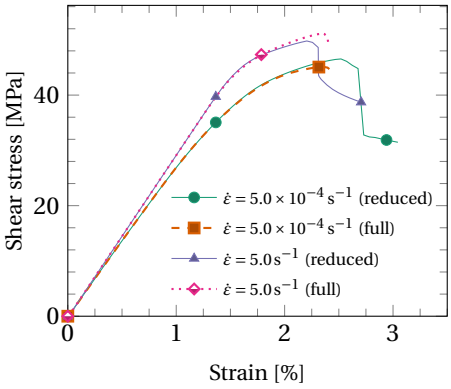

Figure 7.13: Reduced RVE model response for untrained scenarios of mechanical tests at different strain rates.

to transverse shear at strain rates both 100 times faster and slower than the one used for training are shown in Fig. 7.13. In both cases, the reduced model correctly extrapolates the time-dependent material response in both the elastic and plastic regimes, while once again showing only a limited loss of accuracy in terms failure strain. As expected, the reduced model tends to exhibits behaviors closer to the ones used for training, leading to underestimated values of peak load and failure strain for the very fast strain rate and overestimated values for the very slow rate. For both studies on untrained load cases (water concentration and strain rate), the additional error caused by hyper-reduction (ECM), computed by comparing the norm of the reduced global internal force vectors with and without ECM, is at most 6 %. Both the POD-reduced and the hyper-reduced models are therefore considered suitable for representing the full-order model, with significant acceleration and only limited loss of accuracy even upon considerable extrapolation from the load cases used in training.

A multiscale/multiphysics model of a three-point bending interlaminar shear test is performed. At the macroscale, symmetry along the x- and z-axes is exploited, and only one quarter of the short-beam is modeled (Fig. 7.14). The model is meshed with 8-node hexagonal elements. It is a known issue that an RVE ceases to exist upon microscopic strain localization, with the amount of energy dissipated by the macroscopic model being dependent on the size of the microdomain [15]. In order to bypass this issue, the thickness of a band of elements close to the specimen center along its thickness, where strain localization is expected, is made equal to the size of the micromodel [16]. The complete mesh comprises 1536 elements with a total of 5120 embedded micromodels. In order to further reduce computational effort, micromodels with a coarser mesh are used for material points located after the support along the length of the specimen, a region which is mostly free of stresses. The resultant mesh can be seen in Fig. 7.15. The analysis begins with a pre-conditioning phase with a time step $\Delta t = 25\,\mathrm{h}$, during which a constant water concentration of 3.2 % is applied at the boundary. After the immersion phase, the virtual specimen is cooled down from 50 °C to 23 °C at a rate of $5.5\,^{\circ}\mathrm{C}\,\mathrm{min}^{-1}$, after which a mechanical test is performed in three-point bending at $1\,\mathrm{mm}\,\mathrm{min}^{-1}$ and the resultant load is used to compute the apparent interlaminar shear stresses using

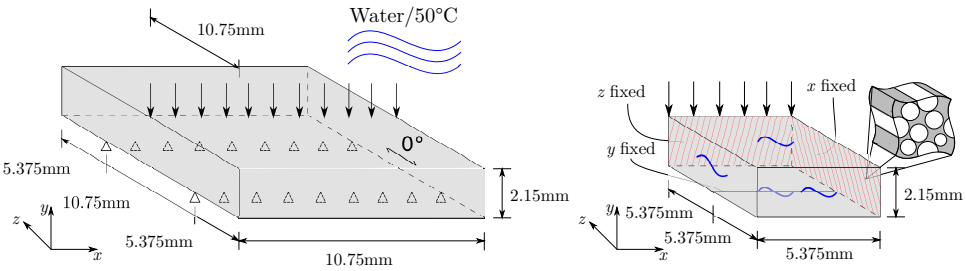

(a) Immersion problem (a) Modeling approach

Figure 7.14: Multiscale model of the aging and mechanical test of a short-beam specimen.

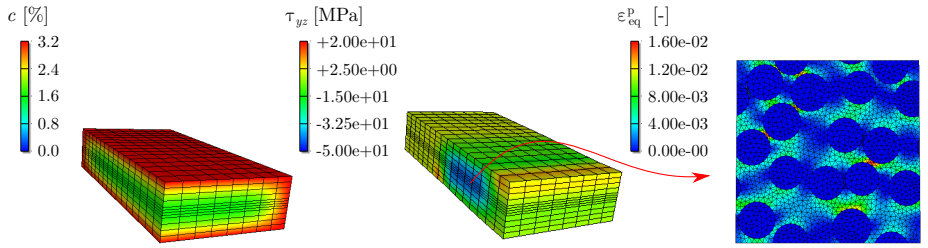

Figure 7.15: Snapshot of the multiscale analysis of a specimen immersed for 250 h at the onset of failure.

Eq. (7.4).

The multiscale model is used to obtain load-displacement curves for a dry specimen and specimens immersed for 250 h, 500 h and 1000 h, after which the water concentration field inside the specimen is non-homogeneous. In these situations, a stand-alone micromechanical analysis of the point of maximum concentration is not enough to derive the behavior of the macroscopic specimen, which is instead dictated by stress redistribution between regions with different water concentrations and suffers the influence of transient swelling stresses caused by the non-uniform concentration field.

Fig. 7.16a shows the obtained stress-displacement curves for each condition up until the point when interlaminar failure occurs at the center of the specimen. Although the mechanical response for the unaged sample is similar to the one obtained for a single RVE in pure transverse shear (Fig. 7.11), the same does not hold after aging. For an isolated micromodel saturated with water, failure occurs at approximately 34 MPa, which is slightly higher but still reasonably close to the experimentally obtained strength (Fig. 7.3a). On the other hand, the multiscale model points to a higher peak load of 39 MPa for the saturated specimen. This increase, which can only be captured in a multiscale analysis, results from the highly non-linear behavior of the saturated material prior to strain localization (Fig. 7.11), leading to stress redistribution along the specimen thickness. Predicting the interlaminar shear response of an aged specimen is therefore a more complex task than simply computing the micromechanical response of an isolated material point at its center.

Nevertheless, the gradual degradation behavior with water concentration observed

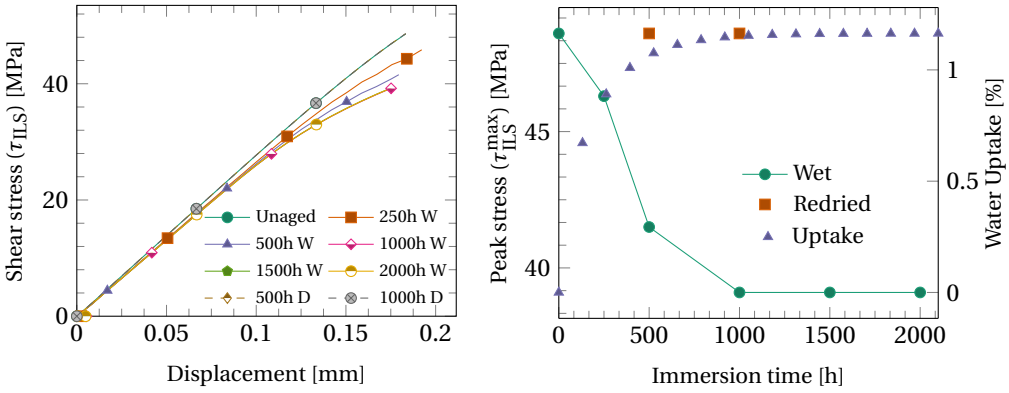

(a) Stress-displacement curves

(b) Peak stresses and uptake.

Figure 7.16: Numerical ILSS results.

in Fig. 7.3a is qualitatively reproduced by the multiscale model (Fig. 7.16b). The numerically obtained peak stress for the unaged case is approximately 7 MPa lower than the average value obtained from the experiments. Since failure in the dry specimen is driven by resin fracture, such discrepancy is not surprising given the fact that no reliable measurement for the fracture toughness of the present epoxy resin is currently available. Furthermore, the fiber bundles and resin-rich regions seen in Fig. 7.5 are not modeled, which would result in differences in crack propagation during the simulation. The high saturated peak stress levels predicted by the model suggest that interface degradation is significantly worse than the one used as input ($d_w^\infty = 0.42$ from Table 7.4). This indicates that the saturated properties obtained through SFFT are overestimations of the actual degraded interface performance. Given the large measurement scatter obtained in those experiments (Section 7.2.3), the adopted values for X_{sh} and G_{IIc} are estimated with a high level of uncertainty.

Results on redried micromodels do not show any permanent degradation, with a peak stress of approximately 49 MPa being obtained for both unaged and redried specimens. This suggests that plastic strain development and interface debonding due to swelling are not responsible for the observed irreversible degradation, since the effect of swelling is already captured by the model. These results reinforce the hypothesis of chemical reactions permanently degrading interface performance, a mechanism also observed in the tomographic scans of Section 7.3. This can be modeled in a phenomenological way by introducing a concentration threshold that assures a minimum level of degradation even upon subsequent redrying.

As a last numerical example, it is interesting to take advantage of the computational efficiency of the reduced model in order to investigate the effect of cyclic immersion-redrying on the transverse shear strength of the composite material. For this example, the effect of cycling on a point close to the specimen surface is considered, for which complete saturation is supposed to be reached after 300 s. For simplicity, the mechanical test is performed on the completely dry material (after cycling), eliminating the need for

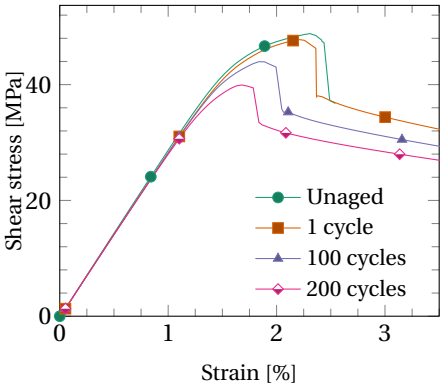

Figure 7.17: Reduced model response for testing after multiple immersion-redrying cycles.

a concurrent multiscale approach.

Fig. 7.17 shows the model stress-strain response after 1, 100 and 200 immersion-drying cycles. Due to the viscous nature of the epoxy model and its dissipation-dependent fracture surface, and since saturation and redrying happen at relatively fast rates, cyclic differential swelling stresses promote a gradual strength decrease. Although it is reasonable to suppose the occurrence of such gradual degradation, further experimental evidence is required in order to confirm this trend.

7

7.5. CONCLUSIONS

This chapter presented a combined experimental and numerical study on hygrothermal aging of unidirectional glass/epoxy composites. Macroscopic material degradation was investigated through mechanical tests on short-beam specimens tested in three-point bending. Specimens were tested unaged, after having been immersed in water for various durations and after immersion-redrying cycles. Microscopic hygrothermal degradation was investigated through mechanical tests on single-fiber fragmentation specimens and by performing fractographic analyses on aged specimens through X-ray computed tomography. An attempt was made to numerically reproduce the observed degradation with a concurrent multiscale/multiphysics finite element model with hyper-reduced micromodels equipped with a viscous resin model and cohesive fiber-matrix interfaces with friction.

The mechanical properties of the fiber-matrix interface were estimated through a combination of single-fiber fragmentation tests and reverse modeling. Significant reductions in strength, friction and fracture toughness were observed after aging. However, the relatively low failure strain of the resin led to a large number of fragments for which no information could be extracted. Furthermore, the small number of valid fragments showed a large scatter in debonding behavior.

Results from interlaminar shear tests on specimens aged at 50 °C showed a gradual strength decrease which had a strong correlation with the amount of water absorbed by the specimens. After saturation at 1000 h of immersion, the strength remained un-

changed for another 1000 h. Upon redrying, permanent degradation was observed for immersion times as short as 500 h. Microscopic observations on these specimens through X-ray computed tomography revealed no signs of widespread interface debonding, in contrast with observations on specimens aged at 65 °C. It is concluded that an osmotic mechanism is activated at the higher temperature, leading to extensive debonding and additional water uptake. At 50 °C, it is hypothesized that diffusion and reaction are sufficiently slow as to allow the reaction products to leach out of the specimen before extensive osmosis occurs. In any case, these observations strongly suggest the occurrence of chemical damage at fiber-matrix interfaces.

The aging phenomenon was numerically simulated in a multiscale/multiphysics framework. A combination of the POD and ECM reduced-order modeling techniques was used to construct a reduced model which runs up to 300 times faster than the full-order one with limited loss of accuracy. The resultant model is able to qualitatively capture the experimentally observed dependency of interlaminar shear strength with water concentration, although uncertainties related to the fracture toughness of the resin and interface strength and toughness lead to incorrect predictions of both dry and saturated strengths.

REFERENCES

[1] I. B. C. M. Rocha, F. P. van der Meer, S. Raijmaekers, F. Lahuerta, R. P. L. Nijssen, L. P. Mikkelsen, and L. J. Sluys, *A combined experimental/numerical investigation on hygrothermal aging of fiber-reinforced composites,* European Journal of Mechanics - A/Solids **73**, 407 (2019).

[2] *ISO 14130 - Fibre-reinforced plastic composites - Determination of apparent interlaminar shear strength by short-beam method*, Tech. Rep. (ISO, 1997).

[3] B. F. Sørensen, *Micromechanical model of the single fiber fragmentation test,* Mechanics of Materials **104**, 38 (2017).

[4] B. W. Kim and J. A. Nairn, *Observations of fiber fracture and interfacial debonding phenomena using the fragmentation test in single fiber composites,* Journal of Composite Materials **36**, 1825 (2002).

[5] U. A. Mortensen, T. L. Andersen, J. Christensen, and M. A. M. Maduro, *Experimental investigation of process induced strain during cure of epoxy using optical fiber bragg grating and dielectric analysis,* in *In: Proceedings of the 18th European Conference on Composite Materials* (2018).

[6] F. P. van der Meer, S. Raijmaekers, and I. B. C. M. Rocha, *Interpreting the single fiber fragmentation test with numerical simulations,* Under Review (2018).

[7] F. Naya, C. González, C. S. Lopes, S. van der Veen, and F. Pons, *Computational micromechanics of the transverse and shear behaviour of unidirectional fiber reinforced polymers including environmental effects,* Composites: Part A (2016).

[8] A. Gagani and A. T. Echtermeyer, *Fluid diffusion in cracked composite laminates - Analytical, numerical and experimental study,* Composites Science and Technology **160**, 86 (2018).

[9] L. Gautier, B. Mortaigne, and B. V., *Interface damage study of hydrothermally aged glass-fibre-reinforced polyester composites,* Composites Science and Technology **59**, 2329 (1999).

[10] B. Dewimille and A. R. Bunsell, *Accelerated ageing of a glass fibre-reinforced epoxy resin in water,* Composites , 35 (1983).

[11] A. Arefi, F. P. van der Meer, M. R. Forouzan, and M. Silani, *Formulation of a consistent pressure-dependent damage model with fracture energy as input,* Composite Structures **201**, 208 (2018).

[12] Z. P. Bažant and B. Oh, *Crack band theory for fracture of concrete,* Matériaux et Construction **16**, 155 (1983).

[13] G. Alfano and E. Sacco, *Combining interface damage and friction in a cohesive-zone model,* International Journal for Numerical Methods in Engineering **68**, 542 (2006).

[14] Jive - Software development kit for advanced numerical simulations, http://jive.dynaflow.com, accessed: 04-03-2018.

[15] V. P. Nguyen, O. Lloberas Valls, M. Stroeven, and L. J. Sluys, *On the existence of representative volumes for softening quasi-brittle materials - a failure zone averaging scheme,* Computer Methods in Applied Mechanics and Engineering **199**, 45 (2010).

[16] I. M. Gitman, H. Askes, and L. J. Sluys, *Coupled-volume multi-scale modelling of quasi-brittle material,* European Journal of Mechanics - A/Solids **27**, 302 (2008).

Glass fibers				
K_∞ [MPa]	43452			
G_∞ [MPa]	29918			
α_t [K^{-1}]	$5.4 \cdot 10^{-6}$			
Epoxy resin				
K_∞ [MPa]	3205			
G_∞ [MPa]	912			
K_u [MPa]	125	182	625	143
G_v [MPa]	36	52	178	41
k_u [s]	$4.16 \cdot 10^{-2}$	$2.30 \cdot 10^{0}$	$4.22 \cdot 10^{1}$	$3.11 \cdot 10^{4}$
g_v [s]	$1.46 \cdot 10^{-1}$	$8.08 \cdot 10^{0}$	$1.48 \cdot 10^{2}$	$1.09 \cdot 10^{5}$
σ_t [MPa]	$64.80 - 33.6e^{-\epsilon^p_{eq}/0.003407} - 10.21e^{-\epsilon^p_{eq}/0.06493}$			
σ_c [MPa]	$81.0 - 42.0e^{-\epsilon^p_{eq}/0.003407} - 12.77e^{-\epsilon^p_{eq}/0.06493}$			
η_p [s]	$3.49 \cdot 10^{12}$			
m_p [-]	7.305			
ν_p [-]	0.32			
X_t [MPa]	$83.8 - 5.99\,\Upsilon$			
X_c [MPa]	$104.7 - 7.48\,\Upsilon$			
G_c [N/mm]	1.9			
d_w^∞ [-]	0.14			
α_t [K^{-1}]	$6.0 \cdot 10^{-5}$			
α_{sw} [%$^{-1}$]	0.002			
Fiber-matrix interface				
K [MPa]	10^6			
X_n/X_{sh} [MPa]	52			
G_{Ic}/G_{IIc} [N/mm]	0.093			
μ [-]	0.4			
d_w^∞ [-]	0.42			
Diffusion				
c_∞ [%]	3.2			
D_x/D_y [µm/s]	0.520			
D_z [µm/s]	1.638			

Table 7.4: Properties used for numerical modeling.

8

COMPUTATIONAL IMPLEMENTATION

Having neither flesh nor souls, they
are just binary numbers. They both
exist and do not exist at the same time.

Citan Uzuki, *Xenogears*

8.1. INTRODUCTION

The numerical formulations presented in the preceding chapters were implemented in an in-house finite element code based on the open-source *Jem-Jive* libraries. In this chapter, details on these implementations will be presented in order to aid future replication and expansion efforts. First, a small introduction on the base libraries will be presented which will help to identify at which points of a general finite element implementation the formulations treated in this thesis fit. This will be followed by details on the material models of Chapters 3 to 5, the multiphyics/multiscale numerical framework of Chapter 4 and the acceleration techniques of Chapter 6. Finally, a brief mention will be made of a number of additional numerical tools used throughout the thesis.

8.2. THE JEM/JIVE LIBRARY

Jem and *Jive* are two programming libraries written in *C++* that provide a set of classes aimed at facilitating the implementation of numerical methods [1]. *Jem* performs lower-level tasks related to memory allocation and garbage collection, input/output, mathematical operations involving multi-dimensional arrays, among others. *Jive* is a higher-level library that builds upon *Jem* and provides tools for handling degrees of freedom and solving large systems of equations, managing nodes, elements and element shapes,

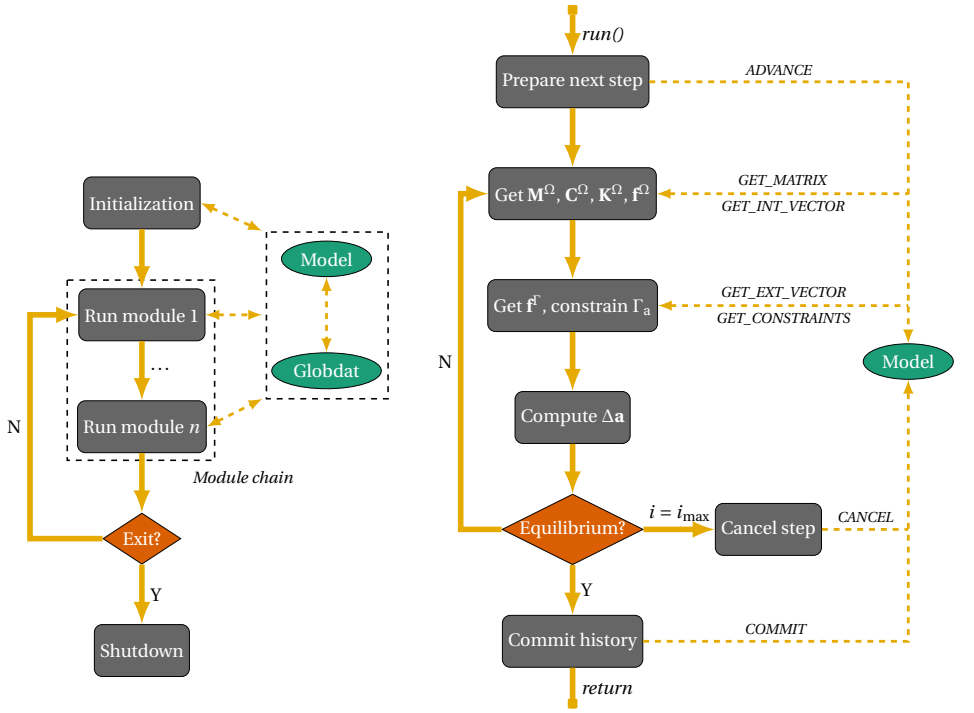

(a) *Jive* application flow (b) Solver module *run* routine

Figure 8.1: Solution of an FE problem: Analysis flow and communication between modules and models.

handling boundary conditions, among others. Both libraries are used in implementing the formulations described in this chapter, but most of the modifications and new developments are performed at an implementation level handled by *Jive*.

A *Jive* application is composed of two parts: A *Model*, which represents the physical problem being solved (*e.g.* a finite element problem), and a *Module* which operates on the model data (*e.g.* a solver). Between these two components lies the *globdat*, a communication database through which model and module exchange data. In all but the simplest applications, it is necessary to employ a number of different modules acting on the same model (*e.g.* an input module, a solver module and a postprocessing module). For this purpose, a wrapper class called *ChainModule* can be used to construct a module chain which executes each of the modules in a predefined order.

Modules have three main components: An *init* function which is executed only once and handles initialization tasks, a *run* function which is executed at each analysis step and a *shutdown* function executed at the end of the analysis. Fig. 8.1a shows the basic execution flow of a *Jive* application, with dashed arrows representing data exchange between components. Communication between a module and the model being solved is done through the *takeAction* function, which instructs the model to perform a certain task and store the resultant data in *Globdat* so that it can be accessed by the module. Fig. 8.1b shows the basic workflow of the *run* function of a solver module. The degrees

of freedom a (*e.g.* displacements or concentrations) are stored in *Globdat* as a *StateVecor* object and the mapping between nodes and degrees of freedom of different types as a *DofSpace* object, accessible by both model and module. For transient problems, the solver asks the model for the mass $\mathbf{M}^{\Omega}$, damping $\mathbf{C}^{\Omega}$ and stiffness $\mathbf{K}^{\Omega}$ matrices as well as for internal $\mathbf{f}^{\Omega}$ and external $\mathbf{f}^{\Gamma}$ force vectors and uses them to compute the iterative correction $\Delta\mathbf{a}$. The relevant actions interpreted by the model are written in capital letters.

8.3. BASE MODELS

Given the data required by the solver module, a suitable model must be constructed such that all relevant action requests made by the module are properly answered. Conceivably, every action could be handled by a single model class. This would, however, result in a convoluted — and therefore error-prone — implementation. Instead, a set of models can be bundled together through the wrapper class *MultiModel*, which relays action calls to every submodel. Each relayed action can either be handled or ignored by each of the models. This effectively allows for an organized division of tasks, with models dealing with applying constraints ignore actions related to assembling global matrices while matrix models ignore calls for constraints. In the following, models required for solving the base finite element problems of Section 1.4.1 will be briefly presented. Most of the models were implemented from the ground up for the purpose of the work in this thesis, but some of them were based on initial versions previously used in other works, on which case the relevant references will be provided.

StressModel This model assembles the necessary matrices for bulk equilibrium problems. The displacement field is stored in a *DofSpace* object, the finite element mesh is handled by *NodeSet* and *ElementSet* objects and a continuum *Shape* object handles numerical integration. The constitutive behavior is obtained through the *update* function of the *Material* class, which receives the strains at the material point and returns stresses and stiffness. *Main actions: GET_MATRIX, GET_INT_VECTOR, COMMIT.*

InterfaceModel This model handles tractions across a discontinuity through an interface *Shape* object [2]. When used in conjunction with *StressModel*, both models operate on the same degrees of freedom, but assemble different parts of the stiffness matrix and internal force vector. The constitutive response is obtained through the *update* function of the *CohesiveMaterial* class. *Main actions: GET_MATRIX, GET_INT_VECTOR, COMMIT.*

FickModel This model handles transient mass diffusion problems solved using Fick's laws of diffusion. It operates on a *DofSpace* containing nodal concentrations and assembles the global diffusion and capacity matrices as well as the global flux vector. Material diffusivity and the flux at a material point are obtained from a *FickMaterial* object which can feature either isotropic or anisotropic diffusivity. *Main actions: GET_MATRIX, GET_INT_VECTOR.*

LoadModel This is responsible for applying either Dirichlet- or Neumann-type boundary conditions to specific node groups. A *Constraints* object is obtained from *Globdat* and prescribed displacements or concentrations are added for later use by the solver. Alternatively, the model can assemble the external force vector $\mathbf{f}^{\Gamma}$. The boundary conditions can either be constant or change in time, the shape of which can be specified by a user-defined mathematical expression. This also allows the application of cyclic boundary conditions. *Main actions: ADVANCE, GET_EXT_VECTOR, GET_CONSTRAINTS, COMMIT, CANCEL.*

PeriodicBCModel, ConcPBCModel These models can be used to apply periodic boundary conditions to the boundaries of micromodels, both in terms of displacements [3] as well as concentrations. The helper module *GroupInputModule* is employed to identify the nodes at relevant boundaries and the periodic constraints described in Sections 3.3.1 and 4.2.3 are applied to them. *Main actions: ADVANCE, GET_CONSTRAINTS, COMMIT, CANCEL.*

8.4. MATERIAL MODELS

When building new material models, the main concern lies in the implementation of the *update* function, which receives the strain vector and returns the stress vector and the consistent tangent stiffness matrix. All material models are derived from an abstract *Material* (or *CohesiveMaterial*) base class. Specialized materials are derived from the base class through polymorphism, implementing their own *update* functions and having their own parameter sets.

For linear materials, the *update* function basically consists in multiplying the strains by a constant stiffness tensor to obtain the stresses. For nonlinear materials, a helper *Hist* class provides a data structure and relevant functions for handling internal variables. As a general rule, the *update* function only operates on the history variables of the last converged time step (*preHist*) and sets their new candidate values (*newHist*). Upon convergence (when the *COMMIT* action is called), history is permanently updated by assigning the new values to *preHist*.

Fig. 8.2a shows a flowchart of the *update* function of a bulk material with plasticity, damage, hygrothermal degradation and swelling and thermal strains. This general implementation can describe both the inviscid epoxy model used in Chapter 4 (expanded from the implementation in [3]) as well as the viscous variants of Chapters 5 to 7. For viscoelasticity, historical and viscous stresses are included in $\boldsymbol{\sigma}^{\text{tr}}$ while viscoplasticity is included by modifying the return mapping algorithm that computes the change in plastic multiplier $\Delta\gamma$. For all models, the simplifying assumption is made that plasticity ceases to evolve after damage activation, allowing for the energy dissipation during softening to be controlled by the damage model.

Fig. 8.2b shows the *update* function for the mixed-mode cohesive zone model with friction [2] described in Chapter 7. If the algorithm is stopped after first computing the tractions and stiffness, it can also represent the model without friction of Chapter 4. This update procedure is performed in the local coordinate system of the interface element (Fig. 1.6). It is therefore necessary to apply coordinate transformations to compute the

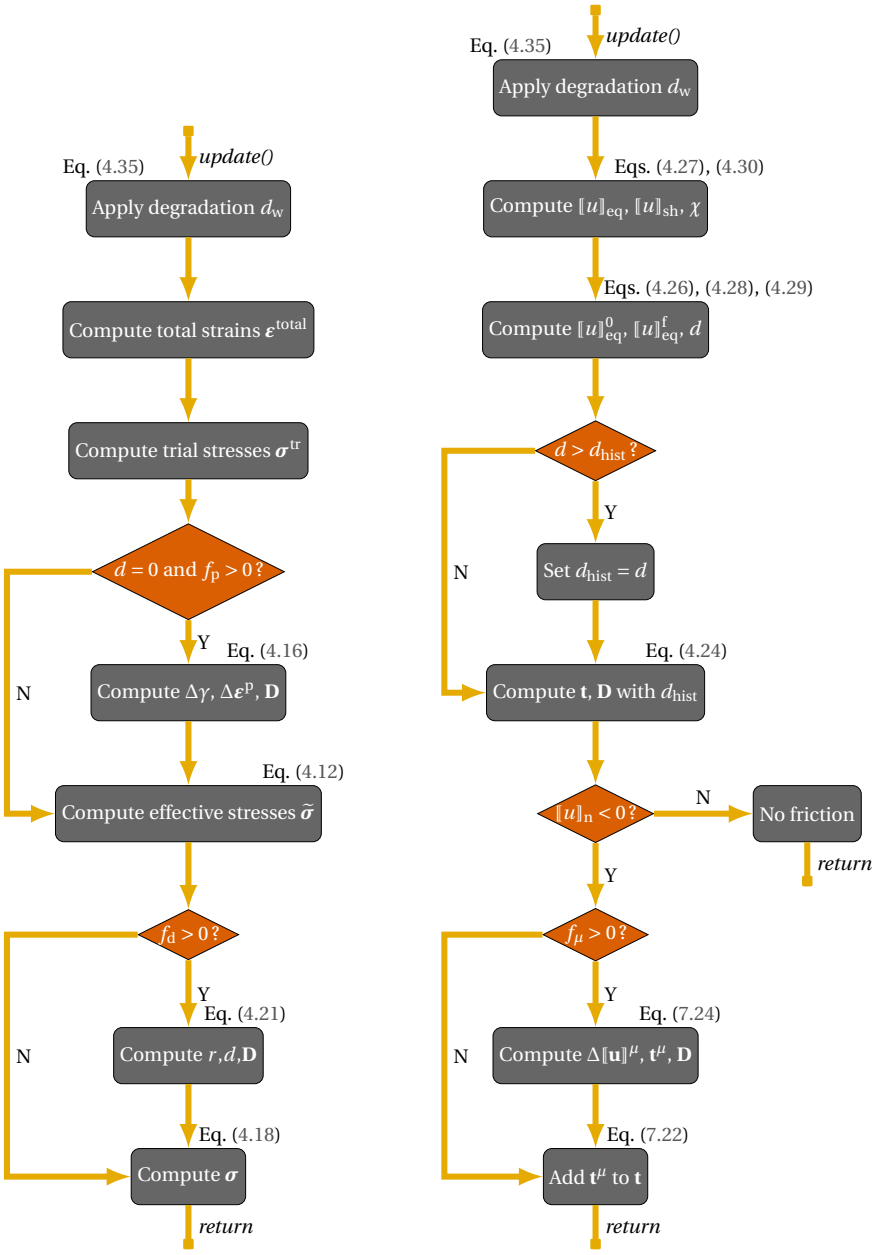

(a) Bulk model with plasticity and damage

(b) Cohesive-zone model with friction

Figure 8.2: Nonlinear material models for bulk and interfaces.

local displacement jump and the global tractions and stiffness. These transformations are performed by *InterfaceModel* before and after the *update* function is called.

8.5. ADAPTIVE SOLVER MODULES

For monotonic loading and simple material models, the global system of equations can be readily solved by the Newton-Raphson incremental/iterative procedure implemented in the *NonlinModule* included in the standard *Jive* implicit solver package. For materials undergoing sharp stiffness transitions, such as the transition from loading to unloading or when the behavior changes from plasticity to damage, achieving convergence can be considerably more difficult. In such cases, employing modified solvers or adding wrapper modules that adaptively modify solver behavior becomes a necessity. In the following, three different strategies used in Chapters 4 and 7 are briefly described.

XNonlinModule This is a modified version of the built-in *NonlinModule* with two main changes. First, a configurable maximum residual level is included through which the current step is cancelled if the Newton-Raphson residual becomes too high. This dramatically improves the efficiency of the solver when material models with Return Mapping algorithms are used. For these materials, convergence of the local root finding algorithm is significantly degraded if the global solver starts to diverge, which can lead, in extreme cases, to a complete freeze of the analysis. In these cases, it is therefore more reasonable to cancel the current increment before the maximum number of iterations is reached. Second, the solver is configured to detect oscillatory behavior in the residual and switch to a modified Newton-Raphson strategy that identifies the material points responsible for the oscillations and forces them to use secant versions of their stiffness matrices [4]. This strategy is crucial for achieving convergence while using the continuum damage models of Chapters 4, 5 and 7. For this work, the original algorithm was expanded to include more complex oscillatory patterns.

AdaptiveStepModule This module, a slightly modified version of the one described in [4], is wrapped around *XNonlinModule* and adaptively changes the analysis step size based on the convergence behavior of the last load increment. An optimum number of iterations can be set and the step size is increased if the solver is converging with less iterations or decreased if more iterations are necessary, respectively. If no convergence is achieved, the current step is cancelled and the increment for the next step is reduced. After a lower step size limit is reached, the module instead tries to increase the step size until an upper bound is reached. The analysis is shut down only after both strategies fail.

FlexArclenModule This module was employed to obtain the failure envelopes of Chapter 4. The original implementation described in [4, 5] was left unmodified but the dissipative term $\Delta\overline{\mathbf{u}}^{\mathrm{T}}\mathbf{f}_0^*$ from Eq. (4.58), computed at material level, was modified to account for the presence of swelling strains. The algorithm constrains the dissipated energy instead of performing an incremental step in terms of loads or displacements. This allows for equilibrium paths with a snapback to be correctly captured.

8.6. MULTISCALE/MULTIPHYSICS FRAMEWORK

In Chapters 4 and 7, a staggered multiphysics approach was adopted in order to couple diffusion and stress equilibrium models acting on the same macroscopic finite element mesh. Since the two models are not fully coupled — in which case every iteration would entail the execution of both model components — they are given their own *ChainModule*, *Globdat* and *Model* objects.

Starting from a single chain, the *ForkModule* is used to create one additional chain and duplicating the original *Globdat* during the initialization phase. These two instances of *Globdat* share data initialized before duplication (*e.g.* mesh data), but have different *DofSpaces*. Further data sharing is handled by *ForkModule*. For each time step, the diffusion chain is executed, the water concentration field is copied to the stress *Globdat* and only then the stress chain is executed (Fig. 8.3). An optional $t_{\max}$ parameter is added in order to allow for a pre-conditioning coupled phase followed by a mechanical test during which the water concentration field is kept constant. Once stored in *Globdat*, the nodal water concentration field is accessed by *StressModel* and *InterfaceModel*, used to compute the concentration at the integration points and subsequently relayed to the materials. In order to trigger this process, a simple module called *MultiPhysicsModule* was created which looks for the water concentration field in *Globdat* at each time step. If it is found, the action *APPLY_WATER* is called asking the models to retrieve the field.

The implementation of a concurrent multiscale (FE^2) analysis is based on the models used in [6] but were heavily modified for use in Chapters 4 and 7. The micromodels embedded at each macroscopic integration point can be conceptually seen as a material, and are therefore implemented as a subclass of *Material*. The new class, called *MacroMicroInterface*, can be directly used as material by the *StressModel* employed at the macroscale. Although no further modifications are necessary at this level, a new *GET_MATRIX* implementation is added in order to execute the constitutive updates in parallel. This exploits the fact that the input for each micromodel depends only on the strain at the macroscopic material point associated with it and can therefore be independently computed. The parallelization is done in a shared-memory environment using the *pthread* library.

In the *update* function, a child module chain is created for each macroscopic material point. Since they are used to implement the microscopic material domain, these new chains use a different mesh from that of the macroscale and a different set of models. By default, all micromodels use the same mesh geometry, but the option to use different meshes for each macroscopic point is also available. Analogous to the *Hist* objects used for conventional material models, each micromodel has two associated *MicroState* objects, one for the new state and another for the state corresponding to the latest converged macroscopic equilibrium point.

The new material state corresponding to the current macroscopic strain is applied to the micro chain: Strains are applied as prescribed displacements to the corner nodes of the micromodel (Section 4.2.3) and water concentration and temperature are relayed in the same way as performed by *MultiPhysicsModule*. The micro chain is executed and checked for convergence. If not converged, a modified version of the substepping procedure from [7] is used. This is a function that takes two *MicroState* objects representing an interval which is applied in two parts (both strain, concentration, temperature and

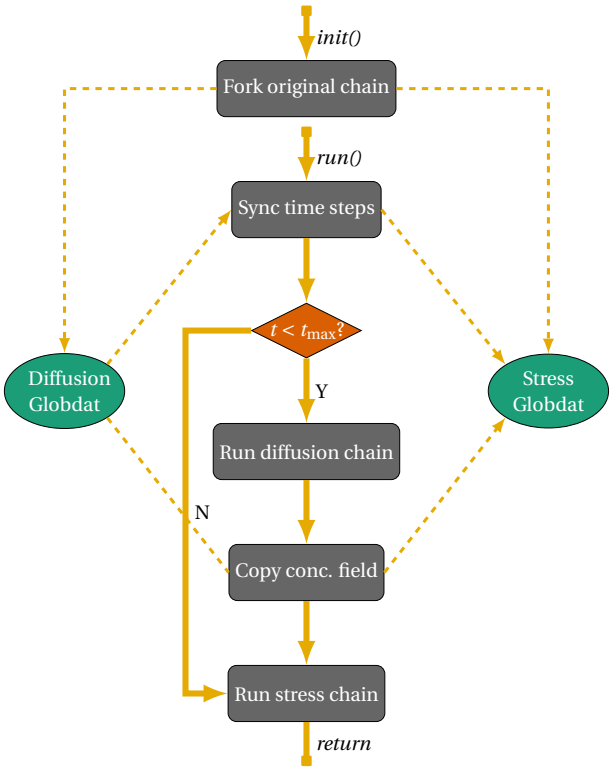

Figure 8.3: Multiphysics analysis flow.

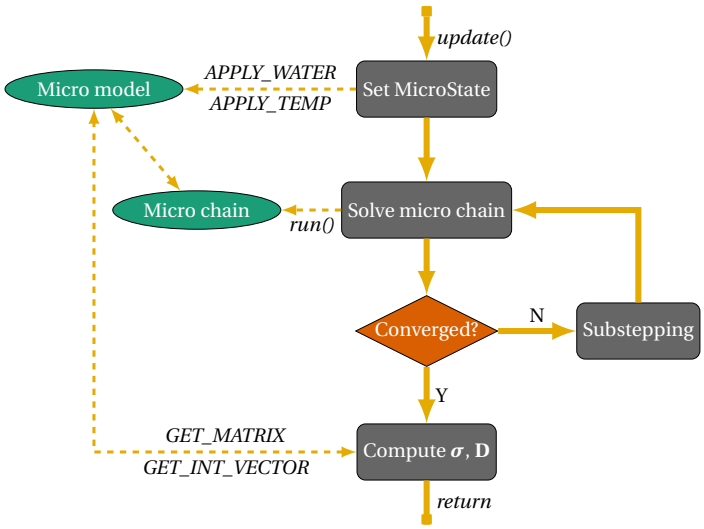

Figure 8.4: *MacroMicroInterface*: Material model for concurrent multiscale analysis.

time are divided). If convergence is not achieved in either half of the interval, the same function is called recursively. After the micromodel successfully converges to the current material state, the stresses and stiffness are computed through the method described in Section 4.2.4.

8.7. ACCELERATION TECHNIQUES

Performing the time-homogenized VE/VP analysis of Section 6.3 involves the modified load model *THLoadModel* and the viscoelastic/viscoplastic material *THMaterial* and is controlled by the solver wrapper *FatigueModule*. At the beginning of each time step, the module chooses between a macrochronological and a microchronological solver objects. Having separate solvers for each time scale is useful because micro steps are purely viscoelastic and additional time savings can be obtained by switching to a less computationally demanding linear solver.

The load model is then asked for a new time increment and load/displacement values, all of which depend on the time scale. The nested solver is executed and *THMaterial* chooses between performing a VE update and storing the stresses or performing a VP update combining the current macro stresses and the stored micro stresses. After convergence, the module determines the time scale of the next step: If the current step is macrochronological and the next micro cycle is not going to be skipped, the analysis moves to the microscale. If the current step is microchronological but one more micro time increment would complete a full load cycle, the analysis moves to the macroscale. It is worth mentioning that *THMaterial* keeps $\widetilde{\boldsymbol{\sigma}}$ values for every micro time step of the latest cycle. If the module skips the next cycle and instead jumps to the next macro time step, the same values are going to be used for the next VP update, which is the expected behavior. The complete analysis flowchart is shown in Fig. 8.5.

The reduced-order modeling techniques of Chapter 6 involve two distinct phases: An *offline* phase during which the model is trained and an *online* phase in which the resultant accelerated model is employed. Training is performed by combining a model which runs the *offline* analyses (*TrainingModel*) with a module (*ROMModule*) that uses the collected displacement or stress snapshots to compute the reduced displacement basis (POD), the reduced set of integration points (ECM) and the clusters for history reconstruction (clustered Gappy Data). The training process is therefore entirely integrated within *Jive* and does not involve extensive reading and writing operations involving data files.

Fig. 8.6 shows the procedures involved in the training process. When asked to perform a training round, the *TrainingModel* class uses a child *ChainModule* object (analogous to the embedded micromodels of *MacroMicroInterface*) to initialize the first model on a list of user-defined model configuration files representing the different load cases used for training and solves them while collecting displacement snapshots. After the last time step is reached, the next model is initialized and the process is repeated until all models have been executed. The snapshots are gathered by a helper class called *ROMData*, the reference of which is stored in *Globdat*.

After performing the first reduction step by computing the POD basis matrix $\boldsymbol{\Phi}$ (Fig. 8.7), the modes are written to a data file for future *online* use and injected back into *TrainingModel* in order to perform the second (hyper reduction) training round. In this second

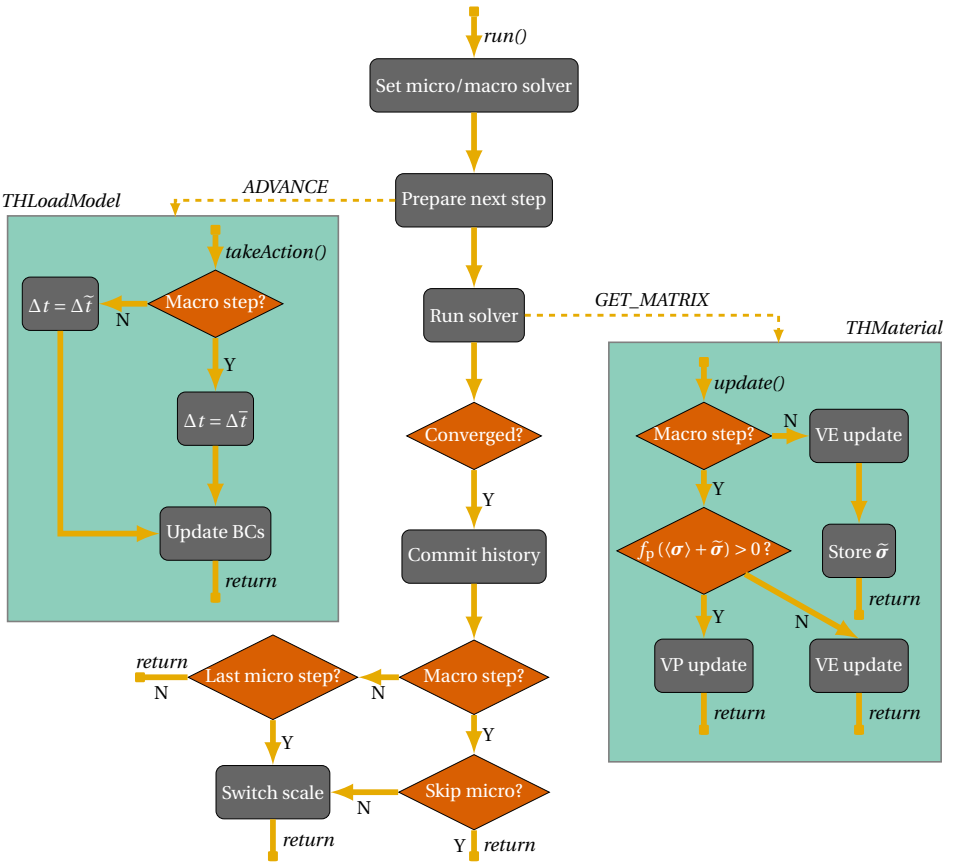

Figure 8.5: *FatigueModule* used to perform time-homogenized VE/VP analysis.

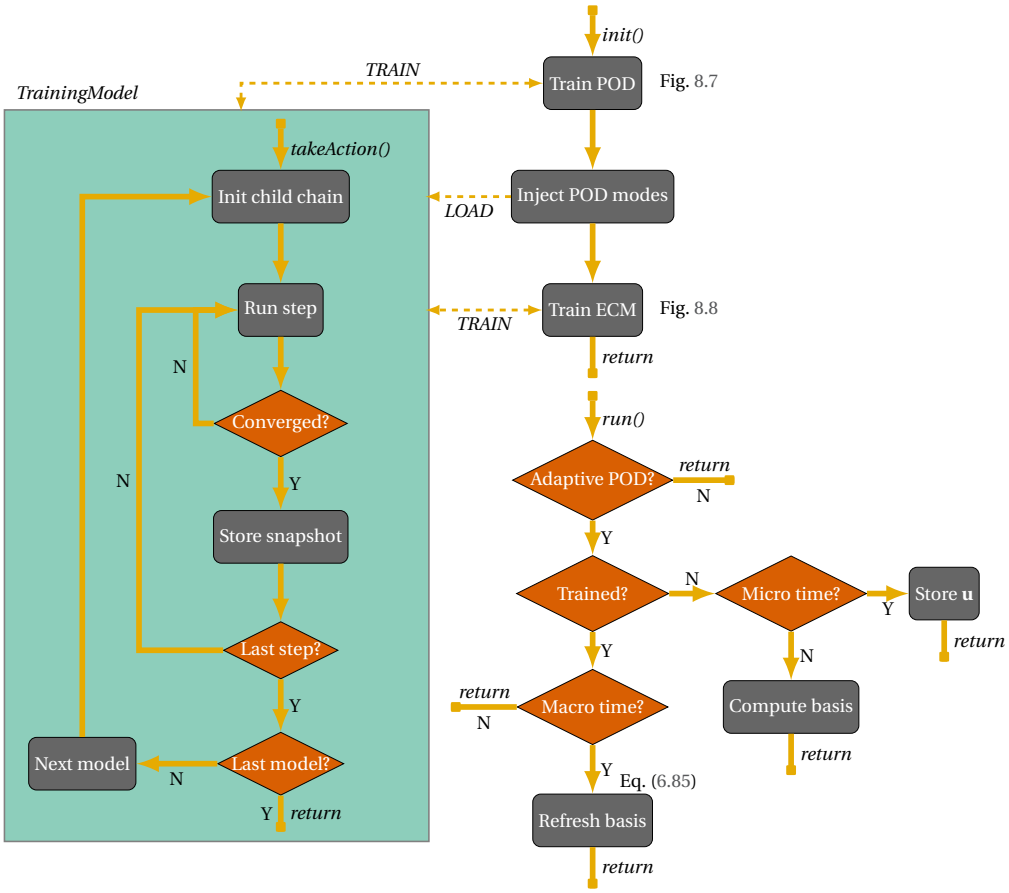

Figure 8.6: *ROMModule*: Offline POD/ECM training or online adaptive POD.

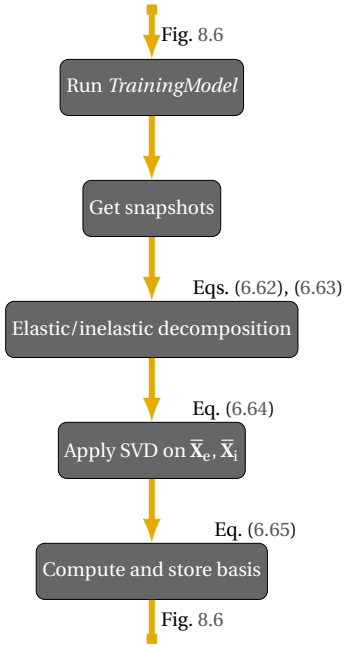

Figure 8.7: POD training.

phase, stress/traction snapshots are gathered, as well as history snapshots if a Gappy Data reconstruction of material history is sought. The ECM method is then applied to obtain the reduced set of integration points and their modified weights, with an optional step of computing the Gappy recovery matrix for material history (Fig. 8.8). The points, clusters and recovery matrix are written to data files for *online* use.

It is worth mentioning that even though the SVD is applied to snapshot matrices composed of stresses or tractions, the basis matrix $\mathbf{\Lambda}$ is composed of reduced internal force components. This conversion is done in two parts: First, the model (the latest child model solved by *TrainingModel*) is asked to pre-multiply the stresses or tractions by $\mathbf{B}^{\mathrm{T}}$ (Eq. (1.14)). The resultant full-order internal force is stored in *ROMData* which then pre-multiplies it by $\mathbf{\Phi}^{\mathrm{T}}$ in order to obtain the force components in the reduced space. It is also important to note that the cubature procedure is performed separately for bulk elements (recovering the original mesh volume) and for interface elements (recovering the original sum of surface areas of all interfaces). This is an expansion of the original method proposed by Hernández *et al.* [8]

If data files containing the reduced displacement modes for POD-reduction are given at the beginning of the analysis, *ROMModule* skips the training process and assumes an *online* analysis is to be executed. The data is loaded into a *ROMData* object, stored in *Globdat* and sent to the model through the *LOAD_DATA* action. Optionally, data files containing ECM and history recovery data can also be provided. This description now moves to the *online* phase.

By default, both models and modules operate on the same *DofSpace*: The solver finds

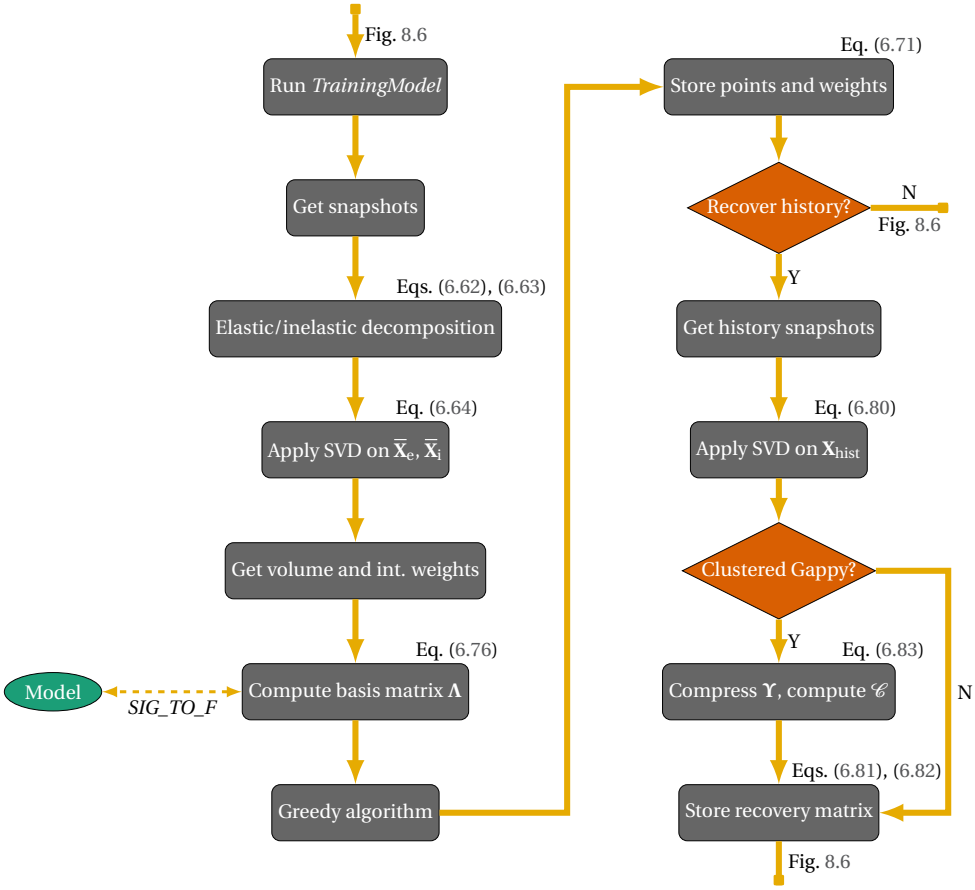

Figure 8.8: ECM training.

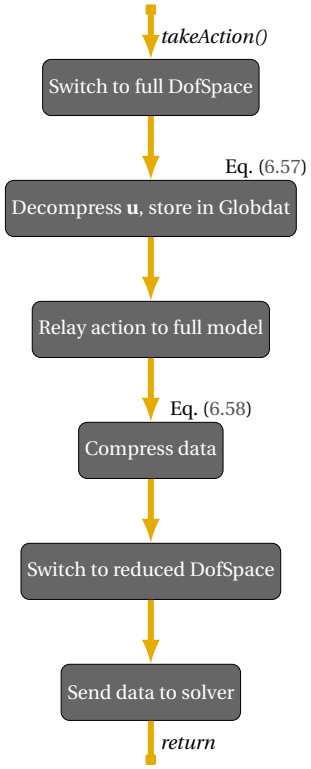

Figure 8.9: *PODModel*: Communication layer between a full-order model and a reduced-order solver.

new values for the degrees of freedom and the models use them to compute updated versions of $\mathbf{f}^{\Omega}$ and $\mathbf{K}^{\Omega}$. This behavior is modified when a POD-reduced model is used: The solver is not aware of the full size of the problem and solves it in a reduced *DofSpace*, while the model is not aware of the reduction and uses a full-order *DofSpace* to compute global vectors and matrices. To achieve this, an intermediate layer which wraps around the full-order models (*PODModel*) is employed in order to perform the transitions between full and reduced solution spaces using the matrix of displacement modes $\mathbf{\Phi}$ of Eq. (6.56). Fig. 8.9 shows the general behavior of the model when the solver requests information on the reduced space.

Adding ECM reduction to the *online* model requires only minor modifications to *StressModel* and *InterfaceModel*. Since the number of integration points is reduced, the standard loop through the points, in which the *update* function is called, is substituted by a loop through ECM points. The standard integration weights computed by the *Shape* class are substituted by the modified weights obtained during training. For history recovery, an additional step is performed after committing material history which performs the Gappy reconstruction at non-ECM points. If clustering is used, the cluster values are reconstructed and subsequently copied inside each of them.

It is important to note that when using the hyper-reduced model with the concur-

rent multiscale strategy of Fig. 8.4, computing $\boldsymbol{\sigma}$ and $\mathbf{D}$ through the technique presented in Section 4.2.4 would entail solving the unreduced system once for each strain component (*i.e.* 3 times for a 2D problem or 6 times for a 3D problem). This effectively negates a significant portion of the speed-up obtained through model order reduction. The alternative adopted here consists in computing a matrix $\mathbf{H}_\mathrm{r} \in \mathbb{R}^{n \times s}$, with n being the number of reduced degrees of freedom and s the number of strain components, such as to satisfy:

$$\boldsymbol{\alpha} = \mathbf{H}_\mathrm{r} \boldsymbol{\varepsilon}^\mathrm{M} \tag{8.1}$$

which is analogous to Eq. (4.49) but involves all reduced degrees of freedom, as the POD reduction implies that the displacement of any corner node is computed through a linear combination of modes and thus depends on all values of $\boldsymbol{\alpha}$. The $\mathbf{H}_\mathrm{r}$ matrix is then used to compute $\boldsymbol{\sigma}$ and $\mathbf{D}$ as:

$$\boldsymbol{\sigma} = \mathbf{H}_\mathrm{r} \mathbf{f}_\mathrm{r} \quad \mathbf{D} = \mathbf{H}_\mathrm{r} \mathbf{K}_\mathrm{r}^\Omega \mathbf{H}_\mathrm{r}^\mathrm{T} \tag{8.2}$$

ROMModule is also responsible for implementing the adaptive POD scheme of Section 6.4.5. Adopting this strategy means skipping both the *offline* training and the process of loading the data for *online* use, which are actions performed during the initialization of the module (*init* function). On the other hand, the adaptive strategy involves a gradual training process as an *online* full-order analysis progresses and is thus performed in the *run* function, as shown in Fig. 8.6. Therefore, the *init* function of *ROMModule* has three distinct behaviors:

- *No data files given, adaptive POD deactivated*: Perform POD and ECM training, optionally computing the Gappy reconstruction matrix and clusters. Store the data in files and immediately trigger a *shutdown*, ending the analysis
- *Data files given, adaptive POD deactivated*: Load the data and send it to the model. Skip the *run* function for the current analysis
- *Adaptive POD active*: Skip the whole *init* function. Perform the adaptive reduction procedures with the *run* function

The analysis starts unreduced and the module collects snapshots until the first microchronological cycle is reached. When the next macrochronological point is reached, the basis is computed through SVD but skipping the elastic/inelastic decomposition of Fig. 8.7. This basis is then used to run all subsequent micro cycles while a full-order analysis is employed at macro steps. The adaptive strategy requires that a third nested solver is added to *FatigueModule* (Fig. 8.5), which will then contain a full solver for the macro steps, a full solver for the first micro cycle and a reduced solver for the remaining micro cycles.

8.8. OTHER MODELS AND MODULES

This chapter is completed by a list of additional models and modules that do not fit in any of the previous sections but that were nonetheless important in order to obtain the results shown in the previous chapters:

- *OptimizationModule*: This module implements a bounded BFGS nonlinear optimization algorithm that handles inequality constraints using an *Active Set* approach. It can be used to efficiently solve parameter identification problems. This module is used to obtain the fitted diffusivities of Section 2.3.1 and to calibrate the constitutive model of Chapter 5.

- *IdentificationModel*: This model is used in conjunction with *OptimizationModule*. It contains a nested *ChainModule* and associated model whose parameters are being identified. At each iteration of the optimization process, the current design variables (*i.e.* material parameters) are set by the module and the model is executed for a number of pre-defined inputs extracted from experimental data. The objective function is computed as the sum of the squared differences between the numerical and experimental responses for each set of inputs.

- *InterfaceNodesModule*: This helper module takes as input two element groups and identifies the nodes belonging to both groups simultaneously (*i.e.* the interfaces between groups). These nodes are then duplicated and used to build interface elements. This module is used to generate the interface elements for the RVE simulations of Chapters 4 and 7.

- *StaticLevelSetModel*: This class constructs three-dimensional (cylindrical) level sets around the fibers of a micromodel with a pre-defined radius. It is based on a model previously used for level set simulations [9]. In this work, this simplified version of the model is used in Chapter 3 to define the interphase region around the fibers.

REFERENCES

[1] Jive - Software development kit for advanced numerical simulations, http://jive.dynaflow.com, accessed: 04-03-2018.

[2] F. P. van der Meer and L. J. Sluys, *Mesh-independent modeling of both distributed and discrete matrix cracking in interaction with delamination in composites,* Engineering Fracture Mechanics **77**, 719 (2010).

[3] F. P. van der Meer, *Micromechanical validation of a mesomodel for plasticity in composites,* European Journal of Mechanics - A/Solids **60**, 58 (2016).

[4] F. P. van der Meer, *Mesolevel modeling of failure in composite laminates: Constitutive, kinematic and algorithmic aspects,* Archives of Computational Methods in Engineering **19**, 381 (2012).

[5] M. A. Gutiérrez, *Energy release control for numerical simulations of failure in quasi-brittle solids,* Communications in Numerical Methods in Engineering **20**, 19 (2004).

[6] V. P. Nguyen, O. Lloberas-Valls, M. Stroeven, and L. J. Sluys, *Computational homogenization for multiscale crack modelling. implementation and computational aspects,* International Journal for Numerical Methods in Engineering **89**, 192 (2012).

[7] D. D. Sommer, E. A. de Souza Neto, W. G. Dettmer, and D. Perić, *A sub-stepping scheme for multi-scale analysis of solids,* Computer Methods in Applied Mechanics and Engineering **198**, 1006 (2009).

[8] J. A. Hernández, M. A. Caicedo, and A. Ferrer, *Dimensional hyper-reduction of nonlinear finite element models via empirical cubature,* Computer Methods in Applied Mechanics and Engineering **313**, 687 (2017).

[9] F. P. van der Meer, N. Moës, and L. J. Sluys, *A level set model for delamination – modeling crack growth without cohesive zone or stress singularity,* Engineering Fracture Mechanics **79**, 191 (2012).

9

CONCLUSION

We all make choices, but
in the end our choices make us.

Andrew Ryan, *Bioshock*

In this thesis, the phenomenon of hygrothermal aging in laminated composites was investigated using a combination of experiments and numerical modeling. The relevant microscopic degradation mechanisms are identified through experiments on pure resin and composite samples. A high-fidelity multiscale/multiphysics numerical framework is developed in order to describe hygrothermal degradation across spatial scales. Material nonlinearity at the microscale is captured through a viscoelastic/viscoplastic damage epoxy model and cohesive zone models with friction for the fiber/matrix interfaces. The framework is made efficient through a set of acceleration techniques combining time homogenization and reduced-order modeling.

CONTRIBUTIONS

The following contributions were made to the current knowledge on hygrothermal aging of laminated composites and on relevant modeling techniques for fast and accurate simulation of aging:

- A new extensive set of experiments on hygrothermal aging degradation of unidirectional glass/epoxy specimens was performed. The relative degradations of resin and interface were assessed through tests on pure resin specimens. The irreversible part of the degradation was investigated through redried tests.
- The evolution of hygrothermal degradation in composite samples was investigated by testing specimens after different conditioning durations. Time-dependent degradation processes were assessed by testing specimens conditioned for significantly longer than their saturation times.

- Anisotropic diffusion behavior in unidirectional composites was experimentally and numerically investigated. The relative contributions of barrier effects and anisotropic interphase diffusion were determined.

- A new set of monotonic and cyclic tests on pure resin at different strain rates was performed. The viscoelastic behavior of the polymer was investigated through DMA tests.

- A new approach for obtaining interface properties through the single fiber fragmentation tests combining analytical and numerical solutions was proposed. The combination allows the estimation of both strength and fracture toughness properties.

- A multiphysics and multiscale numerical framework for hygrothermal aging was proposed. A degradation model for plasticization and interface degradation with a single degradation factor was introduced.

- The inviscid elastoplastic model by Melro *et al.* was modified to include viscoelasticity, viscoplasticity and rate-dependent fracture initiation. The idea of a shrinking fracture surface based on the total dissipated energy was introduced.

- The time homogenization formulation by Yu and Fish was applied to the new pressure-dependent viscoelastic/viscoplastic model. A return mapping algorithm with numerical time integration capable of dealing with multiaxial stress states was developed.

- The Empirical Cubature Method (ECM) proposed by Hernández *et al.* was extended to treat interface elements. An efficient stress and history recovery method combining Gappy Data and k-means clustering was developed.

- An adaptive model-order reduction scheme combining POD and time homogenization was proposed which introduces no additional approximation errors to the time-homogenized full-order model and requires no *offline* training.

CONCLUSIONS

From the performed experiments and numerical analyses, a number of conclusions can be made regarding the hygrothermal aging behavior of the present glass/epoxy material system and the progress made in its modeling:

- For immersion in demineralized water at 50 °C, diffusion in pure resin is well described by Fick's law. For composites, non-Fickian secondary absorption mechanisms related to the fiber/matrix interfacial region occur at longer immersion times.

- Hygrothermal degradation consists in the combination of resin plasticization, differential swelling and physicochemical weakening of interfacial adhesion. Only part of the degradation is reversible upon redrying.

- Diffusion occurs at a faster rate inside a transition region between fibers and bulk resin (interphase). This effect, combined with the barrier effect caused by the presence of fibers, leads to anisotropic water diffusion behavior. Although the exact mechanism is still unclear, results point to additional anisotropy within the interphase, with faster diffusion along the fibers.
- Large micromodels (with at least 25 fibers) are necessary in order to accurately capture macroscopic hygrothermal degradation through homogenization. Due to the combined effect of differential swelling, plasticization and transient macroscopic swelling, the degradation level inside a specimen is higher at regions close to its surface, although this difference is very small.
- The present epoxy resin exhibits a number of time-dependent phenomena such as strain-rate plasticity and fracture, ratcheting, stress relaxation and hysteresis. An inviscid elastoplastic model with damage is not able to capture any of these phenomena and is therefore unsuitable for modeling cyclic loadings or loading situations with varying strain rates (*e.g.* the slow process of hygrothermal aging followed by a rapid mechanical test).
- The implemented viscoelastic/viscoplastic/damage epoxy model can accurately represent the strain-rate dependent response of the polymer in both dry and saturated conditions. However, the model significantly overestimates the amount of permanent strain upon unloading.
- Time homogenization allows for reducing the cost of a cyclic analysis to one nonlinear step per load cycle with a very limited loss of accuracy of approximately 2 % for the analyzed case. If the microchronological cycle does not change throughout the analysis, it can computed only once, leading to significant time savings.
- The combination of POD and ECM leads to speed-ups as high as 120 for 7×7 micromodels. Combining these reduction techniques with time homogenization increases the acceleration to more than 1000 with an additional loss of accuracy of less than 1 %.
- Combining time homogenization and reduced-order modeling techniques with the developed multiscale/multiphysics model results in a fast and accurate framework suitable for long-term prediction of material degradation due to a combination of aging and cyclic loads.
- The framework qualitatively reproduces the experimentally observed stiffness and strength degradation in dry, saturated and partially saturated interlaminar shear specimens. Further experiments on the fracture behaviors of resin and interface are necessary in order to obtain reliable properties and improve the predictive capabilities of the framework.

FUTURE PERSPECTIVE

Although this work represents a step forward in better understanding hygrothermal aging of laminated composites and developing relevant tools for its computational simu-

lation, a large number of open questions remain. In the following, a number of potential improvements for future works are listed.

Additional aging experiments The hygrothermal aging experiments performed in this work were focused on water immersion in demineralized water at 50 °C of unidirectional interlaminar shear short-beams. Further knowledge can be gained on the aging mechanisms as experiments are performed under different conditions and with different specimen types. Immersion at different temperatures is expected to drastically change degradation behavior and should be the immediate focus of future studies on this subject. Although the effect of temperature on the diffusivity is well documented in literature, the effect on hygrothermal degradation is less so, and consistent comparisons between pure resin and composite samples and of dry, saturated and redried specimens at multiple temperatures have not been found.

Tests with different types of water (*e.g.* seawater) are expected to yield different degradation behaviors, since diffusion, chemical bonds and chemical reactions strongly depend on the chemical composition of the immersion environment. Conditioning at different levels of relative humidity would also be interesting. More specifically, a comparison between immersion and a condensation environment would yield new and valuable knowledge.

Investigations on different specimen types are also recommended, particularly in specimens with different layups. Most importantly, this work did not dwell upon the subject of fiber leaching and the consequent reduction in strength in the fiber direction that such mechanism would cause. Once again, such a study should be conducted at different temperatures, conditioning environments and for multiple aging durations.

Micromechanical experiments A number of tests on pure resin specimens were performed throughout the present work, but only a limited attempt on micromechanical characterization of the fiber/matrix interface behavior was performed. Further development of the single fiber fragmentation test is necessary, both regarding the manufacturing and test setups as well as the processing of the results and property determination, matters for which no literature consensus exists at present. Since the development of fragments happens rather late for this composite system — often coinciding with necking of the dog-bone specimen — more tests are necessary in order to obtain a statistically significant estimation of interface properties. Additional tests at different immersion times, both shorter and longer than the saturation time, would give useful data on the evolution of interface degradation with water concentration and time. Tests on redried specimens are also essential in order to determine the irreversible part of the degradation. Lastly, the presence of friction in wet fragmentation samples — for which differential swelling leads to tension radial stresses — is still an open question. Other micromechanical tests could also be explored, such as micro- and nanoindentation, pushout tests and micro-droplet tests.

Water movement through cracks The present development only considers diffusion through continuum media in order to compute the water concentration field. At the same time, a multitude of failure phenomena that effectively create discontinuities and

empty spaces inside the material, including interface and resin cracks, are predicted by stress analysis. The contradiction involved in combining these two approaches and the consequent loss in analysis fidelity is obvious. A better description of water movement through and across discontinuities would be a valuable addition to the present framework. When combined with a suitable description of the time-dependent chemical degradation of the interphase, the water moving through the newly created empty spaces would help to reproduce the secondary uptake process observed experimentally.

Chemical damage and blistering The present framework predicts only a limited amount of permanent degradation after a complete immersion-redrying cycle. This implies that plasticization and differential swelling are not enough to explain the complete hygrothermal degradation process in the present material system and that an appropriate description of chemical damage is necessary. A suitable model for tracking the concentrations of the various chemical compounds involved in hydrolytic chemical reactions would be a first step in developing a model that accounts for the extensive blistering process observed through tomography on specimens aged at 65 °C (Section 7.3).

Temperature dependency Although immediately obvious from results of DMA tests on the present epoxy resin, changes in stiffness and viscous behavior with temperature are not taken into account by the constitutive models formulated in this work. This also implies that properties obtained from tests at room temperature are used to describe the aging phenomenon occurring at higher temperatures. Inclusion of the effect of temperature on the viscoelastic/viscoplastic resin properties, ideally with the inclusion of a realistic model for the glass transition phenomenon [1], would be a beneficial step in expanding the current framework.

Nonlinear viscoelasticity Although the viscoelastic/viscoplastic formulation adopted in this work reproduces the rate-dependent monotonic material behavior accurately, the unloading behavior is not correctly captured as the amount of plastic strain is overestimated. Inclusion of a nonlinear viscoelastic model would improve predictions of the cyclic behavior of the polymer. However, additional experiments would be necessary since the added material parameters would need to be calibrated.

Longer time scales The time-homogenized viscoelastic/viscoplastic formulation used in this work reduces the computational effort of a cyclic analysis by allowing the use of a single time step per load cycle. However, given the significantly slower time scale associated with water diffusion, the inclusion of a consistent way of performing cycle jumps, therefore further increasing the size of the time steps, would be beneficial. Including a third time scale in the time homogenization formulation or solving higher-order problems associated with the asymptotic expansion of the mechanical response fields would allow for larger time steps to be considered with only limited loss of accuracy.

Adaptive ROM strategies The reduction techniques used in this work, based on projecting the solution onto a lower-dimensional subspace, are pushed to their limit if a correct prediction of structural behavior after strain localization is sought. In practice, this

means that a large number of POD modes and ECM points will be necessary for correctly describing the failure behavior of a micromodel subjected to complex loading scenarios, negating a significant part of the speed-up attained through the reduction process.

A definitive solution to the problem of representing strain localization with reduced models does not exist at this point in time and research on the subject is still in its infancy. One class of solutions that has been producing promising results involves the use of adaptive reduction strategies, for instance solving only part of the mesh in the reduced space while using a full-order solver at regions with localized strain [2, 3]. Alternatively, machine learning techniques can be used to select, at the beginning of each time step, an optimized subset of displacement modes among a larger pool of modes and using only these selected modes to solve the equilibrium problem [4].

Strain localization with FE^2 Upon strain localization, the homogenized mechanical response of the micromodel ceases to be objective with respect to the size of the microscopic domain — the larger the RVE the more brittle its homogenized softening response is. Therefore, if the conventional homogenization procedure is used, an RVE does not exist for softening. In this work, this issue is bypassed either by stopping the analysis before localization or by matching the size of the macroscopic element with the one of the microscopic domain. In future developments, incorporating a definitive solution for this problem, such as the one proposed by Nguyen *et al.* [5, 6] would be beneficial.

Molecular Dynamics This work sought to investigate hygrothermal aging at the microscale in an attempt to avoid the significant amount of phenomenological characterization necessary when a purely macroscopic approach is adopted. By focusing on degradation mechanisms acting on a lower scale, changes in macroscopic behavior emerge in a natural way. However, even at the microscale, both the aging phenomenon as well as the mechanical behavior of resin and interphase are still exceedingly complex and their modeling still requires an enormous amount of calibration experiments. It seems, therefore, that further downscaling is necessary. Molecular- or atomic-level modeling through Molecular Dynamics could be an interesting approach to aid the development and calibration of higher-scale models as well as improve the understanding of experimentally observed phenomena.

REFERENCES

[1] C. Yu, G. Kang, and K. Chen, *A hygro-thermal-mechanical coupled cyclic constitutive model for polymers with considering glass transition,* International Journal of Plasticity **89**, 29 (2017).

[2] P. Kerfriden, J. C. Passieux, and S. P. A. Bordas, *Local/global model order reduction strategy for the simulation of quasi-brittle failure,* International Journal for Numerical Methods in Engineering **89**, 154 (2012).

[3] P. Kerfriden, O. Goury, T. Rabczuk, and S. P. A. Bordas, *A partitioned model order reduction approach to rationalise computational expenses in nonlinear fracture mechanics,* Computer Methods in Applied Mechanics and Engineering **256**, 169 (2013).

[4] F. Ghavamian, P. Tiso, and A. Simone, *POD-DEIM model order reduction for strain-softening viscoplasticity,* Computer Methods in Applied Mechanics and Engineering **317**, 458 (2017).

[5] V. P. Nguyen, O. Lloberas Valls, M. Stroeven, and L. J. Sluys, *On the existence of representative volumes for softening quasi-brittle materials - a failure zone averaging scheme,* Computer Methods in Applied Mechanics and Engineering **199**, 45 (2010).

[6] V. P. Nguyen, O. Lloberas-Valls, M. Stroeven, and L. J. Sluys, *Computational homogenization for multiscale crack modelling. implementation and computational aspects,* International Journal for Numerical Methods in Engineering **89**, 192 (2012).

Propositions

accompanying the dissertation

NUMERICAL AND EXPERIMENTAL INVESTIGATION OF HYGROTHERMAL AGING IN LAMINATED COMPOSITES

by

Iuri BARCELOS CARNEIRO MONTENEGRO DA ROCHA

1. Water is one of the simplest chemical compounds found in nature. Yet it still offers boundless potential for new scientific discoveries.
2. The complex degradation mechanisms involved in hygrothermal aging make purely macroscopic experimental and modeling efforts inadequate.
3. Capturing multiple long-term degradation processes with an accurate multiscale model either requires efficient acceleration techniques or a great deal of patience.
4. A great portion of the time of a computational mechanics researcher is spent trying to get models to converge. Nevertheless, matters of robustness are seldom reported and should deserve more space in discussion.
5. The excitement of trying new ideas and stumbling upon interesting new ways to combine existing methods is so great, one often forgets to question if using them is even necessary in the first place.
6. Juggling between the idealized version of reality provided by computational models and the ever unpredictable world of real experiments is a tricky balancing act.
7. Sometimes two different research communities study the exact same thing, but they often cannot understand each other's works.
8. Rooting for a model that is struggling to converge is as thrilling as rooting for your favorite sports team.
9. Implicit methods often need local and global iterative schemes. Writing articles with many authors can also be seen as an implicit process: Iterate on your own until you are satisfied with the draft and global convergence will come more easily.
10. Prejudice arises because the human brain finds it much easier to categorize people into well-defined stereotypes, cultures or social groups instead of struggling to cope with the infinite complexity of human behavior. "To define is to limit." (Oscar Wilde, *The Picture of Dorian Gray*).

These propositions are regarded as opposable and defendable, and have been approved as such by the promotor prof. dr. ir. L. J. Sluys.

Stellingen

behorende bij het proefschrift

NUMERICAL AND EXPERIMENTAL INVESTIGATION OF HYGROTHERMAL AGING IN LAMINATED COMPOSITES

door

Iuri BARCELOS CARNEIRO MONTENEGRO DA ROCHA

1. Water is een van de eenvoudigste chemische verbindingen in de natuur. Toch biedt het onbegrensde mogelijkheden voor wetenschappelijke uitvindingen.
2. De complexe degradatiemechanismen die een rol spelen bij hygrothermische veroudering maken pure macroscopische experimentele en numerieke benaderingen ongeschikt.
3. Het modelleren van meerdere langdurige degradatieprocessen met een nauwkeurig multischaal model vereist efficiënte versnellingstechnieken óf veel geduld.
4. Een groot deel van de tijd van een onderzoeker van computationele mechanica is besteed aan pogingen om modellen te laten convergeren. Niettemin worden discussies over stabiliteit, die veel belangstelling verdienen, maar zelden gerapporteerd.
5. Omdat het uitproberen van nieuwe ideeën en het vinden van nieuwe manieren om bestaande technieken te combineren zo opwindend is, vergeet de onderzoeker vaak om na te denken of de ideeën überhaupt nuttig zijn.
6. Het balanceren tussen de geïdealiseerde wereld van computermodellen en de onvoorspelbare werkelijkheid van echte experimenten is een lastige taak.
7. Soms bestuderen twee verschillende onderzoeksgemeenschappen precies hetzelfde onderwerp, maar toch kunnen ze elkaars werken niet begrijpen.
8. Het juichen voor een model dat het moeilijk heeft om te convergeren is even spannend als het juichen voor je favoriete sportteam.
9. Vaak eisen impliciete methoden locale en globale iteratieve algoritmen. Het schrijven van artikelen met veel auteurs kan ook worden gezien als een impliciet proces: itereer in je eentje tot je helemaal tevreden bent met de tekst en globale convergentie zal sneller komen.
10. Vooroordelen ontstaan omdat het menselijke brein het veel makkelijker vindt om mensen toe te wijzen aan welomschreven stereotypes, culturen of maatschappelijke groepen in plaats van te worstelen met de oneindige complexiteit van menselijk gedrag. "Definiëren is beperken."(Oscar Wilde, *Het Portret van Dorian Gray*).

Deze stellingen worden opponeerbaar en verdedigbaar geacht en zijn als zodanig goedgekeurd door de promotor prof. dr. ir. L. J. Sluys.

CURRICULUM VITÆ

Iuri BARCELOS CARNEIRO MONTENEGRO DA ROCHA

27-03-1988 Born in Fortaleza, Brazil.

EDUCATION

2006–2010 *Bachelor in Civil Engineering*
Department of Civil Engineering
Federal University of Ceará, Brazil
Thesis: Analysis and optimization of composite tubes
Promotor: Prof. dr. Evandro Parente Junior

2011 – 2013 *Master of Science in Computational Mechanics*
Department of Structural Engineering
Federal University of Ceará, Brazil
Thesis: Analysis and optimization of laminated shells with geometric nonlinearity and progressive failure
Promotor: Prof. dr. Evandro Parente Junior

2014 – 2018 *PhD candidate in Computational Mechanics*
Materials Research Group
Knowledge Centre WMC, the Netherlands
Department of Civil Engineering and Geosciences
Delft University of Technology, the Netherlands
Supervisors: Dr. ir. R. P. L. Nijssen and Dr. ir. F. P. van der Meer
Promotor: Prof. dr. L. J. Sluys

LIST OF PUBLICATIONS

JOURNAL ARTICLES

6. **I. B. C. M. Rocha**, F.P. van der Meer, S. Raijmaekers, F. Lahuerta, R.P.L. Nijssen, L.P. Mikkelsen, L.J. Sluys. *A combined experimental/numerical investigation on hygrothermal aging of fiber-reinforced composites.* European Journal of Mechanics - A/Solids, **73**, 407-419 (2019).

5. **I. B. C. M. Rocha**, F.P. van der Meer, L.J. Sluys. *Efficient micromechanical analysis of fiber-reinforced composites subjected to cyclic loading through time homogenization and reduced-order modeling.* Computer Methods in Applied Mechanics and Engineering, **345**, 644-670 (2019).

4. **I. B. C. M. Rocha**, F.P. van der Meer, S. Raijmaekers, F. Lahuerta, R.P.L. Nijssen, L.J. Sluys. *Numerical/experimental study of the monotonic and cyclic vistoelastic/viscoplastic/fracture behavior of an epoxy resin.* Under review.

3. **I. B. C. M. Rocha**, F.P. van der Meer, R.P.L. Nijssen, L.J. Sluys. *A multiscale and multiphysics numerical framework for modelling of hygrothermal ageing in laminated composites.* International Journal for Numerical Methods in Engineering, **112**, 360-379 (2017).

2. **I. B. C. M. Rocha**, S. Raijmaekers, F.P. van der Meer, R.P.L. Nijssen, H.R. Fischer, L.J. Sluys. *Combined experimental/numerical investigation of directional moisture diffusion in glass/epoxy composites.* Composites Science and Technology, **151**, 16-24 (2017).

1. **I. B. C. M. Rocha**, S. Raijmaekers, R.P.L. Nijssen, F.P. van der Meer, L.J. Sluys. *Hygrothermal ageing behaviour of a glass/epoxy composite used in wind turbine blades.* Composite Structures, **174**, 110-122 (2017).

CO-AUTHORED JOURNAL ARTICLES

1. F.P. van der Meer, S. Raijmaekers, **I. B. C. M. Rocha**. *Interpreting the single fiber fragmentation test with numerical simulations.* Under review.

CONFERENCE ARTICLES

3. **I. B. C. M. Rocha**, S. Raijmaekers, R.P.L. Nijssen, F.P. van der Meer, L.J. Sluys. *Experimental/numerical study of anisotropic water diffusion in glass/epoxy composites.* IOP Conference Series: Materials Science and Engineering, **139**, 1-8 (2016).

2. **I. B. C. M. Rocha**, S. Raijmaekers, R.P.L. Nijssen, F.P. van der Meer, L.J. Sluys. *Experimental/numerical characterization of hygrothermal ageing in glass/epoxy composites.* In: 17th European Conference on Composite Materials, Munich (2016).

1. **I. B. C. M. Rocha**, S. Raijmaekers, R.P.L. Nijssen, F.P. van der Meer. *Hydrothermal ageing of glass/epoxy composites for wind turbine blades.* In: 20th International Conference on Composite Materials (ICCM), Copenhagen (2015).

CONFERENCE ABSTRACTS

5. **I. B. C. M. Rocha**, F.P. van der Meer, L.J. Sluys. *Efficient micromechanical modeling of fatigue in composites through time homogenization and reduced-order modeling.* In: 10th European Solid Mechanics Conference (ESMC), Bologna (2018).

4. **I. B. C. M. Rocha**, F.P. van der Meer, S. Raijmaekers, R.P.L. Nijssen, L.J. Sluys. *Experimental/numerical study of monotonic and cyclic hygrothermal ageing in glass/epoxy composites.* In: 6th ECCOMAS Thematic Conference on the Mechanical Response of Composites, Eindhoven (2017).

3. **I. B. C. M. Rocha**, F.P. van der Meer, R.P.L. Nijssen, L.J. Sluys. *Micromechanical multitemporal analysis of hygrothermal effects on the durability of glass/epoxy composites.* In: 20th International Conference on Composite Structures, Paris (2017).

2. **I. B. C. M. Rocha**, F.P. van der Meer, R.P.L. Nijssen, L.J. Sluys. *Multispatial/multitemporal homogenisation analysis of hygrothermal fatigue in glass/epoxy composites.* In: Fifth International Conference on Computational Modeling of Fracture and Failure of Materials and Structures, Nantes (2017).

1. **I. B. C. M. Rocha**, R.P.L. Nijssen, F.P. van der Meer, L.J. Sluys. *Multiphysics analysis of hygrothermal ageing of glass/epoxy composites in an FE^2 framework.* In: 7th European Congress on Computational Methods in Applied Sciences and Engineering, Crete (2016).